キレート型カルベン配位子を持つ発光性異種多核金属錯体に関する研究

A Study on Luminescent Heteropolynuclear Complexes Having NHC-based Chelate Ligands

2019

長崎大学大学院工学研究科

MOON SANGJOON

Contents

Chapter 1

General introduction

1-1. Phosphorescence Pt(II) complex

It is known that d^6 low-spin complexes such as Ru(II), Os(II), Rh(III), Ir(III) and Re(I) complexes, d^8 square planar complexes such as Pt(II) and Pd(II) complexes and lanthanide complexes have tendency to show bright luminescence.[1] These d^6 and d^8 complexes often accompany aromatic amine ligands. In 1983, von Zelewsky and his co-worker reported the first homoleptic Pt(II) complex having bis(C^N) chelate by using 2-phenylpyridinate (ppy).[2] It is interesting that the Pt(II) complex, $[Pt(ppy)_2]$, showed very strong emission. They also prepared related bis(C^N) chelate Pt(II) complexes, $[Pt(thpy)_2]$ and $[Pt(bhq)_2]$, and studied their photophysical properties at room temperature as well as at low temperature.[3] However,

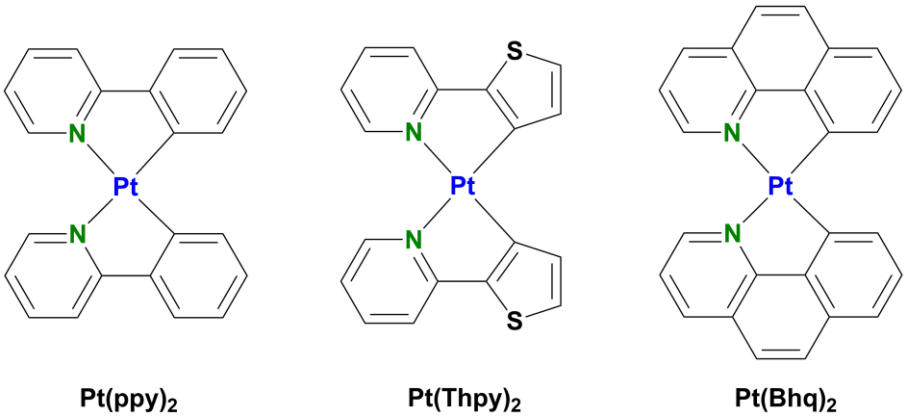

Figure 1-1. Structures of luminescent Pt(II) complexes.[2,3]

detailed theoretical considerations were not performed in their work. We had to wait for the discussions of photophysical properties of Pt(II) complexes from the theoretical viewpoints until 1990s. Miskowski and Houlding measured emission spectra of mononuclear Pt(II) complexes having α-diimine chelate ligands such as 2,2'-bipyridine (bpy) and 1,10-phenanthroline (phen) and discussed their photophysical properties in detail.[4] Then, Gray, Connick and Che participated in this research field, and they studied photophysical properties of not only Pt(II) complexes having C^N and N^N bidentate chelate ligands[5] but also those with tridentate ligands such as terpyridine precursor (**Figure 1-2**).[6,7]

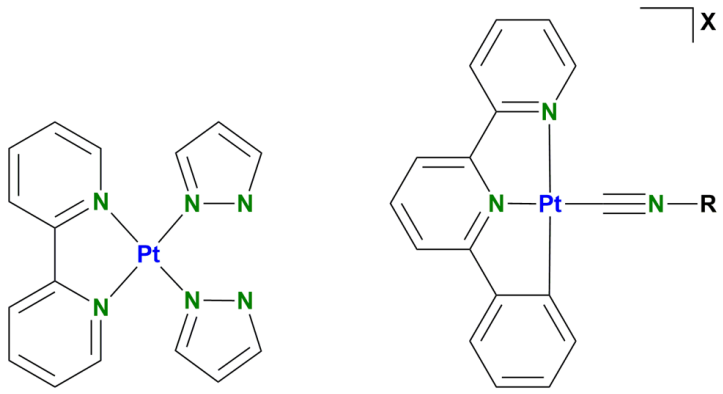

Figure 1-2. Square-planar mononuclear Pt(II) complexes having N^N and N^N^C chelate ligands.[5,8]

Generally, mononuclear Pt(II) complexes having α-diimine (N^N chelate) or ppy derivatives (C^N chelate) exhibit emission attributed to the emissive states derived from metal-to-ligand charge transfer (MLCT) transitions or intra-ligand (IL) transitions depending on the nature of chelate ligands (**Figure 1-3**).[8] In addition, when the Pt···Pt interaction increases due to the formation of butterfly-shaped dinuclear complex or the stacking of planar complexes in the solid state, the MLCT emission bands shift to lower energy. These lower energy bands are particularly called metal-metal-to-ligand charge transfer (MMLCT) bands. For example, it was reported for the butterfly-shaped dinuclear Pt(II) complexes having pyrazolate bridging ligands that the ratio of the dual emission derived from triplet excited states can be controlled by the systematic change of bulkiness of substituent groups on the bridging ligands and C^N chelate ligands (**Figure 1-4**).[9,10] Similar dependence of emission energy on the intramolecular Pt···Pt distances has also been reported in several other butterfly-shaped dinuclear Pt(II) complexes.[11,12]

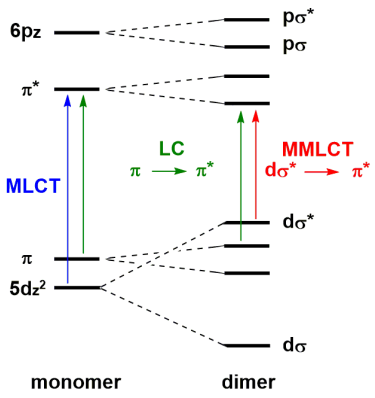

Figure 1-3. Schematic molecular orbital diagram illustrating mononuclear and dinuclear Pt(II) complexes.

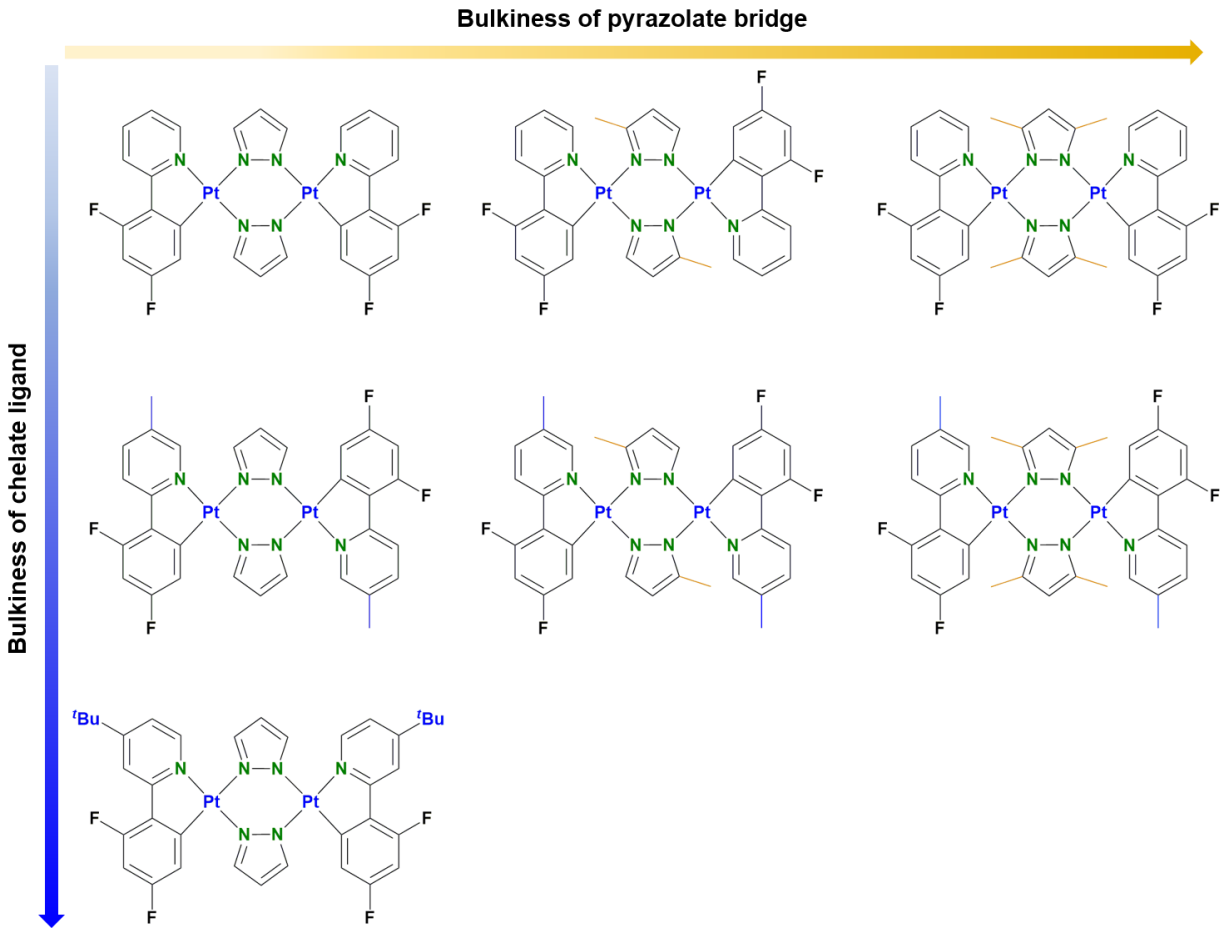

Figure 1-4. Chemical structures of pyrazolate-bridged binuclear platinum complexes with difluorophenylpyridine (dfppy) based ligands as the butterfly wings and pyrazolate (PZ) ligands as the butterfly body.[9]

Solid state intermolecular interactions and metal···metal interactions have also been attracting much attention, because the emission energy shifts based on the change of these interactions are observed as the emission color changes by mechanical grinding of solid samples (mechanochromism) or vapor diffusion to them (vapochromism) (**Figure 1-5**a).[13–15] The shift of emission energy by mechanochromism and vapochromism have been observed not only for Pt(II) complexes but also for a variety of d^{10} transition metal complexes, and Ito and his co-workers reported interesting these phenomena (**Figure 1-5**b).[16]

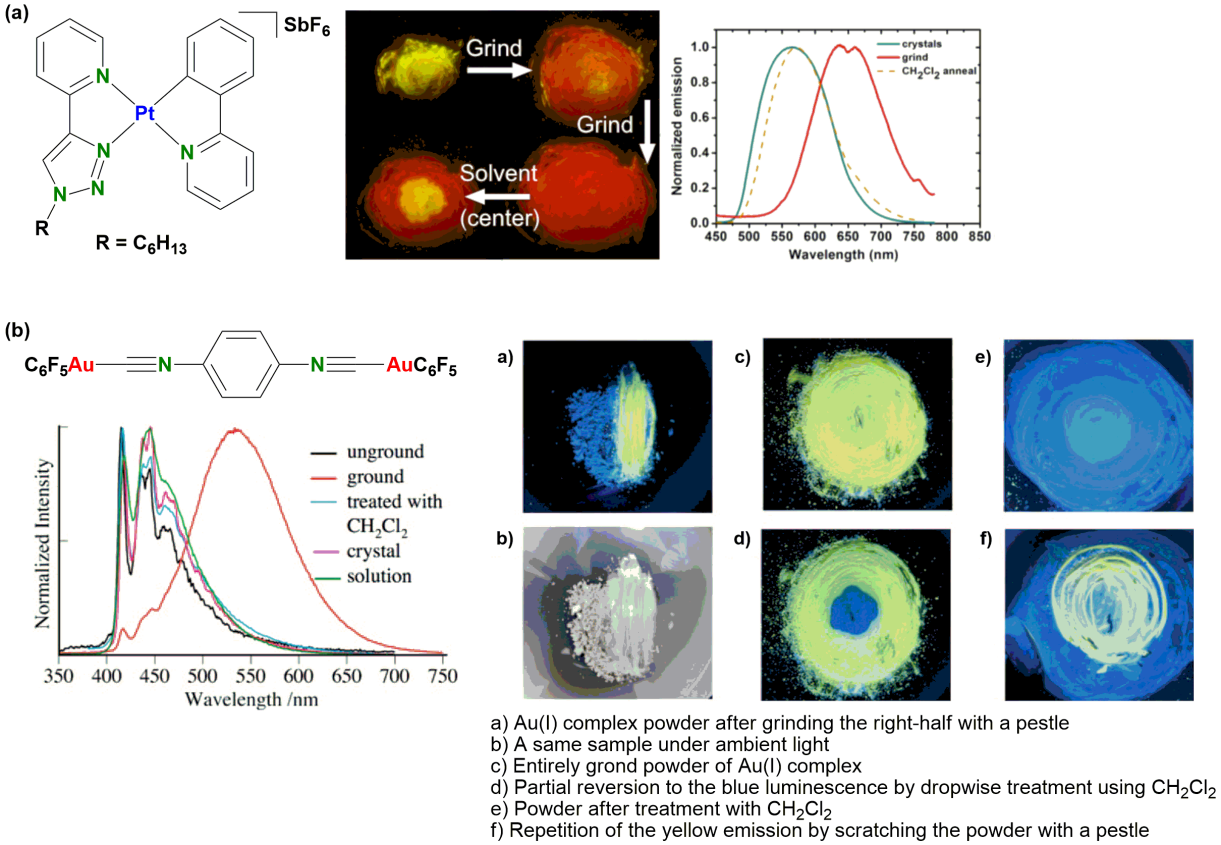

a) Au(I) complex powder after grinding the right-half with a pestle
b) A same sample under ambient light
c) Entirely grond powder of Au(I) complex
d) Partial reversion to the blue luminescence by dropwise treatment using CH_2Cl_2
e) Powder after treatment with CH_2Cl_2
f) Repetition of the yellow emission by scratching the powder with a pestle

Figure 1-5. Mechanochromic behavior. (a) Square-planar Pt(II) complex showing red-shift of phosphorescence by intermolecular Pt···Pt and/or π-π interaction.[14] (b) Emission spectra and photographs of Au(I) complex.[16]

Luminescent Pt(II) complexes are recognized as good candidates for dopant of organic light-emitting diodes (OLEDs).[17–23] Particularly blue-emitting materials have recently attracted considerable interest, leading to the development of blue-emitting Pt(II) complexes with high color purity. The Pt(II) complexes having tetradentate chelate ligand or carbene containing chelate ligands are expected to show intense blue emission.

1-2. Carbene complex

A carbene is a molecule having neutral carbon atom with two unshared valance electrons, and thus six electrons in valence shell. The general formula of carbene are R-(C:)-R' or R=C:. Generally, carbene has two electronic state such as singlet and triplet as shown in **Figure 1-6**. Among these carbenes, N-Heterocyclic Carbenes (NHCs) and Cyclic Alkyl(Amino) Carbenes (CAACs) are commonly used (**Figure 1-6**b).[24–26] Especially, NHCs are defined as heterocyclic species containing a carbene carbon atom and at least one nitrogen atom within the ring structure. A general electronic structure of NHC is shown in **Figure 1-7**. The adjacent nitrogen atoms having σ-electron withdrawing and π-electron donating nature stabilize this cyclic structure both inductively by lowering the energy of the occupied σ-orbital and mesomerically by donating electron density into the empty p-orbital (**Figure 1-7**).[27] The lone pair situated in the plane of the heterocyclic ring of NHCs renders these compounds nucleophilic. The principal consequence of this characteristic is the tendency of NHCs to play a role as σ-donor and bind to a wide range of metallic and non-metallic species.

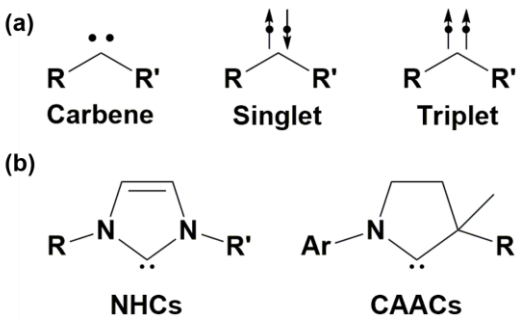

Figure 1-6. (a) Singlet and triplet carbenes. (b) NHCs and CAACs.

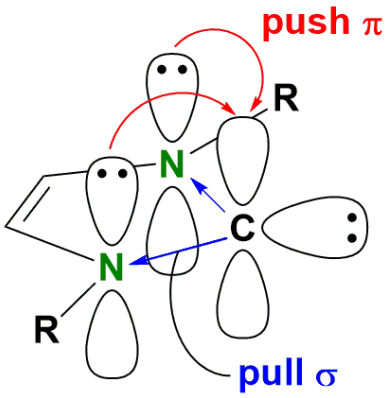

Figure 1-7. Ground state electronic structure of N-heterocyclic carbene.

When NHCs are incorporated into chelate ligands, the NHC groups influence on a metal center by thier σ-donating and π-withdrawing nature.[28–30] Since σ-donating nature of carbene group destabilizes triplet metal-centered (MC) d-d state, the non-radiative decay from ^{3}MC

excited state decreases. Thus, transition metal complexes having NHC ligand have high quantum yield (**Figure 1-8**).[31] Especially, Pt(II) complexes having NHC chelate ligand showed deep-blue emission color in the solid state and PMMA film with high emission quantum yield.[24,32–38] Therefore, Pt(II) complexes having NHC chelate ligand have attracted attention as a blue emitter.

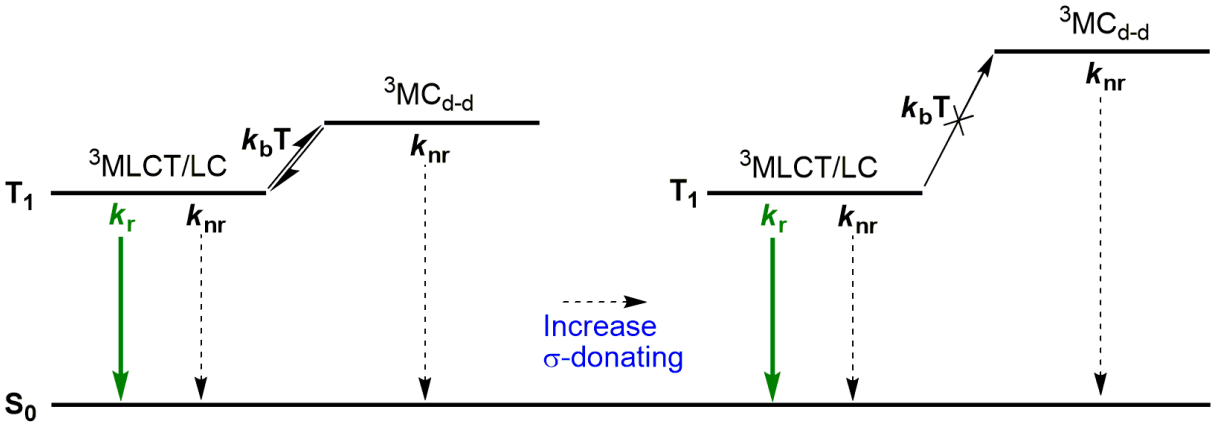

Figure 1-8. Partial excited state diagram for metal complexes having NHC chelate ligand. When strong σ-donating chelate ligand are incorporated, energy level of ^{3}MC excited state increases.[31]

1-3. Heteropolynuclear metal complex and dative bond

Similarly to the homometallic metal–metal interactions such as intramolecular Pt···Pt interactions of dinuclear Pt(II) complexes and intermolecular Pt···Pt interactions of square-planar mononuclear Pt(II) complexes, the heterometallic metal–metal interactions are also were observed in the heteropolynuclear metal complexes. If heterometallic metal–metal interactions are observed in the ground state, the metal–metal distances between heterometal atoms are shorter than the sum of the van der waals radii of each atoms. And, the heterometallic metal–metal interactions in excited state can be observed as the change of emission energies corresponding to the incorporated heterometal atoms (**Figure 1-9**).[39,40] This

phenomenon can be explained by the bonding interaction among heterometal atoms in the excited state.

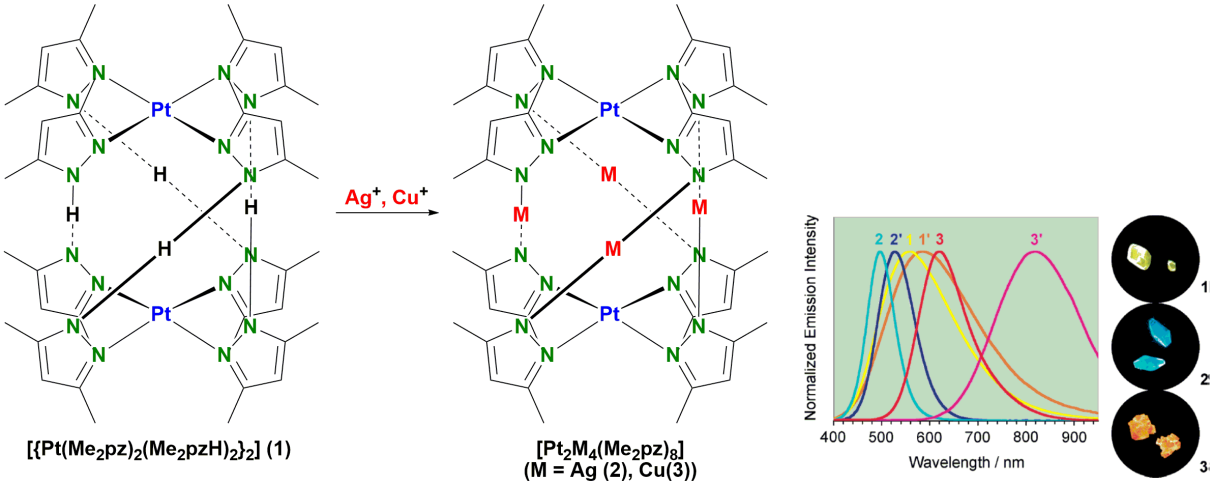

Figure 1-9. Preparation methods of heteropolynuclear complexes, $[Pt_2M_4(Me_2pz)_8]$ (M = Ag(I), Cu(I)) and the emission spectra.[39]

In particular case where the chelate ligand possesses ipso carbon atom, strong metal–metal interactions between heterometal atoms lead to the formation of dative bond. The dative bond in metal complex is usually formed by electron donation from a filled d-orbital of metal atom to a vacant orbital of other metal atom.[41–52] Although the Pt → M (M = Cu(I), Ag(I), Au (I)) dative bonds are observed in various kinds of heteropolynuclear complexes, one of the most popular dative bonds is the Pt → Ag dative bond. For example, it is known that the reactions of anionic mononuclear Pt(II) complexes bearing cyclometalated benzoquinolinate and two pentahalophenyl ligands with Ag(I) ions afford heteropolynuclear complexes with Pt → Ag dative bonds.[45,47] However, it is likely that the heteropolynuclear complexes containing Pt → Ag dative bonds formed by the reaction of the mononuclear precursor complex (or complex ion) with the Ag(I) ion are less stable in solution, owing to the labile nature of the Pt → Ag dative bonds. This is in contrast to the Pt → Au complex containing Pt → Au dative bonds, which is more stable in solution without supporting bridging ligands.[51] Since the reactivity and

photophysical properties of Pt-Ag complexes containing Pt → Ag dative bonds are not fully understood,[41,53,54] it is important to construct a system stable in solution for elucidating the nature of the Pt → Ag dative bond. The strength of Pt → M dative bond can be estimated by the extent of downfield shift of the ^{195}Pt NMR signal. It is also interesting that the isomerization rate of heteropolynuclear complex can be controlled by the formation of Pt → M dative bond.[55]

1-4. Aim and outline of this thesis

Square-planar mononuclear Pt(II) complexes with carbene chelate ligand have tendency to show high-energy phosphorescence in the solid state. Pt(II) center in the mononuclear complex can function as an electron donor, forming Pt → M dative bond with Lewis acidic metal atoms such as Cu(I), Ag(I) and Au(I). In this thesis, the synthesis and development of new types of heteropolynuclear Pt(II) complexes consisting of group 11 element and chelate ligand based on N-heterocyclic carbene are intended. These complexes are strongly expected to show remarkable photophysical properties and interesting dynamic behavior.

This thesis is composed of five chapters. In chapter 1, the background of a research and the purpose of this thesis are described.

Chapter 2 describes the synthesis and photophysical properties of butterfly-shaped dinuclear Pt(II) complex. Dinuclear Pt(II) complex was obtained by the reaction of mononuclear Pt(II) complex with 3,5-dimethyl pyrazole in the presence of base. The molecular structure of dinuclear complex was confirmed by single crystal X-ray analysis. Dinuclear complex showed bluish-green emission in the solid state at room temperature.

In chapter 3, synthesis and properties of heteropolynuclear metal complexes having pyridyl-NHC chelate ligand are described. Heteropolynuclear metal complex was obtained by

the reaction of mononuclear Pt(II) complex having pyridyl-NHC chelate ligand and Me_2pz ligands with $AgPF_6$ in the presence of base. Molecular structures of heteropolynuclear metal complex was confirmed by single crystal X-ray analysis. heteropolynuclear metal complex showed green emission color in the solid state. Also heteropolynuclear metal complex showed dynamic behavior in $CDCl_3$.

Chapter 4 describes the synthesis, structural and photophysical properties of Pt(II) complexes having phenyl-NHC chelate ligand. The heteropolynuclear Pt_2Ag_3 complex was obtained from mononuclear Pt(II) complex having phenyl-NHC chelate ligand and dimethyl pyrazole. The formation of Pt_2Ag_3 complex was confirmed by NMR spectroscopy, ESI-MS, elemental analysis and single crystal X-ray analysis. Intramolecular Pt → Ag dative bond was observed by single crystal X-ray analysis and ^{195}Pt NMR spectroscopy. Also, the Pt_2Ag_3 complex showed novel dynamic behavior in solution, which was revealed by VT NMR spectroscopy.

In chapter 5, summary of this thesis and future prospects of this research are described.

1-5. Reference

(1) Sasaki, Y. *Bull. Jpn. Soc. Coord. Chem.* **2006**, *48*, 50–59.

(2) Chassot, L.; von Zelewsky, A. *Helv. Chim. Acta* **1983**, *66* (8), 2443–2444.

(3) Maestri, M.; Sandrini, D.; Balzani, V.; Chassot, L.; Jolliet, P.; Von Zelewsky, A. *Chem. Phys. Lett.* **1985**, *122* (4), 375–379.

(4) Miskowski, V. M.; Houlding, V. H. *Inorg. Chem.* **1991**, *30* (23), 4446–4452.

(5) Connick, W. B.; Miskowski, V. M.; Houlding, V. H.; Gray, H. B. *Inorg. Chem.* **2000**, *39* (12), 2585–2592.

(6) Bailey, J. A.; Miskowski, V. M.; Gray, H. B. *Inorg. Chem.* **1993**, *32* (4), 369–370.

(7) Lai, S. W.; Chan, M. C. W.; Cheung, T. C.; Peng, S. M.; Che, C. M. *Inorg. Chem.* **1999**, *38* (18), 4046–4055.

(8) Lai, S.-W.; Che, C.-M. *Top. Curr. Chem.* **2004**, *241*, 27–63.

(9) Zhou, C.; Tian, Y.; Yuan, Z.; Han, M.; Wang, J.; Zhu, L.; Tameh, M. S.; Huang, C.; Ma, B. *Angew. Chem. Int. Ed.* **2015**, *54* (33), 9591–9595.

(10) Ma, B.; Li, J.; Djurovich, P. I.; Yousufuddin, M.; Bau, R.; Thompson, M. E. *J. Am. Chem. Soc.* **2005**, *127* (1), 28–29.

(11) Zhou, C.; Yuan, L.; Yuan, Z.; Doyle, N. K.; Dilbeck, T.; Bahadur, D.; Ramakrishnan, S.; Dearden, A.; Huang, C.; Ma, B. *Inorg. Chem.* **2016**, *55* (17), 8564–8569.

(12) Han, M.; Tian, Y.; Yuan, Z.; Zhu, L.; Ma, B. *Angew. Chem. Int. Ed.* **2014**, *53* (41), 10908–10912.

(13) Yam, V. W. W.; Au, V. K. M.; Leung, S. Y. L. *Chem. Rev.* **2015**, *115* (15), 7589–7728.

(14) Krikorian, M.; Liu, S.; Swager, T. M. *J. Am. Chem. Soc.* **2014**, *136* (8), 2952–2955.

(15) Kato, M. *Bull. Chem. Soc. Jpn.* **2007**, *80* (2), 287–294.

(16) Ito, H.; Saito, T.; Oshima, N.; Kitamura, N.; Ishizaka, S.; Hinatsu, Y.; Wakeshima, M.; Masako, K.; Kiyoshi, T.; Masaya, S. *J. Am. Chem. Soc.* **2008**, *130* (31), 10044–10045.

(17) D'Andrade, B. W.; Brooks, J.; Adamovich, V.; Thompson, M. E.; Forrest, S. R. *Adv. Mater.* **2002**, *14* (15), 1032–1036.

(18) Furuta, P. T.; Deng, L.; Garon, S.; Thompson, M. E.; Fréchet, J. M. J. *J. Am. Chem. Soc.* **2004**, *126* (47), 15388–15389.

(19) Ma, B.; Djurovich, P. I.; Garon, S.; Alleyne, B.; Thompson, M. E. *Adv. Funct. Mater.* **2006**, *16* (18), 2438–2446.

(20) Borek, C.; Hanson, K.; Djurovich, P. I.; Thompson, M. E.; Aznavour, K.; Bau, R.; Sun, Y.; Forrest, S. R.; Brooks, J.; Michalski, L.; Brown, J. *Angew. Chem. Int. Ed.* **2007**, *46* (7), 1109–1112.

(21) Hang, X.-C.; Fleetham, T.; Turner, E.; Brooks, J.; Li, J. *Angew. Chemie Int. Ed.* **2013**, *52* (26), 6753–6756.

(22) Fleetham, T.; Li, G.; Wen, L.; Li, J. *Adv. Mater.* **2014**, *26* (41), 7116–7121.

(23) Liao, K.-Y.; Hsu, C.-W.; Chi, Y.; Hsu, M.-K.; Wu, S.-W.; Chang, C.-H.; Liu, S.-H.; Lee, G.-H.; Chou, P.-T.; Hu, Y.; Robertson, N. *Inorg. Chem.* **2015**, *54* (8), 4029–4038.

(24) Visbal, R.; Gimeno, M. C. *Chem. Soc. Rev.* **2014**, *43* (10), 3551–3574.

(25) Romanov, A. S.; Bochmann, M. *Organometallics* **2015**, *34* (11), 2439–2454.

(26) Hamze, R.; Jazzar, R.; Soleilhavoup, M.; Djurovich, P. I.; Bertrand, G.; Thompson, M. E. *Chem. Commun.* **2017**, *53* (64), 9008–9011.

(27) Hopkinson, M. N.; Richter, C.; Schedler, M.; Glorius, F. *Nature* **2014**, *510* (7506), 485–496.

(28) Budagumpi, S.; Haque, R. A.; Salman, A. W. *Coord. Chem. Rev.* **2012**, *256* (17-18), 1787-1830.

(29) Gu, S.; Xu, H.; Zhang, N.; Chen, W. *Chem. Asian J.* **2010**, *5* (7), 1677–1686.

(30) Lee, J.; Chen, H. F.; Batagoda, T.; Coburn, C.; Djurovich, P. I.; Thompson, M. E.; Forrest, S. R. *Nat. Mater.* **2016**, *15* (1), 92–98.

(31) Na, H.; Cañada, L. M.; Wen, Z.; I-Chia Wu, J.; Teets, T. S. *Chem. Sci.* **2019**, *10* (25), 6254–6260.

(32) Fuertes, S.; Chueca, A. J.; Arnal, L.; Martín, A.; Giovanella, U.; Botta, C.; Sicilia, V. *Inorg. Chem.* **2017**, *56* (9), 4829–4839.

(33) Fuertes, S.; Chueca, A. J.; Perálvarez, M.; Borja, P.; Torrell, M.; Carreras, J.; Sicilia, V. *ACS Appl. Mater. Interfaces* **2016**, *8* (25), 16160–16169.

(34) Arnal, L.; Fuertes, S.; Martín, A.; Sicilia, V. *Chem. Eur. J.* **2018**, *24* (37), 9377–9384.

(35) Fuertes, S.; García, H.; Perálvarez, M.; Hertog, W.; Carreras, J.; Sicilia, V. *Chem. Eur. J.* **2015**, *21* (4), 1620–1631.

(36) Pinter, P.; Mangold, H.; Stengel, I.; Münster, I.; Strassner, T. *Organometallics* **2016**, *35* (5), 673–680.

(37) Tenne, M.; Metz, S.; Wagenblast, G.; Münster, I.; Strassner, T. *Dalton Trans.* **2015**, *44* (18), 8444–8455.

(38) Tenne, M.; Metz, S.; Wagenblast, G.; Münster, I.; Strassner, T. *Organometallics* **2015**, *34* (18), 4433–4440.

(39) Umakoshi, K.; Kojima, T.; Saito, K.; Akatsu, S.; Onishi, M.; Ishizaka, S.; Kitamura, N.; Nakao, Y.; Sakaki, S.; Ozawa, Y. *Inorg. Chem.* **2008**, *47* (12), 5033–5035.

(40) Umakoshi, K.; Saito, K.; Arikawa, Y.; Onishi, M.; Ishizaka, S.; Kitamura, N.; Nakao, Y.; Sakaki, S. *Chem. Eur. J.* **2009**, *15* (17), 4238–4242.

(41) Uson, R.; Fornies, J.; Tomas, M.; Casas, J. M.; Cotton, F. A.; Falvello, L. R.; Llusar, R. *Organometallics* **1988**, *7* (11), 2279–2285.

(42) Yamaguchi, T.; Yamazaki, F.; Ito, T. *J. Am. Chem. Soc.* **2001**, *123* (4), 743–744.

(43) Falvello, L. R.; Forniés, J.; Martín, A.; Sicilia, V.; Villarroya, P. *Organometallics* **2002**, *21* (22), 4604–4610.

(44) Janzen, D. E.; Mehne, L. F.; VanDerveer, D. G.; Grant, G. J. *Inorg. Chem.* **2005**, *44* (23), 8182–8184.

(45) Forniés, J.; Ibáñez, S.; Martín, A.; Sanz, M.; Berenguer, J. R.; Lalinde, E.; Torroba, J. *Organometallics* **2006**, *25* (18), 4331–4340.

(46) Moret, M. E.; Chen, P. *J. Am. Chem. Soc.* **2009**, *131* (15), 5675–5690.

(47) Forniés, J.; Ibáñez, S.; Lalinde, E.; Martín, A.; Moreno, M. T.; Tsipis, A. C. *Dalton Trans.* **2012**, *41* (12), 3439–3451.

(48) Fuertes, S.; Brayshaw, S. K.; Raithby, P. R.; Schiffers, S.; Warren, M. R. *Organometallics* **2012**, *31* (1), 105–119.

(49) Martín, A.; Belío, Ú.; Fuertes, S.; Sicilia, V. *Eur. J. Inorg. Chem.* **2013**, No. 12, 2231–2247.

(50) Baya, M.; Belío, Ú.; Forniés, J.; Martín, A.; Perálvarez, M.; Sicilia, V. *Inorg. Chim. Acta* **2015**, *424*, 136–149.

(51) Baya, M.; Belío, Ú.; Fernández, I.; Fuertes, S.; Martín, A. *Angew. Chem. Int. Ed.* **2016**, *55* (24), 6978–6982.

(52) Moussa, J.; Chamoreau, L. M.; Gullo, M. P.; Degli Esposti, A.; Barbieri, A.; Amouri, H. *Dalton Trans.* **2016**, *45* (7), 2906–2913.

(53) Usón, R.; Fornies, J.; Tomas, M.; Casas, J. M.; Cotton, F. A.; Falvello, L. R. *Inorg. Chem.* **1987**, *26* (21), 3482–3486.

(54) Usón, R.; Forniés, J.; Tomás, M.; Casas, J. M. *Angew. Chemie Int. Ed. Engl.* **1989**, *28* (6), 748–750.

(55) Ueda, M.; Horiuchi, S.; Sakuda, E.; Nakao, Y.; Arikawa, Y.; Umakoshi, K. *Chem. Commun.* **2017**, *53* (48), 6405–6408.

Chapter 2

Synthesis and Photophysical Properties of Butterfly-shaped Dinuclear Pt(II) Complex Having NHC-based chelate ligand

2-1. Introduction

Luminescent square-planar Pt(II) complexes have been increasingly studied as photocatalysts,[1–3] emitting materials,[4–8] and chemical sensors.[9–11] Some luminescent Pt(II) complexes show intermolecular Pt···Pt interactions in the solid state and in concentrated solutions, incorporating characteristic photophysical properties, such as aggregation-induced emission (AIE)[12–16] and white-colored dual emission.[17–20] Their emitting states are attributed to a variety of low-energy excited states depending on the nature of π-type ligands and the extent of in- termolecular metal–metal interactions. The tuning of intramolecular Pt···Pt distances in dinuclear Pt(II) complexes have been achieved by careful selection of substituent groups on the bridging pyrazolate ligands, exhibiting unique photophysical properties in solutions.[21–25]

The Pt(II) complexes having chelating N-heterocyclic carbene (NHC) ligands such as phenyl-NHC,[26–28] bis-NHC[29,30] and pyridyl-NHC[31] have recently been developed as luminescent materials owing to their attractive features. They are expected to show bright emission, because strong σ-donating nature of carbene ligands effectively destabilizes unoccupied 5d-orbital of Pt(II) ion and in conjunction with phenyl, NHC or pyridyl moiety it also destabilizes the LUMO.[32] Another advantage of chelating NHC ligands is bidentate coordination to the central metal ion, which can endow them with thermal stability in the structure. These rigid and robust complexes are likely to show desirable luminescent properties due to effective inhibition of thermal nonradiative pathways. Therefore, Pt(II) complexes having chelating carbene ligands are widely used to develop luminescent materials showing blue emission.

Our group has reported structures and emission properties of heteropolynuclear Pt(II) complexes supported by pyrazolate bridging ligands.[33–39] These heteropolynuclear complexes consist of Pt(II) and group 11 metal ions and are usually prepared from mononuclear Pt(II) complexes having pyrazole and/or pyrazolate acting as monodentate ligands. Moreover,

butterfly-shaped PtPd complex can also be prepared from the mononuclear Pt(II) complex containing bipyrimidine chelate ligand and dimethylpyrazole (Me_2pzH).[35] The mononuclear Pt(II) complexes containing N^N, N^C or C^C chelate ligands and pyrazoles have tendency to form butterfly-shaped dinuclear Pt(II) complexes due to their lower thermal stability. In the course of preparation of heteropolynuclear Pt(II) complex having pyridyl-NHC chelate ligands,[39] I also encountered the formation of butterfly-shaped dinuclear Pt(II) complex.

It is known that employment of NHC carbene donor leads to a significant increase in the LUMO energy, and consequently increases the relative emission energy for the corresponding Ir(III) complexes.[40] The pyridyl-NHC chelate ligand is one of the strong σ-donating neutral ligand, which delocalizes less electron density on Pt atom compared with C^N chelate ligands possessing negative charge such as 2-phenylpyridinate (ppy). Therefore, the dinuclear Pt(II) complexes having pyridyl-NHC chelate ligands are expected to show higher-energy emissions than those having ppy and its derivatives due to weaker Pt···Pt interactions. They are also expected to show unique photophysical properties derived from intra- and intermolecular Pt···Pt interactions.[41] In this chapter, I will describe the selective synthesis and photophysical properties of butterfly-shaped dinuclear Pt(II) complex having pyridyl-NHC chelate ligands and bridging Me_2pz ligands.

2-2. Synthesis of complexes having Py-NHC chelate ligand

The ligand precursor (1-(2-pyridyl)-3-isopropylimidazolium iodide)[42,43] and $[Pt(COD)Cl_2]$[44] was prepared according to the literature methods with slight modifications.

2-2-1. Preparation of [(Py-NHC)PtCl$_2$] (1)

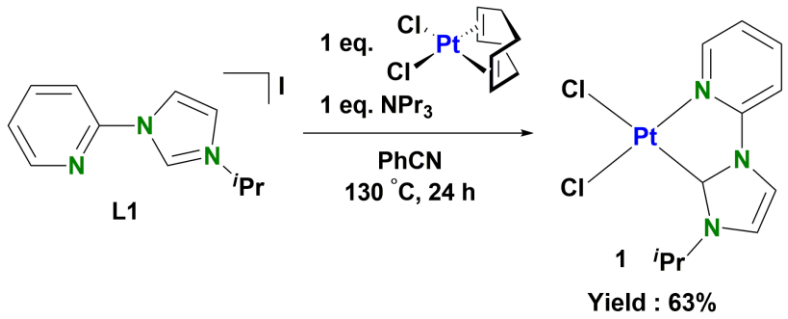

Scheme 2-1. Synthesis of [(Py-NHC)$PtCl_2$] (**1**).

This complex was prepared according to the literature method with slight modifications.[41] A mixture of 1-(2-pyridyl)-3-iso-propylimidazolium iodide (779 mg, 2.47 mmol) and [Pt(COD)Cl2] (COD=1,5-cyclooctadiene) (919 mg, 2.46 mmol) in benzonitrile (50 mL) was heated at 130 °C with stirring for 24 h. After concentration of the reaction mixture under reduced pressure, acetonitrile (10 mL) was added to the mixture and the solution was cooled at 4 °C for 12 h. The yellow crystals were collected, washed with acetonitrile and diethyl ether, and dried in vacuum. Yield 768 mg (63%). Anal. Calcd for $C_{11}H_{13}N_3Cl_2Pt$: C, 29.20; H, 2.90; N, 9.29. Found: C, 29.27; H, 2.60; N, 9.75. ^{1}H NMR (500 MHz, DMSO-d_6, 25 °C): δ = 9.55 (d, J = 6.1 Hz, 1H, H_a), 8.38 (d, J = 2.1 Hz, 1H, H_e), 8.35 (t, J = 7.6 Hz, 1H, H_c), 8.07 (d, J = 8.6 Hz, 1H, H_d), 7.87 (d, J = 2.3 Hz, 1H, H_f), 7.57 (t, J = 6.5 Hz, 1H, H_b), 6.06 (sept, J = 6.4 Hz, 1H, H_g), 1.41 (d, J = 6.7 Hz, 6H, H_h). ^{13}C{^{1}H} NMR (125 MHz, DMSO-d_6, 25 °C): δ = 152.7 (C_i), 148.3 (C_a), 142.7 (C_c), 141.7 (C_j), 123.1 (C_b), 120.7 (C_f), 117.4 (C_e), 112.3 (C_d), 50.3 (C_g), 22.7 (C_h).

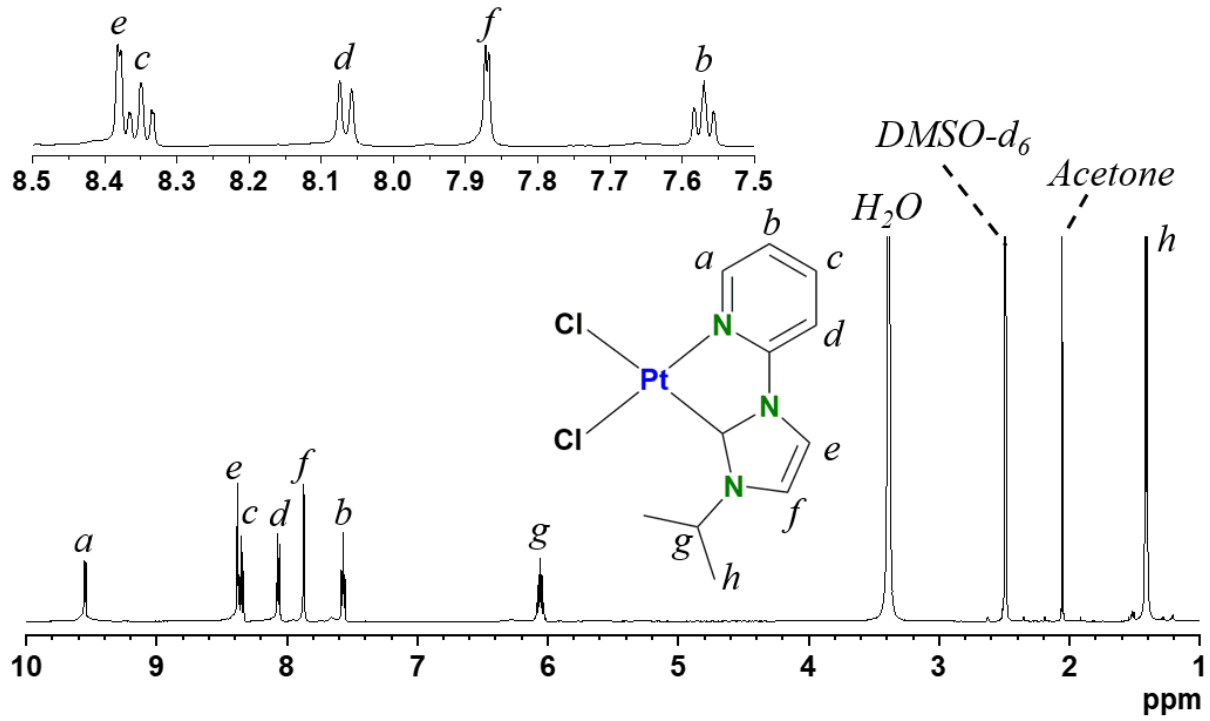

Figure 2-1. ^{1}H NMR spectrum (500 MHz, DMSO-d_6, 25 ℃) of [(Py-NHC)PtCl$_2$] (**1**).

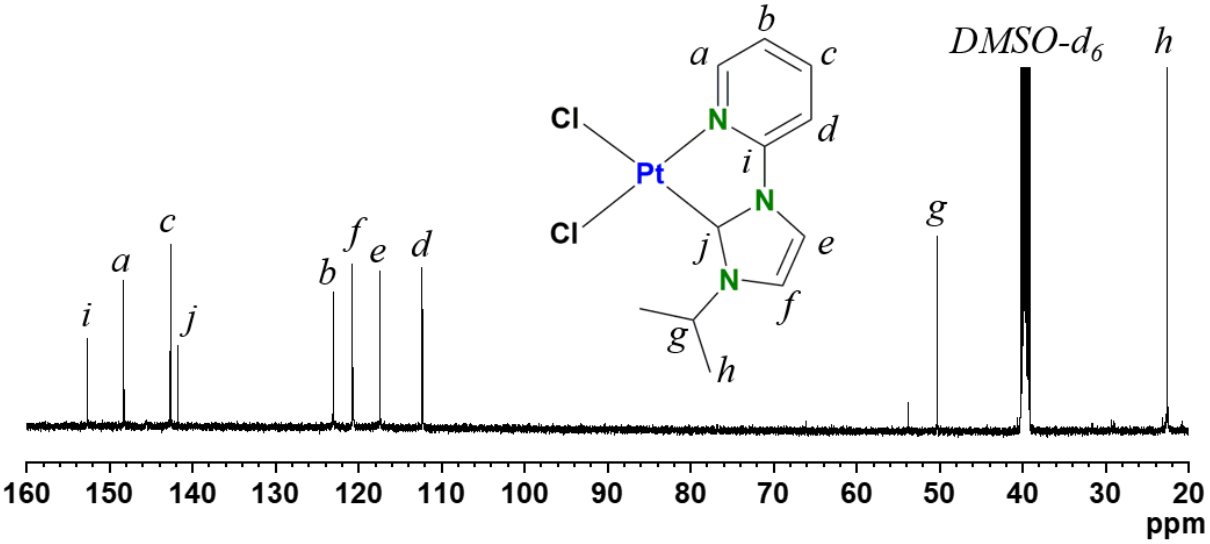

Figure 2-2. ^{13}C{^{1}H} NMR spectrum (125 MHz, DMSO-d_6, 25 ℃) of [(Py-NHC)PtCl$_2$] (**1**).

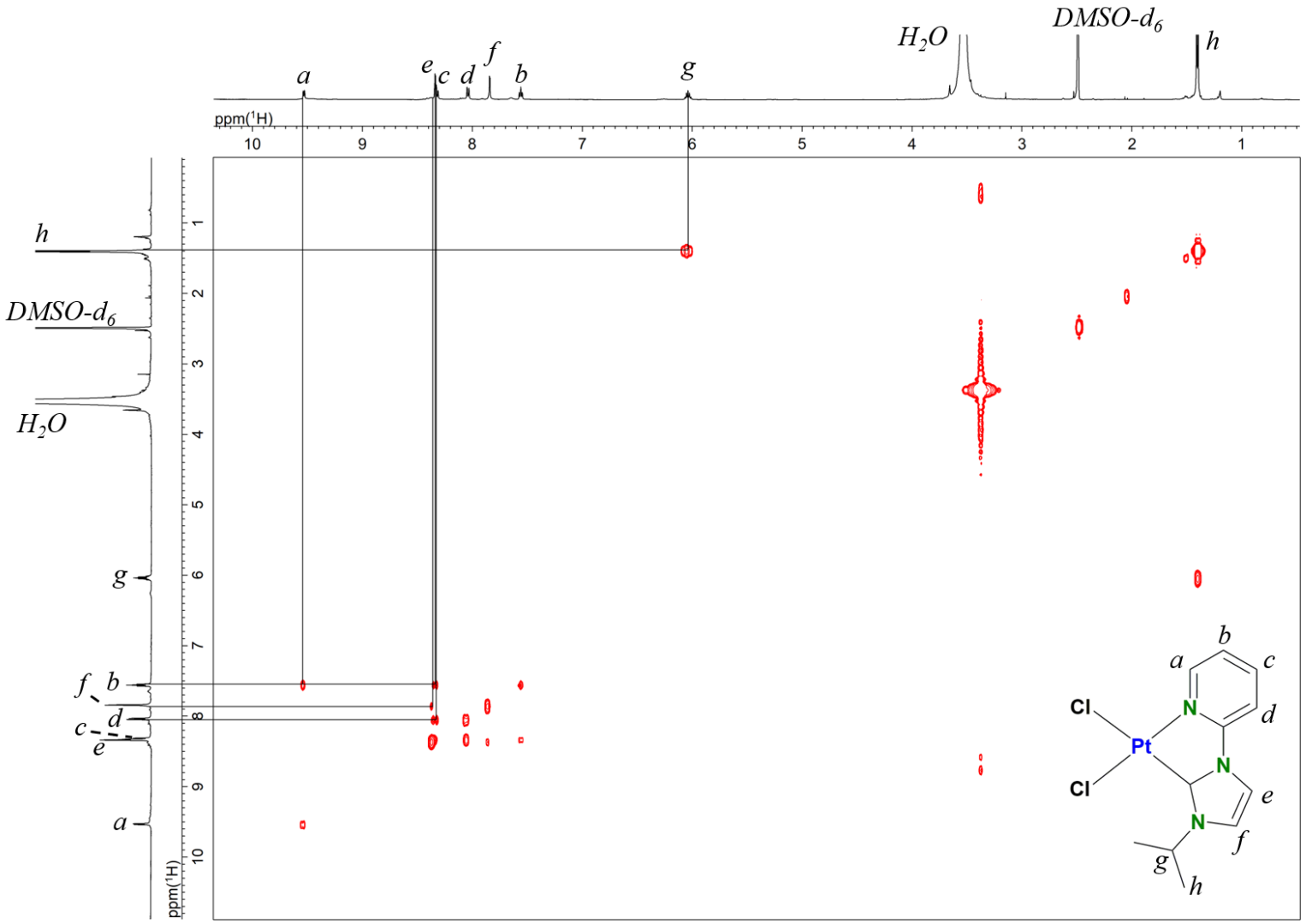

Figure 2-3. ^{1}H-^{1}H COSY spectrum (500 MHz, DMSOe-d_6, 25 ℃) of [(Py-NHC)PtCl$_2$] (**1**).

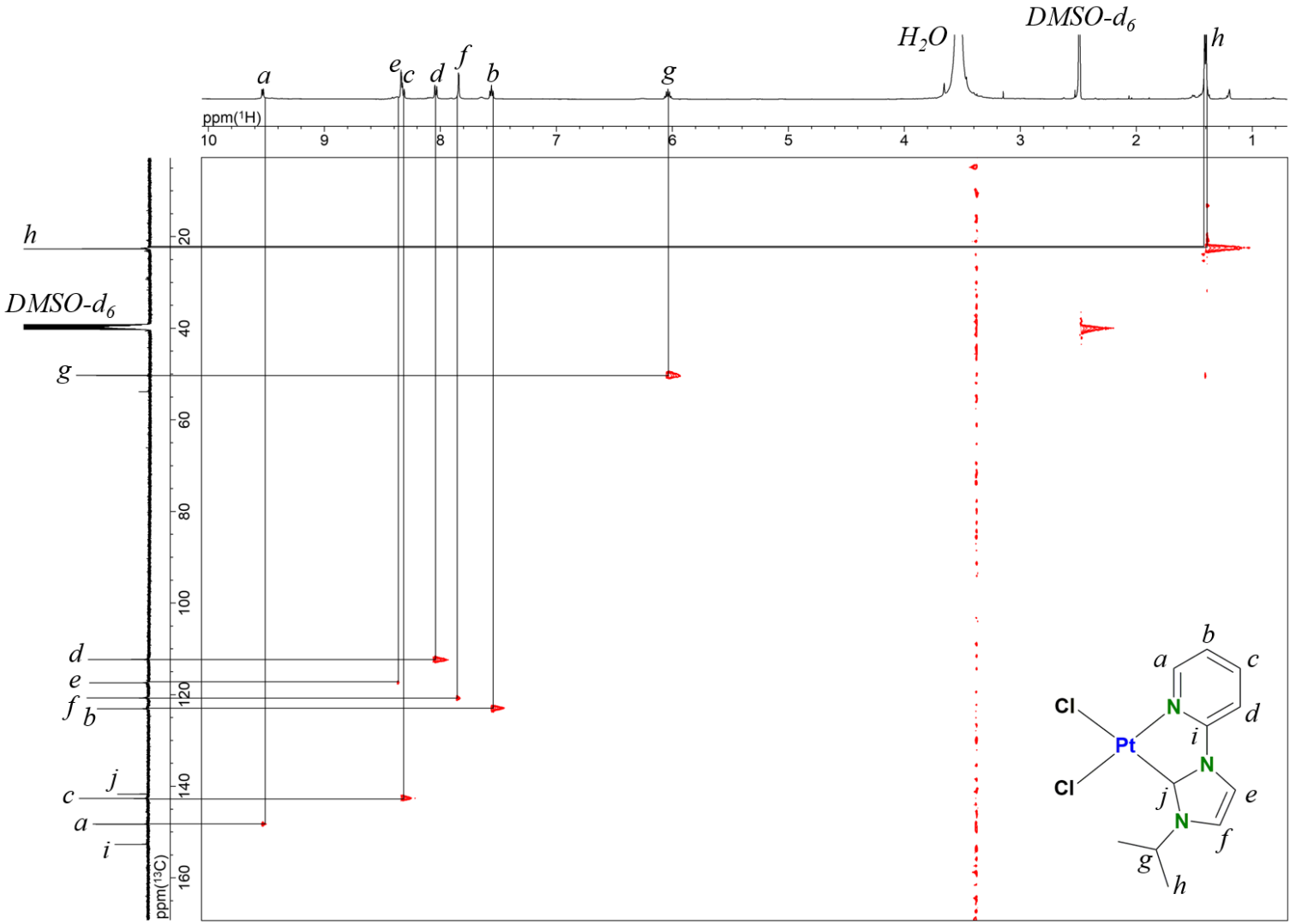

Figure 2-4. ^{1}H-^{13}C HSQC spectrum (500 MHz, DMSOe-d_6, 25 °C) of [(Py-NHC)$PtCl_2$] (**1**).

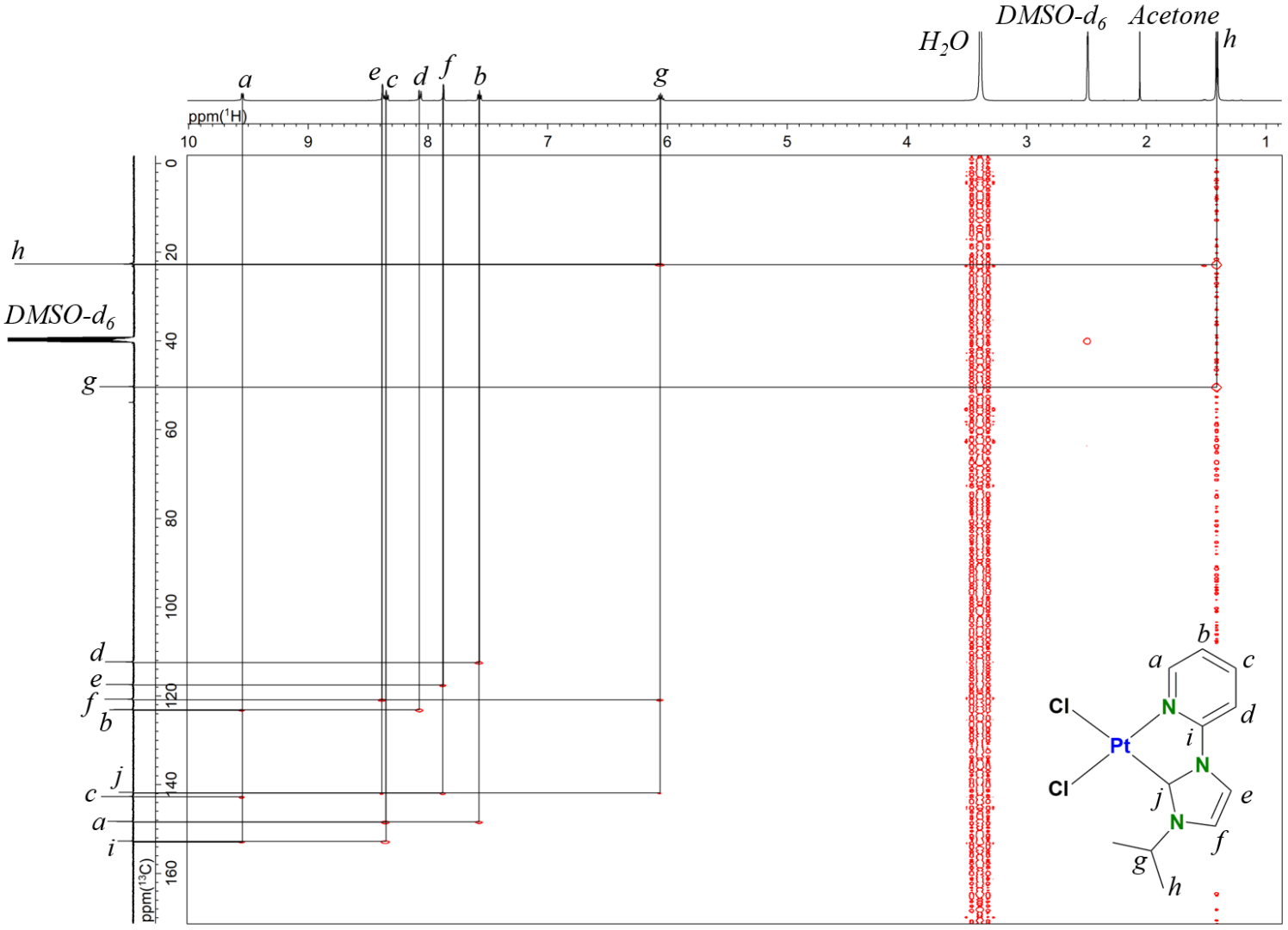

Figure 2-5. ^{1}H-^{13}C HMBC spectrum (500 MHz, DMSOe-d_6, 25 °C) of [(Py-NHC)$PtCl_2$] (**1**).

2-2-2. Preparation of [(Py-NHC)$_2$Pt$_2$(μ-Me$_2$pz)$_2$](BF$_4$)$_2$ (2)

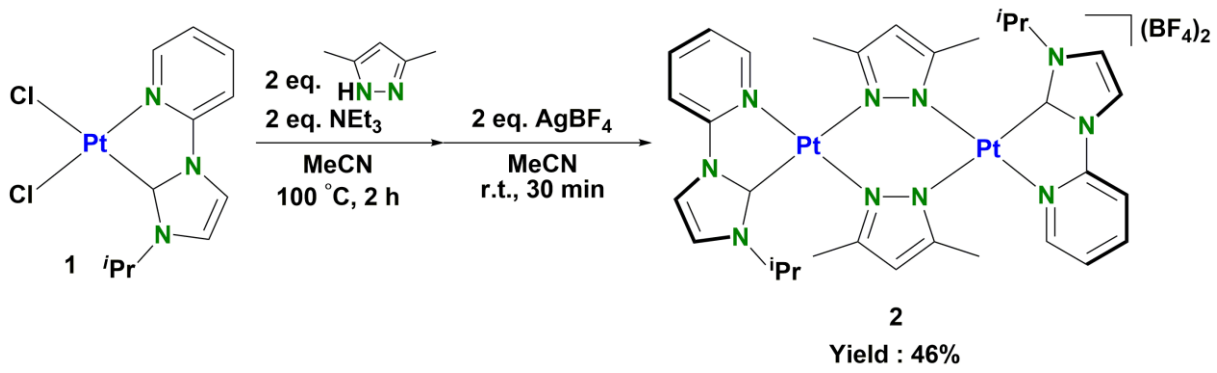

Scheme 2-2. Synthesis of [(Py-NHC)$_2$Pt$_2$(μ-Me$_2$pz)$_2$](BF$_4$)$_2$ (**2**).

A mixture of [(Py-NHC)PtCl$_2$] (47 mg, 0.11 mmol), Me$_2$pzH (26 mg, 0.27 mmol) and NEt$_3$ (30 μL, 0.21 mmol) in acetonitrile (5 mL) was refluxed for 2 h. After heating, AgBF$_4$ (51 mg, 0.26 mmol) was added to the reaction mixture and it was stirred for 30 min at room temperature. The reaction mixture was filtered to remove white precipitate (AgCl). The resulted white precipitate was collected, washed with water and diethyl ether, and dried in vacuo. Yield 28 mg (46%). It was recrystallized from acetonitrile/diethyl ether. Anal. Calcd for $C_{32}H_{40}N_{10}B_2F_8Pt_2$: C, 34.03; H, 3.57; N, 12.41. Found: C, 34.43; H, 3.47; N, 12.75. ^{1}H NMR (500 MHz, Acetonitrile-d_3, 25 ℃): δ = 8.33 (d, J = 5.8 Hz, 2H, H$_a$), 8.30 (ddd, J = 7.8, 7.8, 5.9 Hz, 2H, H$_c$), 7.92 (d, J = 2.5 Hz, 2H, H$_e$), 7.85 (d, J = 8.3 Hz, 2H, H$_d$), 7.45 (ddd, J = 5.9, 5.9, 1.2 Hz, 2H, H$_b$), 7.41 (d, J = 2.4 Hz, 2H, H$_f$), 6.14 (s, 2H, H$_l$), 4.06 (sept, J = 6.6 Hz, 2H, H$_g$), 2.30 (s, 12H, H$_m$), 1.42 (d, J = 6.7 Hz, 6H, H$_h$), 1.04 (d, J = 6.7 Hz, 6H, H$_h$). ^{13}C{^{1}H} NMR (125 MHz, Acetonitrile-d_3, 25 ℃): δ = 154.7 (C$_i$), 150.9 (C$_a$), 150.9 (C$_n$), 150.5 (C$_n$), 150.1 (C$_j$), 145.4 (C$_c$), 125.2 (C$_b$), 121.3 (C$_f$), 119.6 (C$_e$), 114.0 (C$_d$), 107.6 (C$_h$), 51.2 (C$_g$), 24.9 (C$_h$), 22.7 (C$_h$), 15.1 (C$_m$), 14.0 (C$_m$). ESI-MS for [(Py-NHC)$_2$Pt$_2$(μ-Me$_2$pz)$_2$](BF$_4$)$_2$: m/z = 1041.3 [M + BF$_4$]$^+$.

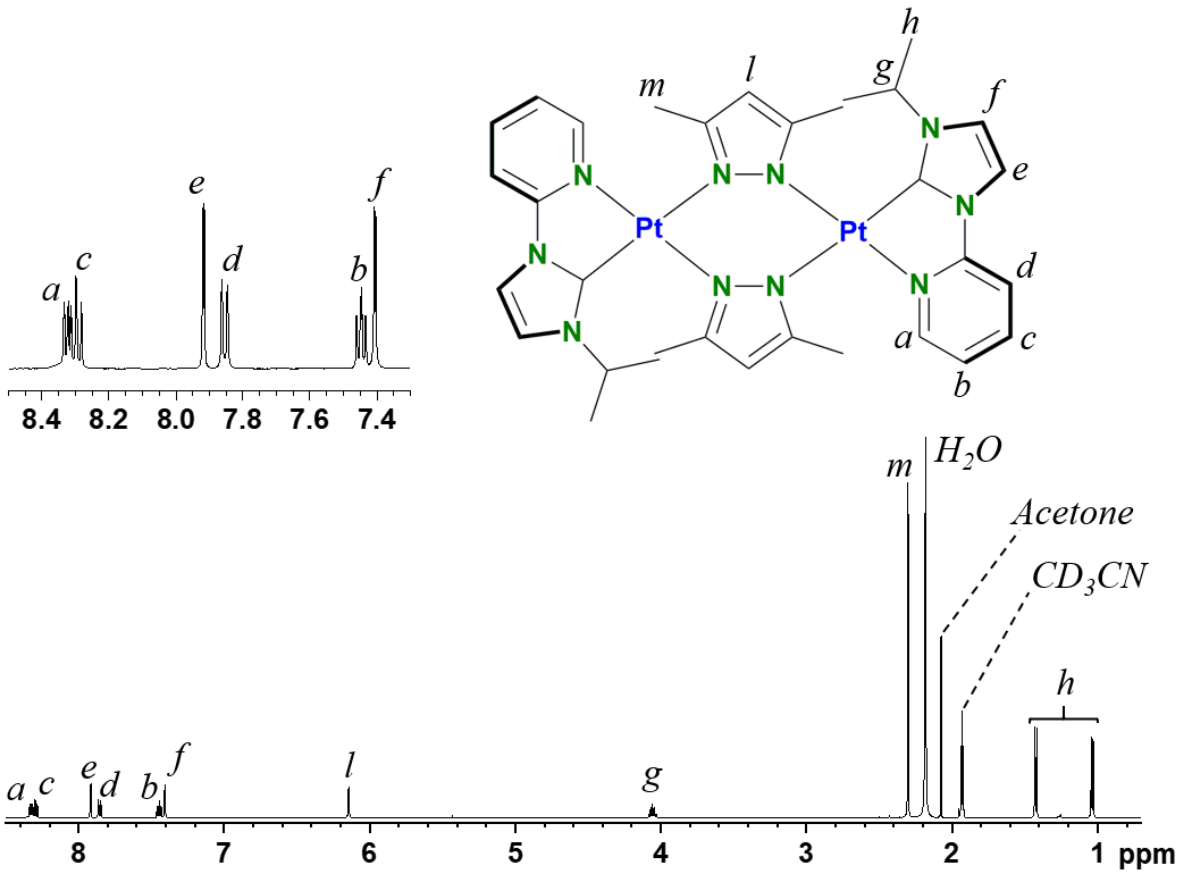

Figure 2-6. ^{1}H NMR spectrum (500 MHz, Acetonitrile-d_3, 25 °C) of $[(\text{Py-NHC})_2\text{Pt}_2(\mu\text{-Me}_2\text{pz})_2](\text{BF}_4)_2$ (**2**).

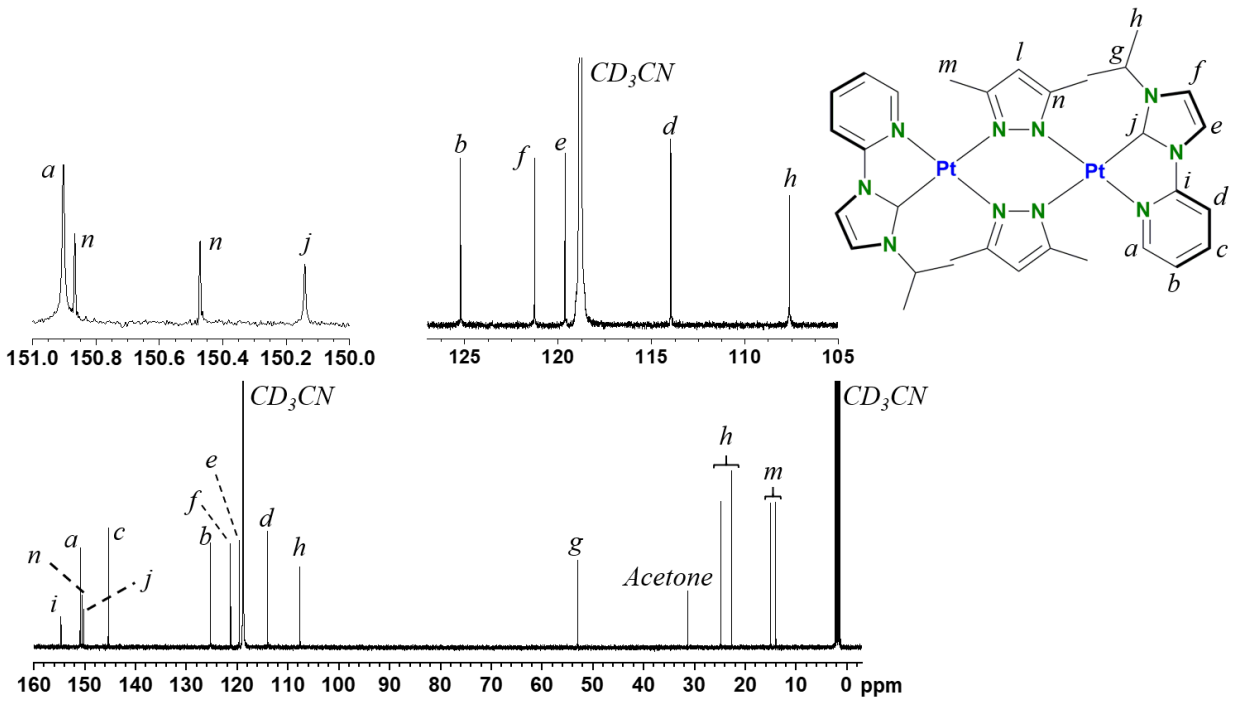

Figure 2-7. $^{13}C\{^{1}H\}$ NMR spectrum (125 MHz, Acetonitrile-d_3, 25 ℃) of $[(Py\text{-}NHC)_2Pt_2(\mu\text{-}Me_2pz)_2](BF_4)_2$ (**2**).

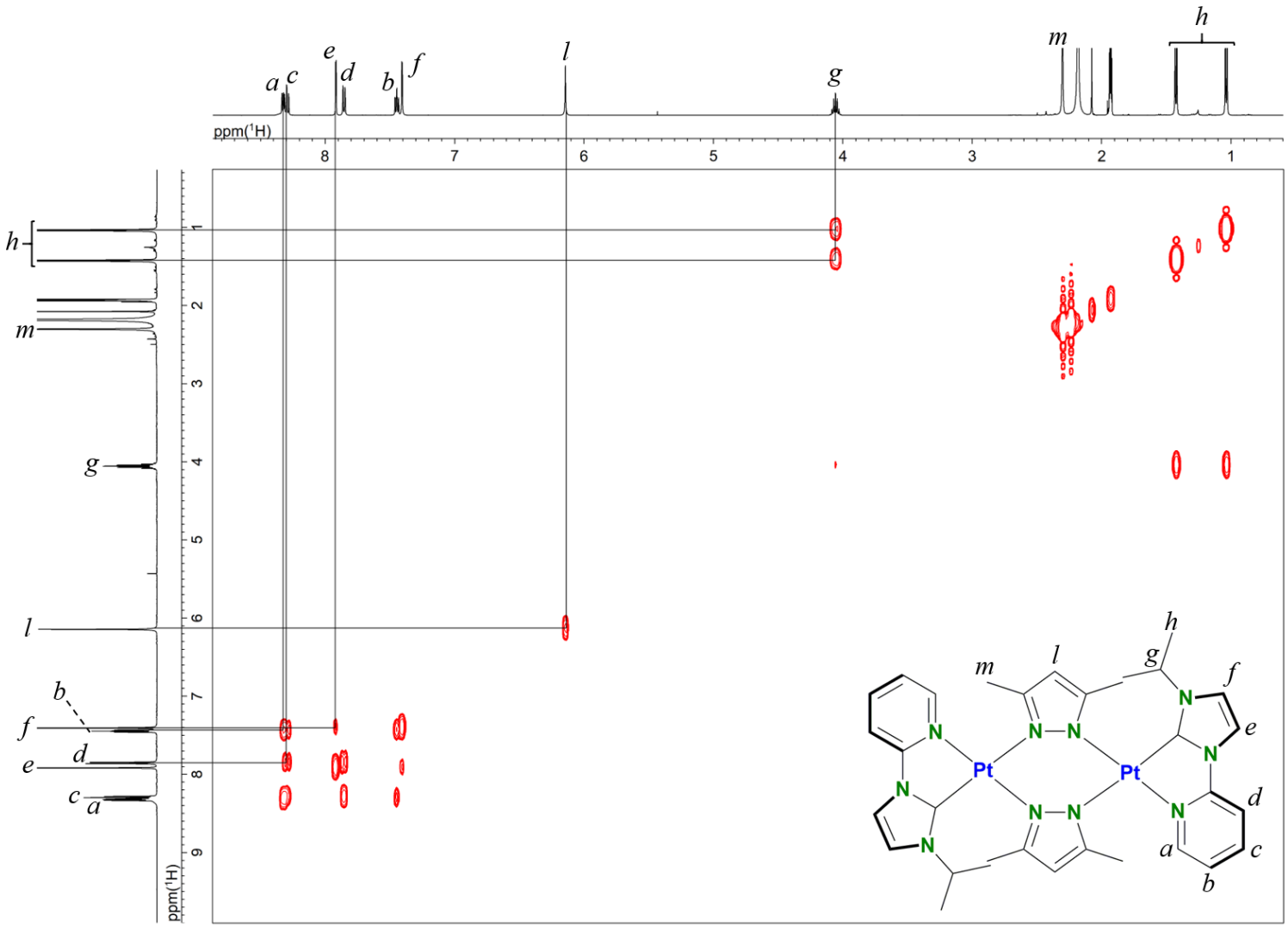

Figure 2-8. ^{1}H-^{1}H COSY spectrum (500 MHz, Acetonitrile-d_3, 25 °C) of $[(\text{Py-NHC})_2\text{Pt}_2(\mu\text{-Me}_2\text{pz})_2](\text{BF}_4)_2$ (**2**).

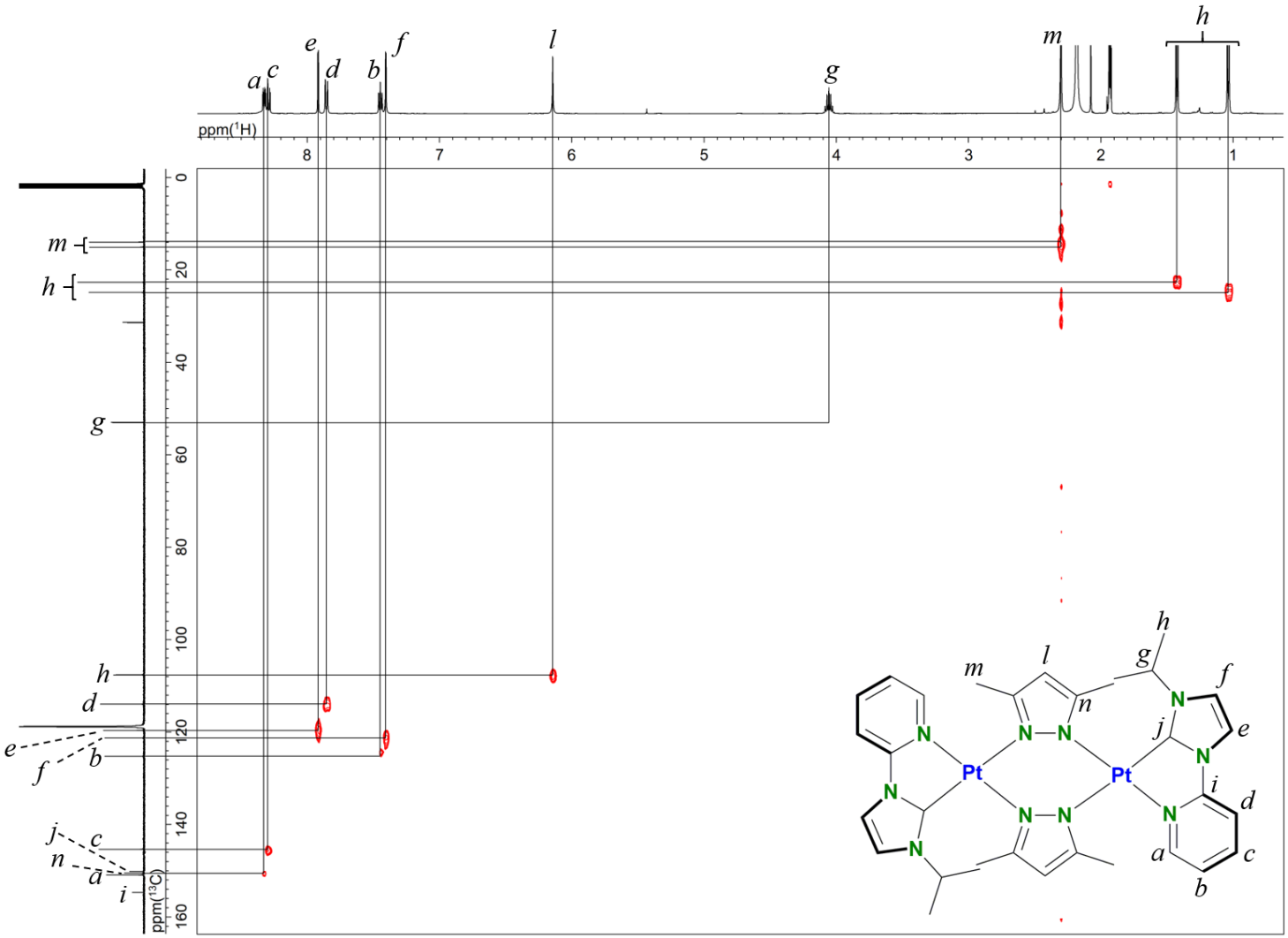

Figure 2-9. ^{1}H-^{13}C HSQC spectrum of (500 MHz, Acetonitrile-d_3, 25 °C) of $[(Py\text{-}NHC)_2Pt_2(\mu\text{-}Me_2pz)_2](BF_4)_2$ (**2**).

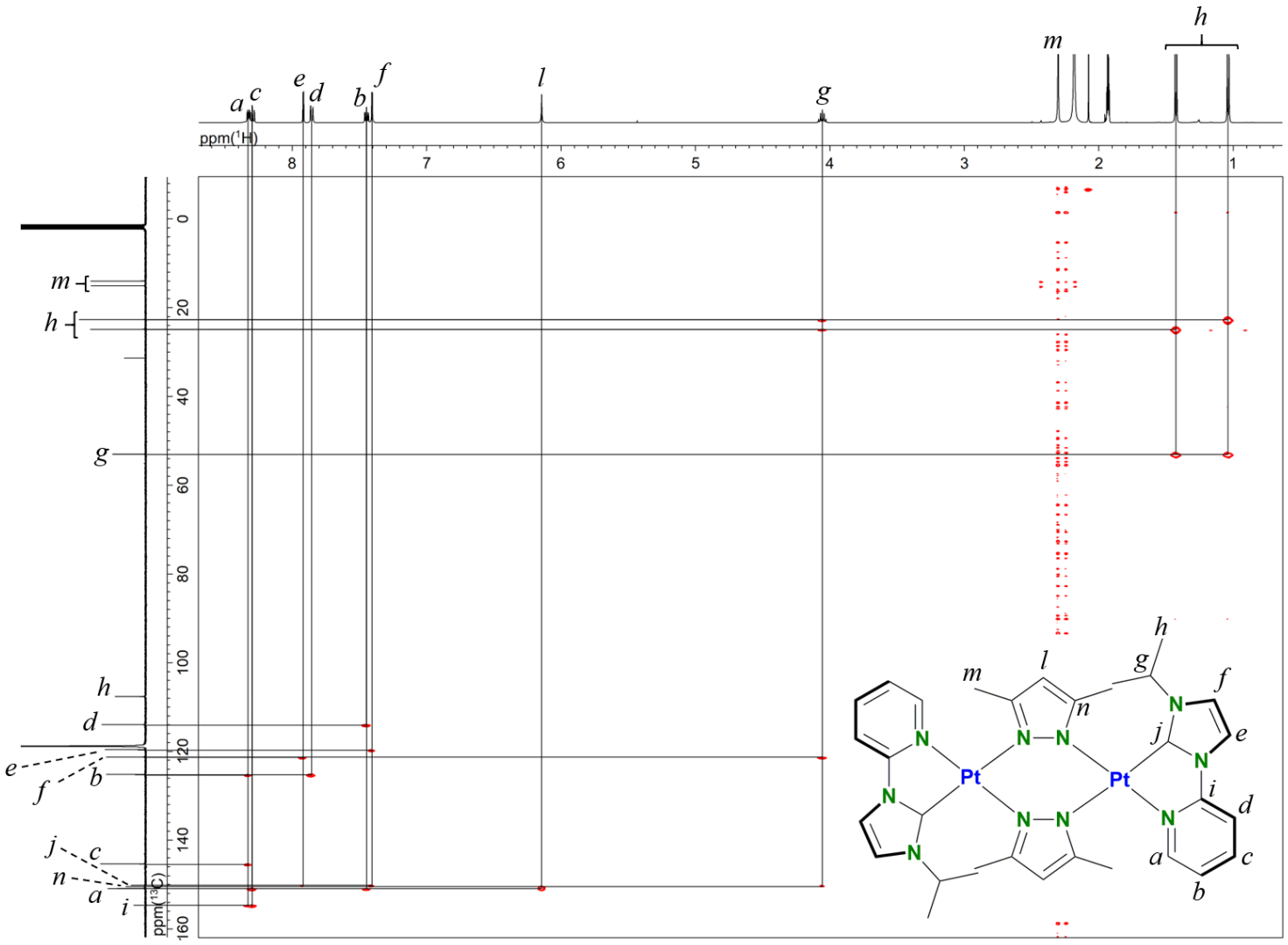

Figure 2-10. ^{1}H-^{13}C HMBC spectrum of (500 MHz, Acetonitrile-d_3, 25 °C) of $[(Py\text{-}NHC)_2Pt_2(\mu\text{-}Me_2pz)_2](BF_4)_2$ (**2**).

2-3. Structural character of (Py-NHC)$_2$Pt$_2$(μ-Me$_2$pz)$_2$](BF$_4$)$_2$ (2)

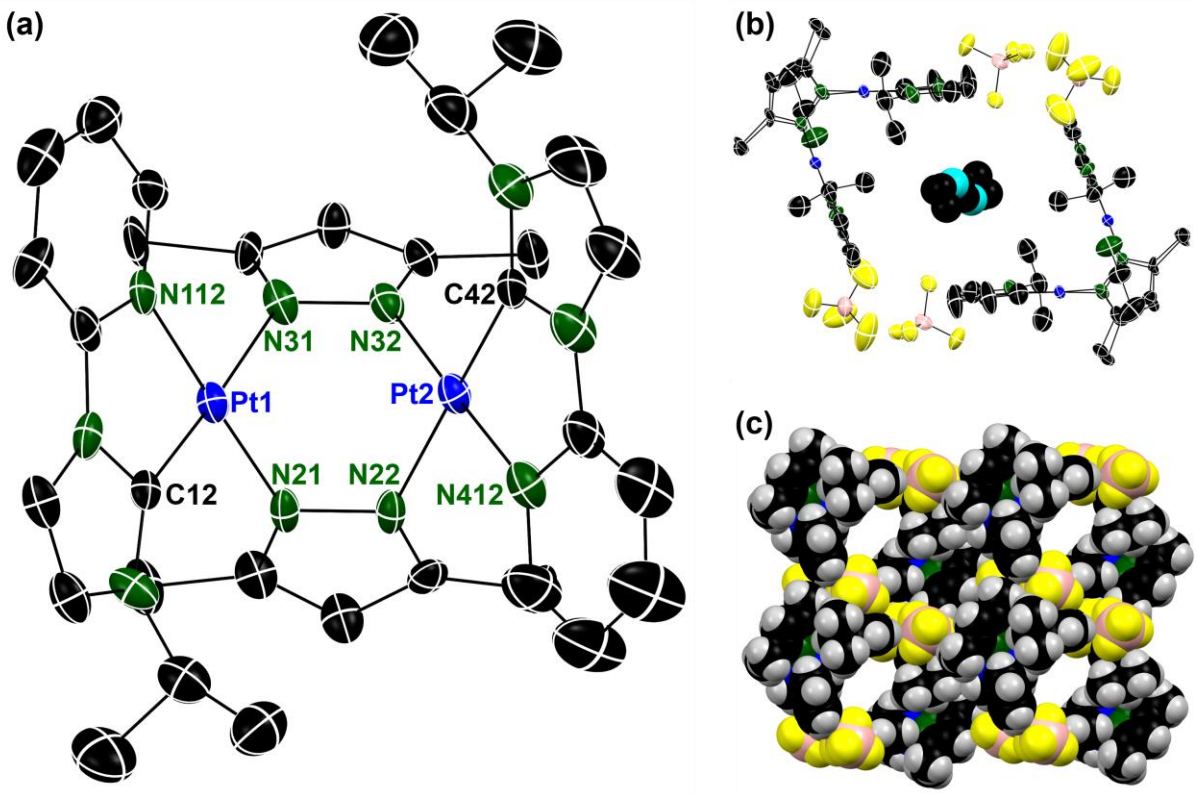

Figure 2-11. (a) ORTEP representation (50% probability ellipsoids) of [(Py-NHC)$_2$Pt$_2$(μ-Me$_2$pz)$_2$]$^{2+}$ ([**2**]$^{2+}$). Hydrogen atoms were omitted for clarity. (b, c) Packing structure of **2** and diethyl ether (solvent molecule). Solvent molecules are trapped in the infinite one-dimensional pore constructed by butterfly-shaped Pt$_2$ moieties. Selected bond length (Å): Pt1···Pt2 3.1287(9), Pt1-N31 2.039(8), Pt2-N21 2.006(8), Pt2-N22 2.061(8), Pt1-N112 2.029(8), Pt2-N412 2.011(9), Pt1-C12 1.963(9) and Pt2-C42 1.961(10).

The molecular structure of [(Py-NHC)$_2$Pt$_2$(μ-Me$_2$pz)](BF$_4$)$_2$ (**2**) was confirmed by single crystal X-ray structural analysis (**Figure 2-11**). A single crystal suitable for X- ray crystallographic analysis was obtained from CH$_3$CN/Et$_2$O solution. Similarly to analogous butterfly-shaped Pt$_2$ complexes having bridging pyrazolate ligands,[24,35] the complex cation [**2**]$^{2+}$ also had the butterfly-shaped structure with short Pt···Pt contact. The Pt···Pt distance (3.129(9) Å) in [**2**]$^{2+}$ is shorter than those in [Pt$_2$(ppy)$_2$(μ-Me$_2$pz)$_2$] (ppy = 2-phenylpyridinate) (3.1904(13) Å)[24] and [Pt$_2$(bpym)$_2$(μ-Me$_2$pz)$_2$](PF$_6$)$_2$ (bpym = 2,2-bipyrimidine) (3.1968(7) Å)[35] and the

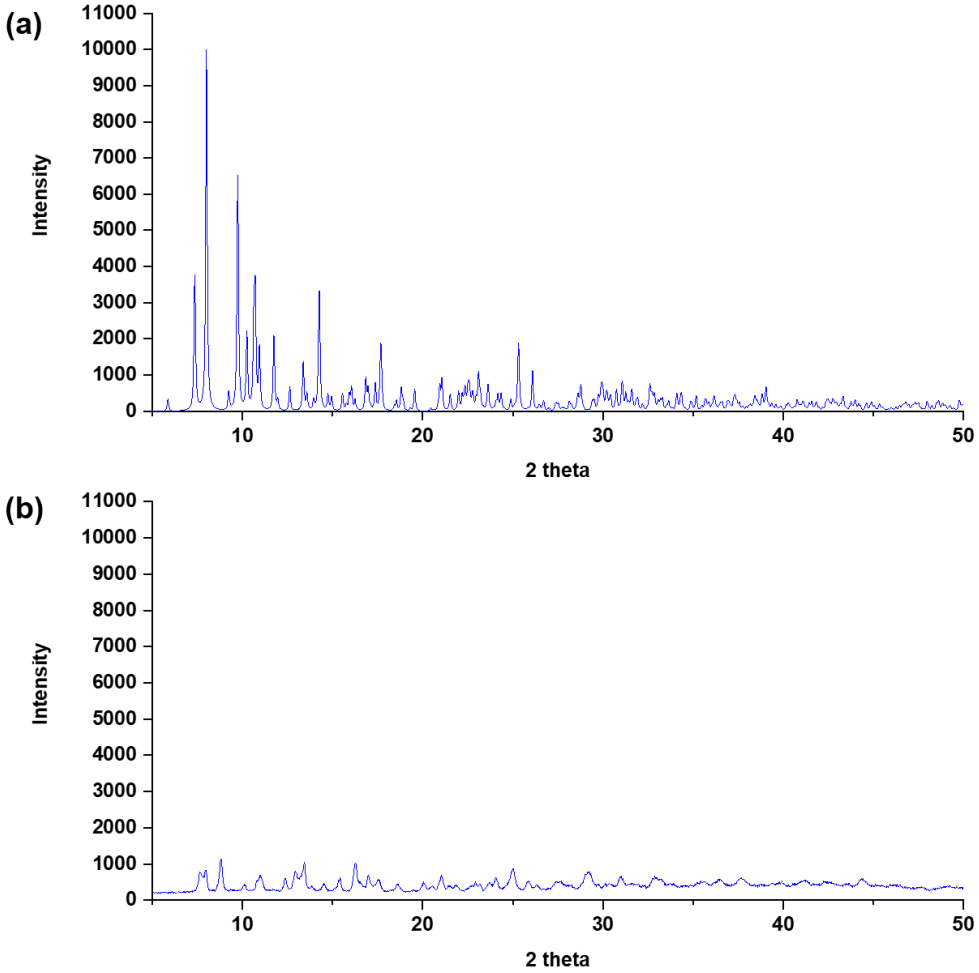

Figure 2-12. Powder X-ray diffraction (PXRD) spectra of complex **2**. (a) The simulated PXRD pattern of single crystal of **2**. (b) PXRD pattern of evacuated single crystal of **2**.

sum of the van der Waals radius of Pt atom (3.5 Å). The Pt1-N31 and Pt2-N22 distances trans to Pt-C_{NHC} bonds are approximately 0.04 Å longer than the Pt1-N21 and Pt2-N32 distances trans to the Pt-N_{py} bonds. These differences in Pt-N bond lengths resulted from stronger trans influence of carbene carbon atom in NHC moiety. The single crystal of complex **2** has interesting packing structure containing infinite one-dimensional pore which is fulfilled by diethyl ether (**Figure 2-11**b and c). The diethyl ether molecule and the counter anions (BF_4^-) locate between two complex cations, $[\mathbf{2}]^{2+}$, suggesting no intermolecular Pt···Pt interaction in the single crystal state. Unfortunately, the single crystal of complex **2** easily loses solvent molecules from crystal lattice, leading to the crystalline-to-amorphous transformation (**Figure**

2-12). It indicates that the one-dimensional infinite pore cannot be preserved after losing solvent molecules from crystal lattice.

Table 2-1. Crystallographic data for [(Py-NHC)$_2$Pt$_2$(μ-Me$_2$pz)$_2$](BF$_4$)$_2$·0.5C$_2$H$_5$OC$_2$H$_5$} (**3**·CH$_3$CN·0.5C$_2$H$_5$OC$_2$H$_5$)

	2·0.5C$_2$H$_5$OC$_2$H$_5$
Empirical formula	$C_{36}H_{48}B_2F_8N_{11}O_{0.5}Pt_2$
Formula weight	1206.64
Temperature (K)	93(1)
Wavelength (Å)	0.71075
Crystal system	triclinic
Space group	*P*-1 (#2)
Unit cell dimensions	
a (Å)	11.868(4)
b (Å)	12.527(5)
c (Å)	15.714(6)
α (deg)	106.359(6)
β (deg)	92.480(5)
γ (deg)	91.760(5)
V (Å^3)	2237.2(14)
Z	2
ρ_{calcd} (g/cm^3)	1.791
μ(Mo Kα) (mm^{-1})	6.296
F(000)	1166
Index ranges	-14<=h<=13
	-14<=k<=13
	-18<=l<=18
Reflections collected	15529
Independent reflections	7742 [R_{int} = 0.0395]
Data / restraints / parameters	7742 / 10 / 535
Goodness-of-fit on F^2	1.049
Final *R* index [$I>2\sigma(I)$][a]	R_1 = 0.0504
R indices (all data)[a,b]	R_1 = 0.00699
	wR_2 = 0.1057
Largest diff. peak and hole (eÅ^{-3})	1.37 and –1.33
CCDC number	1890891

[a] $R_1 = \sum||F_o| - |F_c||/\sum|F_o|$. [b] $wR_2 = [\sum w(F_o^2 - F_c^2)^2]/\sum[w(F_o^2)^2]]^{1/2}$.

2-4. Photophysical properties of [(Py-NHC)$_2$Pt$_2$(μ-Me$_2$pz)$_2$](BF$_4$)$_2$ (2)

The UV/Vis absorption spectra of [**2**](BF$_4$)$_2$ recorded in CH$_3$CN at room temperature showed the lowest-energy absorption bands at 342 nm, which are higher in energy than those of ppy analogue (λ_{abs} = 377 nm)[22] and bpym analogue (λ_{abs} = 388 nm) (**Figure 2-13**a).[35] These results well reflect the differences in charge and σ-donating nature of chelate ligand (vide infra). The absorbance was proportional to the concentration of Pt$_2$ complex and no significant bands appeared even in high concentration (up to 100 μM), indicating that the intermolecular Pt···Pt interactions are weak or negligible in solution. The Pt$_2$ complex **2** encouraged us to investigate photoluminescence in solution, because ppy analogue shows photo-induced structural changes

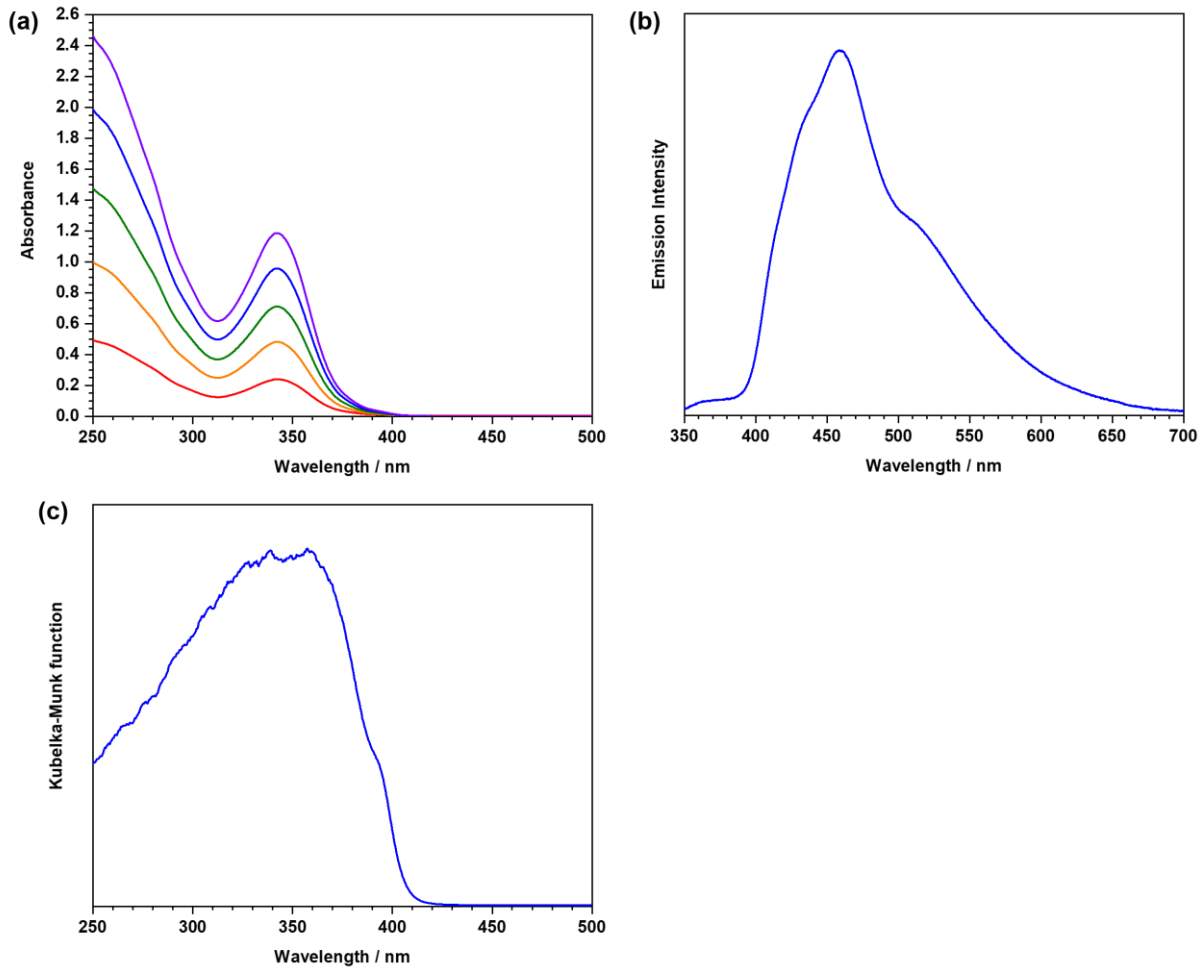

Figure 2-13. (a) UV/Vis absorption spectra of [**2**](BF$_4$)$_2$ in CH$_3$CN (red line: 20 μM, orange line: 40 μM, green line: 60 μM, blue line: 80 μM, purple line: 100 μM). (b) Emission spectrum and (c) diffuse reflectance spectrum of [**2**](BF$_4$)$_2$ in the solid state (λ_{ex}=330 nm).

by shortening of Pt···Pt distance and tunable dual emission in solution.[24] However, I found that **2** was non-emissive in solution. Similar feature was also observed in bpym analogue (Φ_{em}=0.05% in CH_3CN).[35] Possibly, the cationic nature of $[\mathbf{2}]^{2+}$ readily induced solvent association for the photo-induced excited species, resulting in mainly thermal nonradiative pathways in solution. In contrast to the non-emissive nature in solution, **2** showed bluish-green emission (λ_{em} = 459 nm) with moderate quantum yield at room temperature in the solid state (Φ_{em} = 2%, λ_{ex} = 330 nm) (**Figure 2-13**b). Time-resolved emission lifetime measurements revealed the phosphorescence originated from triplet-excited state with the lifetimes of microsecond regime (τ_1 = 0.60 μs (A_1 = 0.90), τ_2 = 3.81 μs (A_2 = 0.10), τ_{ave} = 1.9 μs) (**Table 2-2**).

To shed light on the absorption spectrum of **2**, the absorption bands were theoretically investigated with the time-dependent density functional theory (TD-DFT) method (**Figure 2-14**, **Tables 2-3** and **2-4**). It revealed that the highest-occupied molecular orbital (HOMO) is located on π-orbital of pyrazolate ligands and 5d orbitals of Pt atoms (**Table 2-4**), and the HOMO-1 is manly located on 5d orbitals of Pt atoms. On the contrary, the lowest-unoccupied molecular

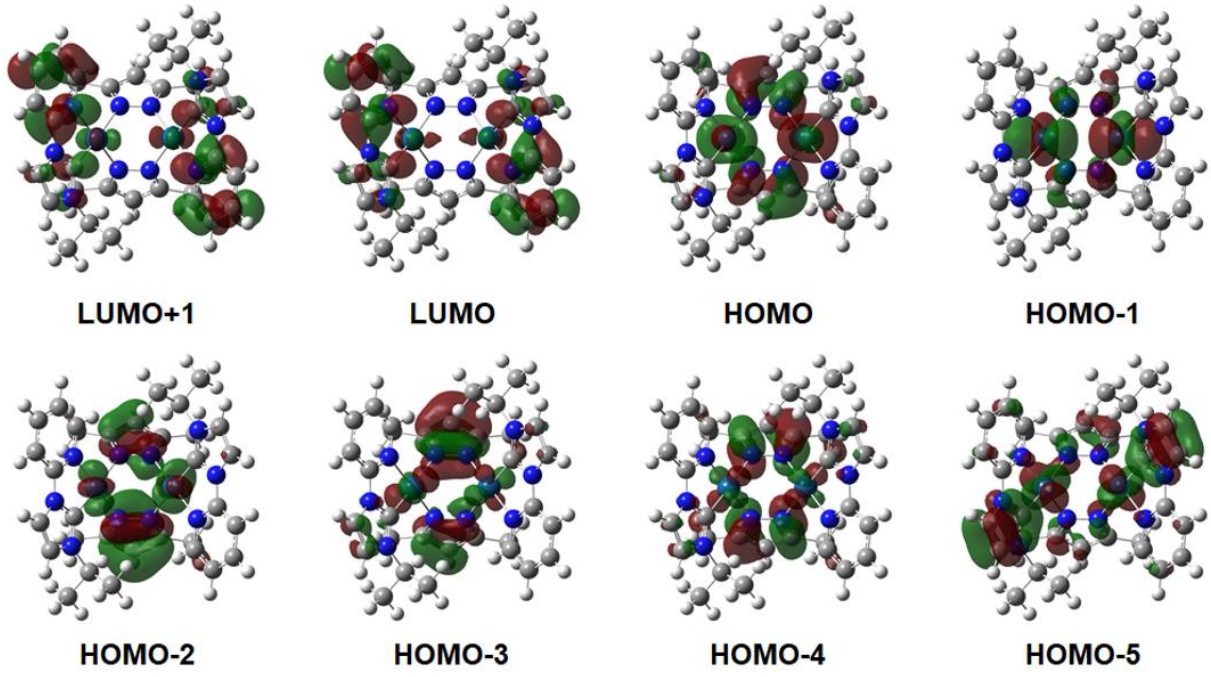

Figure 2-14. Molecular orbitals of the singlet state for $[\mathbf{2}]^{2+}$.

orbital (LUMO) is mainly located on π^*-orbital of Py-NHC chelate ligands and 5d orbitals of the Pt atoms contribute to LUMO slightly. Thus, the lowest-energy absorption bands are mainly assigned to the electronic transitions from S0 to S1 state (HOMO-1 → LUMO and HOMO → LUMO), which are the combination of metal-to-ligand charge transfer (MLCT) and ligand-to-ligand charge transfer (LLCT) transitions. As mentioned above, **2** showed bluish-green emission (λ_{em} = 459 nm) in the solid state, which is higher in energy than that of ppy analogue (λ_{em} = 525 nm).[24] This is in contrast to the observation that the intramolecular Pt···Pt distance in **2** is shorter than that in ppy analogue. To unveil the origin of the differences in the photophysical properties of **2** and ppy analogue, additional DFT calculations on the triplet excited state for $[\mathbf{2}]^{2+}$ were performed as well as the singlet and triplet excited states for ppy analogue (**Tables 2-5**, **2-6** and **2-8**). As shown in **Figure 2-15**, the energy difference between dσ and dσ* in $[\mathbf{2}]^{2+}$ (ΔE = 0.92 eV) is smaller than that in ppy analogue (ΔE = 1.07 eV),

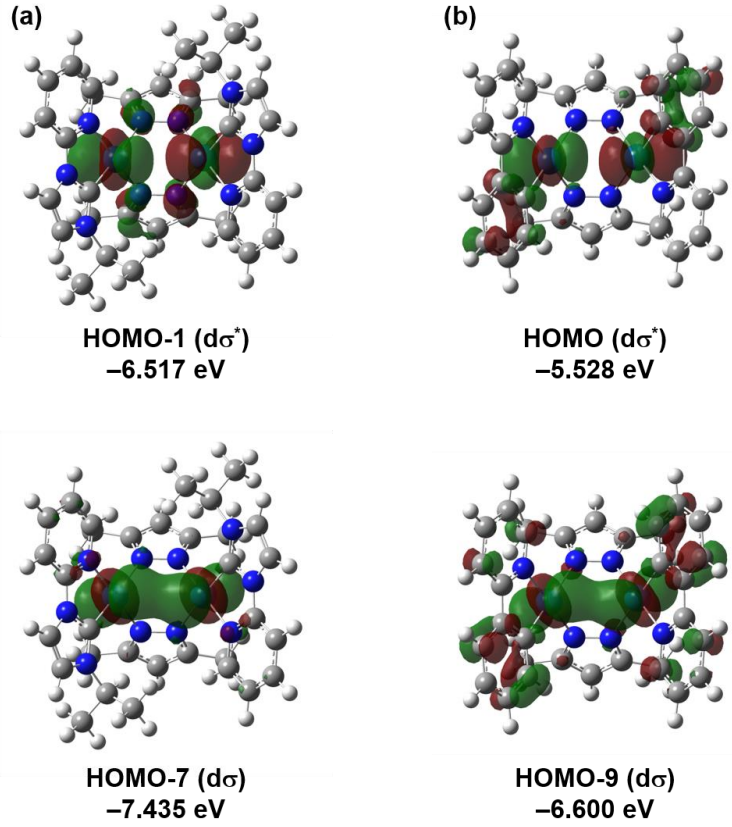

Figure 2-15. Molecular orbitals of dσ and dσ* and their energies for (a) $[\mathbf{2}]^{2+}$ and (b) $[(ppy)_2Pt_2(Me_2pz)_4]$.

indicating that the destabilization of dσ* orbital in $[\mathbf{2}]^{2+}$ is smaller than that in ppy analogue. This may be attributed to the difference of charge on the C^N chelate ligands (neutral Py-NHC ligand vs. negative ppy ligand), which correlates to the electron density on the metal centers (+0.776 for $[\mathbf{2}]^{2+}$, +0.610 for ppy analogue (**Figure 2-16**)). The calculated energies of emission based on the crystal structures of **2** and ppy analogue[25] in **Tables 2-5** and **2-6**, respectively, also agree well with the experimental results described above. Therefore, the dinuclear Pt(II) complexes having pyridyl-NHC chelate ligands have potential as blue emitters.

Table 2-2. Photophysical data for complexes **2**

λ_{abs} / nm ($\varepsilon \times 10^4$ M^{-1} cm^{-1})	λ_{em} / nm[b]	τ_1 (A_1) / μs[a]	τ_2 (A_2) / μs[a]	τ_{ave} / μs	Φ_{em} / %[b]
342 (0.08)	459	0.60 (0.90)	3.81 (0.10)	1.9	2

k_r / $\times 10^4$ s^{-1}	k_{nr} / $\times 10^6$
1.0	0.5

[a] λ_{ex} = 355 nm, [b] λ_{ex} = 330 nm

Table 2-3. Calculated Singlet Excited States (S_1–S_{10}) of $[\mathbf{2}]^{2+}$

Excited State	Transition	Energy (Wavelength)	Oscillator Strength
S1	HOMO-1 → LUMO (73%) HOMO → LUMO (27%)	3.3576 eV (369.27 nm)	0.0616
S2	HOMO → LUMO	3.4787 eV (356.40 nm)	0.0390
S3	HOMO-1 → LUMO+1 (80%) HOMO → LUMO+1 (20%)	3.5112 eV (353.11 nm)	0.0009
S4	HOMO-3 → LUMO+1 (17%) HOMO-2 → LUMO (83%)	3.5749 eV (346.82 nm)	0.0271
S5	HOMO-6 → LUMO (13%) HOMO-3 → LUMO (69%) HOMO → LUMO (18%)	3.5983 eV (344.56 nm)	0.0061
S6	HOMO-4 → LUMO (60%) HOMO-2 → LUMO (27%) HOMO → LUMO+1 (13%)	3.6192 eV (342.58 nm)	0.0010
S7	HOMO-3 → LUMO+1 (14%) HOMO-2 → LUMO (23%) HOMO → LUMO+1 (63%)	3.6879 eV (336.20 nm)	0.0079
S8	HOMO-4 → LUMO+1 (16%) HOMO-2 → LUMO+1 (84%)	3.7639 eV (329.40 nm)	0.0128
S9	HOMO-5 → LUMO (11%) HOMO-4 → LUMO (28%) HOMO-3 → LUMO+1 (49%) HOMO-2 → LUMO+1 (12%)	3.8044 eV (325.89 nm)	0.0019
S10	HOMO-4 → LUMO+1 (73%) HOMO-3 → LUMO (27%)	3.8370 eV (323.13 nm)	0.0003

Table 2-4. Molecular-Orbital populations of selected orbitals in [**2**]$^{2+}$

Molecular Orbital	Eigenvalue / Hartrees[a]	MO population / %			
		Pt	Py-NHC		Me_2pz
			Py	NHC	
LUMO+5	−0.02972	33.56	18.40	20.53	27.51
LUMO+4	−0.03922	41.92	19.52	17.81	20.75
LUMO+3	−0.05826	1.84	15.77	80.85	1.54
LUMO+2	−0.05917	2.31	14.00	81.47	2.22
LUMO+1	−0.08205	7.44	17.08	71.92	3.56
LUMO	−0.08747	8.97	21.97	66.06	3.00
HOMO	−0.23823	36.78	8.39	2.73	52.10
HOMO-1	−0.23950	81.07	0.92	0.68	17.33
HOMO-2	−0.24129	24.27	4.68	1.92	69.13
HOMO-3	−0.24179	20.33	8.52	1.85	69.30
HOMO-4	−0.24509	16.13	8.08	3.10	72.69
HOMO-5	−0.25774	33.64	43.60	7.24	15.52
HOMO-6	−0.25980	33.14	40.86	8.91	17.09
HOMO-7	−0.27322	85.20	5.10	5.44	4.26

[a]1 Hartree = 27.2114 eV

Table 2-5. Calculated triplet excited state of [**2**]$^{2+}$

Excited State	Transition	Energy (Wavelength)
T1	HOMO-4 LUMO (31%) HOMO LUMO (69%)	3.0111 eV (411.75 nm)
T2	HOMO-4 LUMO	3.0705 eV (403.79 nm)
T3	HOMO-7 LUMO (12%) HOMO-3 LUMO+1 (11%) HOMO-1 LUMO (55%) HOMO LUMO (22%)	3.1275 eV (396.43 nm)

Table 2-6. Calculated Singlet Excited States of $[(ppy)_2Pt_2(Me_2pz)_2]$[25]

Excited State	Transition	Energy (Wavelength)	Oscillator Strength
S1	HOMO-1 → LUMO (14%) HOMO → LUMO (86%)	3.0681 eV (404.11 nm)	0.0849
S2	HOMO-1 → LUMO+1 (16%)	3.1860 eV (389.15 nm)	0.0046
S3	HOMO-2 → LUMO (14%) HOMO-2 → LUMO+1 (33%) HOMO-1 → LUMO (53%)	3.2877 eV (377.11 nm)	0.0191
S4	HOMO-4 → LUMO (14%) HOMO-2 → LUMO (53%)	3.2921 eV (376.62 nm)	0.0134
S5	HOMO-3 → LUMO (57%) HOMO-1 → LUMO (43%)	3.4039 eV (364.24 nm)	0.0147
S6	HOMO-4 → LUMO	3.4563 eV (358.72 nm)	0.0273
S7	HOMO-4 → LUMO (40%) HOMO-1 → LUMO+1 (60%)	3.5455 eV (349.70 nm)	0.0006
S8	HOMO-3 → LUMO (27%) HOMO-2 → LUMO+1 (62%) HOMO → LUMO (11%)	3.5955 eV (344.83 nm)	0.0098
S9	HOMO-4 → LUMO (26%) HOMO-3 → LUMO+1 (54%) HOMO-2 → LUMO (20%)	3.6332 eV (341.26 nm)	0.0005
S10	HOMO-4 → LUMO+1 (69%) HOMO-3 → LUMO (31%)	3.6439 eV (340.25 nm)	0.0035

Table 2-7. Molecular-Orbital populations of selected orbitals in $[(ppy)_2Pt_2(Me_2pz)_2]$[25]

Molecular Orbital	Eigenvalue / Hartrees[a]	MO population / %			
		Pt	ppy		Me_2pz
			Ph	py	
LUMO+5	+0.00113	25.24	43.45	10.15	21.16
LUMO+4	−0.00380	19.87	63.75	8.90	7.48
LUMO+3	−0.03731	1.60	12.58	83.94	1.88
LUMO+2	−0.03839	2.56	14.19	81.01	2.24
LUMO+1	−0.06068	6.15	23.27	68.19	2.39
LUMO	−0.06458	7.07	23.05	67.61	2.27
HOMO	−0.20315	79.74	12.76	2.52	4.98
HOMO-1	−0.21068	51.57	9.04	2.25	37.14
HOMO-2	−0.21245	45.91	34.01	7.87	12.21
HOMO-3	−0.21415	39.62	12.82	5.56	42.00

HOMO-4	−0.21530	35.06	5.46	3.43	56.05
HOMO-5	−0.22781	11.65	15.86	7.41	65.08
HOMO-6	−0.22804	10.11	8.74	3.62	77.53
HOMO-7	−0.23629	38.72	42.37	15.40	3.51
HOMO-8	−0.23747	28.69	48.12	16.93	6.26
HOMO-9	−0.24253	63.10	21.92	9.36	5.62

a 1 Hartree = 27.2114 eV

Table 2-8. Calculated triplet excited state of $[(ppy)_2Pt_2(Me_2pz)_2]$[25]

Excited State	Transition	Energy (Wavelength)
T1	HOMO-4 → LUMO+1 (18%) HOMO-2 → LUMO (20%) HOMO → LUMO (62%)	2.5183 eV (492.33 nm)
T2	HOMO-8 → LUMO (11%) HOMO-5 → LUMO+1 (18%) HOMO-3 → LUMO (28%) HOMO-2 → LUMO (10%) HOMO-1 → LUMO (22%) HOMO-1 → LUMO+1 (11%)	2.5410 eV (487.94 nm)
T3	HOMO-5 → LUMO (19%) HOMO-3 → LUMO+1 (18%) HOMO-1 → LUMO (33%) HOMO → LUMO (30%)	2.5713 eV (482.18 nm)

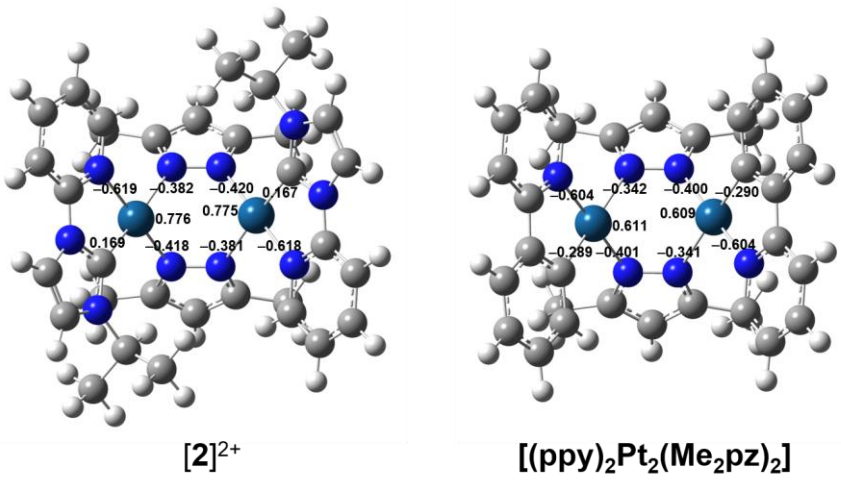

Figure 2-16. Charge distribution of $[\mathbf{2}]^{2+}$ and $[(ppy)_2Pt_2(Me_2pz)_2]$.

2-5. Conclusion

In summary, I studied the effect of Py-NHC chelate ligand on the structure and photophysical properties of the butterfly-shaped dinuclear Pt(II) complex having Me_2pz bridging ligands. The single crystal X-ray analysis revealed that **2** has infinite one dimensional pore in the crystal lattice. The intramolecular Pt···Pt distance in **2** (3.129(9) Å) is shorter than those in analogous Pt_2 complexes having Me_2pz bridging ligands. Although **2** did not show emission in solution, it showed bluish-green emission in the solid state at room temperature. The lowest-energy absorption bands are mainly assigned to the combination of MLCT and LLCT transitions. This study gives an insight into the tuning of emission energy of butterfly-shaped Pt_2 complexes having C^N chelate ligands.

2-6. Experimental

2-6-1. General

All reactions and subsequent work-up manipulations were performed in air unless otherwise noted. Organic solvents and all other reagents were commercially available and used without further purification. The 1D (^{1}H, ^{13}C) and 2D (^{1}H–^{1}H COSY, ^{1}H–^{13}C HSQC, ^{1}H–^{13}C HMBC) NMR spectra were obtained at 300 MHz Varian Gemini 300 or 500 MHz Varian NMR System 500PS spectrometer. UV/Vis spectra were recorded on a Jasco V-560 spectrophotometer at 20 ℃. Diffuse reflectance spectrum was recorded on a Jasco V-670DS spectrophotometer at 20 ℃. The corrected emission spectrum was obtained by using a Hamamatsu PMA-12 multichannel photodetector (excitation wavelength = 355 nm). Emission quantum yields in the solid state were determined by using a Hamamatsu Photonic Absolute PL Quantum Yield Measurement System C9920-02 with an integrating sphere and a PMA-12 multichannel photodetector (excitation wavelength = 300 nm). The emission lifetime measurements were conducted by using a Hamamatsu C11200 streak camera as a photodetector by exciting at 355 nm using a nanosecond Q-switched Nd:YAG laser (Continum® MiniliteTM, fwhm≈10–12 ns, repetition rate = 10 Hz).

2-6-2. X-ray structural analysis

Diffraction data were collected at −180 °C under a stream of cold N_2 gas on a Rigaku RA-Micro7 HFM instrument equipped with a Rigaku Saturn724+CCD detector by using graphite-monochromated Mo-Kα radiation. The frame data were integrated using a Rigaku CrystalClear program package, and the data sets were corrected for absorption using a REQAB program. The calculations were performed with a CrystalStructure software package.[45] The initial structure was solved by Patterson methods (DIRDIF99-PATTY),[46] and refined on F^2 by

the full-matrix least squares methods. Anisotropic refinement was applied to all non-hydrogen atoms with the exception of the crystal solvents (SHELXL-2014/7).[47] All hydrogen atoms were put at calculated positions.

2-6-3. Computational method

Ground-state geometries of the complexes were optimized by using the B3LYP density functional theory (DFT). X-ray structures were used as initial geometries without any geometrical constraints. The LanL2DZ and 6-31G(d,p) basis sets were used to treat the platinum and all other atoms, respectively. Time-dependent (TD)-DFT calculations were then performed to estimate the energies and oscillator strengths *f* of the lowest-energy 50 singlet and 3 triplet absorption transitions. All of the calculations were carried out as in acetonitrile by using a Polarizable Continuum Model (PCM). All calculations were carried out using the Gaussian 16W package.[48] Molecular orbitals with the isovalue of 0.03 were drawn by the GaussView 6.[49]

2-7. Reference

(1) Sakai, K.; Ozawa, H. *Coord. Chem. Rev.* **2007**, *251* (21–24), 2753–2766.

(2) Xu, Q.; Fu, W. F.; Zhang, G.; Bian, Z.; Zhang, J.; Han, X.; Xu, W. *Catal. Commun.* **2008**, *10* (1), 49–52.

(3) Du, P.; Schneider, J.; Jarosz, P.; Eisenberg, R. *J. Am. Chem. Soc.* **2006**, *128* (24), 7726–7727.

(4) Furuta, P. T.; Deng, L.; Garon, S.; Thompson, M. E.; Fréchet, J. M. J. *J. Am. Chem. Soc.* **2004**, *126* (47), 15388–15389.

(5) Chow, P. K.; Cheng, G.; Ong, G. S. M. T.; To, W. P.; Kwong, W. L.; Kowk, C. C.; Ma, C.; Che, C. M. *Angew. Chem. Int. Ed.* **2015**, *54* (7), 2084–2089.

(6) Li, X. L.; Shi, L. X.; Zhang, L. Y.; Wen, H. M.; Chen, Z. N. *Inorg. Chem.* **2007**, *46* (25), 10892–10900.

(7) Lam, E. S. H.; Tsang, D. P. K.; Lam, W. H.; Tam, A. Y. Y.; Chan, M. Y.; Wong, W. T.; Yam, V. W. W. *Chem. Eur. J.* **2013**, *19* (20), 6385–6397.

(8) Cebrián, C.; Mauro, M.; Kourkoulos, D.; Mercandelli, P.; Hertel, D.; Meerholz, K.; Strassert, C. A.; De Cola, L. *Adv. Mater.* **2013**, *25* (3), 437–442.

(9) Wadas, T. J.; Wang, Q. M.; Kim, Y. J.; Flaschenreim, C.; Blanton, T. N.; Eisenberg, R. *J. Am. Chem. Soc.* **2004**, *126* (51), 16841–16849.

(10) Wong, K. M. C.; Tang, W. S.; Lu, X. X.; Zhu, N.; Yam, V. W. W. *Inorg. Chem.* **2005**, *44* (5), 1492–1498.

(11) Zhao, Q.; Huang, C.; Li, F. *Chem. Soc. Rev.* **2011**, *40* (5), 2508–2524.

(12) Hong, Y.; Lam, J. W. Y.; Tang, B. Z. *Chem. Soc. Rev.* **2011**, *40* (11), 5361–5388.

(13) Yu, C.; Chan, K. H. Y.; Wong, K. M. C.; Yam, V. W. W. *Chem. Commun.* **2009**, *0* (25),

(14) Yan, X.; Wang, H.; Hauke, C. E.; Cook, T. R.; Wang, M.; Saha, M. L.; Zhou, Z.; Zhang, M.; Li, X.; Huang, F.; Stang, P. J. *J. Am. Chem. Soc.* **2015**, *137* (48), 15276–15286.

(15) Ikeda, T.; Takayama, M.; Kumar, J.; Kawai, T.; Haino, T. *Dalton Trans.* **2015**, *44* (29), 13156–13162.

(16) Pasha, S. S.; Alam, P.; Dash, S.; Kaur, G.; Banerjee, D.; Chowdhury, R.; Rath, N.; Roy Choudhury, A.; Laskar, I. R. *RSC Adv.* **2014**, *4* (92), 50549–50553.

(17) Pinter, P.; Mangold, H.; Stengel, I.; Münster, I.; Strassner, T. *Organometallics* **2016**, *35* (5), 673–680.

(18) D'Andrade, B. W.; Brooks, J.; Adamovich, V.; Thompson, M. E.; Forrest, S. R. *Adv. Mater.* **2002**, *14* (15), 1032–1036.

(19) Yang, X.; Wang, Z.; Madakuni, S.; Li, J.; Jabbour, G. E. *Adv. Mater.* **2008**, *20* (12), 2405–2409.

(20) Ma, B.; Djurovich, P. I.; Garon, S.; Alleyne, B.; Thompson, M. E. *Adv. Funct. Mater.* **2006**, *16* (18), 2438–2446.

(21) Ma, B.; Li, J.; Djurovich, P. I.; Yousufuddin, M.; Bau, R.; Thompson, M. E. *J. Am. Chem. Soc.* **2005**, *127* (1), 28–29.

(22) Brown-Xu, S. E.; Kelley, M. S. J.; Fransted, K. A.; Chakraborty, A.; Schatz, G. C.; Castellano, F. N.; Chen, L. X. *J. Phys. Chem. A* **2016**, *120* (4), 543–550.

(23) Zhou, C.; Tian, Y.; Yuan, Z.; Han, M.; Wang, J.; Zhu, L.; Tameh, M. S.; Huang, C.; Ma, B. *Angew. Chem. Int. Ed.* **2015**, *54* (33), 9591–9595.

(24) Zhou, C.; Yuan, L.; Yuan, Z.; Doyle, N. K.; Dilbeck, T.; Bahadur, D.; Ramakrishnan, S.; Dearden, A.; Huang, C.; Ma, B. *Inorg. Chem.* **2016**, *55* (17), 8564–8569.

(25) Ghavale, N.; Wadawale, A.; Dey, S.; Jain, V. K. *J. Organomet. Chem.* **2010**, *695* (8), 1237–1245.

(26) Tenne, M.; Metz, S.; Wagenblast, G.; Münster, I.; Strassner, T. *Dalton Trans.* **2015**, *44* (18), 8444–8455.

(27) Fuertes, S.; García, H.; Perálvarez, M.; Hertog, W.; Carreras, J.; Sicilia, V. *Chem. Eur. J.* **2015**, *21* (4), 1620–1631.

(28) Fuertes, S.; Chueca, A. J.; Perálvarez, M.; Borja, P.; Torrell, M.; Carreras, J.; Sicilia, V. *ACS Appl. Mater. Interfaces* **2016**, *8* (25), 16160–16169.

(29) Ahrens, S.; Strassner, T. *Inorg. Chim. Acta* **2006**, *359* (15), 4789–4796.

(30) Li, K.; Guan, X.; Ma, C. W.; Lu, W.; Chen, Y.; Che, C. M. *Chem. Commun.* **2011**, *47* (32), 9075–9077.

(31) Bachmann, M.; Suter, D.; Blacque, O.; Venkatesan, K. *Inorg. Chem.* **2016**, *55* (10), 4733–4745.

(32) Williams, J. A. G. Photochemistry and Photophysics of Coordination Compounds: Platinum. In: Balzani, V.; Campagna, S. (Eds.), Photochemistry and Photophysics of Coordination Compounds II, Springer, Berlin, 2007, pp. 205−268.

(33) Umakoshi, K.; Kojima, T.; Saito, K.; Akatsu, S.; Onishi, M.; Ishizaka, S.; Kitamura, N.; Nakao, Y.; Sakaki, S.; Ozawa, Y. *Inorg. Chem.* **2008**, *47* (12), 5033–5035.

(34) Umakoshi, K.; Saito, K.; Arikawa, Y.; Onishi, M.; Ishizaka, S.; Kitamura, N.; Nakao, Y.; Sakaki, S. *Chem. Eur. J.* **2009**, *15* (17), 4238–4242.

(35) Umakoshi, K.; Kimura, K.; Kim, Y. H.; Tsukimoto, Y.; Arikawa, Y.; Onishi, M.; Ishizaka, S.; Kitamura, N. *Bull. Chem. Soc. Jpn.* **2010**, *83* (12), 1504–1510.

(36) Akatsu, S.; Kanematsu, Y.; Kurihara, T. A.; Sueyoshi, S.; Arikawa, Y.; Onishi, M.; Ishizaka, S.; Kitamura, N.; Nakao, Y.; Sakaki, S.; Umakoshi, K. *Inorg. Chem.* **2012**, *51* (15), 7977–7992.

(37) Nishihara, K.; Ueda, M.; Higashitani, A.; Nakao, Y.; Arikawa, Y.; Horiuchi, S.; Sakuda, E.; Umakoshi, K. *Dalton Trans.* **2016**, *45* (12), 4978–4982.

(38) Ueda, M.; Horiuchi, S.; Sakuda, E.; Nakao, Y.; Arikawa, Y.; Umakoshi, K. *Chem. Commun.* **2017**, *53* (48), 6405–6408.

(39) Horiuchi, S.; Moon, S.; Sakuda, E.; Ito, A.; Arikawa, Y.; Umakoshi, K. *Dalton Trans.* **2018**, *47* (21), 7113–7117.

(40) Chi, Y.; Chou, P. T. *Chem. Soc. Rev.* **2010**, *39* (2), 638–655.

(41) Kato, M.; Omura, A.; Toshikawa, A.; Kishi, S.; Sugimoto, Y. *Angew. Chem. Int. Ed.* **2002**, *41* (17), 3183–3185.

(42) Raba, A.; Anneser, M. R.; Jantke, D.; Cokoja, M.; Herrmann, W. A.; Kühn, F. E. *Tetrahedron Lett.* **2013**, *54* (26), 3384–3387.

(43) Warsink, S.; Bosman, S.; Weigand, J. J.; Elsevier, C. J. *Appl. Organomet. Chem.* **2011**, *25* (4), 276–282.

(44) McDermott, J. X.; White, J. F.; Whitesides, G. M. *J. Am. Chem. Soc.* **1976**, *98* (21), 6521–6528.

(45) Cao, P.; Cabrera, J.; Padilla, R.; Serra, D.; Rominger, F.; Limbach, M.; *Organometallics* **2012**, *31*(3), 921-929.

(46) CrystalStructure 4.2: Crystal Structure Analysis Package, Rigaku Corporation, Tokyo, Japan, 2000-2017.

(47) Sheldrick, G. M. *Acta Cryst.* **2015**, *C71*, 3-8.

(48) Gaussian 16, Revision A.03, Frisch, M. J.; Trucks, G. W.; Schlegel, H. B.; Scuseria, G. E.; Robb, M. A.; Cheeseman, J. R.; Scalmani, G.; Barone, V.; Petersson, G. A.; Nakatsuji, H.; Li, X.; Caricato, M.; Marenich, A. V.; Bloino, J.; Janesko, B. G.; Gomperts, R.; Mennucci, B.; Hratchian, H. P.; Ortiz, J. V.; Izmaylov, A. F.; Sonnenberg, J. L.; Williams-Young, D.; Ding, F.; Lipparini, F.; Egidi, F.; Goings, J.; Peng, B.; Petrone, A.; Henderson, T.; Ranasinghe, D.; Zakrzewski, V. G.; Gao, J.; Rega, N.; Zheng, G.; Liang, W.; Hada, M.; Ehara, M.; Toyota, K.; Fukuda, R.; Hasegawa, J.; Ishida, M.; Nakajima, T.; Honda, Y.; Kitao, O.; Nakai, H.; Vreven, T.; Throssell, K.; Montgomery, J. A., Jr.; Peralta, J. E.; Ogliaro, F.; Bearpark, M. J.; Heyd, J. J.; Brothers, E. N.; Kudin, K. N.; Staroverov,

V. N.; Keith, T. A.; Kobayashi, R.; Normand, J.; Raghavachari, K.; Rendell, A. P.; Burant, J. C.; Iyengar, S. S.; Tomasi, J.; Cossi, M.; Millam, J. M.; Klene, M.; Adamo, C.; Cammi, R.; Ochterski, J. W.; Martin, R. L.; Morokuma, K.; Farkas, O.; Foresman, J. B.; Fox, D. J. Gaussian, Inc., Wallingford CT, 2016.

(49) GaussView, Version 6, Dennington, R.; Keith, T. A.; Millam, J. M. Semichem Inc., Shawnee Mission, KS, 2016.

Chapter 3

U- to Z-shape Isomerization in a Pt_2Ag_2 Framework Containing Pyridyl-NHC Ligands

3-1. Introduction

Metal–metal interactions have been increasingly recognized as a powerful tool to construct supramolecular and crystal engineering systems.[1–6] In particular, metal–metal interactions among different metal atoms are expected to show characteristic features owing to their cooperative effects, giving unique structures, reactivities, and properties. For example, bimetallic interactions in cooperative catalysis offer the unique advantage of metal centers having different nature in close proximity, leading to a significant molecular activation that individual mononuclear complexes cannot achieve.[7–10] Furthermore, structures and photophysical properties of heteropolynuclear complexes involving metal–metal interactions, such as Pt complexes containing group 11 metal ions, have also been widely investigated.[11–19] Some of the heteropolynuclear complexes having metal–metal interactions also show unique molecular rearrangements in solution, owing to their weak bonding nature.[20–23]

Our group has revealed the structures and luminescence properties of heteropolynuclear complexes having various extents of multiple metal–metal interactions.[24–28] For example, [(ppy)Pt_2Ag_2(μ-Me_2pz)$_4$] (ppy = 2-phenylpyridinate and Me_2pz = 3,5-dimethylpyrazolate) and [(bpy)Pt_2M_2(μ-Me_2pz)$_4$]$(PF_6)_2$ (M = Au, Ag and bpy = 2,2′-bipyridine) exist as a mixture of U- and Z-shaped isomers in solution, respectively, whose luminescence properties are almost independent of the incorporated group 11 metal ions. Furthermore, the U-shaped isomer showed reversible trapping of Ag ions within a U-shaped cavity via multiple metal–metal interactions.[28] Although various properties of heteropolynuclear complexes have been investigated by using a variety of C^N chelate ligands represented by ppy and its derivatives, those of heteropolynuclear complexes involving N-heterocyclic carbene (NHC) ligands have not been fully explored.[29] Furthermore, structural isomerization involving rearrangement of a complex framework such as that between U- and Z-shaped structures is still unclear. In this chapter, synthesis, structure, isomerization and emission properties of pyrazolato-bridged Pt_2Ag_2

complexes having a pyridyl–NHC chelate ligand are described. The pyridyl–NHC ligand works as a neutral C^N chelate ligand similarly to N^N chelate ligands (e.g. bipyridines) and has a unique electron donating character on the carbene moiety. The strong σ-donor properties of the NHC ligands were expected to increase the d–d transition energy effectively, resulting in a higher energy emission from the complexes.[30–37] In this chapter, I also elucidated the nature of the pyridyl–NHC ligand as a neutral C^N chelate ligand in the Pt_2Ag_2 system.

3-2. Synthesis of complexes having pyridyl-NHC (Py-NHC) chelate ligand

3-2-1. Preparation of [(Py-NHC)Pt(Me$_2$pzH)$_2$](PF$_6$)$_2$ (3)

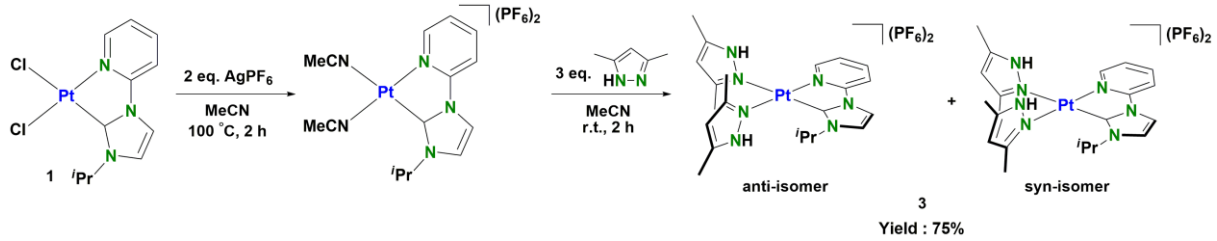

Scheme 3-1. Synthesis of [(Py-NHC)Pt(Me$_2$pzH)$_2$](PF$_6$)$_2$ (**3**).

A mixture of [(Py-NHC)PtCl$_2$] (257 mg, 0.57 mmol) and AgPF$_6$ (318 mg, 1.26 mmol) in acetonitile (30 mL) was refluxed for 2 h. After the precipitate was removed by filtration, Me$_2$pzH (169 mg, 1.76 mmol) was added to the filtrate and stirred for 2 h at toom temperature. The mixture was concentrated and diethyl ether was added to the solution. The resulted white precipitate was collected, washed with diethyl ether, and dried in vacuo, [(Py-NHC)Pt(Me$_2$pzH)$_2$](PF$_6$)$_2$ was isolated as a white solid. Yield 369 mg (75%). It was purified by recrystallization from an acetone/*n*-hexane solution. Anal. Calcd for $C_{21}H_{29}N_7PtP_2F_{12}$: C, 29.16; H, 3.38; N, 11.34. Found: C, 29.45; H, 2.90; N, 11.35. ^{1}H NMR (500 MHz, CD_3CN, 25 ℃) of isomer mixture of [(Py-NHC)Pt(Me$_2$pzH)$_2$](PF$_6$)$_2$: δ = 11.8 (br, 2H, H$_k$), 11.6 (br, 1H, H$_k$), 11.4 (br, 1H, H$_k$), 8.37 (t, *J* = 9.0 Hz, 2H, H$_c$), 7.99 (d, *J* = 2.5 Hz, 1H,

H_e), 7.92 (d, *J* = 8.5 Hz, 2H, H_d), 7.62 (d, *J* = 6.0 Hz, 1H, H_a), 7.49 (d, *J* = 2.5 Hz, 1H, H_f), 7.50-7.43 (m, 2H, H_b), 6.26 (s, 1H, H_l), 6.23 (s, 2H, H_l), 6.22 (s, 1H, H_l), 2.98 (sept, *J* = 7.0 Hz, 1H, H_g), 2.86 (sept, *J* = 7.0 Hz, 1H, H_g), 2.40 (s, 6H, H_m), 2.39 (s, 3H, H_m), 2.36 (s, 3H, H_m), 2.34 (s, 3H, H_m), 2.33 (s, 3H, H_m), 2.30 (s, 3H, H_m), 2.29 (s, 3H, H_m), 1.32 (d, *J* = 7.0 Hz, 3H, H_h), 1.31 (d, *J* = 7.0 Hz, 3H, H_h), 1.28 (d, *J* = 7.0 Hz, 3H, H_h), 1.27 ppm (d, *J* = 7.0 Hz, 3H, H_h). $^{13}C\{^1H\}$ NMR (125 MHz, CD_3CN, 25 ℃) of isomer mixture of $[(Py\text{-}NHC)Pt(Me_2pzH)_2](PF_6)_2$: δ = 154.0, 153.9, 153.0, 152.8, 152.6, 151.8, 150.3, 150.1, 147.0, 146.9, 146.8, 146.5, 145.7, 145.7, 144.6, 144.4, 125.4, 125.3, 121.0, 119.5, 119.4, 113.8, 113.8, 108.4 (Me_2pzH), 108.4 (Me_2pzH), 108.4 (Me_2pzH), 108.4 (Me_2pzH), 108.3 (Me_2pzH), 108.3 (Me_2pzH), 108.3 (Me_2pzH), 108.3 (Me_2pzH), 52.6 (^{i}Pr), 52.6 (^{i}Pr), 23.1 (^{i}Pr), 22.9 (^{i}Pr), 14.8 (Me_2pzH), 14.6 (Me_2pzH), 14.5 (Me_2pzH), 14.1 (Me_2pzH), 11.2 (Me_2pzH), 11.1 (Me_2pzH), 11.1 (Me_2pzH), 11.0 (Me_2pzH) ppm. FAB-MS for $[(Py\text{-}NHC)Pt(Me_2pzH)_2](PF_6)_2$: m/z = 573 $[M\text{-}\{H+2(PF_6)\}]^+$, 719 $[M\text{-}(PF_6)]^+$.

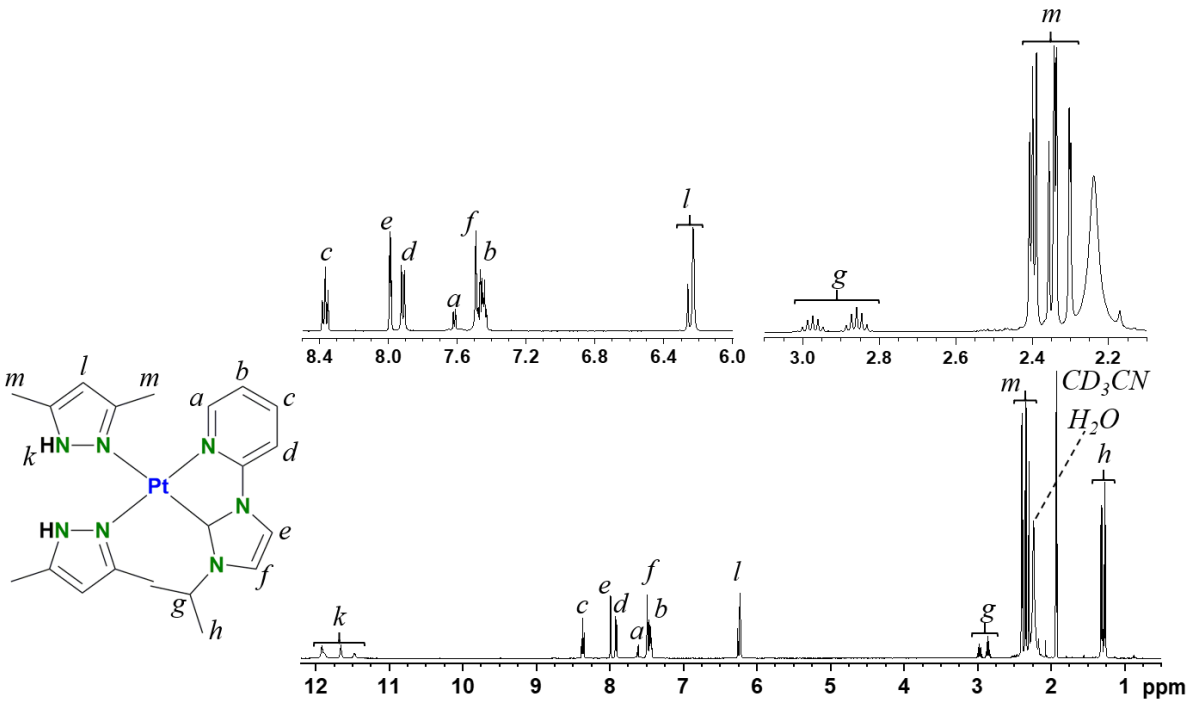

Figure 3-1. ^{1}H NMR spectrum (500 MHz, Acetonitrile-d_3, 25 ℃) of [(Py-NHC)Pt(Me$_2$pzH)$_2$](PF$_6$)$_2$ (**3**).

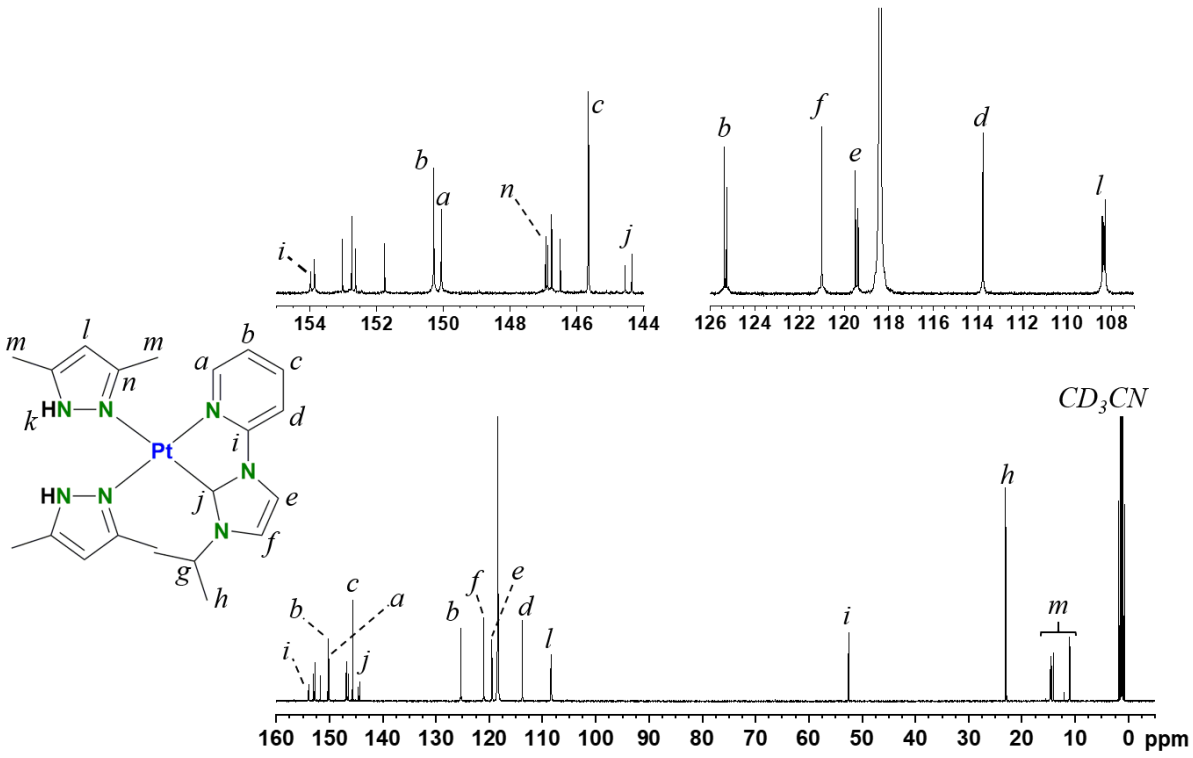

Figure 3-2. ^{13}C{^{1}H} NMR spectrum (125 MHz, Acetonitrile-d_3, 25 ℃) of [(Py-NHC)Pt(Me$_2$pzH)$_2$](PF$_6$)$_2$ (**3**).

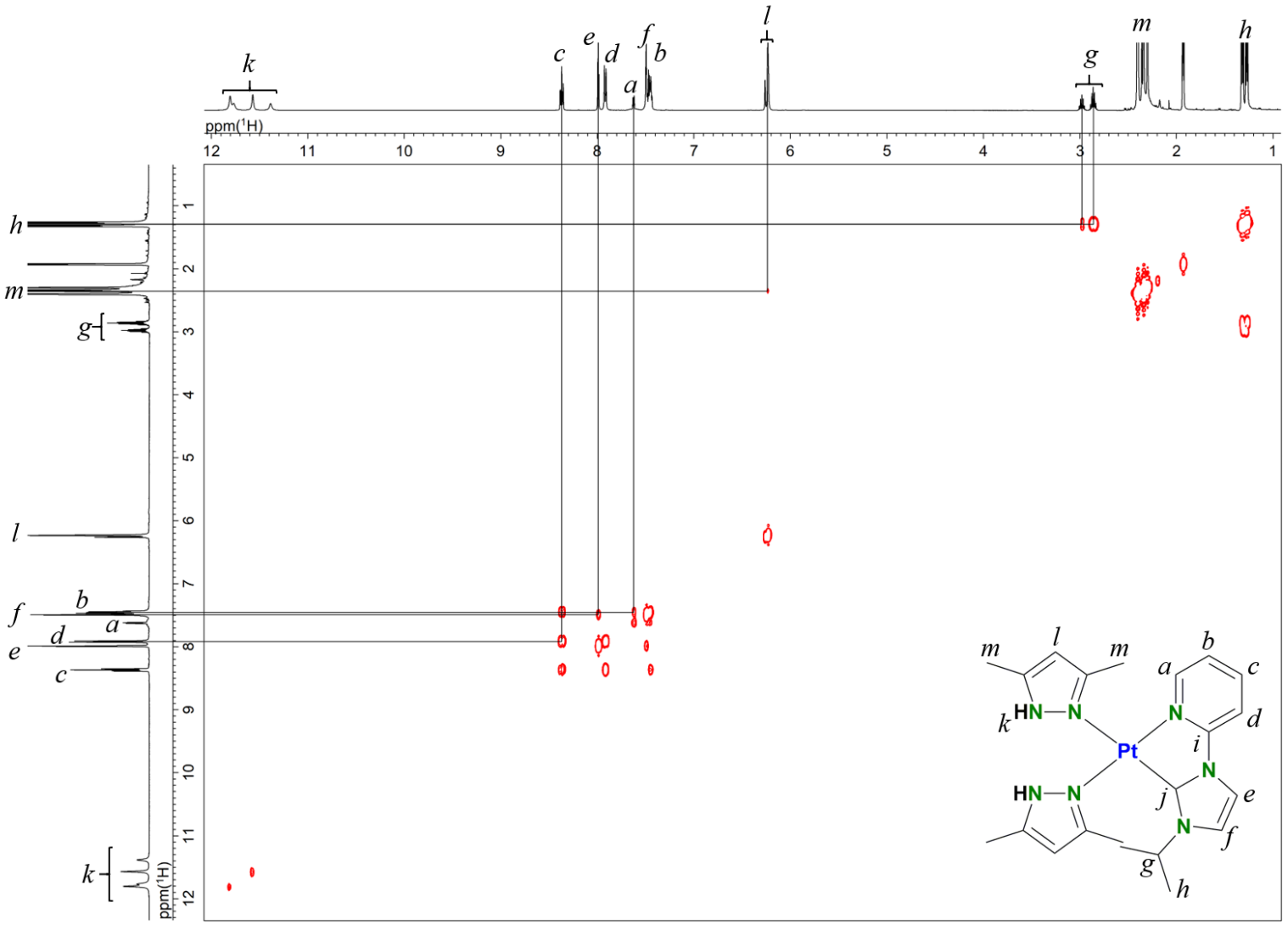

Figure 3-3. ^{1}H-^{1}H COSY spectrum (500 MHz, Acetonitrile-d_3, 25 °C) of [(Py-NHC)Pt($Me_2pzH)_2$]($PF_6)_2$ (**3**).

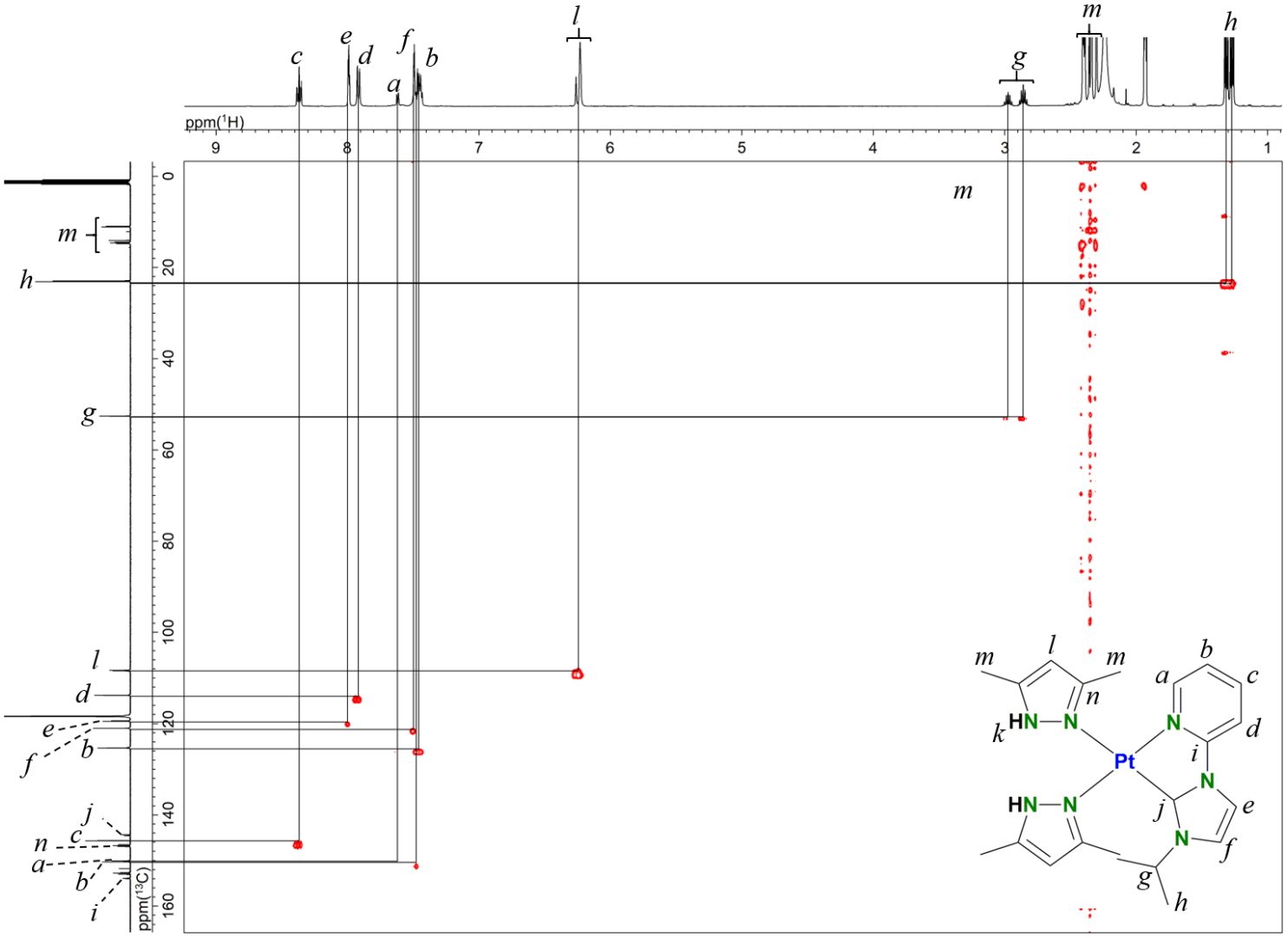

Figure 3-4. ^{1}H-^{13}C HSQC spectrum (500 MHz, Acetonitrile-d_3, 25 °C) of $[(Py\text{-}NHC)Pt(Me_2pzH)_2](PF_6)_2$ (**3**).

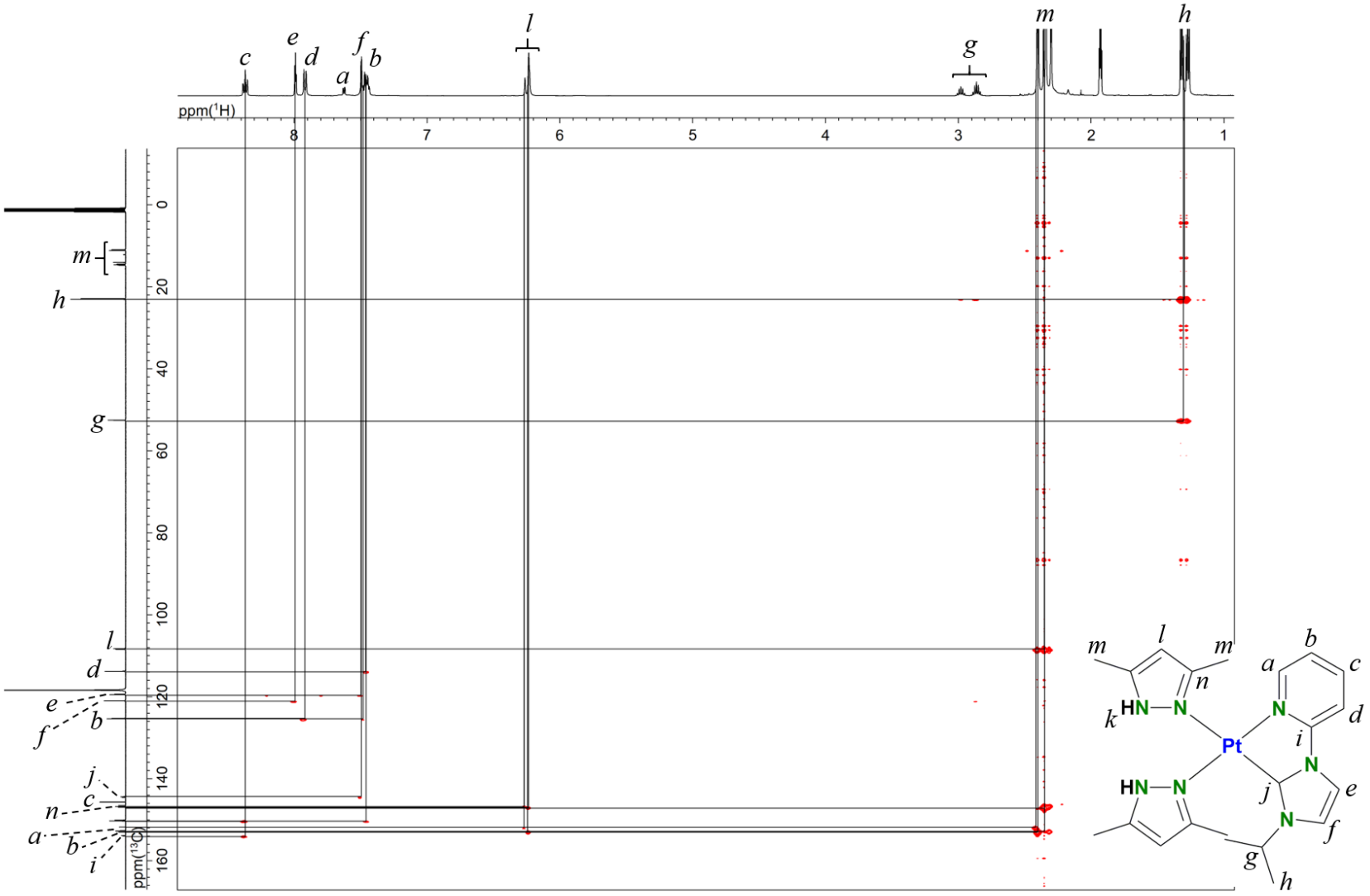

Figure 3-5. ^{1}H-^{13}C HMBC spectrum (500 MHz, Acetonitrile-d_3, 25 °C) of $[(Py\text{-}NHC)Pt(Me_2pzH)_2](PF_6)_2$ (**3**).

3-2-2. Synthesis of [(Py-NHC)$_2$Pt$_2$Ag$_2$(Me$_2$pz)$_4$](PF$_6$)$_2$ (4).

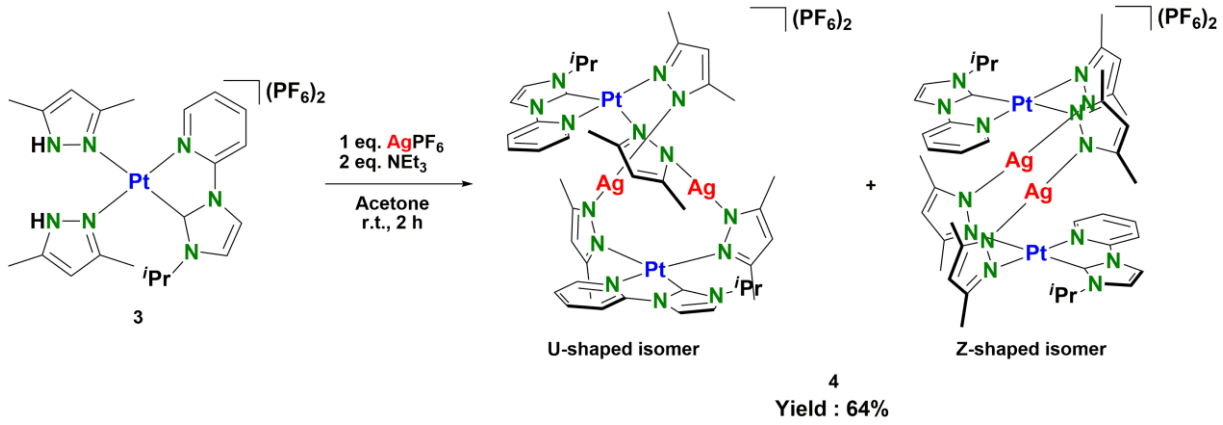

Scheme 3-2. Synthesis of [(Py-NHC)$_2$Pt$_2$Ag$_2$(Me$_2$pz)$_4$](PF$_6$)$_2$ (**4**).

To a solution of [(Py-NHC)Pt(Me$_2$pzH)$_2$](PF$_6$)$_2$ (173 mg, 0.20 mmol) in acetone (10 mL) was added a solution of AgPF$_6$ (57 mg, 0.23 mmol) in acetone (10 mL) and NEt$_3$ (60 μL, 0.43 mmol). The solution was stirred for 2 h at room temperature in the dark. After the solution was dried in vacuo, the residue was dissolved in dichloromethane. The organic layer was washed with water and dried over MgSO$_4$. After filtration, concentration in vacuo, and addition of *n*-hexane to the solution, isomer mixture of the [(Py-NHC)$_2$Pt$_2$Ag$_2$(Me$_2$pz)$_4$](PF$_6$)$_2$ was isolated as a white solid. Yield 106 mg (64%). U-shaped isomer was selectively obtained by recrystallization from an acetone/*n*-hexane solution. Anal. Calcd for C$_{42}$H$_{54}$Ag$_2$N$_{14}$Pt$_2$P$_2$F$_{12}$: C, 30.58; H, 3.30; N, 11.89. Found: C, 30.79; H, 3.34; N, 12.01. ^{1}H NMR (500 MHz, CDCl$_3$, 25 °C, TMS) of U-shaped isomer [(Py-NHC)$_2$Pt$_2$Ag$_2$(Me$_2$pz)$_4$](PF$_6$)$_2$: δ = 8.17 (t, *J* = 8.0 Hz, 2H, H$_c$), 7.97 (s, 2H, H$_e$), 7.86 (d, *J* = 8.0 Hz, 2H, H$_d$), 7.28 (s, 2H, H$_f$), 7.16 (t, *J* = 8.0 Hz, 2H, H$_b$), 6.87 (d, *J* = 6.0 Hz, 2H, H$_a$), 6.09 (s, 2H, H$_l$), 6.02 (s, 2H, H$_l$), 2.93 (sept, *J* = 7.0 Hz, 2H, H$_g$), 2.28 (s, 6H, H$_m$), 2.12 (s, 6H, H$_m$), 2.07 (s, 6H, H$_m$), 1.93 (s, 6H, H$_m$), 1.28 (d, *J* = 7.0 Hz, 6H, H$_h$), 1.22 (d, *J* = 7.0 Hz, 6H, H$_h$); Z-shaped isomer [(Py-NHC)$_2$Pt$_2$Ag$_2$(Me$_2$pz)$_4$](PF$_6$)$_2$: δ = 8.34 (t, *J* = 7.0 Hz, 2H, H$_{c'}$), 7.99 (d, *J* = 7.0 Hz, 2H, H$_{d'}$), 7.81 (s, 2H, H$_{e'}$), 7.51 (t, *J* = 7.0 Hz, 2H, H$_{b'}$), 7.24 (d, *J* = 7.0 Hz, 2H, H$_{d'}$), 7.14 (s, 2H, H$_{f'}$), 6.05 (s, 2H, H$_{l'}$), 6.03 (s, 2H, H$_{l'}$), 2.97 (sept,

J = 7.0 Hz, 2H, $H_{g'}$), 2.23 (s, 6H, $H_{m'}$), 2.20 (s, 6H, $H_{m'}$), 2.14 (s, 6H, $H_{m'}$), 1.99 (s, 6H, $H_{m'}$), 1.19 (d, *J* = 7.0 Hz, 6H, $H_{h'}$), 0.89 (d, *J* = 7.0 Hz, 6H, $H_{h'}$). $^{13}C\{^{1}H\}$ NMR (125 MHz, $CDCl_3$, 25 °C, TMS) of isomer mixture of the $[(Py\text{-}NHC)_2Pt_2Ag_2(Me_2pz)_4](PF_6)_2$: δ = 152.8, 152.6, 150.7, 150.7, 150.5, 150.5, 150.4, 150.4, 150.3, 150,3 149.0, 148.8, 148.8, 148.7, 148.7, 148.2, 148.2, 147.9, 147.7, 147.7, 144.7, 144.2, 124.6, 124.5, 119.7, 119.6, 118.9, 118.3, 113.2, 113.1, 106.3 (Me_2pzH), 105.8 (Me_2pzH), 105.3 (Me_2pzH), 105.1 (Me_2pzH), 51.1 (^{i}Pr), 50.9 (^{i}Pr), 23.8 (^{i}Pr), 22.9 (^{i}Pr), 22.5 (^{i}Pr), 22.3 (^{i}Pr), 14.7 (Me_2pzH), 14.6 (Me_2pzH), 14.5 (Me_2pzH), 14.2 (Me_2pzH), 14.1 (Me_2pzH), 14.1 (Me_2pzH), 13.8 (Me_2pzH), 13.3 (Me_2pzH) ppm. ESI-MS for $[(Py\text{-}NHC)_2Pt_2Ag_2(Me_2pz)_4](PF_6)_2$: m/z 1504.7 $[M\text{-}(PF_6)]^+$.

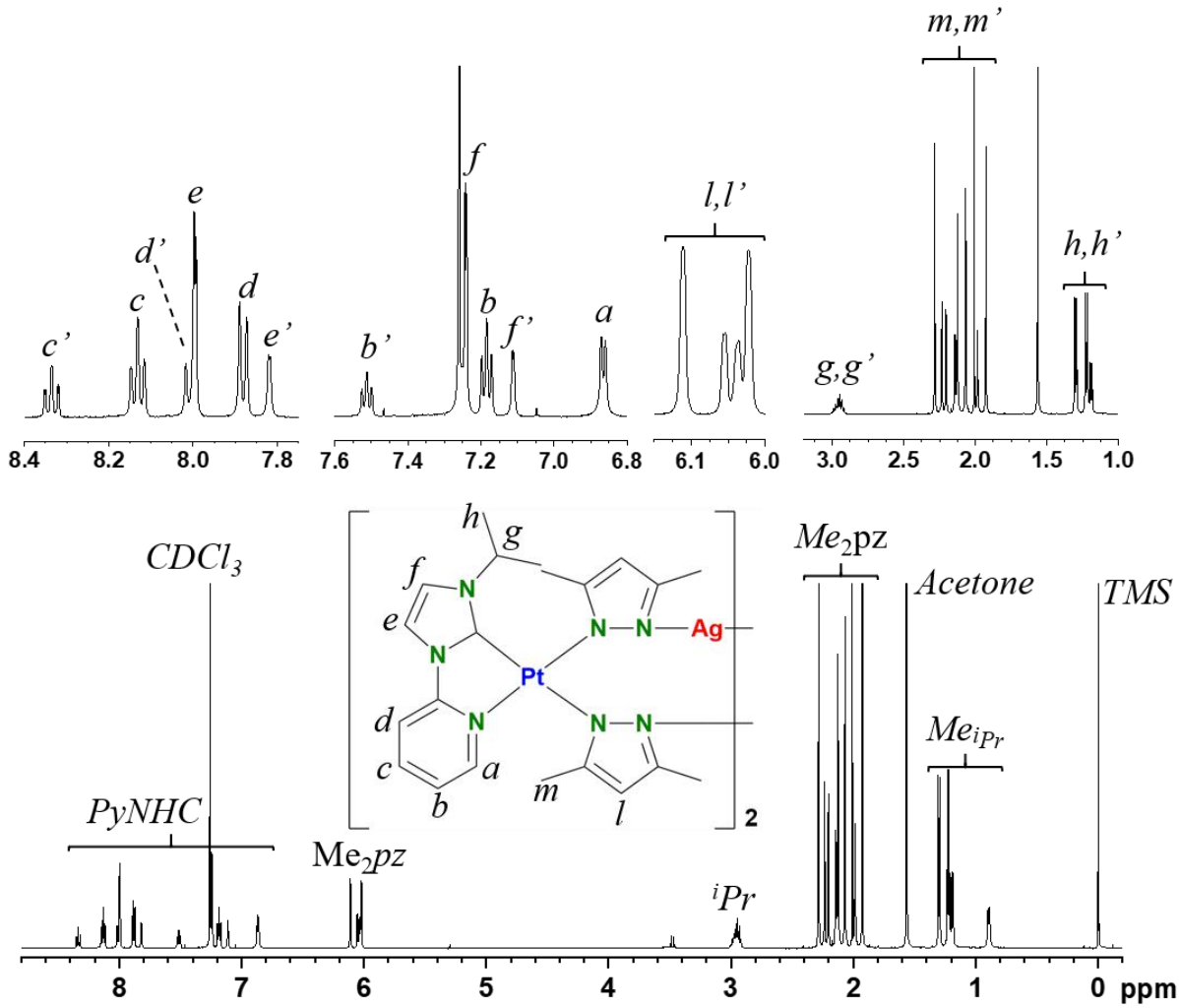

Figure 3-6. ^{1}H NMR spectrum (500 MHz, $CDCl_3$, 25 °C, TMS) of $[(Py\text{-}NHC)_2Pt_2Ag_2(Me_2pz)_4](PF_6)_2$ (**4**).

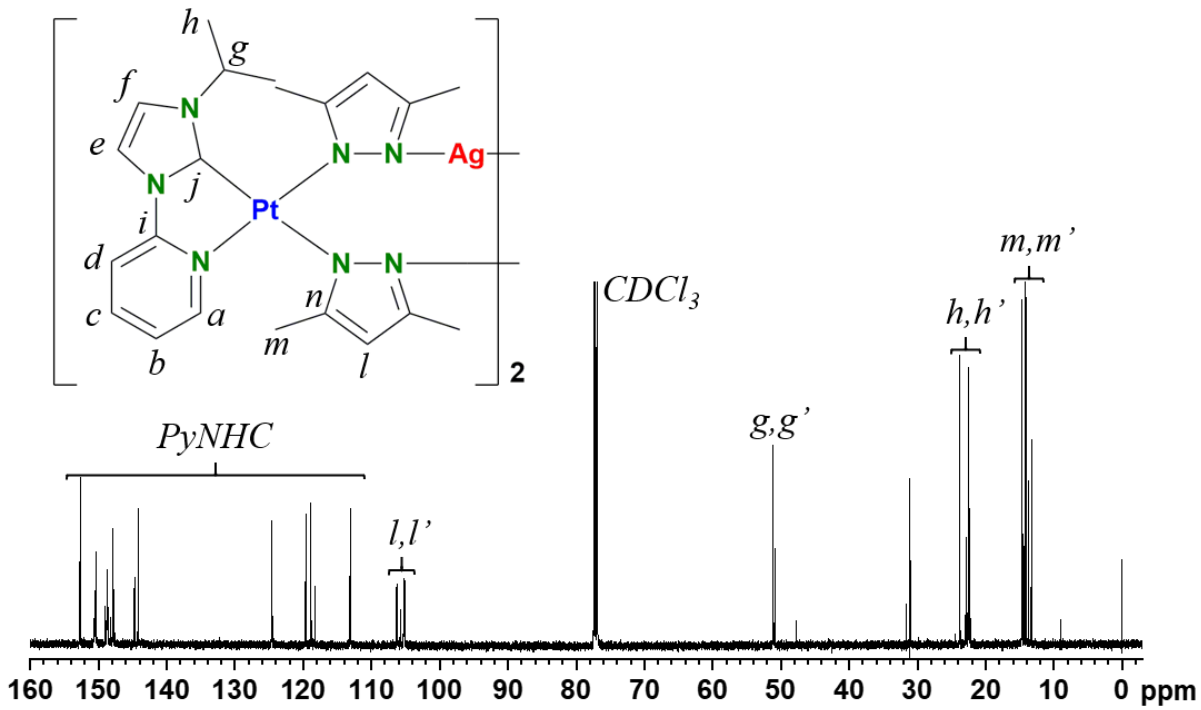

Figure 3-7. $^{13}C\{^{1}H\}$ NMR spectrum (500 MHz, $CDCl_3$, 25 °C, TMS) of $[(Py\text{-}NHC)_2Pt_2Ag_2(Me_2pz)_4](PF_6)_2$ (**4**).

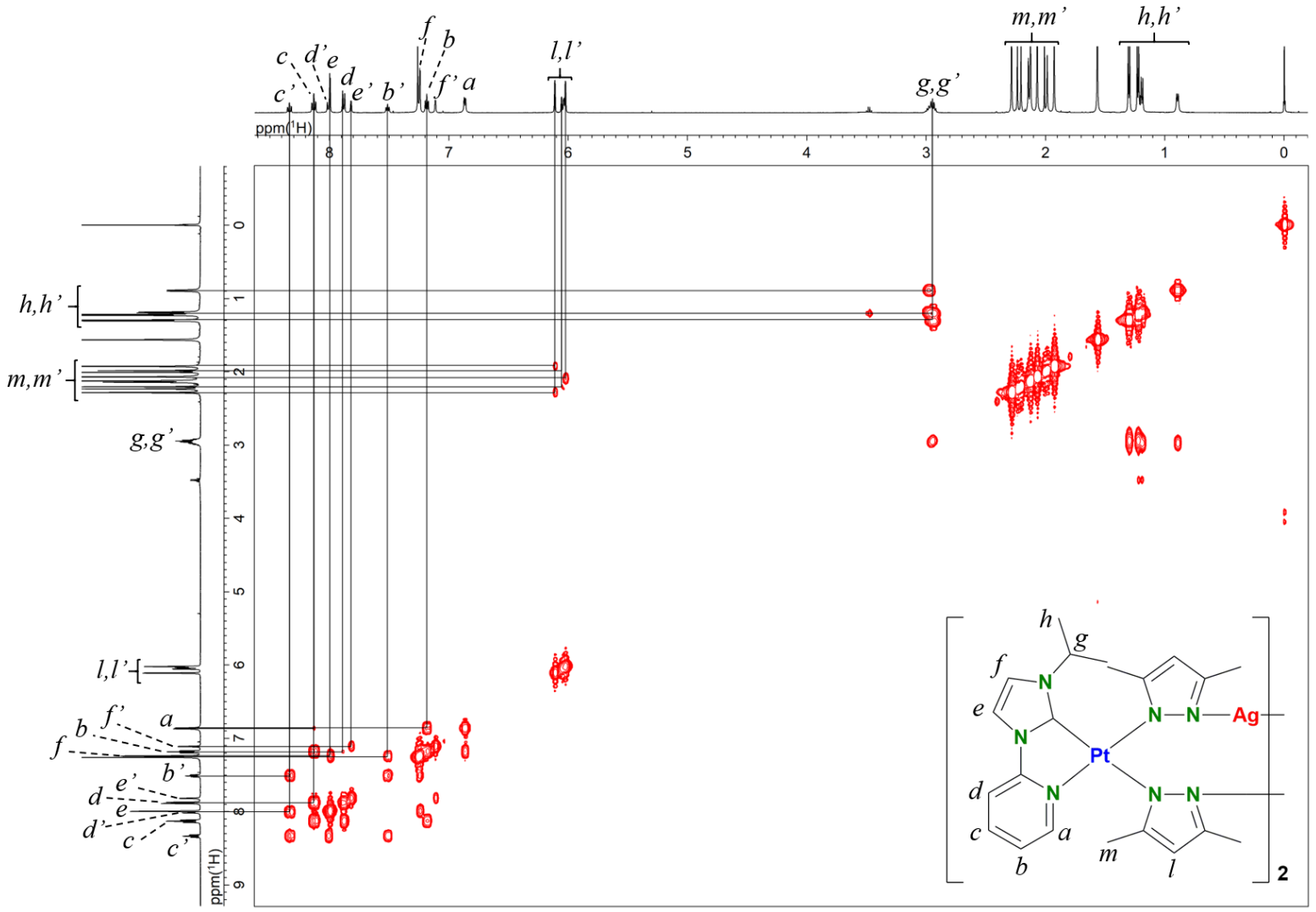

Figure 3-8. ^{1}H-^{1}H COSY spectrum (500 MHz, $CDCl_3$, 25 °C, TMS) of $[(Py\text{-}NHC)_2Pt_2Ag_2(Me_2pz)_4](PF_6)_2$ (**4**).

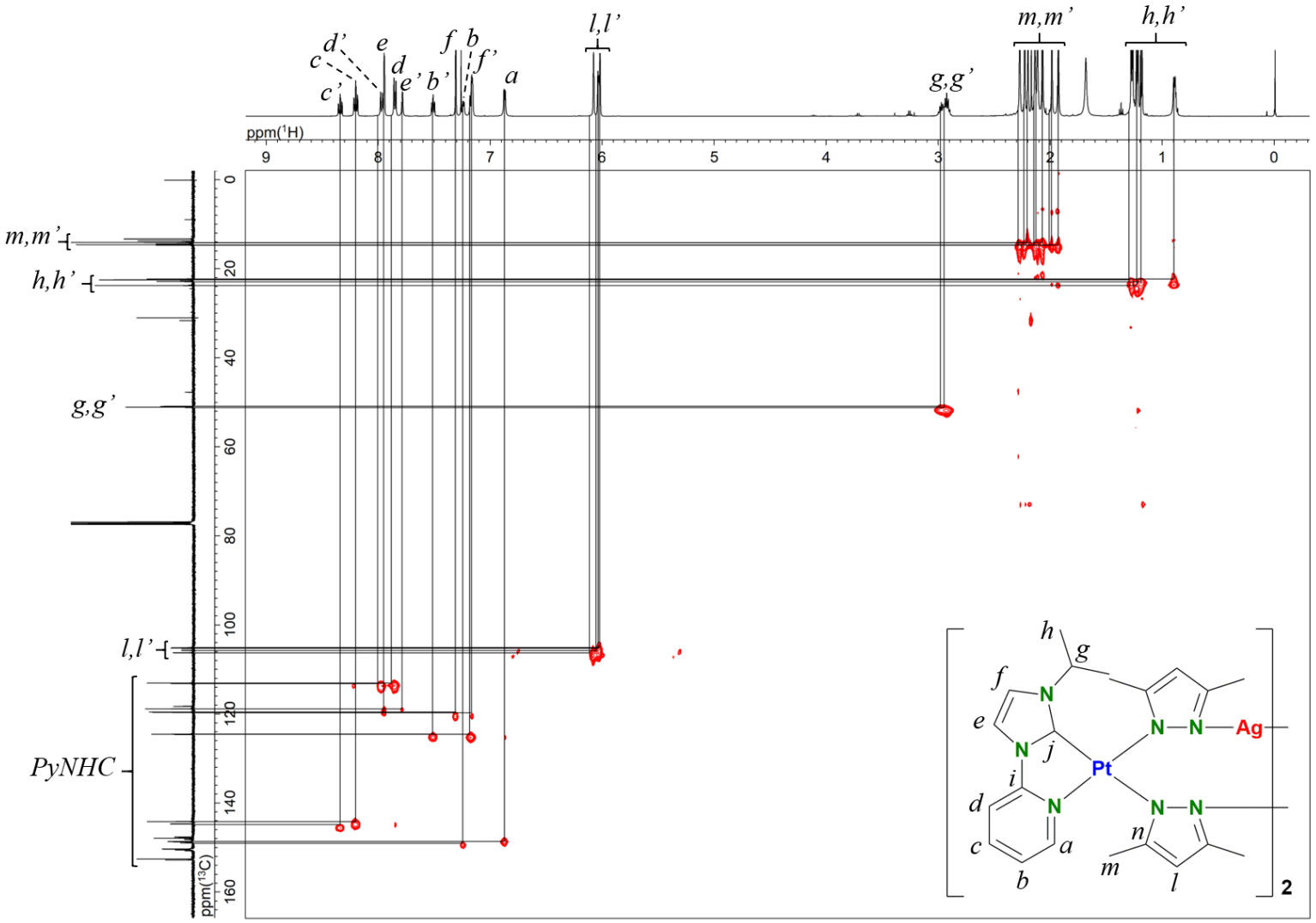

Figure 3-9. ^{1}H-^{13}C HSQC spectrum (500 MHz, $CDCl_3$, 25 °C, TMS) of $[(Py\text{-}NHC)_2Pt_2Ag_2(Me_2pz)_4](PF_6)_2$ (**4**).

3-3. Structral character of complex [(Py-NHC)Pt(Me$_2$pzH)$_2$](PF$_6$)$_2$ (3) and [(Py-NHC)$_2$Pt$_2$Ag$_2$(Me$_2$pz)$_4$](PF$_6$)$_2$ (4)

The pyrazolato-bridged Pt_2Ag_2 complex **4** was synthesized from the mononuclear Pt(II) complex **3** in a similar manner to our previous methods (**Scheme 3-2**).[27] The dimethylpyrazole complex [(Py-NHC)Pt(Me_2pzH)$_2$](PF_6)$_2$ (**3**) was obtained by the reaction of [(Py-NHC)$PtCl_2$] (**1**) with Me_2pzH in the presence of $AgPF_6$ in CH_3CN in 75% yield. The formation of **3** was confirmed by elemental analysis and FAB mass spectrometry. The ^{1}H NMR spectrum of **3** showed upfield shifts ($\Delta\delta$ = –2 to −3 ppm) of the tertiary proton at the ^{i}Pr group and the Pyα proton owing to the shielding effect from Me_2pzH moieties, indicating that the ^{i}Pr proton and the Pyα proton were perpendicularly oriented to the center of each different pyrazole ring, respectively, in solution (**Figure 3-10**). These signals were derived from two stereoisomers having syn- and anti-conformations at pyrazole moieties (**Scheme 3-1**). The structure of the anti-isomer of **3** was undoubtedly confirmed by single crystal X-ray structure analysis (**Figure 3-11**), though the dissolution of single crystals of **3** into Acetonitrile-d_3 gave a thermodynamic equilibrium state within 5 min.

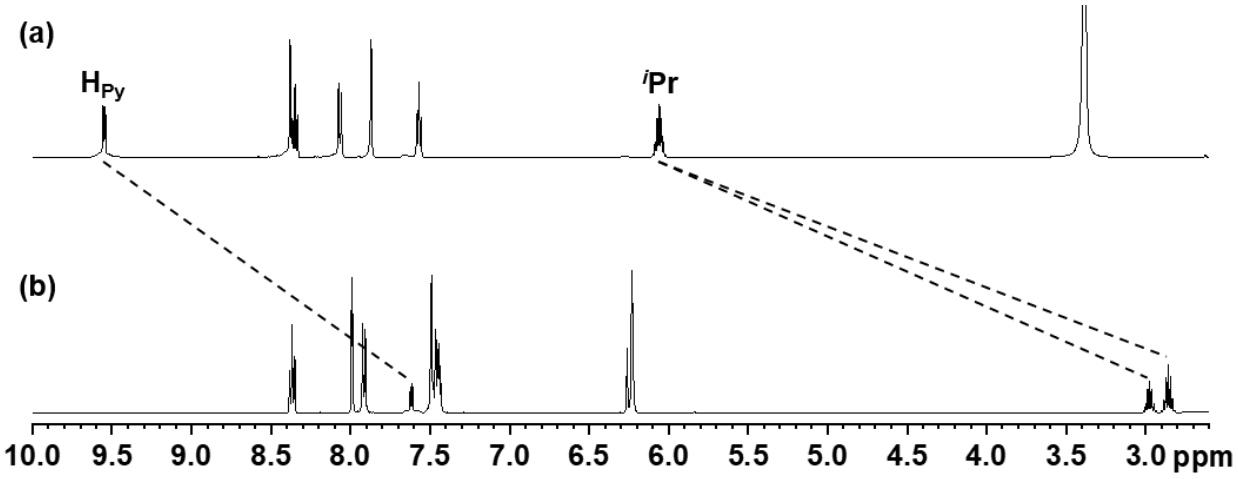

Figure 3-10. ^{1}H NMR spectra (500 MHz, 25 °C) of (a) complex **1** in DMSO-d_6 and complex **3** consisting of two geometrical isomers in acetonitrile-d_3.

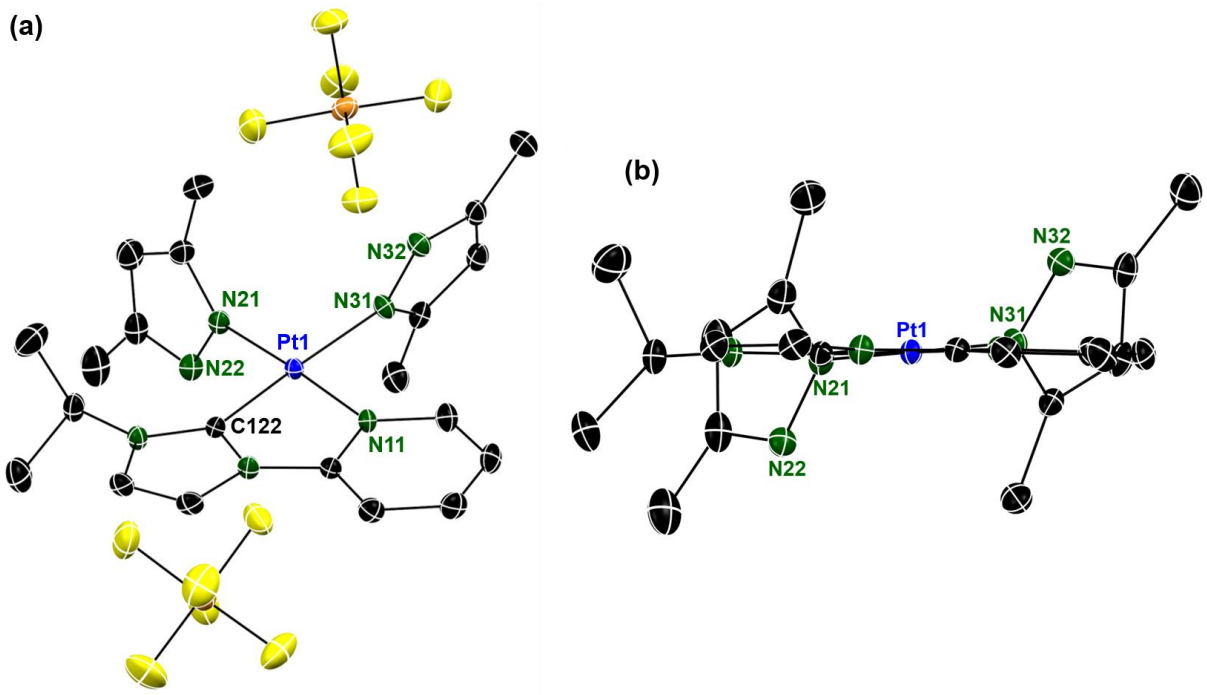

Figure 3-11. ORTEP drawing (50% probability ellipsoids) anti-[(Py-NHC)Pt(Me_2pzH)$_2$](PF_6)$_2$ (**3**). Hydrogen atoms were omitted for clarity. Selected bond length (Å): Pt1–C122 1.973(3), Pt1–N11 2.024(3), Pt1–N21 2.005(3), Pt1–N31 2.066(2).

The reaction of the isomer mixture of **3** with $AgPF_6$ in a 1 : 1 ratio in the presence of NEt_3 afforded a dicationic Pt_2Ag_2 complex having Py-NHC chelate ligands and pyrazolate bridges in 64% yield. Electrospray Ionization (ESI) mass analysis clearly revealed the formation of **4** at m/z 1504.7 which was assigned to $[M-(PF_6)]^+$ fragments. The molecular structure of **4** was determined by single crystal X-ray structure analysis.

A colorless single crystal of **4** suitable for X-ray structure analysis was obtained from an acetone–hexane solution of **4**. The X-ray structure analysis revealed that the complex cation in the crystal has a twisted U-shaped structure (**Figure 3-12**); hereafter $[\mathbf{4}_U]^{2+}$ and $[\mathbf{4}_Z]^{2+}$ denote the complex cations having a U-shaped structure and Z-shaped structure, respectively. The view along the Pt···Pt axis of $[\mathbf{4}_U]^{2+}$ shows that the pyridine rings in each Py-NHC ligand take an eclipsed configuration probably due to the steric hindrance of isopropyl substituents on each NHC ligand. The tertiary protons of isopropyl groups at NHC ligands are located above the

bridging pyrazolato ligands, suggesting that CH–π interactions may contribute to the formation of the Pt_2Ag_2 structure.[38,39] The larger deviation in Pt···Ag distances (3.1537(5), 3.1885(5), 3.5849(6), 3.6208(5) Å) in $[\mathbf{4_U}]^{2+}$ implies a more distorted structure of $[\mathbf{4_U}]^{2+}$ compared with a Pt_2Ag_2 analogue having ppy chelate ligands, $[Pt_2Ag_2(ppy)_2(Ph_2pz)_4]$ (Pt···Ag, 3.2028(5), 3.4249(3) Å).[27,28] These metal–metal distances are shorter than the sum of the van der Waals radius of the metal atoms (Pt: 1.77 Å, Ag: 1.65 Å), suggesting the existence of cooperative metal–metal interactions in $[\mathbf{4_U}]^{2+}$. In contrast, the complex cations and the counter anions were alternately oriented in the crystal, indicating no intermolecular metal–metal interaction in the solid state (**Figure 3-12**c). The $Pt–N_{pyrazolato}$ bond distances at the trans position of NHC moieties are approximately 0.05 Å longer than those at the trans position of pyridine rings. The difference is attributed to the stronger trans influence of the NHC moiety than that of the pyridine moiety.

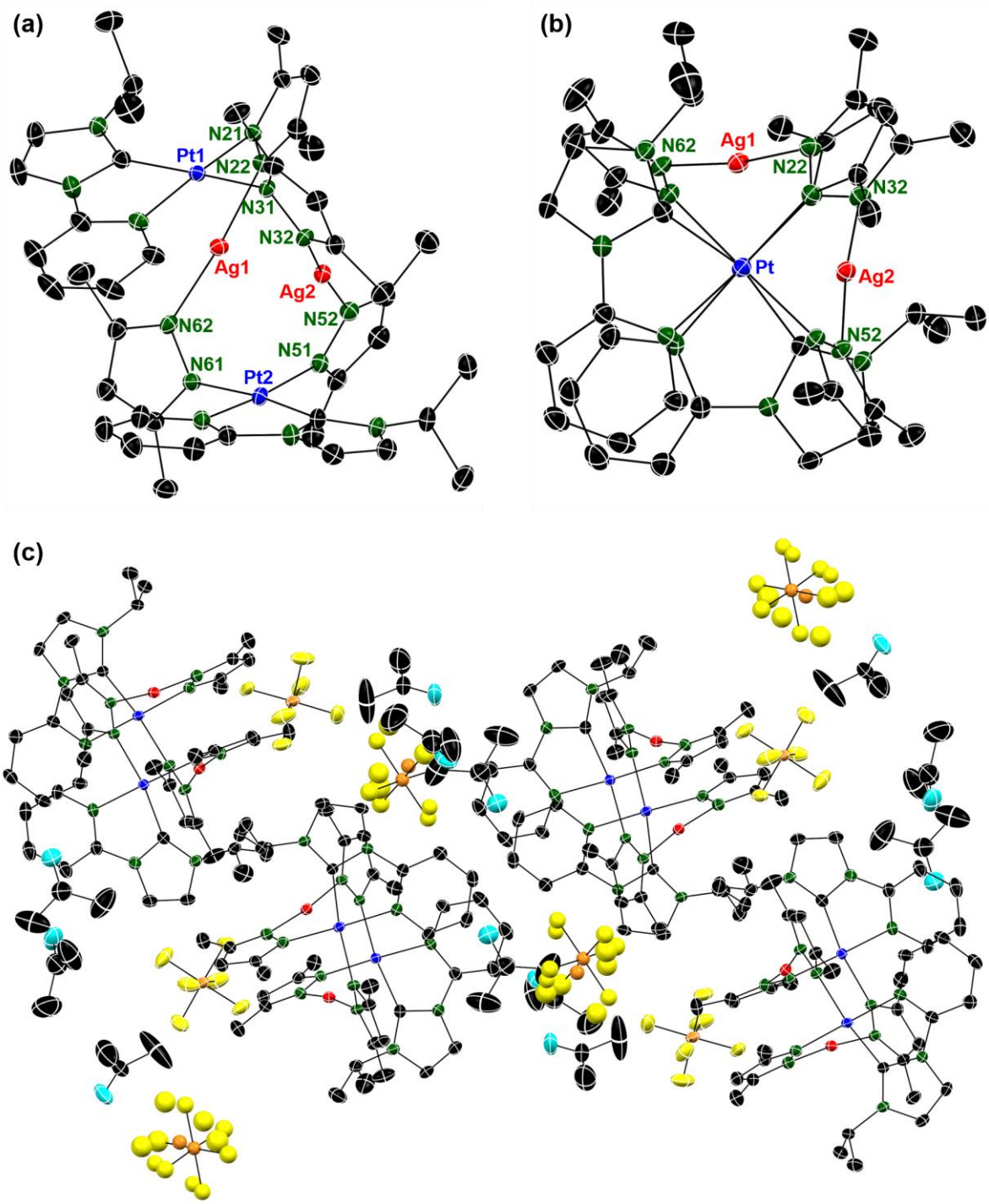

Figure 3-12. ORTEP representation (50% probability ellipsoids) of U-shaped $[(Py\text{-}NHC)_2Pt_2Ag_2(Me_2pz)_4]^{2+}$ ($[\mathbf{4}]^{2+}$) cation: (a) side view, (b) viewed along the Pt···Pt axis and (c) packing structure. Hydrogen atoms, counter anion and solvent molecules were omitted for clarity. Selected bond length (Å): Pt1···Pt2 5.3613(5), Pt1···Ag1 3.1537(5), Pt1···Ag2 3.5849(6), Pt1–N21 1.998(3), Pt1–N31 2.053(3), Pt2···Ag1 3.6208(5), Pt2···Ag2 3.1885(5), Pt2–N51 2.001(3), Pt2–N61 2.050(3), Ag1···Ag2 3.0745(5), Ag1–N22 2.093(3), Ag1–N62 2.076(3), Ag2–N32 2.085(3) and Ag2–N52 2.099(3).

The NMR studies revealed that the U-shaped Pt_2Ag_2 complex $[\mathbf{4}_U]^{2+}$ showed isomerization in the solution, although multiple metal–metal interactions were observed in the crystal structure (**Figure 3-13**a). When the single crystal of the U-shaped isomer $\mathbf{4}_U$ was dissolved in $CDCl_3$, new sets of signals appeared within 5 min and their intensities gradually increased (**Figure 3-14**). The signals assigned to pyridine protons were observed around a downfield region compared with those of $[\mathbf{4}_U]^{2+}$, suggesting that Py-NHC ligands of the new species were not stacked on each other. This behavior is very similar to those of Pt_2Ag_2 analogues, which exist as a mixture of U- and Z-shaped complexes in the solution.[27] Thus the new sets of signals in the ^{1}H NMR spectrum were assigned to the Z-shaped isomer $[\mathbf{4}_Z]^{2+}$. In addition, the integral ratios of the signals reached U : Z = 2 : 1 in a thermodynamic equilibrium state (**Figure 3-13**b). These results suggest that the metal–metal interactions and the Ag–Npyrazolato bonds in $[\mathbf{4}]^{2+}$ are actually labile in solution. The U-shaped isomer is a thermodynamically favored one as evidenced by the integral ratio of U : Z in the ^{1}H NMR spectra, probably because the highly twisted U-shaped structure can induce short contacts among the Pt and Ag ions to provide effective thermodynamic stability by metal–metal interactions. These two sets of signals for $[\mathbf{4}_U]^{2+}$ and $[\mathbf{4}_Z]^{2+}$ were also observed in the crude reaction product (**Figure 3-15**). Thus, the U-shaped isomer $[\mathbf{4}_U](PF_6)_2$ was selectively crystallized via isomerization in the crystallization process. It is noteworthy here that the isomerization rate became slow under diluted conditions, indicating that the reaction took place through an intermolecular process (**Figure 3-13**b). Additionally, the isomerization reaction immediately reached a state of thermodynamic equilibrium when single crystals of the U-shaped isomer $\mathbf{4}_U$ were dissolved in a coordinating solvent, such as Acetonitrile-d_3. It implies that isomerization was accelerated by the coordination of solvent molecules to the Ag ions, which competed with that of the Me_2pz ligands. The VT-NMR spectra of $[\mathbf{4}]^{2+}$ (i.e. the mixture of $[\mathbf{4}_U]^{2+}$ and $[\mathbf{4}_Z]^{2+}$ in the state of thermodynamic equilibrium) recorded even at 313 K in $CDCl_3$ and acetonitrile-d_3 showed no coalescence of

signals, indicating that isomerization between U- and Z-shaped structures is a slow process and does not proceed in the NMR time scale (**Figure 3-16**).

Our group recently reported that U-shaped Pt_2Ag_2 complexes having C^N chelate ligands can show reversible entrapment of Ag(I) ions in the Pt_2Ag_2 framework through Ag···Ag interaction and the formation of Pt → Ag dative bonds.[28] Therefore, the U-shaped Pt_2Ag_2 structure of $\mathbf{4}_U$ encouraged us to elucidate a binding ability for Ag(I) ions in solution. However, the ^{1}H NMR spectrum of $[\mathbf{4}_U]^{2+}$ did not change even by the addition of the excess amount of Ag(I) ions into the solution, indicating that the U-shaped Pt_2Ag_2 complex $[\mathbf{4}_U]^{2+}$ cannot stabilize additional Ag(I) ions in the Pt_2Ag_2 framework *via* multiple metal–metal interactions (**Figure 3-17**). On the other hand, Miguel recently reported that a dicationic $[Ag_2(bisNHC)_2]^{2+}$ complex captures even a cationic $[Ag(NCCH_3)_2]^+$ guest in the molecular cavity of the Ag_2 framework via strong argentophilic interactions, which overcomes the electrostatic repulsion between the complex cation and the Ag ion.[40,41] These results strongly suggest that the π-coordination ability of the C(ipso) atom in the C^N chelate ligand plays an important role in capturing Ag(I) ions into the Pt_2Ag_2 systems through Ag–C(ipso) bonding interaction. The lack of π-coordination ability of the carbene carbon atom in the Py-NHC ligand is attributed to the insensitive behavior of $[\mathbf{4}_U]^{2+}$ toward Ag(I) ions.

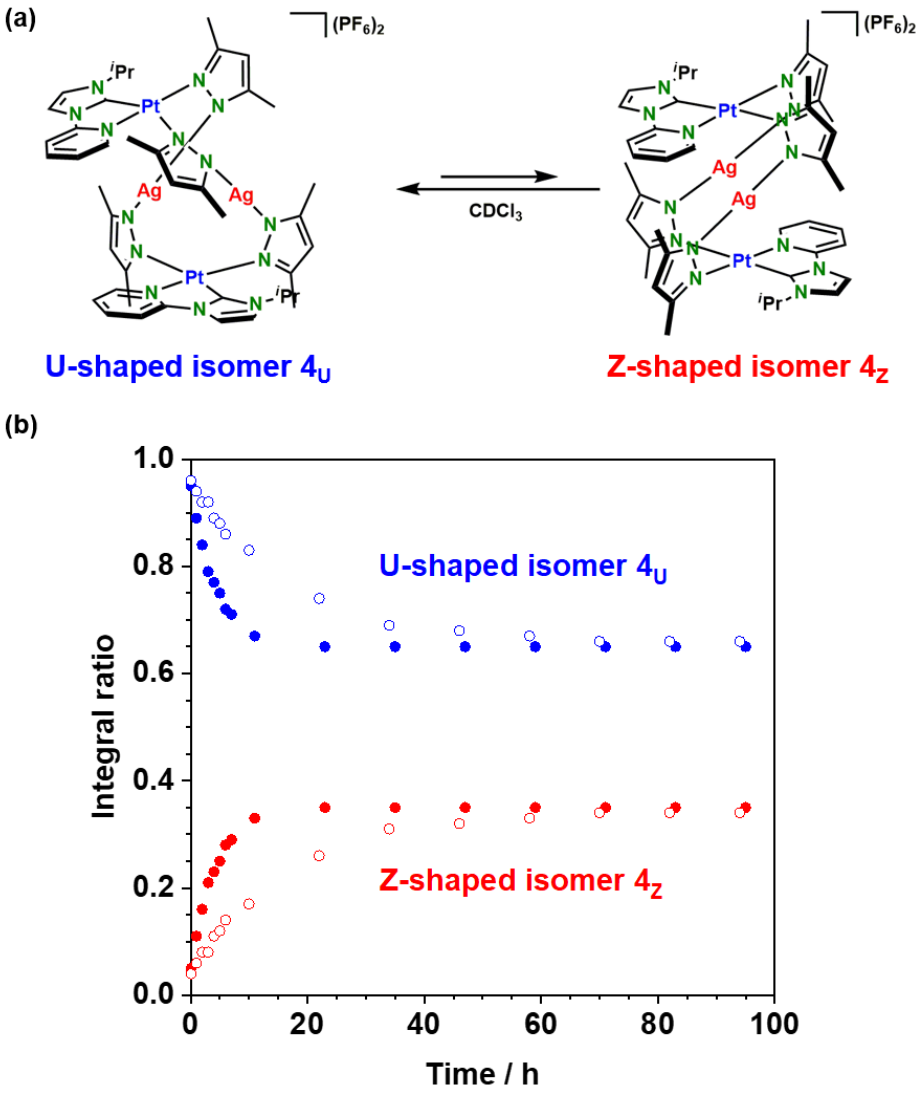

Figure 3-13. (a) Schematic representation of the isomerization from the U-shaped isomer $\mathbf{4_U}$ to the Z-shaped isomer $\mathbf{4_Z}$. (b) The variation with the time of the relative value of the integrated intensities H4 in $[\mathbf{4_U}]^{2+}$ (δ = 8.17 ppm) and $[\mathbf{4_Z}]^{2+}$ (δ = 8.34 ppm), which are proportional to the concentration of $[\mathbf{4U}]^{2+}$ and $[\mathbf{4_Z}]^{2+}$, respectively, after single crystals of $\mathbf{4_U}$ were dissolved in $CDCl_3$ in the dark at 25 °C (circles, 15 mM; hollow circles, 6 mM).

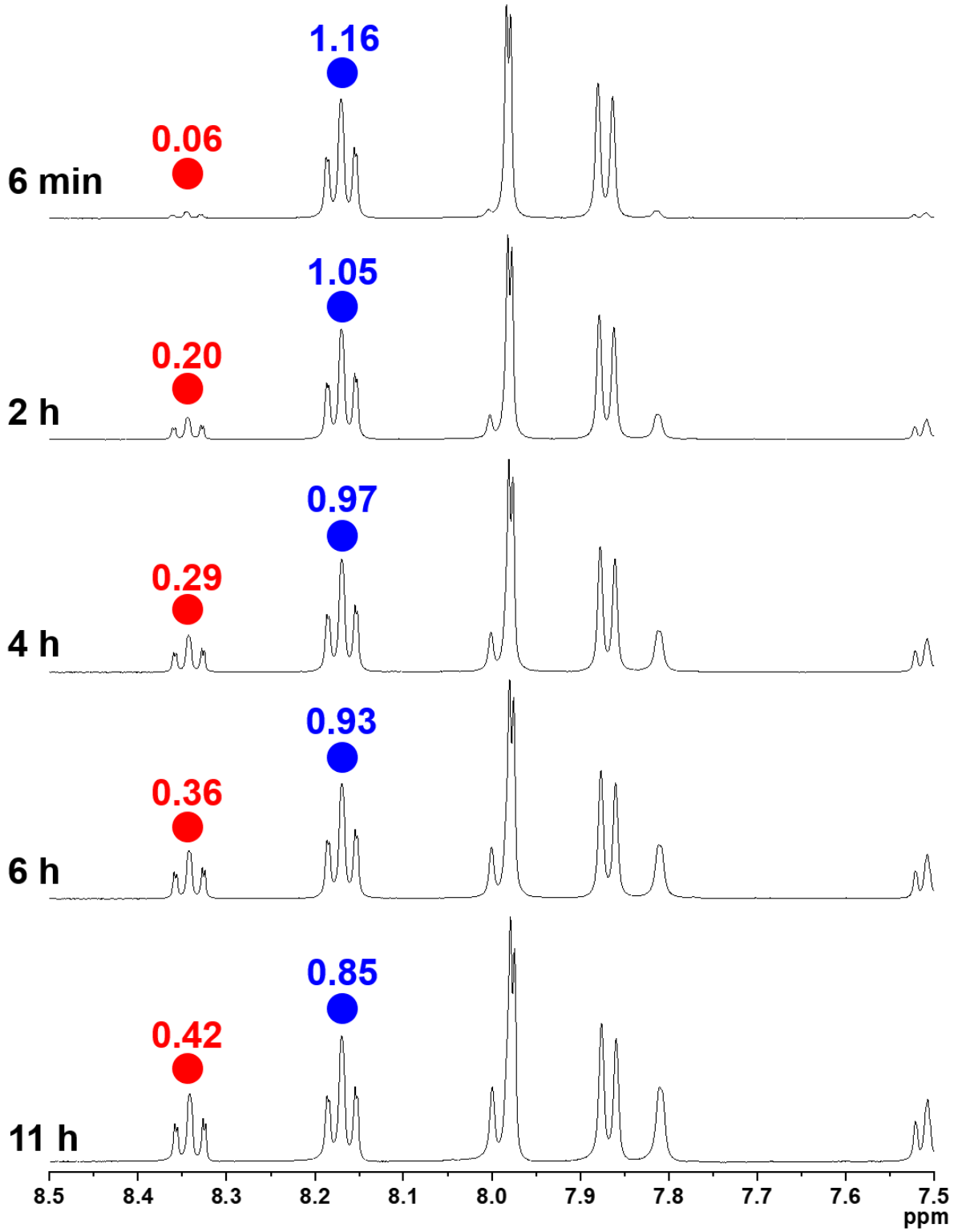

Figure 3-14. ^{1}H NMR spectral variations due to the isomerization of U-shaped isomer **4**$_{U}$ to Z-shaped isomer **4**z.

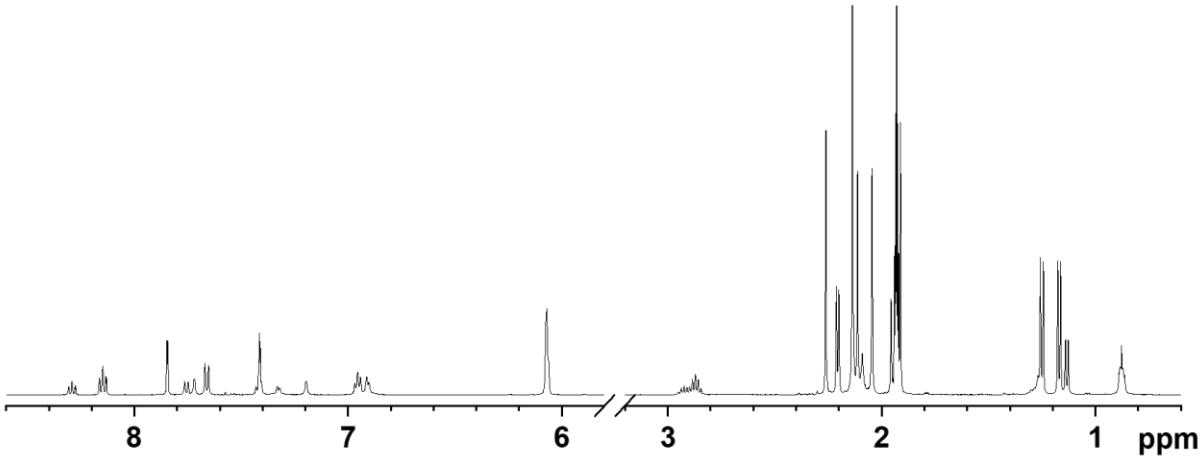

Figure 3-15. ^{1}H NMR spectra (500 MHz, acetonitrile-d_3, 25 °C) of a solution within 5 minutes after single crystals of U-shaped isomer $\mathbf{4_U}$ were dissolved.

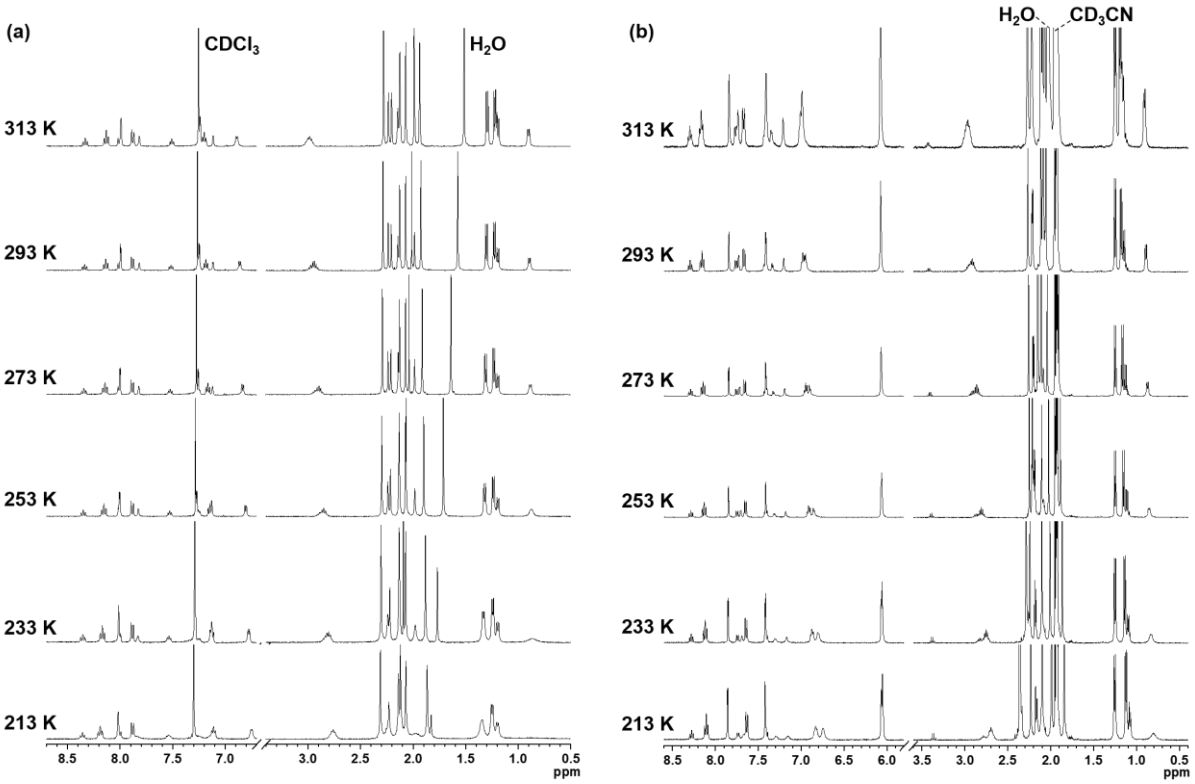

Figure 3-16. VT ^{1}H NMR spectra (400 MHz) of **4** in (a) $CDCl_3$ and (b) acetonitrile-d_3.

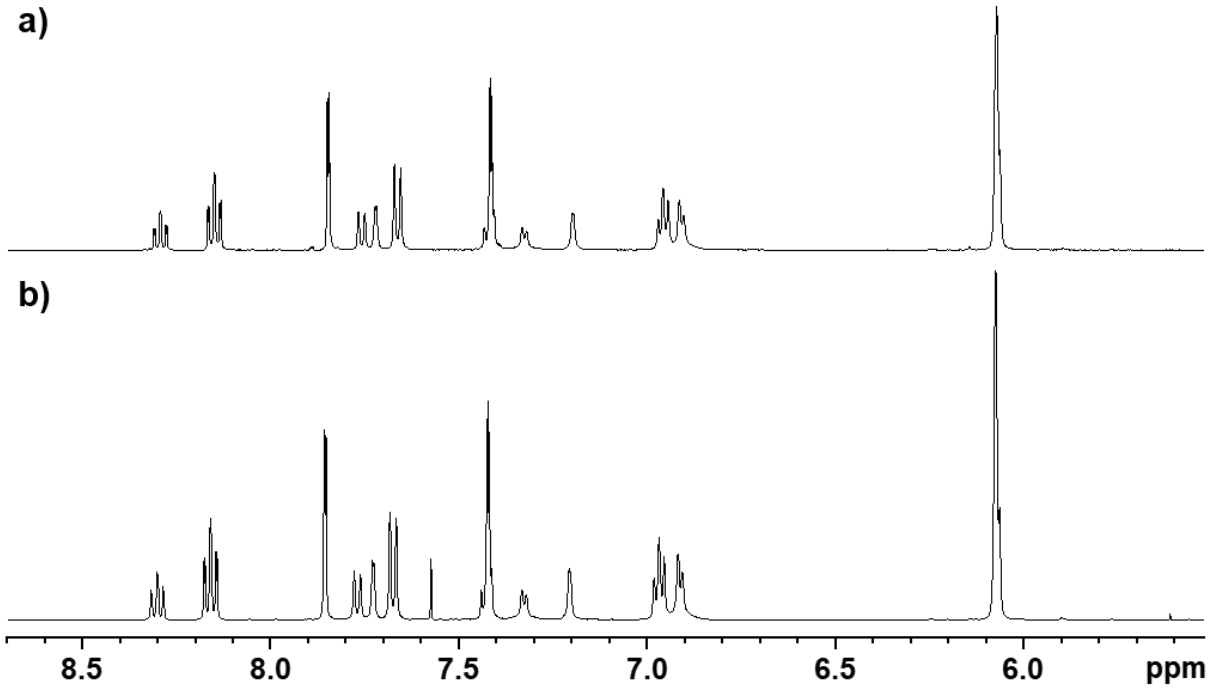

Figure 3-17. ^{1}H NMR spectra (500 MHz, acetonitrile-d_3, 25 °C) of **4** a) before and b) after an addition of $AgPF_6$ (1 eq.).

Table 3-1. Crystallographic data for $[(Py\text{-}NHC)Pt(Me2pzH)_2](PF_6)_2$ (**3**), $[(Py\text{-}NHC)_2Pt_2Ag_2(Me_2pz)_4](PF_6)_2\cdot 3(CH_3COCH_3)$ (**4**$_U\cdot 3CH_3COCH_3$)

	3	**4**$_U\cdot 3CH_3COCH_3$
Empirical formula	$C_{21}H_{29}F_{12}N_7P_2Pt$	$C_{51}H_{72}Ag_2F_{12}N_{14}O_3P_2Pt_2$
Formula weight	864.53	1825.07
Temperature (K)	93(1)	93(1)
Wavelength (Å)	0.71075	0.71075
Crystal system	monoclinic	monoclinic
Space group	*P*21/*c* (#14)	*P*21/*c* (#14)
Unit cell dimensions		
a (Å)	12.454(3)	13.5442(9)
b (Å)	16.341(4)	16.5420(11)
c (Å)	15.741(4)	29.6856(18)
α (deg)	-	-
β (deg)	112.102(4)	90.7088(12)
γ (deg)	-	-
V (Å^3)	2968.0(13)	6643.3(7)
Z	4	4
ρ_{calcd} (g/cm^3)	1.935	1.825
μ(Mo Kα) (mm^{-1})	4.918	5.104
F(000)	1680	3680
Index ranges	–17<=h<=16	–17<=h<=16
	–22<=k<=13	–22<=k<=13
	–21<=l<=11	–21<=l<=11
Reflections collected	16875	57542
Independent reflections	7888 [R_{int} = 0.0266]	17198 [R_{int} = 0.0739]
Data / restraints / parameters	7888 / 0 / 389	17196 / 1 / 792
Goodness-of-fit on F^2	1.031	1.069
Final *R* index [$I>2\sigma(I)$][a]	R_1 = 0.0269	R_1 = 0.0573
R indices (all data)[a,b]	R_1 = 0.0363	R_1 = 0.0283
	wR_2 = 0.0609	wR_2 = 0.0773
Largest diff. peak and hole (eÅ^{-3})	2.14 and –1.63	1.39 and –1.07
CCDC number	1588182	1588197

[a] $R_1 = \sum||F_o| - |F_c||/\sum|F_o|$. [b] $wR_2 = [\sum w(F_o^2 - F_c^2)^2]/\sum[w(F_o^2)^2]]^{1/2}$.

3-4. Photophysical properties of complexes having chelate Py-NHC ligand

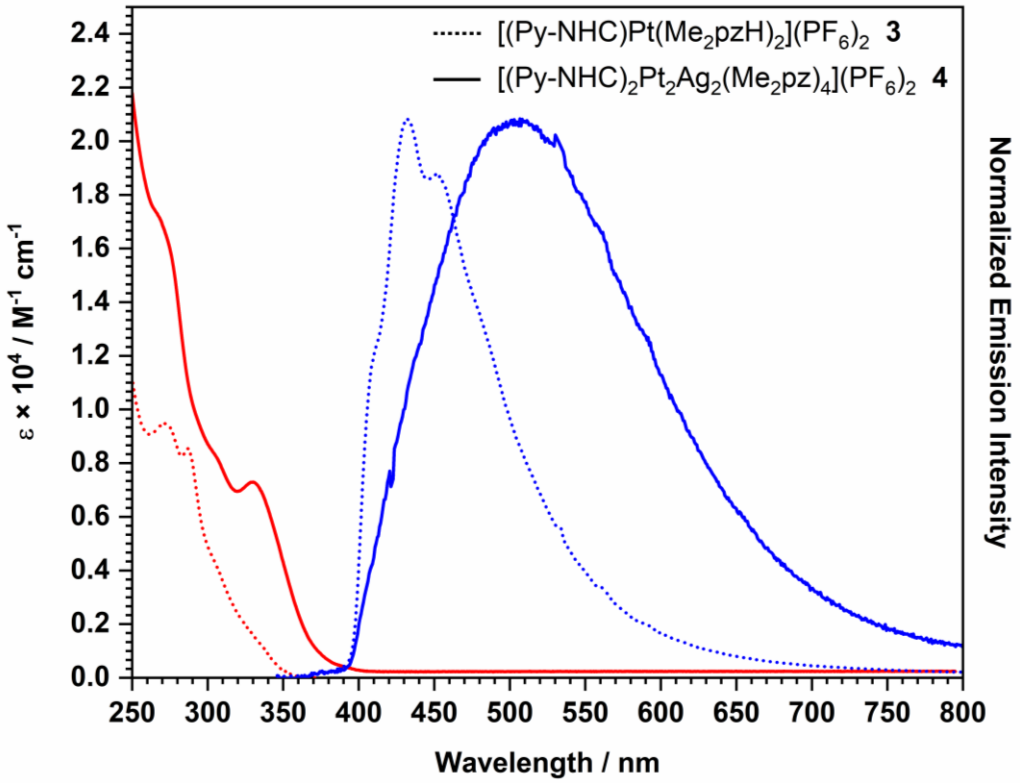

Figure 3-18. UV/Vis absorption spectra (red) of **3** (dashed line) and **4** (solid line) MeCN and their normalized emission spectra (blue) in the solid state at room temperature (λ_{ex} = 355 nm).

The mononuclear Pt(II) complex **3** and Pt_2Ag_2 complex **4** showed the lowest energy absorption bands at 320 nm (sh) and 335 nm, respectively, in CH_3CN at room temperature, whose energies are higher than those of the Pt_2Ag_2 analogue having ppy chelate ligands (**Figure 3-18**).[27] Since the corresponding absorption band is absent in **3**, the band at 335 nm in **4** originates from the formation of the Pt_2Ag_2 structure.

Although the complexes **3** and **4** did not display photoluminescence in solution at room temperature, they showed a structured emission spectrum (λ_{max} = 431 nm) and a broad one (λ_{max} = 507 nm), respectively, in the solid state (**Figure 3-18**). The observed lifetimes of the emission in a few hundreds of nanoseconds indicate that the emissions are phosphorescence (**Table 3-2**). Corresponding to the appearance of lower energy absorption bands in **4**, the

emission bands of **4** significantly red-shifted ($\Delta\lambda_{max}$ = +76 nm) compared with those of **3**, indicating that the incorporation of Ag(I) ions drastically affects the emission energy. To our surprise, the emission quantum yield (Φ_{em}) of **4** (1%) was smaller than that of **3** at room temperature. This is in contrast to our previous results that the formation of mixed-metal complexes having multiple metal–metal interactions affords brighter luminescence than the precursor Pt(II) complex in the solid state.[24–28]

To unveil the origin of the differences in the photophysical properties between **3** and **4**, the time dependent density functional theory (TD-DFT) method was investigated. The DFT calculation clearly visualized the highest-occupied molecular orbitals (HOMOs) and the lowest-unoccupied molecular orbitals (LUMOs) in the complexes (**Tables 3-3** – **3-6**, **Figures 3-19** and **3-20**). The LUMOs of both the complexes are similar to each other and consist of the π^* orbital of the pyridyl moiety, while the HOMOs consist of the π orbital of Me_2pz moieties and the 5d orbital of Pt atoms. Moreover, a large contribution of the 4d orbital of Ag atoms is found in the HOMO−2 of **4**. These calculations suggest that the lowest energy absorption bands of **3** can be assigned mainly to the combination of ligand-to-ligand charge transfer (LLCT) [$Me_2pz \rightarrow \pi^*$(Py–NHC)] and metal-to-ligand charge transfer (MLCT) [Pt → π^*(Py–NHC)] transitions. The assignment for **4** is essentially very similar to that for **3**. However, in addition to the combination of LLCT and MLCT transitions, the metal-to-ligand charge transfer (M′LCT) [Ag → π^*(Py–NHC)] transitions further contribute to the lowest energy absorption band in **4** due to the formation of the Pt_2Ag_2 complex. The features of the emission spectra of **3** and **4** may be attributed to the different nature of their excited states (**Tables 3-5** and **3-6**).

Table 3-2. Photophysical data for complexes **3** and **4** under air atmosphere at room temperature in the solid state

complex	λ_{abs} / nm ($\varepsilon \times 10^4$ M^{-1} cm^{-1})[a]	λ_{em} / nm[b]	τ_1 (A_1) / μs	τ_2 (A_2) / μs
3	271 (0.95), 287 (0.85), 320 sh (0.24)	431	0.32 (0.94)	2.00 (0.05)
4	272 sh (1.72), 308 sh (0.85), 335 (0.73)	507	0.13 (0.81)	0.53 (0.17)

complex	τ_3 (A_3) / μs	τ_{ave} / μs	k_r / $\times 10^4$ s^{-1}	k_{nr} / $\times 10^6$ s^{-1}	Φ_{em} / %
3	16.3 (0.01)	5.2	0.4	0.2	2[a]
4	2.60 (0.02)	0.8	1.3	1.2	1[a]

[a]in acetonitrile.

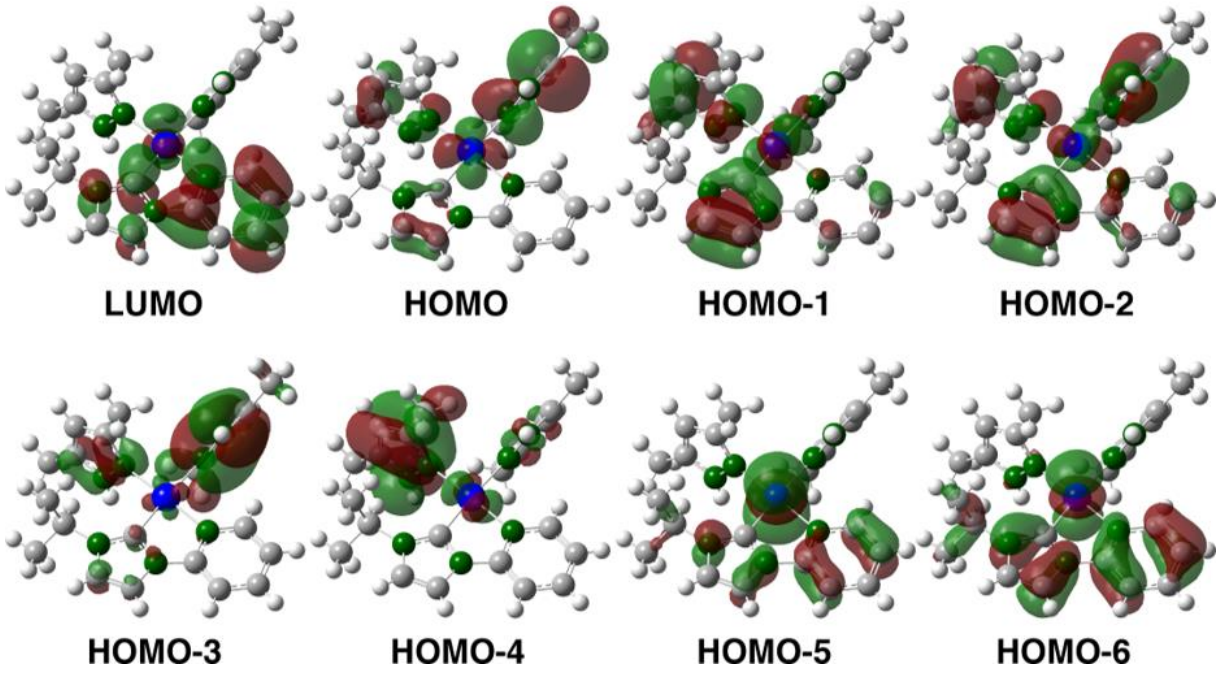

Figure 3-19. Molecular orbitals of the singlet state for $[\mathbf{3}]^{2+}$.

Table 3-3. Calculated Singlet Excited States (S_1–S_{25}) of $[\mathbf{3}]^{2+}$.[a]

Excited State	Transition	Energy (Wavelength)	Oscillator Strength
S1	HOMO-2 → LUMO (15%) HOMO → LUMO (85%)	3.7637 eV (329.42 nm)	0.0090
S2	HOMO-2 → LUMO (30%) HOMO-1 → LUMO (70%)	3.9747 eV (311.94 nm)	0.0148
S3	HOMO-2 → LUMO	4.1890 eV (295.97 nm)	0.0089
S4	HOMO-6 → LUMO (36%) HOMO-5 → LUMO (64%)	4.4130 eV (280.95 nm)	0.0074
S5	HOMO-6 → LUMO (11%) HOMO-5 → LUMO (20%) HOMO-3 → LUMO (69%)	4.4557 eV (278.26 nm)	0.0029
S6		4.6519 eV (266.52 nm)	0.0075
S7		4.7125 eV (263.10 nm)	0.0042
S8		4.7426 eV (261.43 nm)	0.0800
S9		4.8221 eV (257.12 nm)	0.0009
S10		4.8405 eV (256.14 nm)	0.0640
S11		5.0280 eV (246.59 nm)	0.0816
S12		5.1135 eV (242.46 nm)	0.0040
S13		5.1848 eV (239.13 nm)	0.0860
S14		5.2234 eV (237.36 nm)	0.0085
S15		5.3731 eV (230.75 nm)	0.0154
S16		5.3889 eV (230.07 nm)	0.0019
S17		5.4252 eV (228.54 nm)	0.0023
S18		5.6013 eV (221.35 nm)	0.0558
S19		5.6472 eV (219.55 nm)	0.0162
S20		5.6586 eV (219.11 nm)	0.0843
S21		5.7000 eV (217.52 nm)	0.0849
S22		5.7874 eV (214.23 nm)	0.0126
S23		5.8227 eV (212.93 nm)	0.0806
S24		5.8491 eV (211.97 nm)	0.0115
S25		5.9323 eV (209.00 nm)	0.0018

[a] Transition details for S6-S25 are omitted.

Table 3-4. Molecular-Orbital populations of $[\mathbf{3}]^{2+}$.

Molecular Orbital	MO population / %				
	Pt	Py-NHC		Me_2pz (trans to Py)	Me_2pz (trans to NHC)
		Py	NHC		
LUMO	9.88	67.36	18.86	2.42	1.48
HOMO	23.35	2.70	6.85	10.11	56.99
HOMO-1	22.84	4.94	30.53	38.71	2.98
HOMO-2	13.19	7.63	23.53	25.32	30.33
HOMO-3	2.71	2.00	4.02	9.65	81.62
HOMO-4	10.16	0.97	2.07	82.11	4.69
HOMO-5	73.87	11.38	12.28	1.28	1.19
HOMO-6	63.76	26.52	1.92	7.19	0.61

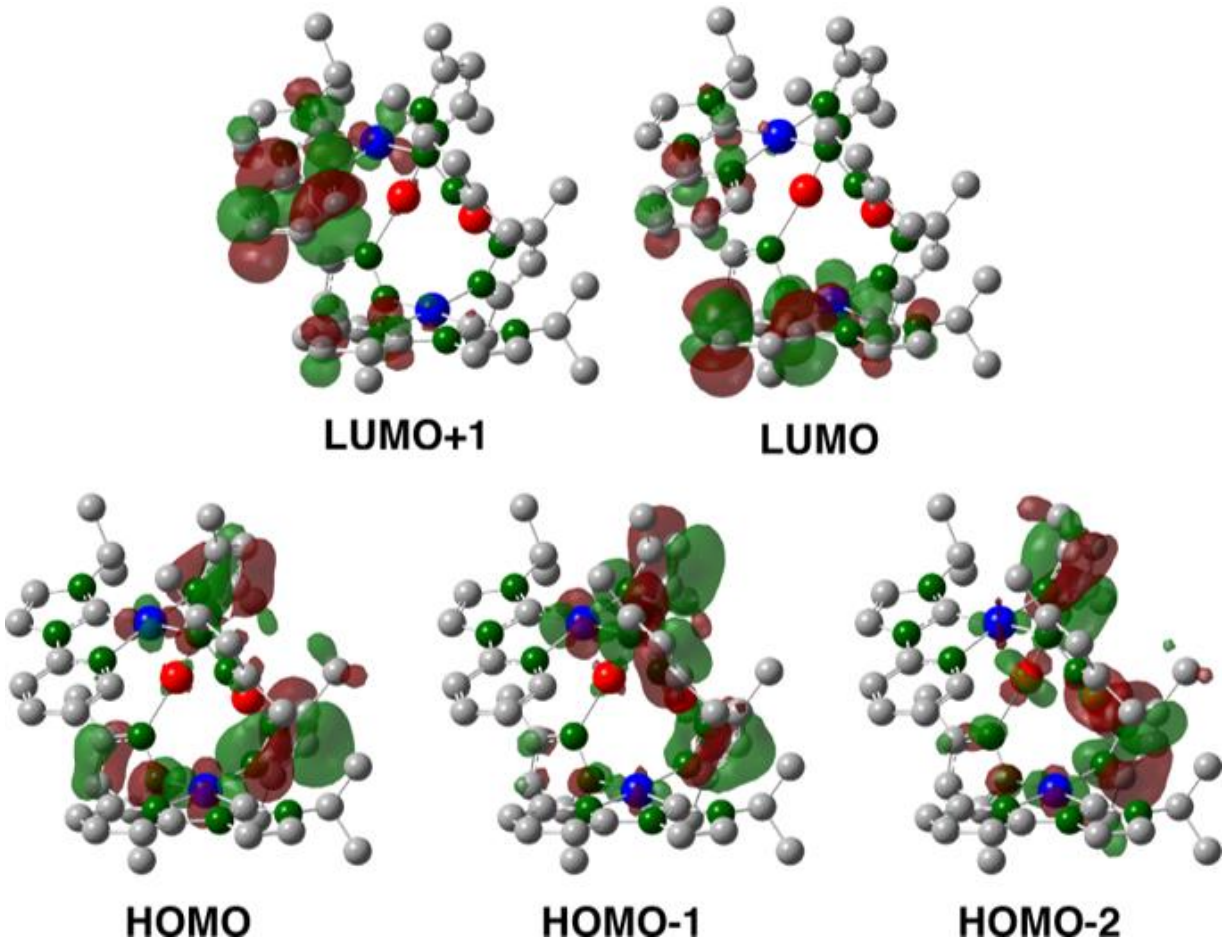

Figure 3-20. Molecular orbitals of the singlet state for $[\mathbf{4}_{\mathrm{U}}]^{2+}$.

Table 3-5. Calculated Singlet Excited States (S_1–S_{25}) of $[\mathbf{4}_U]^{2+}$.[a]

Excited State	Transition	Energy (Wavelength)	Oscillator Strength
S1	HOMO-2 → LUMO (16%) HOMO-1 → LUMO (20%) HOMO → LUMO (64%)	2.7303 eV (454.11 nm)	0.0063
S2	HOMO-2 → LUMO+1 (14%) HOMO-1 → LUMO (31%) HOMO-1 → LUMO+1 (55%)	2.7560 eV (449.88 nm)	0.0052
S3	HOMO-1 → LUMO (62%) HOMO → LUMO+1 (38%)	2.9388 eV (421.88 nm)	0.0004
S4	HOMO-1 → LUMO+1 (44%) HOMO → LUMO (24%) HOMO → LUMO+1 (32%)	2.9497 eV (420.32 nm)	0.0022
S5	HOMO-2 → LUMO (57%) HOMO-1 → LUMO (22%) HOMO → LUMO+1 (21%)	2.9819 eV (415.80 nm)	0.0002
S6		2.9984 eV (413.50 nm)	0.0004
S7		3.0142 eV (411.33 nm)	0.0020
S8		3.0250 eV (409.87 nm)	0.0032
S9		3.0482 eV (406.75 nm)	0.0075
S10		3.0949 eV (400.61 nm)	0.0067
S11		3.1207 eV (397.30 nm)	0.0048
S12		3.1712 eV (390.97 nm)	0.0067
S13		3.2101 eV (386.23 nm)	0.0022
S14		3.2195 eV (385.10 nm)	0.0028
S15		3.2388 eV (382.81 nm)	0.0008
S16		3.2710 eV (379.04 nm)	0.0055
S17		3.3150 eV (374.01 nm)	0.0080
S18		3.3339 eV (371.89 nm)	0.0114
S19		3.4255 eV (361.94 nm)	0.0006
S20		3.4542 eV (358.93 nm)	0.0001
S21		3.4636 eV (357.96 nm)	0.0011
S22		3.4916 eV (355.09 nm)	0.0002
S23		3.6359 eV (341.00 nm)	0.0028
S24		3.6678 eV (338.03 nm)	0.0043
S25		3.7072 eV (334.44 nm)	0.0018

[a] Transition details for S6-S25 are omitted.

Table 3-6. Molecular-Orbital populations of $[\mathbf{4}_{\mathbf{U}}]^{2+}$.

Molecular Orbital	MO population / %					
	Pt	Ag	Py-NHC		Me_2pz (trans to Py)	Me_2pz (trans to NHC)
			Py	NHC		
LUMO+1	9.05	2.15	73.40	11.77	2.13	1.50
LUMO	8.34	1.18	73.71	14.11	1.77	0.89
HOMO	19.33	4.25	2.45	2.64	56.50	14.83
HOMO-1	17.43	5.10	2.37	2.30	53.13	19.67
HOMO-2	6.97	19.79	0.52	2.42	61.95	8.35

3-5. Conclusion

In summary, I synthesized a heteropolynuclear Pt_2Ag_2 complex having pyridyl-NHC chelating ligands with multiple Pt–Ag and Ag–Ag interactions. Although the as-prepared Pt_2Ag_2 complex exists as a mixture of two isomers, it selectively crystallized to afford only a U-shaped isomer in the solid state, allowing us to elucidate the thermodynamically favored isomer as well as the U to Z structural isomerization in solution. The Pt_2Ag_2 complex having pyridyl-NHC chelating ligands showed higher emission energy than the Pt_2Ag_2 analogues having other aromatic C^N chelate ligands like 2-phenylpyridine derivatives. This is probably due to the strong σ-donating ability of the carbene carbon atom on the Py-NHC ligand. These results give us new insight into the relationship between structural transformations and photophysical properties involving weak intramolecular metal–metal interactions, leading to a construction of new types of functional molecules incorporating both dynamic molecular systems and light-emitting properties.

3-6. Experimental section

3-6-1. Materials

[(Py-NHC)$PtCl_2$] (**1**) was prepared according to a modified literature method.[42] All other commercially available reagents were used as purchased. Synthesis of the complexes was carried out under air unless otherwise noted.

3-6-2. Physical measurement and instrumentation

The 1D (^1H, ^{13}C) and 2D (^1H–^1H COSY, ^1H–^{13}C HSQC, ^1H–^{13}C HMBC) NMR spectra were obtained at 500 MHz Varian NMR System 500PS spectrometer. The VT-NMR (variable-temperature NMR) measurements were performed at 400 MHz with JEOL

JNM-AL400. UV/Vis spectra were recorded on a Jasco V-560 spectrophotometer at 20 °C. The corrected emission spectra were obtained by using a Hamamatsu PMA-12 multichannel photodetector (excitation wavelength = 355 nm). Emission quantum yields in the solid state were determined by using a Hamamatsu Photonic Absolute PL Quantum Yield Measurement System C9920-02 with an integrating sphere and a PMA-12 multichannel photodetetor (excitation wavelength = 300 nm). The emission lifetime measurements were conducted by using a Hamamatsu C11200 streak camera as a photodetector by exciting at 355 nm using a nanosecond Q-switched Nd:YAG laser (Continum® MiniliteTM, fwhm ≈ 10–12 ns, repetition rate = 10 Hz).

All measurements were performed at room temperature. Emission decay curve was analysed by the equation ($I(t) = A_1\exp(-t/\tau_1) + A_2\exp(-t/\tau_2) + A_3\exp(-t/\tau_3)$) using the nonlinear least-squares method. The averaged emission lifetime (τ_{ave}) was estimated by the equation ($\tau_{ave} = (A_1\tau_1^2 + A_2\tau_2^2 + A_3\tau_3^2) / (A_1\tau_1 + A_2\tau_2 + A_3\tau_3)$).

3-6-3. X-ray structural determinations

Crystals suitable for X-ray structural analysis were obtained by recrystallization from acetone/*n*-hexane (**3**) and acetone/*n*-hexane (**4**$_U$·3CH_3COCH_3), respectively. The crystal structures were solved by direct method (SHELXS-97).[43] The positional and thermal parameters of non-H atoms were refined anisotropically by the full-matrix least-squares method except for disordering counter anions. All calculations were performed using the CrystalStructure crystallographic software package[44] except for refinement, which was performed using SHELXL-2014/7.[43]

3-6-4. Computational methods

Time-dependent density functional theory (TD-DFT) calculations were performed to estimate the energies and oscillator strengths of the 25 lowest-energy singlet and triplet absorption transitions by using the B3LYP DFT. The LanL2DZ and 6-31G(d,p) basis sets were used to treat the geometrical structures of the platinum/silver and all other atoms, respectively. For all of the calculations, crystallographic data were used as geometries in the crystalline phase. All calculations were carried out using the Gaussian 16W package.[45] Molecular orbitals with the isovalue of 0.03 were drawn by the Gauss View 5.[46]

3-7. References

(1) Che, C. M.; Lai, S. W. *Coord. Chem. Rev.* **2005**, *249* (13–14), 1296–1309.

(2) Schmidbaur, H.; Schier, A. *Chem. Soc. Rev.* **2012**, *41* (1), 370–412.

(3) Schmidbaur, H.; Schier, A. *Angew. Chem. Int. Ed.* **2015**, *54* (3), 746–784.

(4) Schmidbaur, H.; Schier, A. *Organometallics* **2015**, *34* (11), 2048–2066.

(5) Yam, V. W. W.; Au, V. K. M.; Leung, S. Y. L. *Chem. Rev.* **2015**, *115* (15), 7589–7728.

(6) Yoshida, M.; Kato, M. *Coord. Chem. Rev.* **2018**, *355*, 101–115.

(7) Pérez-Temprano, M. H.; Casares, J. A.; Espinet, P. *Chem. Eur. J.* **2012**, *18* (7), 1864–1884.

(8) Buchwalter, P.; Rosé, J.; Braunstein, P. *Chem. Rev.* **2015**, *115* (1), 28–126.

(9) Mankad, N. P. *Chem. Eur. J.* **2016**, *22* (17), 5822–5829.

(10) Powers, I. G.; Uyeda, C. *ACS Catal.* **2017**, *7* (2), 936–958.

(11) Buschbeck, R.; Low, P. J.; Lang, H. *Coord. Chem. Rev.* **2011**, *255* (1–2), 241–272.

(12) Díez, Á.; Lalinde, E.; Moreno, M. T. *Coord. Chem. Rev.* **2011**, *255* (21–22), 2426–2447.

(13) Yamaguchi, T.; Yamazaki, F.; Ito, T. *J. Am. Chem. Soc.* **2001**, *123* (4), 743–744.

(14) Janzen, D. E.; Mehne, L. F.; VanDerveer, D. G.; Grant, G. J. *Inorg. Chem.* **2005**, *44* (23), 8182–8184.

(15) Moret, M. E.; Chen, P. *J. Am. Chem. Soc.* **2009**, *131* (15), 5675–5690.

(16) Jamali, S.; Mazloomi, Z.; Masoud Nabavizadeh, S.; Milić, D.; Kia, R.; Rashidi, M. *Inorg. Chem.* **2010**, *49* (6), 2721–2726.

(17) Fuertes, S.; Woodall, C. H.; Raithby, P. R.; Sicilia, V. *Organometallics* **2012**, *31* (11), 4228–4240.

(18) Zhang, X.; Cao, B.; Valente, E. J.; Hollis, T. K. *Organometallics* **2013**, *32* (3), 752–761.

(19) Kubo, K.; Okitsu, H.; Miwa, H.; Kume, S.; Cavell, R. G.; Mizuta, T. *Organometallics* **2017**, *36* (2), 266–274.

(20) Oberbeckmann-Winter, N.; Morise, X.; Braunstein, P.; Welter, R. *Inorg. Chem.* **2005**, *44* (5), 1391–1403.

(21) Forniés, J.; Fortuño, C.; Ibáñez, S.; Martín, A.; Mastrorilli, P.; Gallo, V. *Inorg. Chem.* **2011**, *50* (21), 10798–10809.

(22) Nebra, N.; Ladeira, S.; Maron, L.; Martin-Vaca, B.; Bourissou, D. *Chem. Eur. J.* **2012**, *18* (27), 8474–8481.

(23) Baya, M.; Belío, Ú.; Fernández, I.; Fuertes, S.; Martín, A. *Angew. Chem. Int. Ed.* **2016**, *55* (24), 6978–6982.

(24) Umakoshi, K.; Kojima, T.; Saito, K.; Akatsu, S.; Onishi, M.; Ishizaka, S.; Kitamura, N.; Nakao, Y.; Sakaki, S.; Ozawa, Y. *Inorg. Chem.* **2008**, *47* (12), 5033–5035.

(25) Umakoshi, K.; Saito, K.; Arikawa, Y.; Onishi, M.; Ishizaka, S.; Kitamura, N.; Nakao, Y.; Sakaki, S. *Chem. Eur. J.* **2009**, *15* (17), 4238–4242.

(26) Akatsu, S.; Kanematsu, Y.; Kurihara, T. A.; Sueyoshi, S.; Arikawa, Y.; Onishi, M.; Ishizaka, S.; Kitamura, N.; Nakao, Y.; Sakaki, S.; Umakoshi, K. *Inorg. Chem.* **2012**, *51* (15), 7977–7992.

(27) Nishihara, K.; Ueda, M.; Higashitani, A.; Nakao, Y.; Arikawa, Y.; Horiuchi, S.; Sakuda, E.; Umakoshi, K. *Dalton Trans.* **2016**, *45* (12), 4978–4982.

(28) Ueda, M.; Horiuchi, S.; Sakuda, E.; Nakao, Y.; Arikawa, Y.; Umakoshi, K. *Chem. Commun.* **2017**, *53* (48), 6405–6408.

(29) Han, Z.; Bates, J. I.; Strehl, D.; Patrick, B. O.; Gates, D. P. *Inorg. Chem.* **2016**, *55* (10), 5071–5078.

(30) Lee, C. S.; Sabiah, S.; Wang, J. C.; Hwang, W. S.; Lin, I. J. B. *Organometallics* **2010**, *29* (2), 286–289.

(31) Lee, C. S.; Zhuang, R. R.; Sabiah, S.; Wang, J. C.; Hwang, W. S.; Lin, I. J. B. *Organometallics* **2011**, *30* (14), 3897–3900.

(32) Zhang, Y.; Garg, J. A.; Michelin, C.; Fox, T.; Blacque, O.; Venkatesan, K. *Inorg. Chem.* **2011**, *50* (4), 1220–1228.

(33) Leung, S. Y. L.; Lam, E. S. H.; Lam, W. H.; Wong, K. M. C.; Wong, W. T.; Yam, V. W. W. *Chem. Eur. J.* **2013**, *19* (31), 10360–10369.

(34) Zhang, Y.; Clavadetscher, J.; Bachmann, M.; Blacque, O.; Venkatesan, K. *Inorg. Chem.* **2014**, *53* (2), 756–771.

(35) Pinter, P.; Mangold, H.; Stengel, I.; Münster, I.; Strassner, T. *Organometallics* **2016**, *35* (5), 673–680.

(36) Bachmann, M.; Suter, D.; Blacque, O.; Venkatesan, K. *Inorg. Chem.* **2016**, *55* (10), 4733–4745.

(37) Leopold, H.; Tenne, M.; Tronnier, A.; Metz, S.; Münster, I.; Wagenblast, G.; Strassner, T. *Angew. Chem. Int. Ed.* **2016**, *55* (51), 15779–15782.

(38) Nishio, M.; Umezawa, Y.; Hirota, M.; Takeuchi, Y. *Tetrahedron* **1995**, *51* (32), 8665–8701.

(39) Takahashi, O.; Kohno, Y.; Nishio, M. *Chem. Rev.* **2010**, *110* (10), 6049–6076.

(40) Vellé, A.; Cebollada, A.; Iglesias, M.; Sanz Miguel, P. J. *Inorg. Chem.* **2014**, *53* (19), 10654–10659.

(41) Cebollada, A.; Vellé, A.; Iglesias, M.; Fullmer, L. B.; Goberna-Ferrõn, S.; Nyman, M.; Sanz Miguel, P. J. *Angew. Chem. Int. Ed.* **2015**, *54* (43), 12762–12766.

(42) Cao, P.; Cabrera, J.; Padilla, R.; Serra, D.; Rominger, F.; Limbach, M. *Organometallics* **2012**, *31* (3), 921–929.

(43) Sheldrick, G. M. *Acta Cryst.* **2008**, *A64*, 112-122.

(44) CrystalStructure 4.2: Crystal Structure Analysis Package, Rigaku Corporation, Tokyo, Japan, 2000-2017.

(45) Gaussian 16, Revision A.03, Frisch, M. J.; Trucks, G. W.; Schlegel, H. B.; Scuseria, G. E.; Robb, M. A.; Cheeseman, J. R.; Scalmani, G.; Barone, V.; Petersson, G. A.; Nakatsuji, H.; Li, X.; Caricato, M.; Marenich, A. V.; Bloino, J.; Janesko, B. G.; Gomperts, R.; Mennucci, B.; Hratchian, H. P.; Ortiz, J. V.; Izmaylov, A. F.; Sonnenberg, J. L.; Williams-Young, D.; Ding, F.; Lipparini, F.; Egidi, F.; Goings, J.; Peng, B.; Petrone, A.; Henderson, T.; Ranasinghe, D.; Zakrzewski, V. G.; Gao, J.; Rega, N.; Zheng, G.; Liang, W.; Hada, M.; Ehara, M.; Toyota, K.; Fukuda, R.; Hasegawa, J.; Ishida, M.; Nakajima, T.; Honda, Y.; Kitao, O.; Nakai, H.; Vreven, T.; Throssell, K.; Montgomery, J. A., Jr.; Peralta, J. E.; Ogliaro, F.; Bearpark, M. J.; Heyd, J. J.; Brothers, E. N.; Kudin, K. N.; Staroverov, V. N.; Keith, T. A.; Kobayashi, R.; Normand, J.; Raghavachari, K.; Rendell, A. P.; Burant, J. C.; Iyengar, S. S.; Tomasi, J.; Cossi, M.; Millam, J. M.; Klene, M.; Adamo, C.; Cammi, R.; Ochterski, J. W.; Martin, R. L.; Morokuma, K.; Farkas, O.; Foresman, J. B.; Fox, D. J. Gaussian, Inc., Wallingford CT, 2016.

(46) GaussView, Version 5, Dennington, R.; Keith, T. A.; Millam, J. M. Semichem Inc., Shawnee Mission, KS, 2009.

Chapter 4

Fluxional Nature and Photo Luminescence of Ag Clusters Sandwiched by Pt Complex Units

4-1. Introduction

Multinuclear sandwich complexes, which can extend a structural concept of classical metal complex ferrocene $(C_5H_5)_2Fe$, have been intensively developed because of their fascinating structure and properties (**Figure 4-1**).[1–3] Although the sandwich structures are stabilized dramatically by multiple metal–metal bond and concerted coordinations from their π-conjugated ligands, they often show fluxional behaviors, such as dynamic rotation of the ligands,[2] reversible metalation–demetalation sequence,[4] translocation of metal clusters,[5,6] which will represent new horizon in cluster and material chemistry.

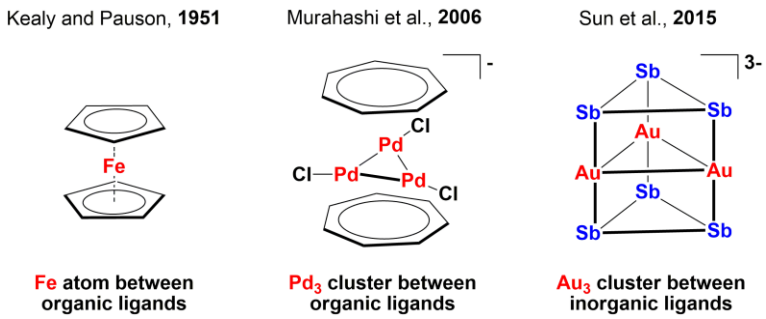

Figure 4-1. Multinuclear sandwich complexes.[1-3]

Coinage d^{10} metal ions (Cu(I), Ag(I) and Au(I)) show strong metallophilic interactions to form metal clusters in the presence of suitable organic and inorganic ligands.[3,7,8] In particular, pyrazolate ligands (pz) can bind three metal ions as side-capping ligands to give triangular M_3 complexes which can show fascinating luminescence properties.[9,10] These triangular M_3 complexes also provide a suitable platform to construct supramolecular 1D stacking structure in the solid state,[11–18] owing to their strong π-acidic/basic nature of the M_3 cores.[19] This structural motif motivated us to construct new types of multinuclear sandwich complexes consisting of coinage M_3 core and novel face-capping ligands, which can show both fluxional behavior and photo-luminescence. Recently, in the synthesis of heteropolynuclear metal complexes consisting of coinage metal ions and Pt complex units,[20–22] I encountered the desired Pt complex units as face-capping ligands to afford the multinuclear sandwich complexes exhibiting both remarkable fluxional behaviors and photoluminescence.

In this chapter, synthesis and properties of heteropolynuclear Ag cluster sandwiched by Pt(II) units having phenyl-NHC (Ph-NHC) chelate ligand will be described.

4-2. Synthesis of complexes having phenyl-NHC (Ph-NHC) chelate ligand

4-2-1. Preparation of [{(Ph-NHC)Pt(μ-Cl)}$_2$] (5)

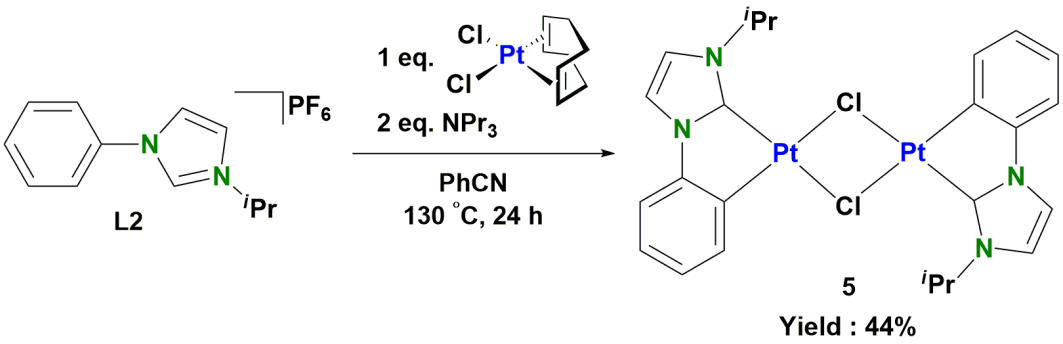

Scheme 4-1. Synthesis of [{(Ph-NHC)Pt(μ-Cl)$_2$}$_2$] (**5**).

A benzonitrile solution (50 mL) of (COD)PtCl$_2$ (455 mg, 1.22 mmol), and 3-phyenyl-1-isopropylimidazolium hexafluorophosphate (405 mg, 1.22 mmol) in the presence of tripropylamine (466 mL, 2.44 μmol) was heated at 130 ºC for 24 h in Ar atmosphere. After the volume of the solution was reduced in vacuo, the product was purified by a column chromatography and precipitation using *n*-hexane to afford a pale yellow solid of **5**. The solid was collected and dried in vacuo. Yield 187 mg (0.225 mmol, 44%). Anal. Calcd for $C_{24}H_{26}Cl_2N_4Pt_2 \cdot CH_2Cl_2$: C, 34.12; H, 3.21; N, 6.37. Found: C, 34.27; H, 2.60; N, 6.13. ^{1}H NMR (500 MHz, DMSO-d_6, 25 ℃): δ = 8.30 (d, J = 7.5 Hz, 2H, H_a), 8.07 (d, J = 2.0 Hz, 2H, H_e), 7.69 (d, J = 2.0, Hz, 2H, H_f), 7.35 (dd, J = 7.5, 1.0 Hz, 2H, H_d), 7.08 (td, J = 7.5, 1.0 Hz, 2H, H_c), 6.88 (td, J = 7.5, 1.5 Hz, 2H, H_b), 6.18 (sept, J = 6.5 Hz, 2H, H_g), 1.40 ppm (d, J = 6.5 Hz, 12H, H_h); ^{13}C{^{1}H} NMR (125 MHz, DMSO-d_6, 25 ℃): δ = 153.8 (C_j), 145.7 (C_k), 134.4 (C_a),

126.5 (C_i), 124.9 (C_b), 124.6 (C_c), 119.1 (C_f), 116.0 (C_e), 111.7 (C_d), 49.6 (C_g), 23.0 (C_h) ppm.

FAB-MS for [{(Ph-NHC)Pt(μ-Cl)}$_2$]: *m/z* = 831 [*M*].

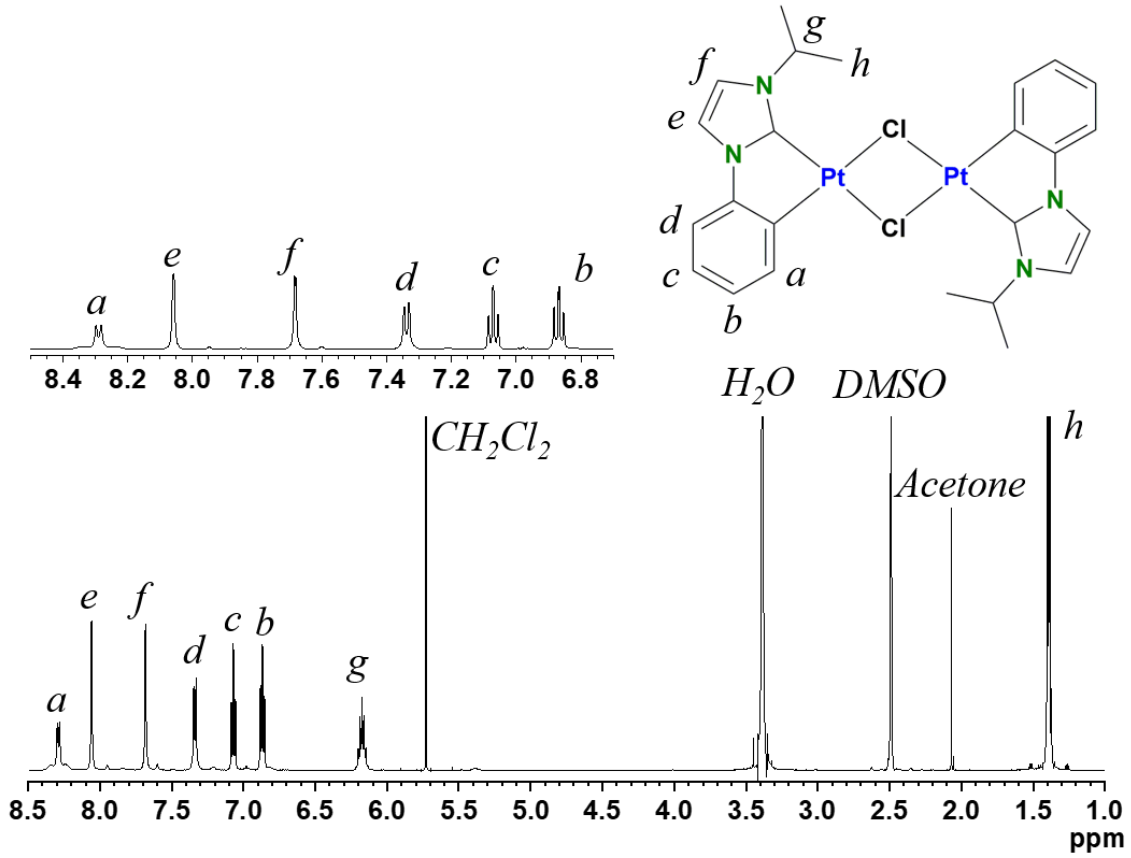

Figure 4-2. ^{1}H NMR spectrum (500 MHz, DMSO-d_6, 25 °C) of [{(Ph-NHC)Pt(μ-Cl)}$_2$] (**5**).

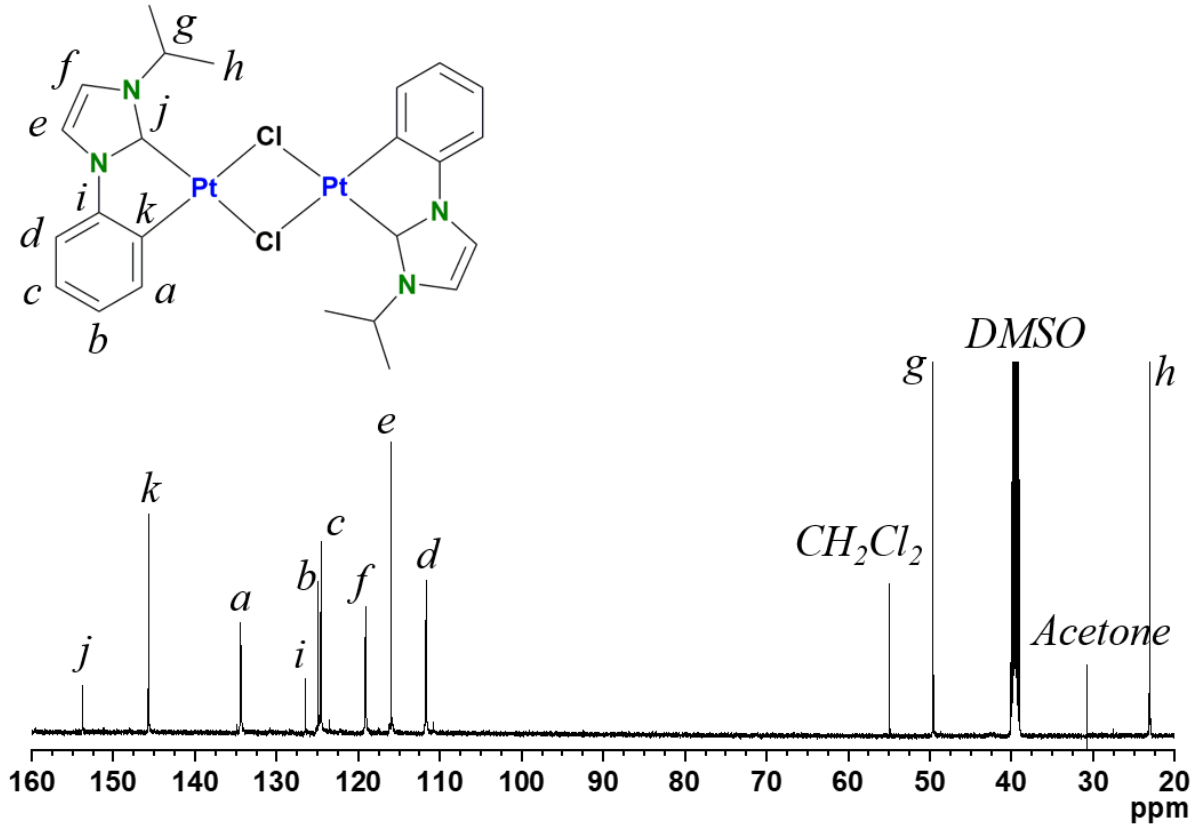

Figure 4-3. $^{13}C\{^{1}H\}$ NMR spectrum (125 MHz, DMSO-d_6, 25 °C) of [{(Ph-NHC)Pt(μ-Cl)}$_2$] (**5**).

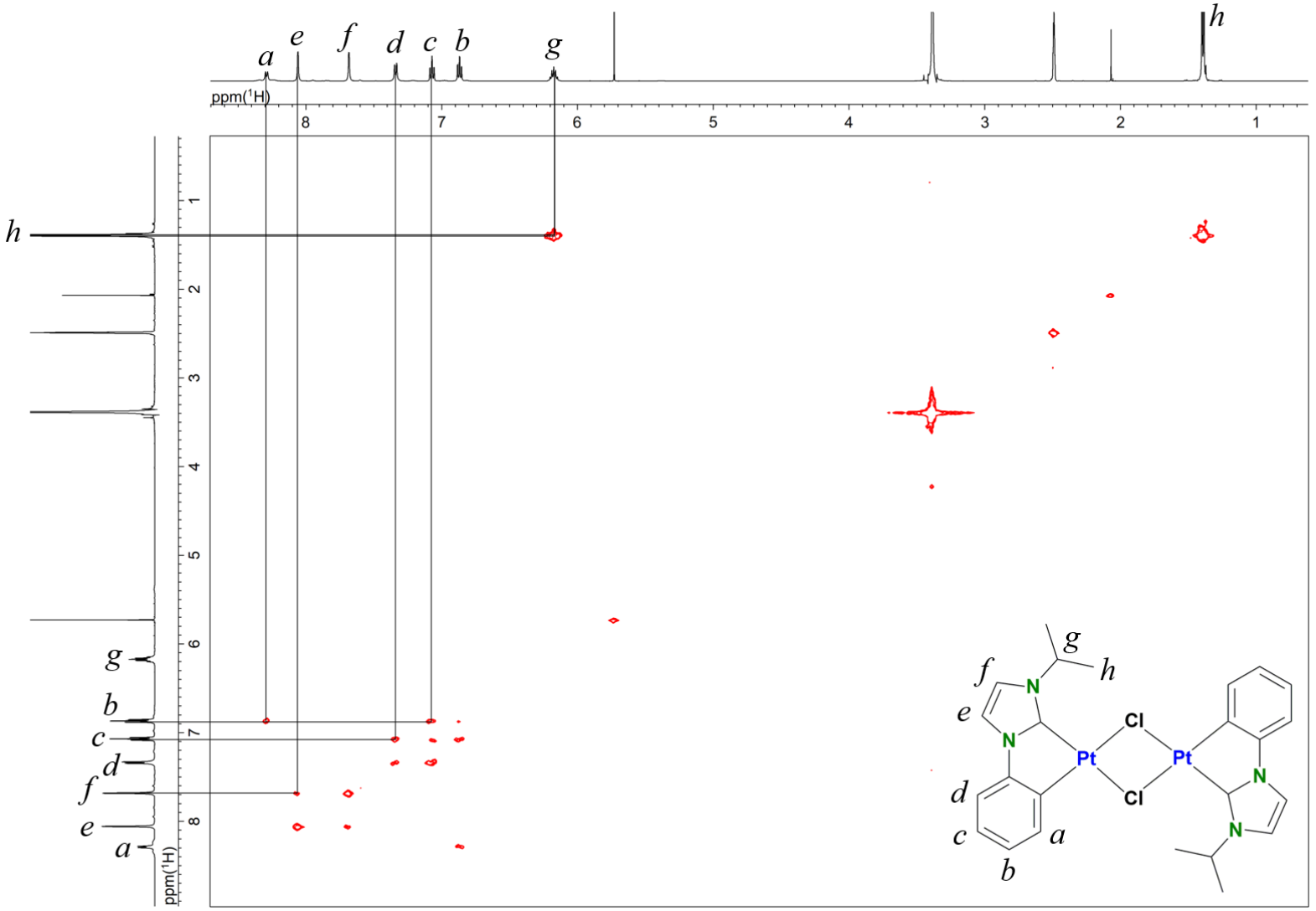

Figure 4-5. ^{1}H-^{1}H COSY spectrum (500 MHz, DMSO-d_6, 25 °C) of [{(Ph-NHC)Pt(μ-Cl)}$_2$] (**5**).

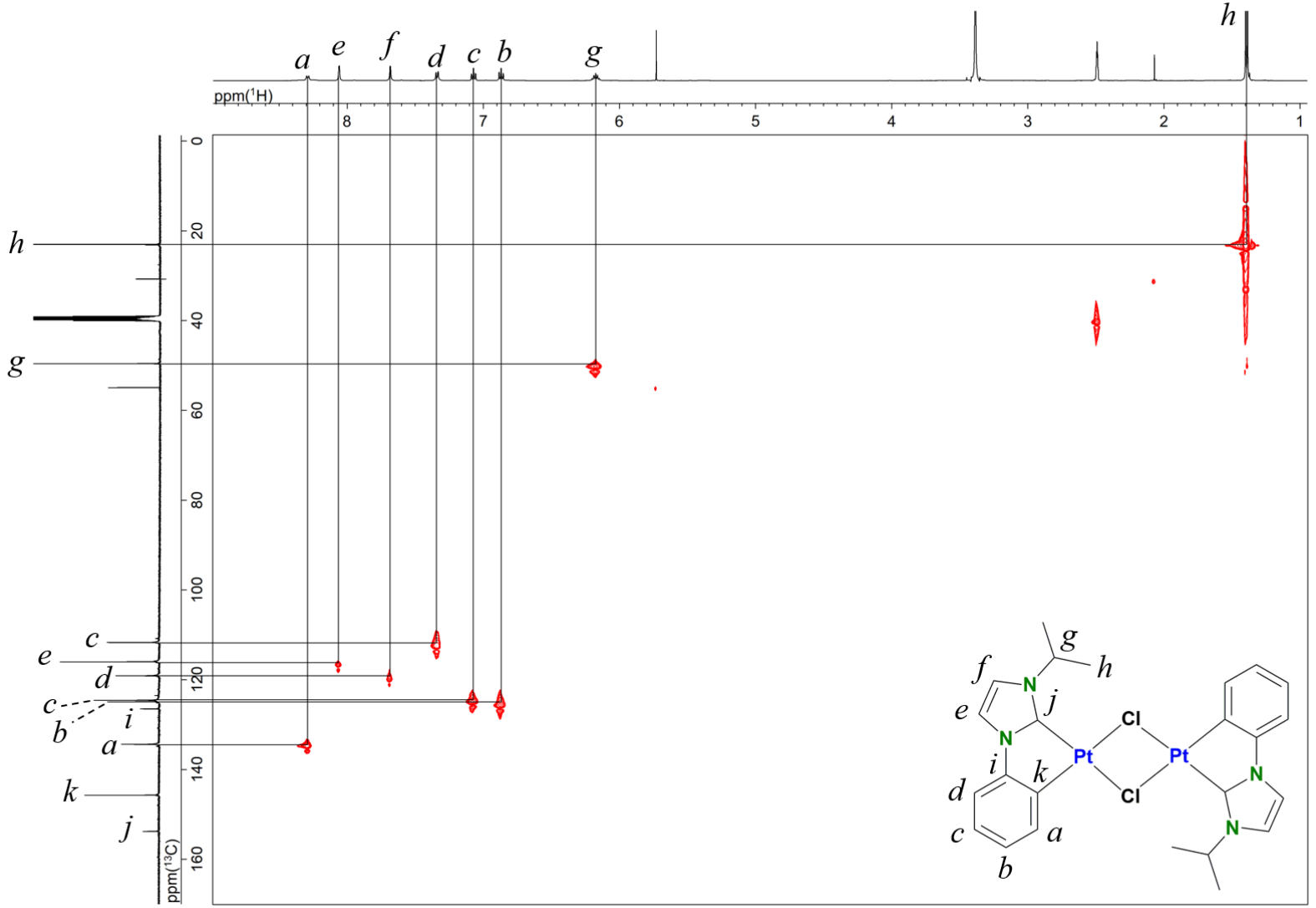

Figure 4-6. ^{1}H-^{13}C HSQC spectrum (500 MHz, DMSO-d_6, 25 °C) of [{(Ph-NHC)Pt(μ-Cl)}$_2$] (**5**).

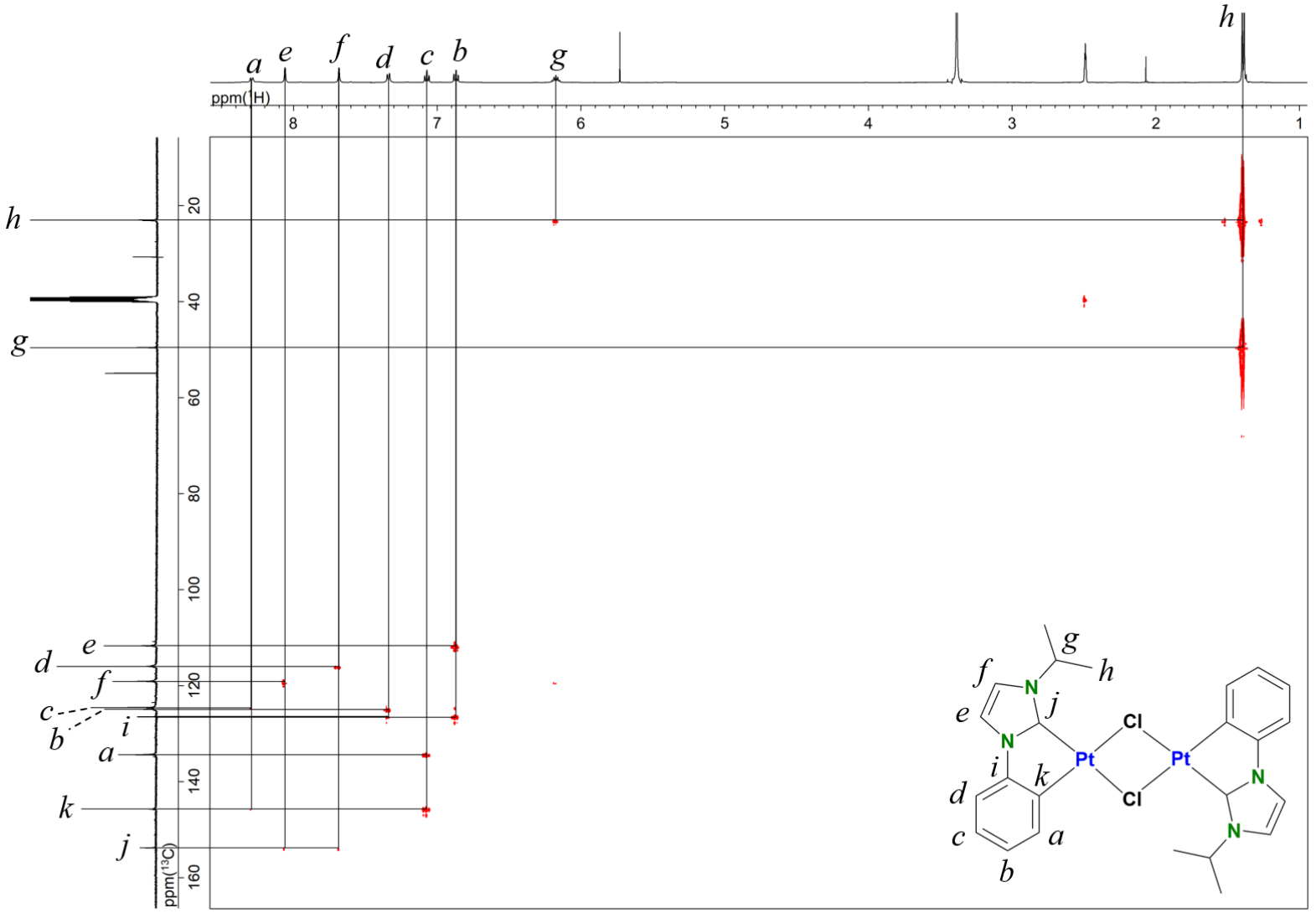

Figure 4-7. ^{1}H-^{13}C HMBC spectrum (500 MHz, DMSO-d_6, 25 °C) of [{(Ph-NHC)Pt(μ-Cl)}$_2$] (**5**).

4-2-2. Synthesis of [(Ph-NHC)Pt(Me$_2$pzH)$_2$]Cl (6)

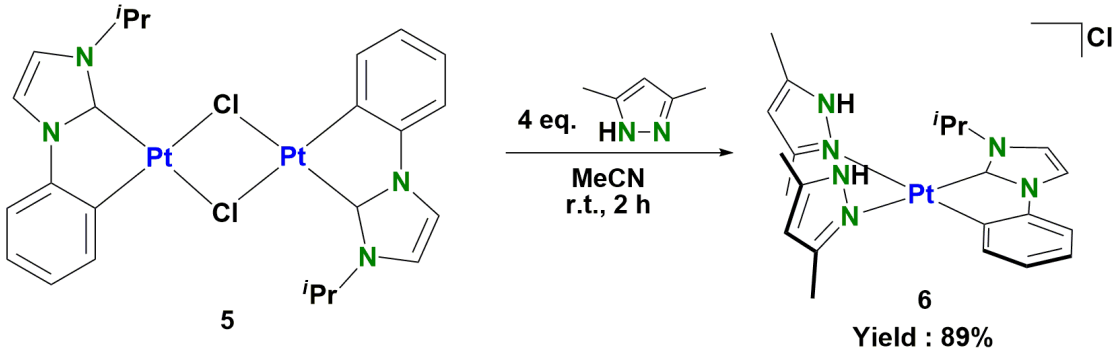

Scheme 4-2. Synthesis of [(Ph-NHC)Pt(Me$_2$pzH)$_2$]Cl (**6**).

A mixture of [{(Ph-NHC)Pt(μ-Cl)}$_2$] (68 mg, 0.08 mmol) and 3,5-dimethyl pyrazole (38 mg, 0.40 mmol) in acetonitrile (10 mL) was stirred at ambient temperature for 2 h. After the reaction mixture was dried under reduced pressure, the residue was dissolved into dichloromethane and then *n*-hexane was added to the solution. The resulted white precipitate was collected, washed with *n*-hexane and dried in vacuo. Yield 82 mg (0.14 mmol, 89%). A single crystal was obtained by recrystallization from dichloromethane/*n*-hexane. Anal. Calcd for $C_{22}H_{29}N_6ClPt$: C, 43.48; H, 4.81; N, 13.84. Found: C, 43.39; H, 4.61; N, 13.81. ^{1}H NMR (500 MHz, $CDCl_3$, 25 ℃, TMS): δ = 14.3 (s, 1H, H_o), 14.0 (s, 1H, H_o), 7.29 (d, J = 2.0 Hz, 1H, H_e), 6.98 (ddd, J = 7.5, 1.0 Hz, 1H, H_c), 6.93 (dd, J = 8.0, 1.0 Hz, 1H, H_d), 6.91 (d, J = 2.0 Hz, 1H, H_f), 6.75 (ddd, J = 7.5, 1.5 Hz, 1H, H_b), 6.23 (dd, J = 7.5, 1.5 Hz, 1H, H_a), 5.96 (s, 1H, H_l), 5.93 (s, 1H, H_l), 3.31 (sept, J = 6.5 Hz, 1H, H_g), 2.40 (s, 3H, H_m), 2.38 (s, 6H, H_m), 2.35 (s, 3H, H_m), 1.24 (d, J = 7.0 Hz, 3H, H_h), 1.20 (d, J = 6.7 Hz, 3H, H_h). ^{13}C{^{1}H} NMR (125 MHz, $CDCl_3$, 25 ℃, TMS): δ = 153.3 (C_j), 148.8 (C_n), 147.8 (C_n), 146.8 (C_i), 142.7 (C_n), 142.2 (C_n), 134.2 (C_a), 128.0 (C_k), 125.0 (C_b), 124.2 (C_c), 115.3 (C_f), 115.2 (C_e), 110.3 (C_d), 105.4 (C_l), 105.3 (C_l), 49.4 (C_g), 24.2 (C_h), 22.9 (C_h), 14.6 (C_m), 14.4 (C_m), 11.1 (C_m), 11.0 (C_m) ppm. ^{195}Pt NMR (86 MHz, $CDCl_3$, 30 ℃, H_2PtCl_6 in D_2O): δ = –2728 ppm. ESI-MS for [(Ph-NHC)Pt(Me$_2$pzH)$_2$]Cl: m/z = 572.2 $[M]^+$.

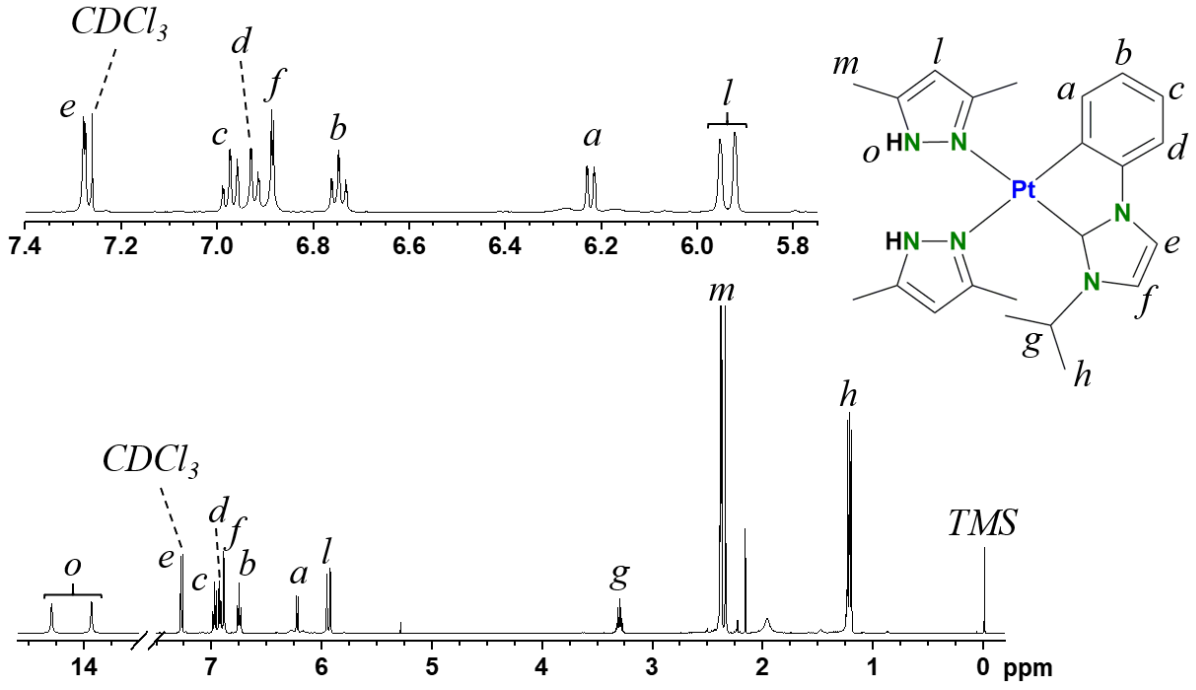

Figure 4-8. ^{1}H NMR spectrum (500 MHz, $CDCl_3$, 25 °C, TMS) of [(Ph-NHC)Pt($Me_2pzH)_2$]Cl (**6**).

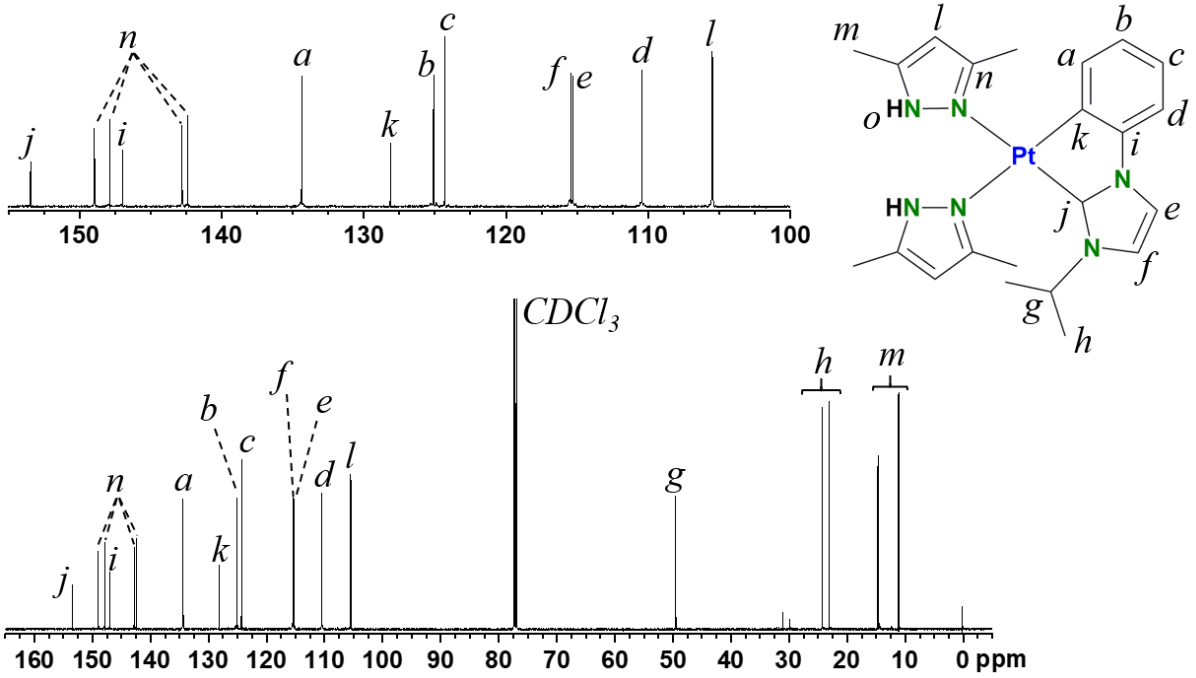

Figure 4-9. ^{13}C{^{1}H} NMR spectrum (125 MHz, $CDCl_3$, 25 °C, TMS) of [(Ph-NHC)Pt($Me_2pzH)_2$]Cl (**6**).

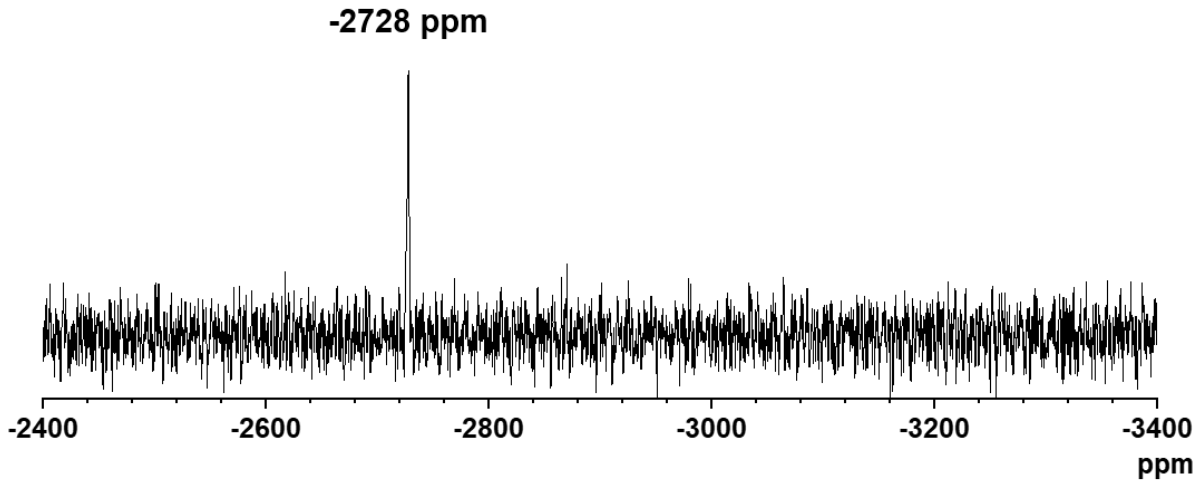

Figure 4-10. ^{195}Pt NMR spectrum (86 MHz, DMSO-d_6, 30 °C, H_2PtCl_6 in D_2O) of [(Ph-NHC)Pt($Me_2pzH)_2$]Cl (**6**).

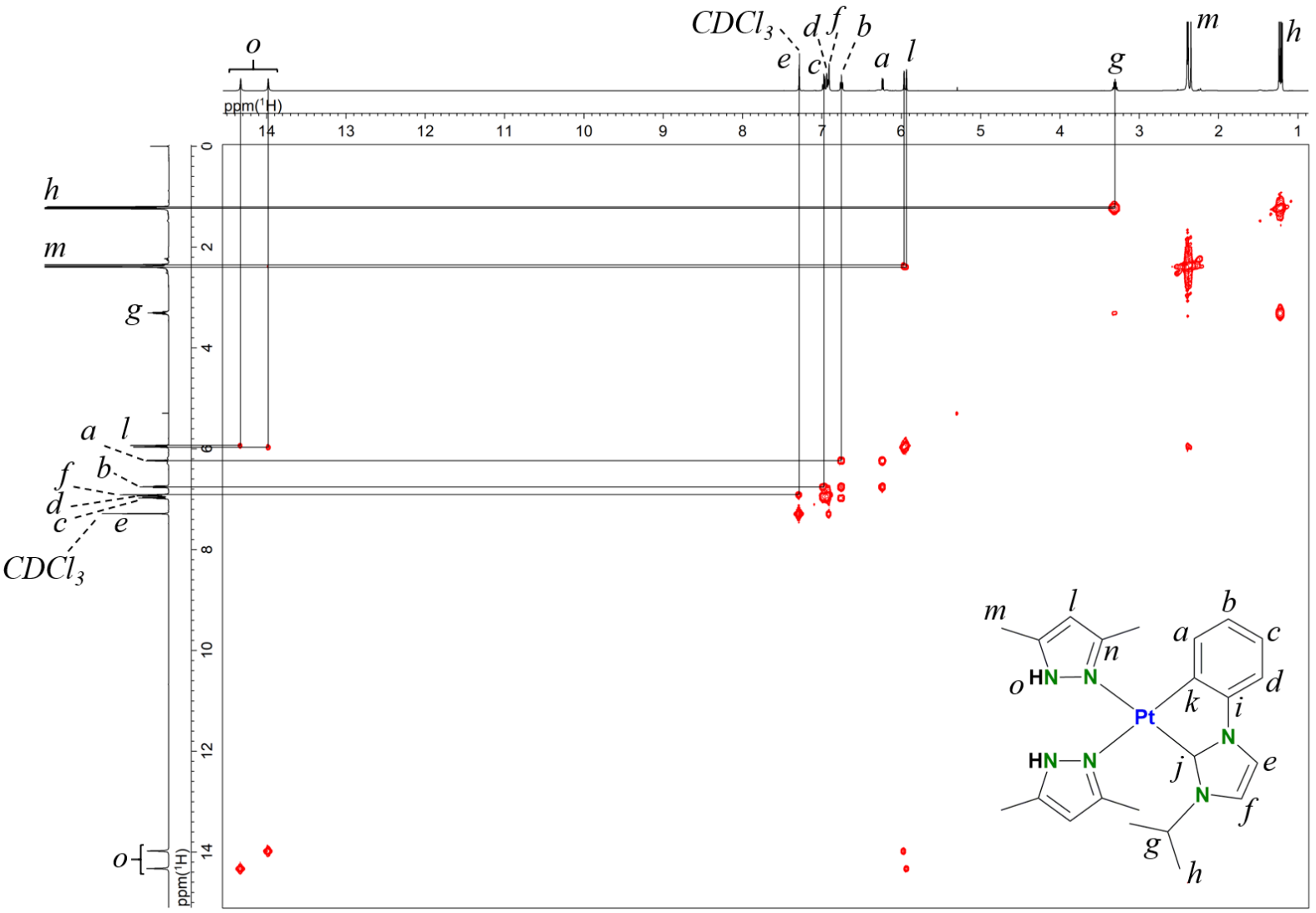

Figure 4-11. ^{1}H-^{1}H COSY spectrum (500 MHz, $CDCl_3$, 25 °C, TMS) of [(Ph-NHC)Pt($Me_2pzH)_2$]Cl (**6**).

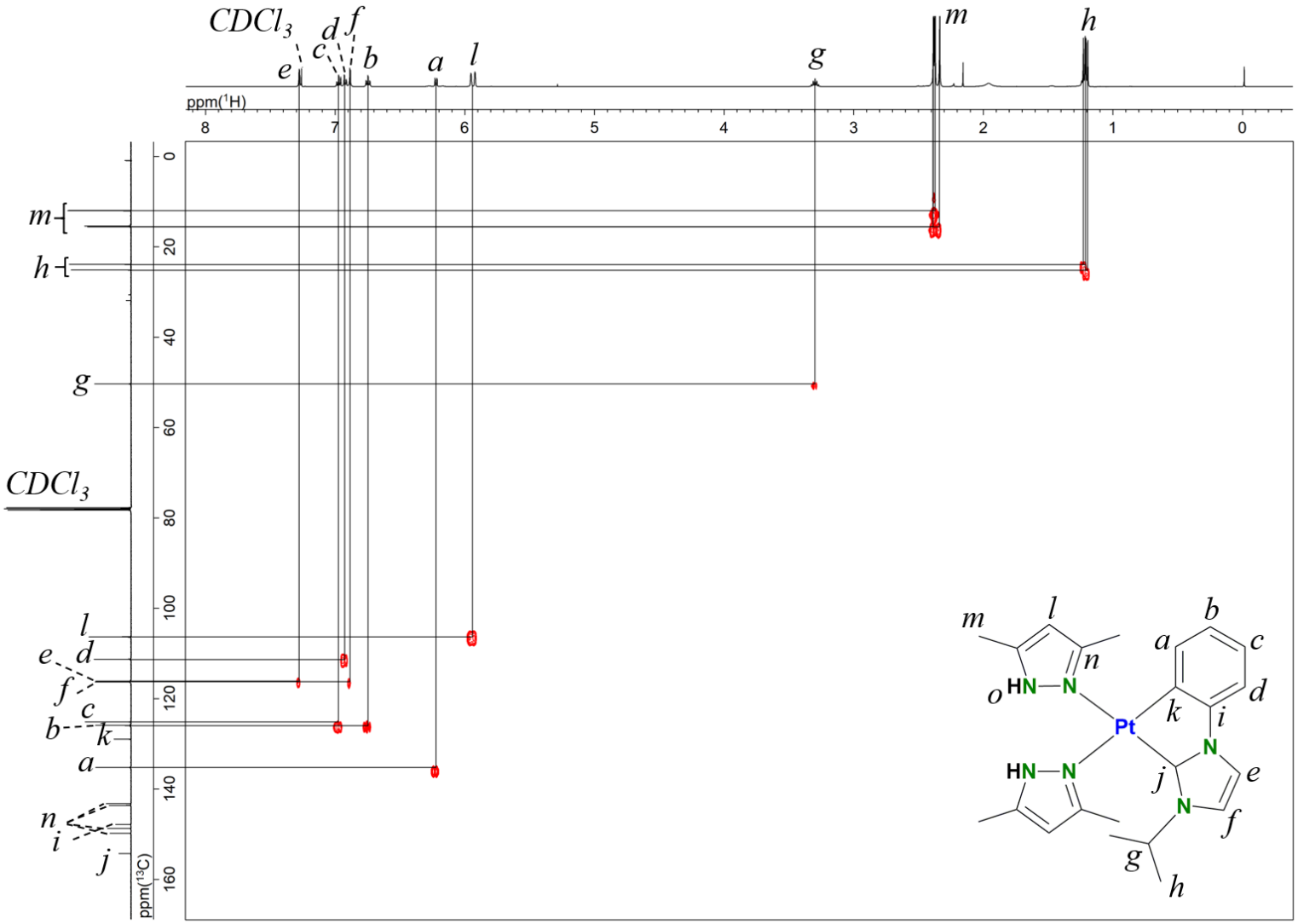

Figure 4-12. ^{1}H-^{13}C HSQC spectrum (500 MHz, $CDCl_3$, 25 °C, TMS) of [(Ph-NHC)Pt($Me_2pzH)_2$]Cl (**6**).

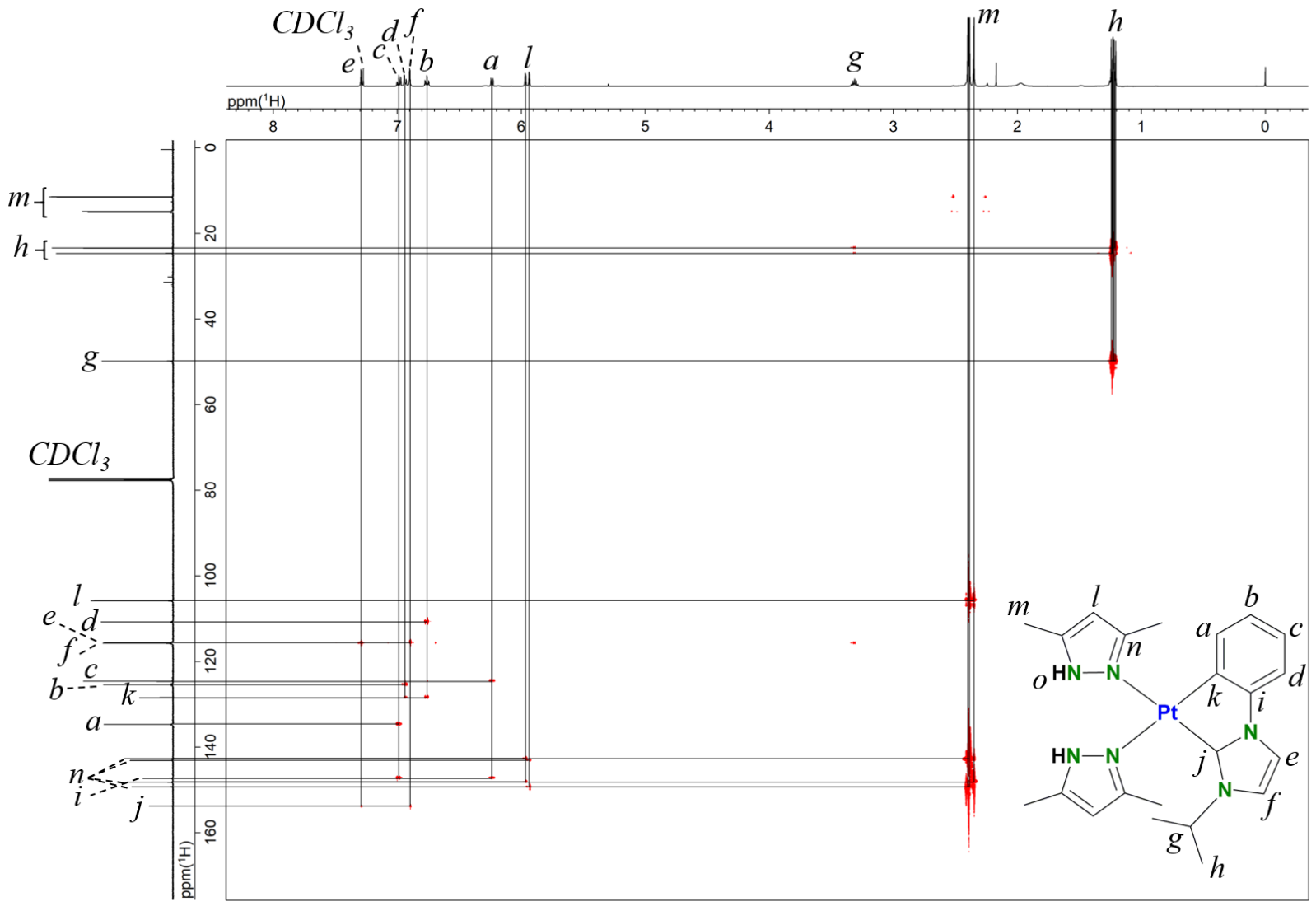

Figure 4-13. ^{1}H-^{13}C HMBC spectrum (500 MHz, $CDCl_3$, 25 °C, TMS) of [(Ph-NHC)Pt($Me_2pzH)_2$]Cl (**6**).

4-2-3. Synthesis of [(Ph-NHC)$_2$Pt$_2$Ag$_3$(Me$_2$pz)$_4$]BF$_4$ (7)

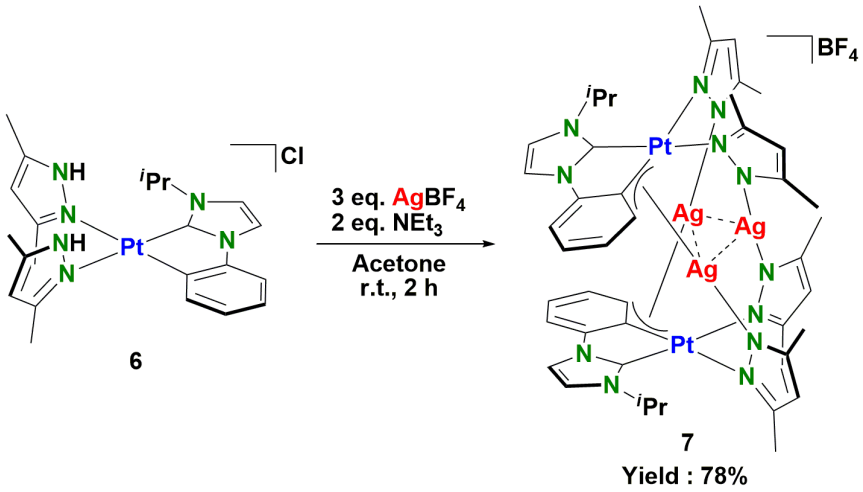

Scheme 4-3. Synthesis of [(Ph-NHC)$_2$Pt$_2$Ag$_3$(Me$_2$pz)$_4$]BF$_4$ (**7**).

A mixture of [(Ph-NHC)Pt(Me$_2$pzH)$_2$]Cl (217 mg, 0.36 mmol), AgBF$_4$ (227 mg, 1.17 mmol) and NEt$_3$ (110 μL, 0.78 mmol) was stirred in acetone at room temperature for 2 h. The yellow reaction mixture was concentrated and the residue was dissolved into dichloromethane. The solution was filtered, washed with water and dried over MgSO$_4$. The solution was concentrated and *n*-hexane was added to the solution. The greenish yellow precipitate was collected and dried in vacuo. It was recrystallized from chloroform/*n*-pentane. Yield: 213 mg (78%). Anal. Calcd for C$_{44}$H$_{54}$Ag$_3$N$_{12}$Pt$_2$BF$_4$: C, 34.06; H, 3.51; N, 10.83. Found: C, 34.16; H, 3.54; N, 10.34. ^{1}H NMR (500 MHz, CDCl$_3$, 25 ℃, TMS): δ = 7.98 (s, 2H, H_e), 7.31 (d, J = 8.4 Hz, 2H, H_d), 7.21 (t, J = 7.2 Hz, 2H, H_c), 7.03 (s, 2H, H_f), 6.88 (brs, 2H, H_b), 6.80 (brs, 2H, H_a), 6.11 (s, 2H, H_l), 5.92 (s, 2H, H_l), 2.84 (brs, 2H, H_g), 2.33 (s, 6H, H_m), 2.05 (s, 6H, H_m), 1.97 (s, 6H, H_m), 1.93 (s, 6H, H_m) ppm. ^{13}C{^{1}H} NMR (125 MHz, CDCl$_3$ 25 ℃, TMS): δ = 151.3 (br), 149.2, 147.9, 147.3, 131.1, 129.8, 125.9, 118.8 (br), 118.3, 113.1, 104.8, 104.2, 49.5, 30.9, 24.5, 22.4, 14.8, 14.5, 13.2 (br), 12.7. ^{195}Pt NMR (86 MHz, CDCl$_3$, 30 ℃, H$_2$PtCl$_6$ in D$_2$O): δ = –3247 (d, J(^{195}Pt-$^{109/107}$Ag) = 542 Hz). FAB-MS for [(Ph-NHC)$_2$Pt$_2$Ag$_3$(Me$_2$pz)$_4$]BF$_4$: *m/z* 1465 [*M*-BF$_4$]$^+$.

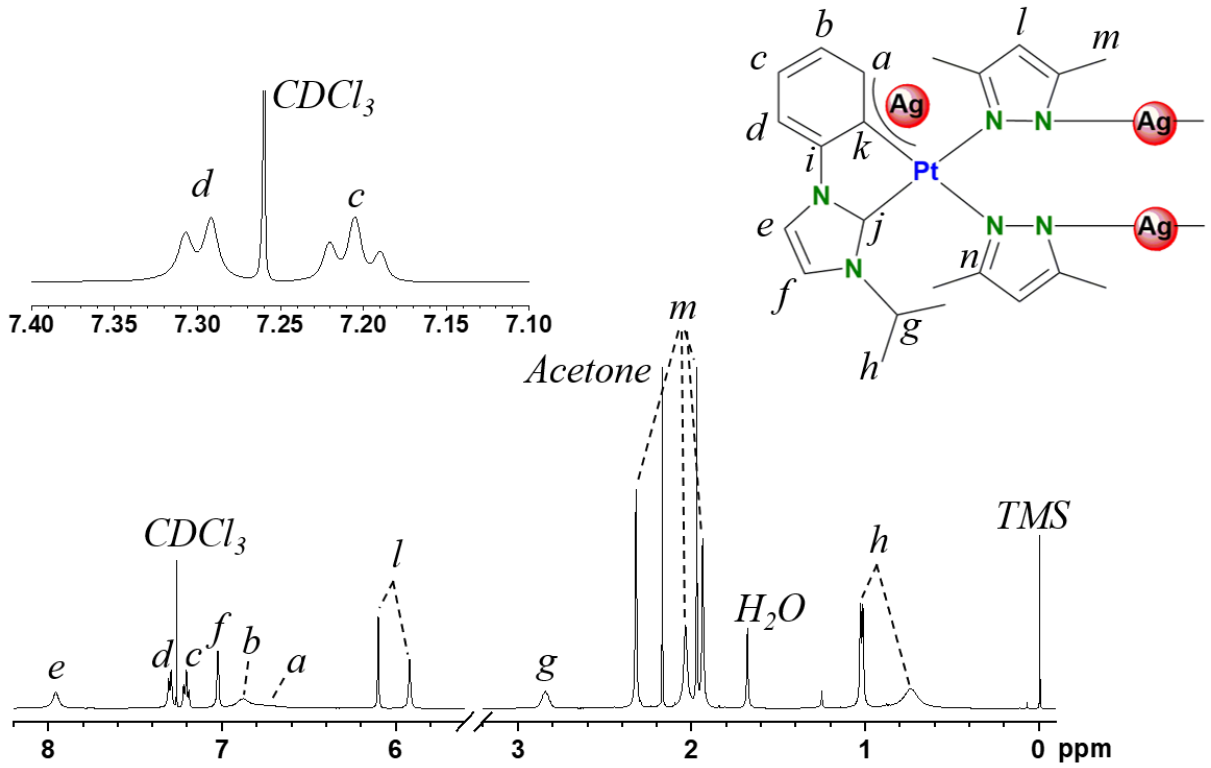

Figure 4-14. ^{1}H NMR spectrum (500 MHz, $CDCl_3$, 25 ℃, TMS) of $[(Ph\text{-}NHC)_2Pt_2Ag_3(Me_2pz)_2]BF_4$ (**7**).

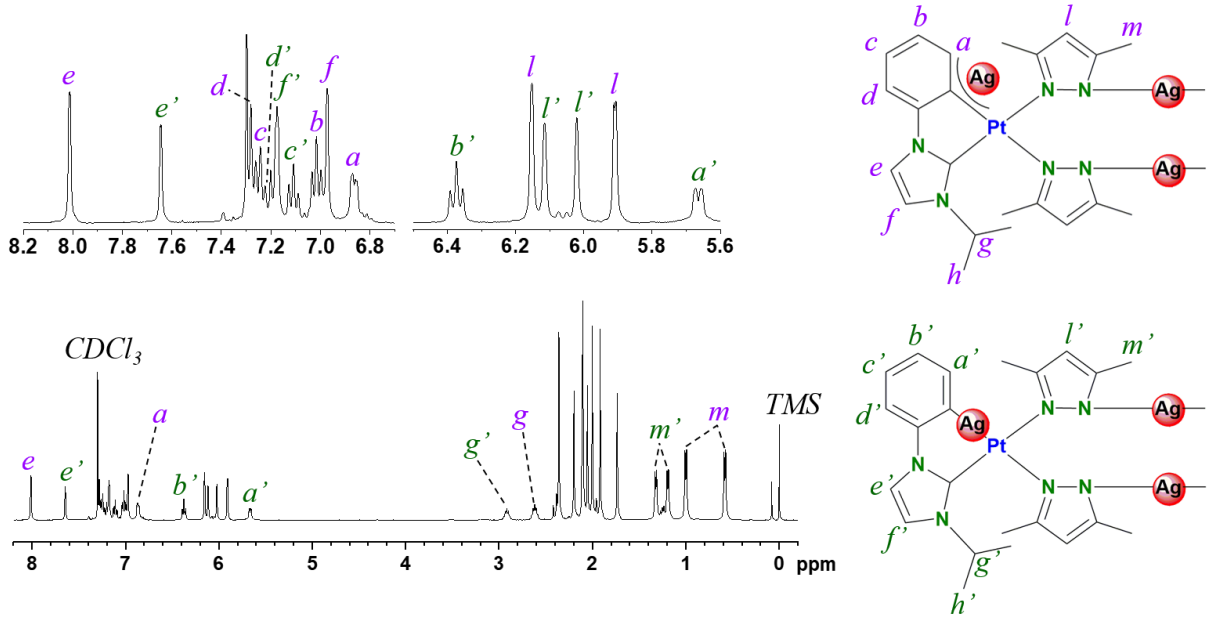

Figure 4-15. ^{1}H NMR spectrum (500 MHz, $CDCl_3$, –50 ℃, TMS) of $[(Ph\text{-}NHC)_2Pt_2Ag_3(Me_2pz)_2]BF_4$ (**7**).

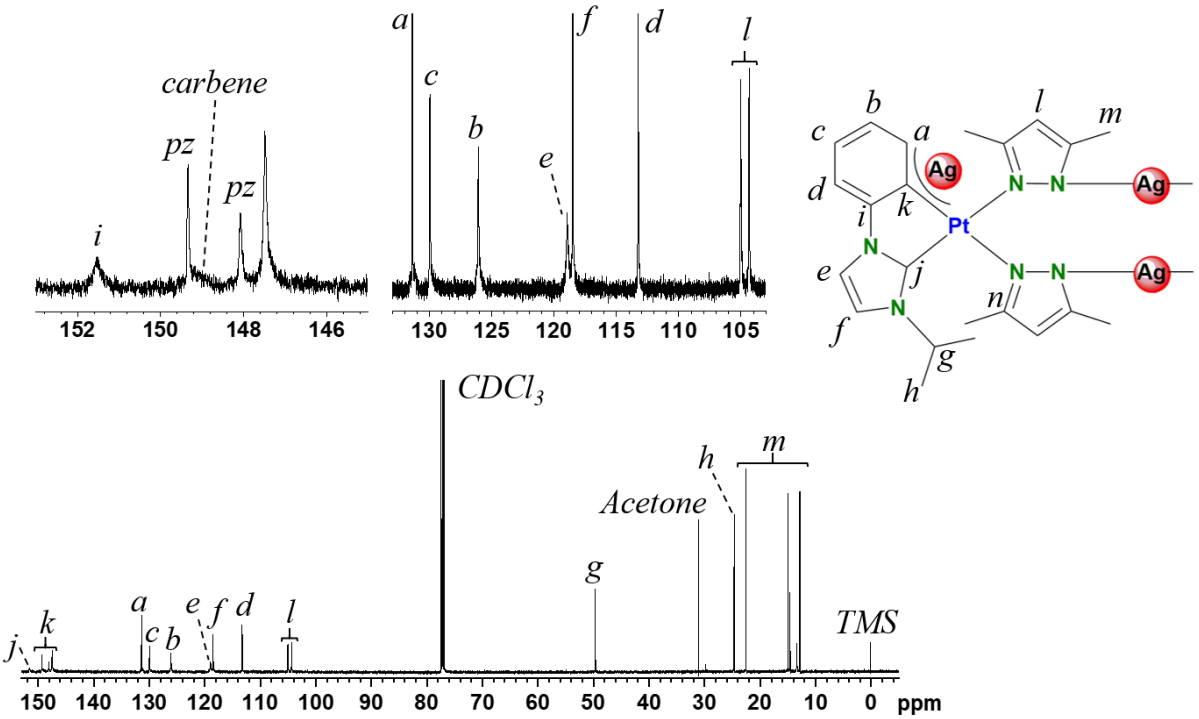

Figure 4-16. $^{13}C\{^{1}H\}$ NMR spectrum (125 MHz, $CDCl_3$, 25 ℃, TMS) of $[(Ph\text{-}NHC)_2Pt_2Ag_3(Me_2pz)_2]BF_4$ (**7**).

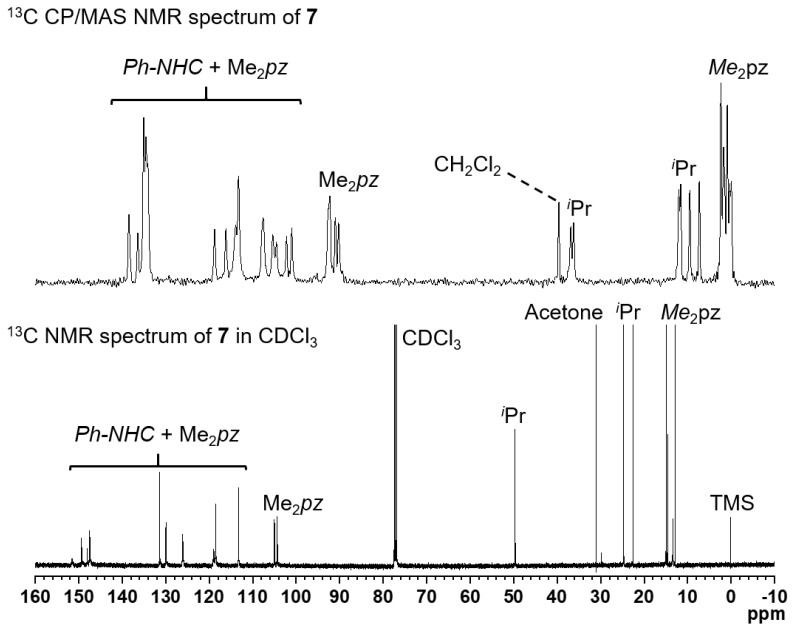

Figure 4-17. ^{13}C CP/MAS NMR spectrum (125 MHz, 30 ℃, adamantane) of $[(Ph\text{-}NHC)_2Pt_2Ag_3(Me_2pz)_2]BF_4$ (**7**) in the crystalline state. Two sets of the signals were observed in contrast to the solution spectrum, indicating that the two different structural isomers were inequivalently exist in the crystalline state.

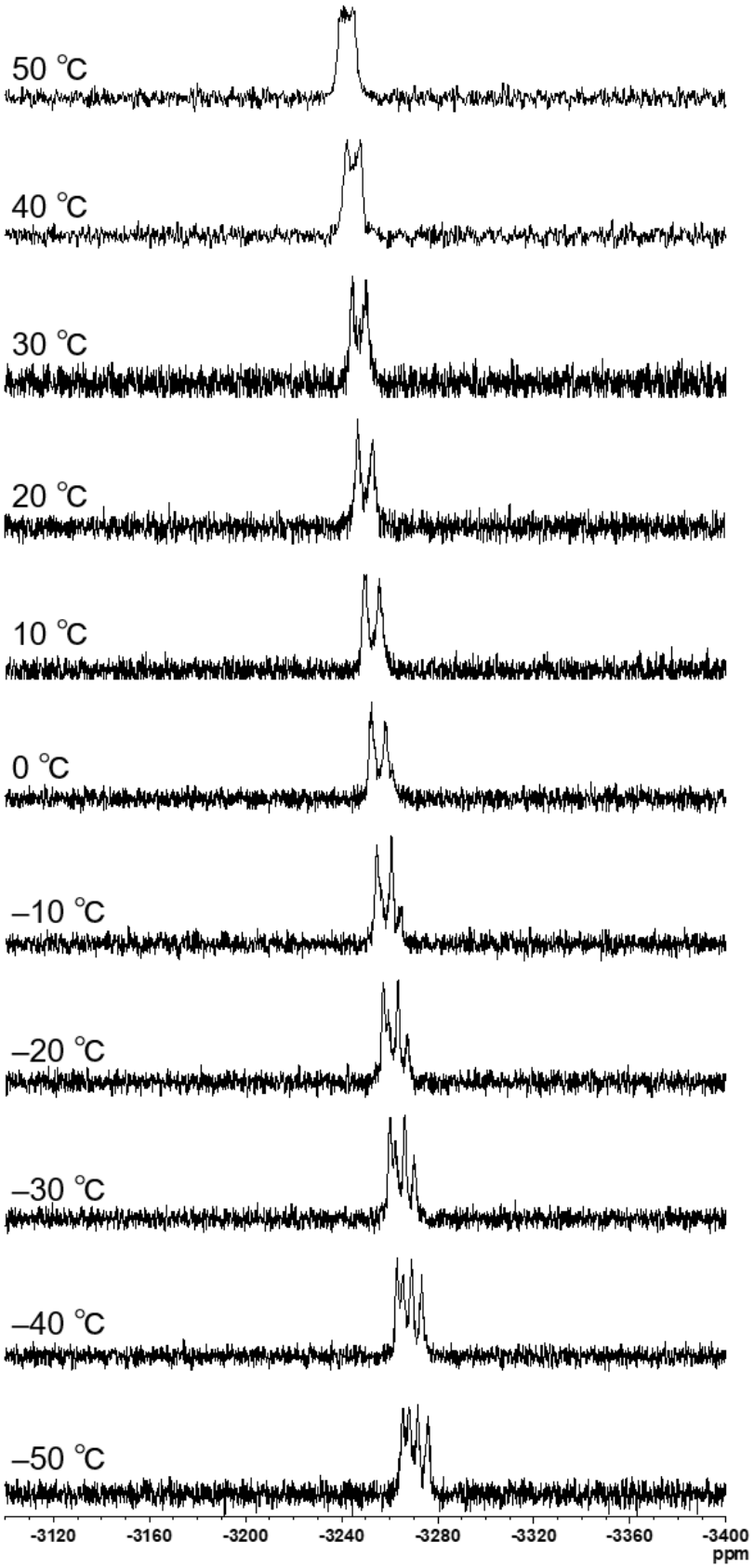

Figure 4-18. VT ^{195}Pt NMR spectra (86 MHz, $CDCl_3$, H_2PtCl_6 in D_2O) of $[(Ph\text{-}NHC)_2Pt_2Ag_3(Me_2pz)_2]BF_4$ (**7**).

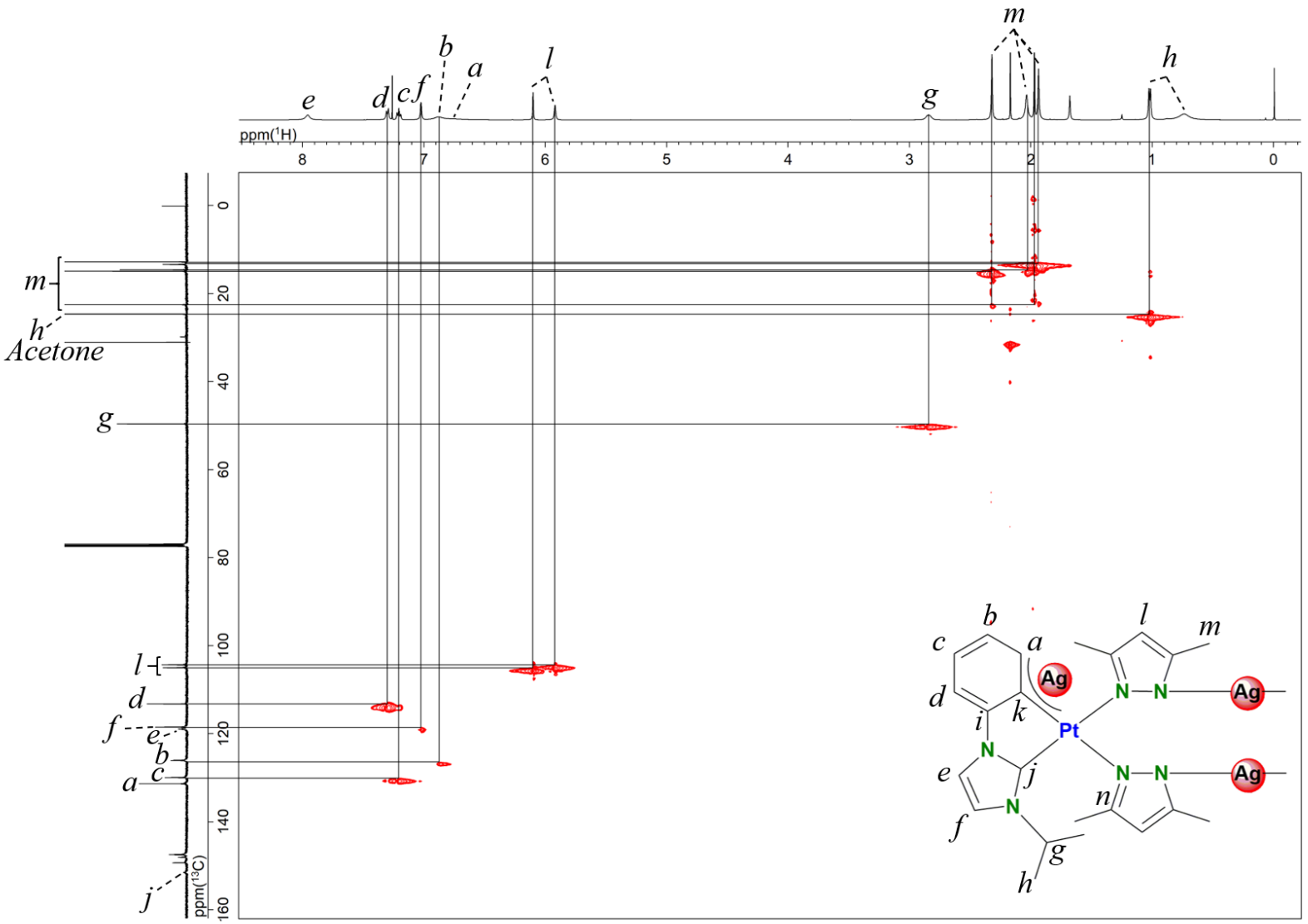

Figure 4-19. ^{1}H-^{13}C HSQC spectrum (500 MHz, $CDCl_3$, 25 °C, TMS) of $[(Ph\text{-}NHC)_2Pt_2Ag_3(Me_2pz)_2]BF_4$ (**7**).

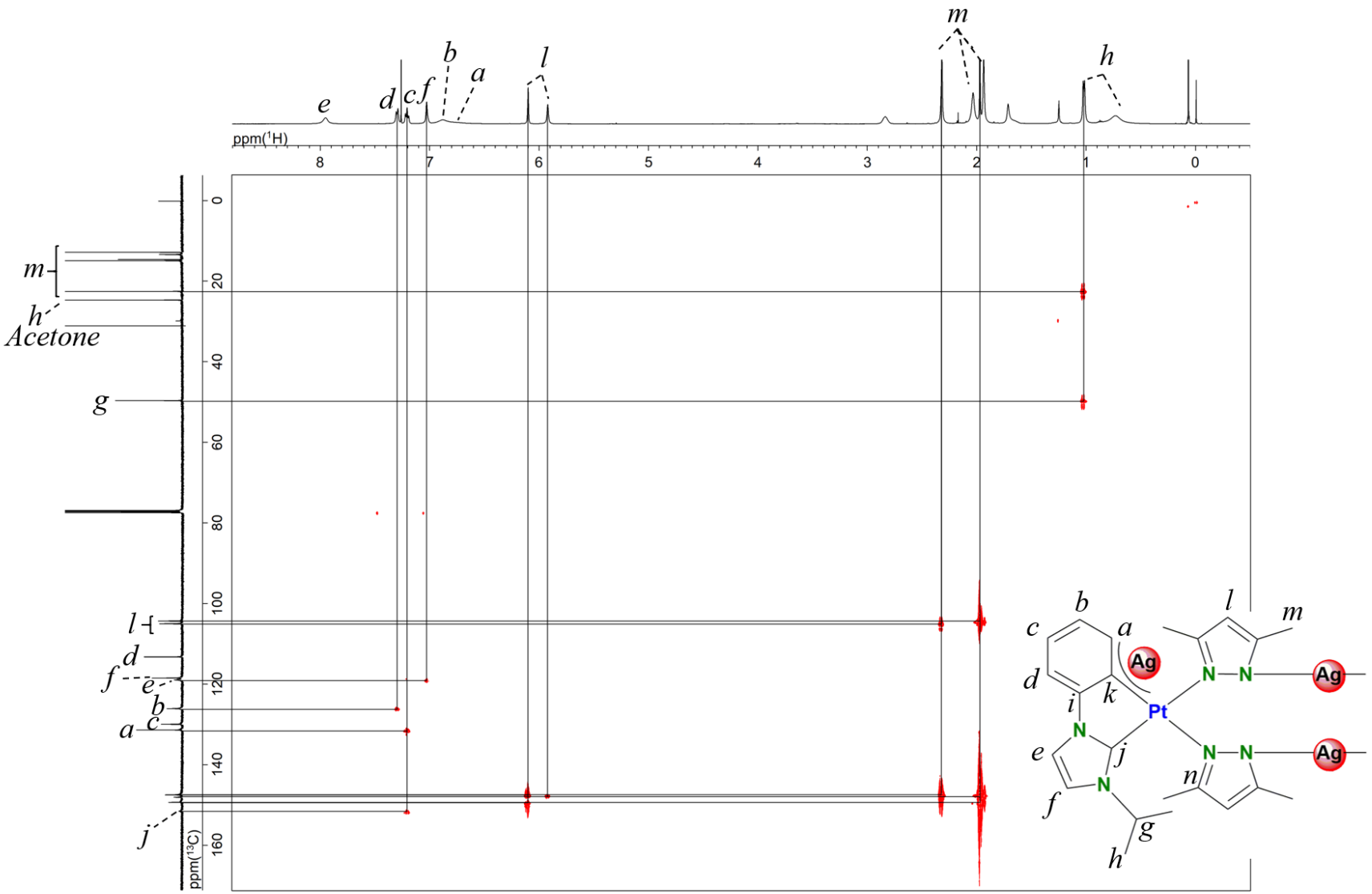

Figure 4-20. ^{1}H-^{13}C HMBC spectrum (500 MHz, $CDCl_3$, 25 °C, TMS) of $[(Ph\text{-}NHC)_2Pt_2Ag_3(Me_2pz)_2]BF_4$ (**7**).

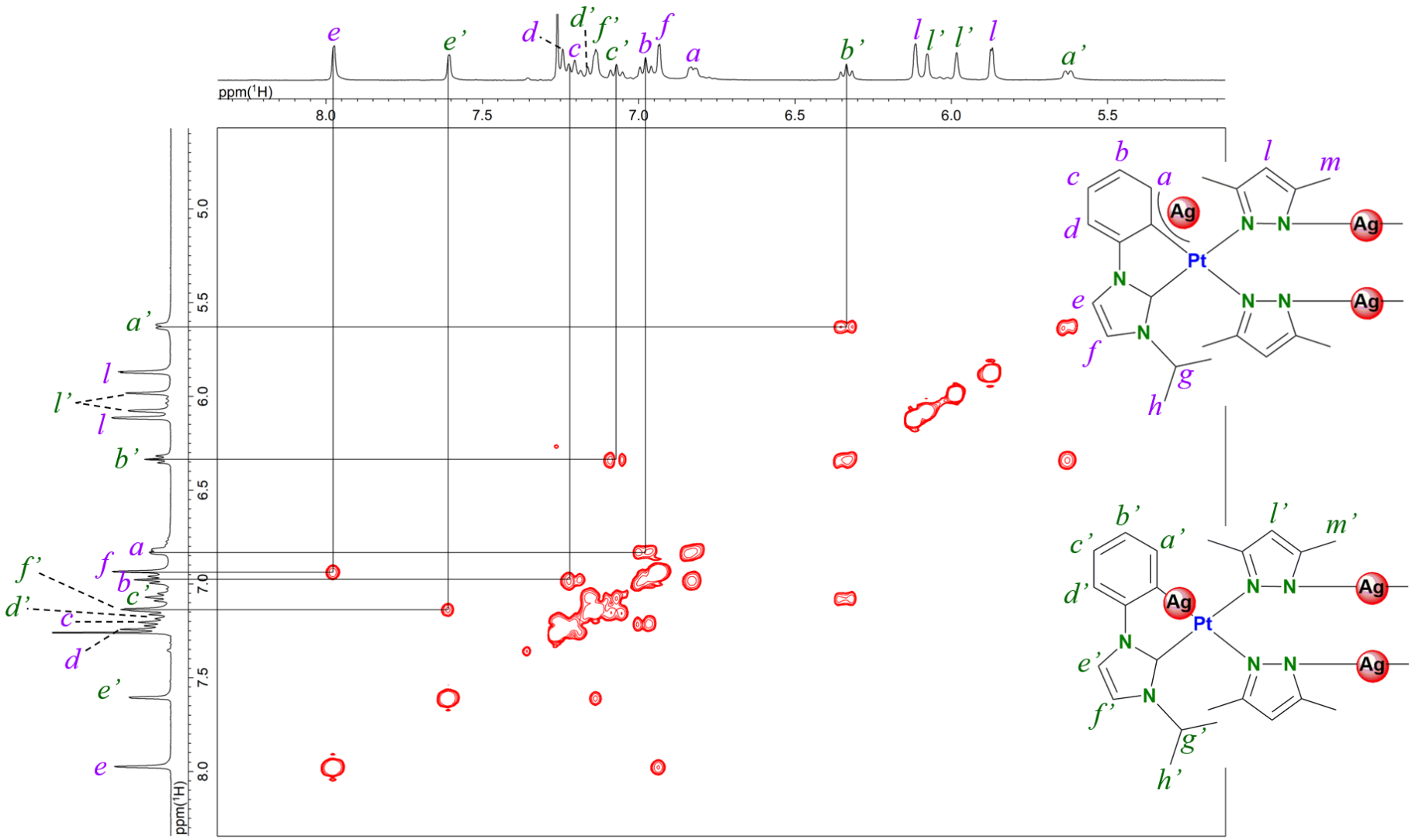

Figure 4-21. ^{1}H-^{1}H COSY spectrum (400 MHz, $CDCl_3$, –50 °C, TMS) of $[(Ph\text{-}NHC)_2Pt_2Ag_3(Me_2pz)_2]BF_4$ (**7**).

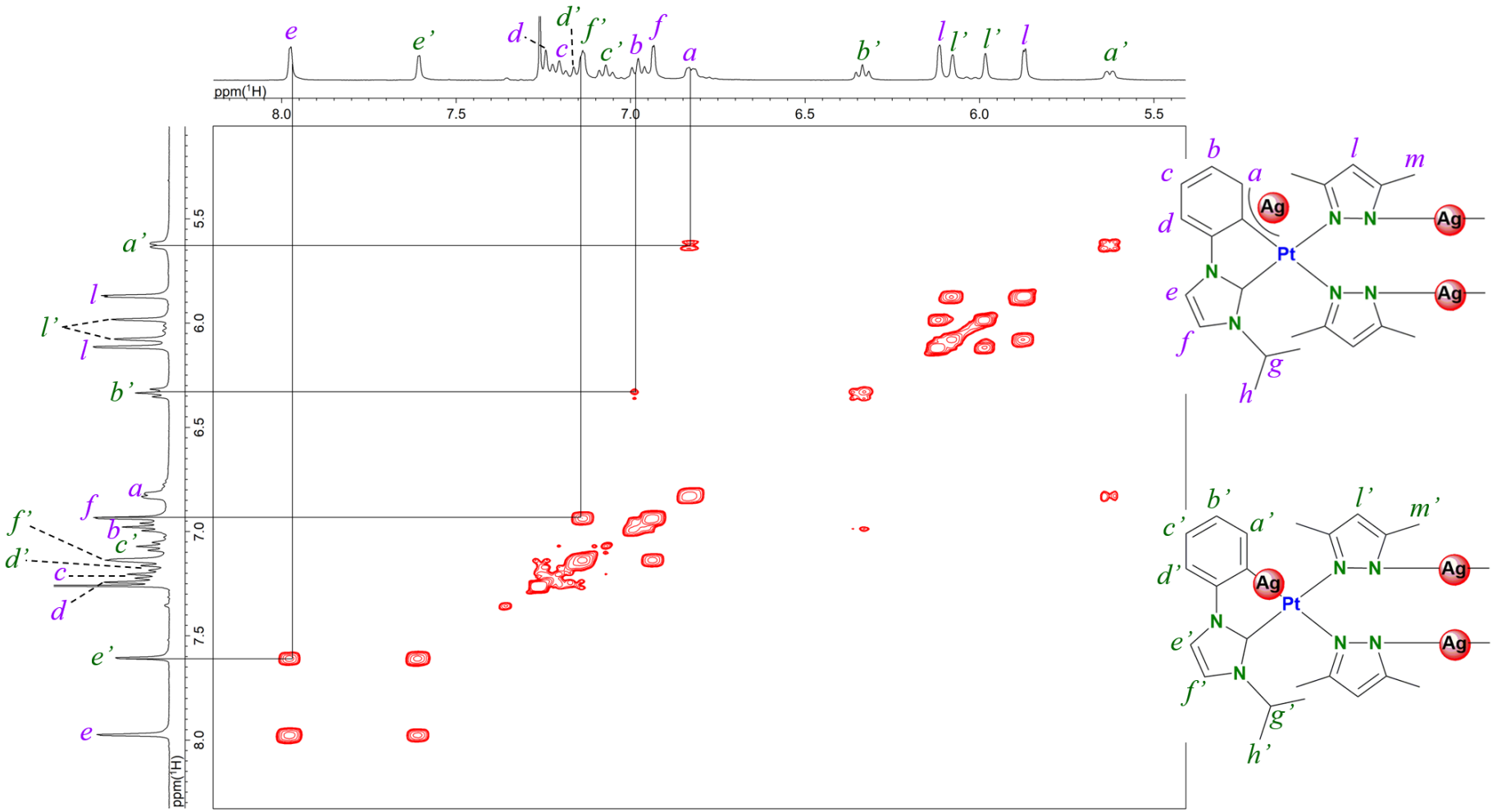

Figure 4-22. 2D ^{1}H EXchange SpectrocopY (EXSY) spectrum (400 MHz, $CDCl_3$, –50 °C, TMS, mixing time = 300 ms) of $[(Ph\text{-}NHC)_2Pt_2Ag_3(Me_2pz)_2]BF_4$ (**7**).

4-2-4. Preparation of [(Ph-NHC)$_2$Pt$_2$Ag$_2$(Me$_2$pz)$_4$] (8)

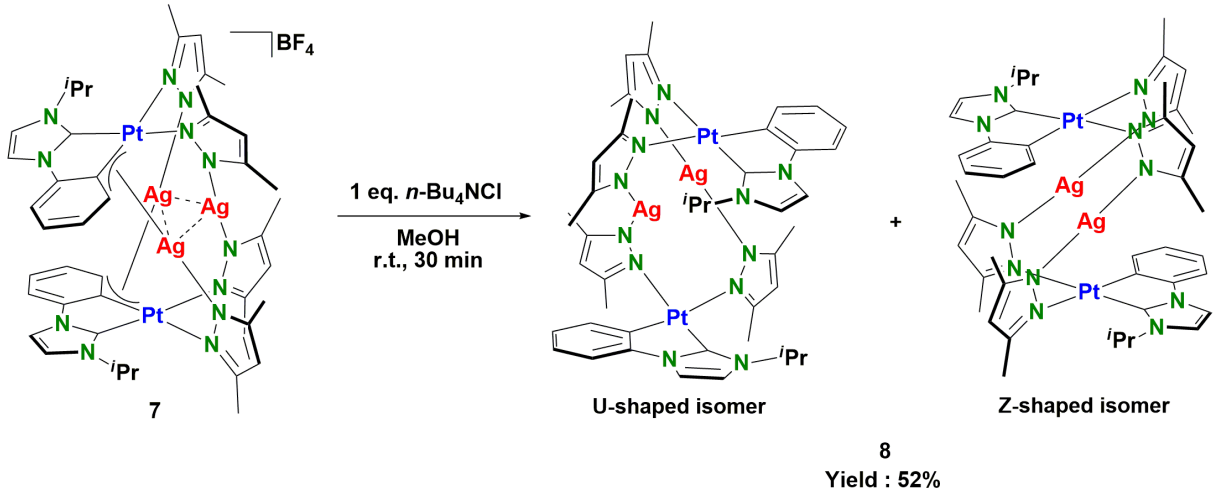

Scheme 4-4. Synthesis of [(Ph-NHC)$_2$Pt$_2$Ag$_2$(Me$_2$pz)$_4$] (**8**).

A mixture of **7** (39 mg, 25 μmol) and tetrabutylammonium chloride (*n*-Bu$_4$NCl) (7.1 mg, 26 μmol) in acetone (10 mL) was stirred at room temperature for 2 h. After the reaction mixture was filtered to remove white precipitate (AgCl), the filtrate was concentrated to dryness and dissolved again into MeOH. White precipitate was collected and dried in vacuo. A single crystal of **8**$_U$ was obtained from DCM/*n*-hexane solution. Yield: 17 mg (12 μmol, 52%). Anal. Calcd for $C_{44}H_{54}Ag_2N_{12}Pt_2$: C, 38.95; H, 4.01; N, 12.39. Found: C, 39.03; H, 3.79; N, 12.36. ^{1}H NMR (500 MHz, $CDCl_3$, 25 °C, TMS) of **8**$_U$: δ = 7.08 (s, 2H, H_e), 6.90 (t, J = 8.0 Hz, 2H, H_c), 6.78 (t, J = 8.0 Hz, 2H, H_d), 6.75 (d, J = 8.0 Hz, 2H, H_b), 6.67 (s, 2H, H_f), 6.33 (d, J = 8.0 Hz, 2H, H_a), 5.92 (s, 2H, H_l), 5.79 (s, 2H, H_l), 2.91 (br, 2H, H_g), 2.30 (s, 6H, H_m), 2.16 (s, 6H, H_m), 2.05 (br, 6H, H_m), 1.67 (s, 6H, H_m), 1.05 (d, J = 8.0 Hz, 6H, H_h), 0.45 (br, 6H, H_h) ppm. ^{13}C{^{1}H} NMR (125 MHz, $CDCl_3$, 25 °C, TMS) of isomer mixture of **8**: δ = 157.6 (C_j), 148.8 (Me$_2$*pz*), 148.2 (Me$_2$*pz*), 147.9 (Me$_2$*pz*), 147.6 (Me$_2$*pz*), 147.4 (Me$_2$*pz*), 147.4 (C_i), 146.5 (Me$_2$*pz*), 146.2 (Me$_2$*pz*), 136.8 (C_a), 136.4 (C_a), 133.5 (C_k), 125.3 (C_b), 125.0 (C_b), 123.1 (C_c), 114.7 (C_e), 114.6 (C_f), 109.7 (C_d), 109.5 (C_d), 103.2 (C_l), 102.9 (C_l), 102.9 (C_l), 102.7 (C_l), 102.7 (C_l), 102.6 (C_l), 102.4 (C_l), 24.3 (C_h), 23.7 (C_h), 23.2 (C_h), 22.2 (C_h), 22.1 (C_h), 14.4 (C_m), 14.3 (C_m), 14.2 (C_m),

14.2 (C_m), 13.9 (C_m), 13.9 (C_m), 13.7 (C_m) ppm. ^{195}Pt NMR (86 MHz, $CDCl_3$, 30 °C, H_2PtCl_6 in D_2O): δ = –3719 ppm. FAB-MS for [(Ph-NHC)$_2$Pt$_2$Ag$_2$(Me$_2$pz)$_4$]: m/z = 1356 $[M]^+$.

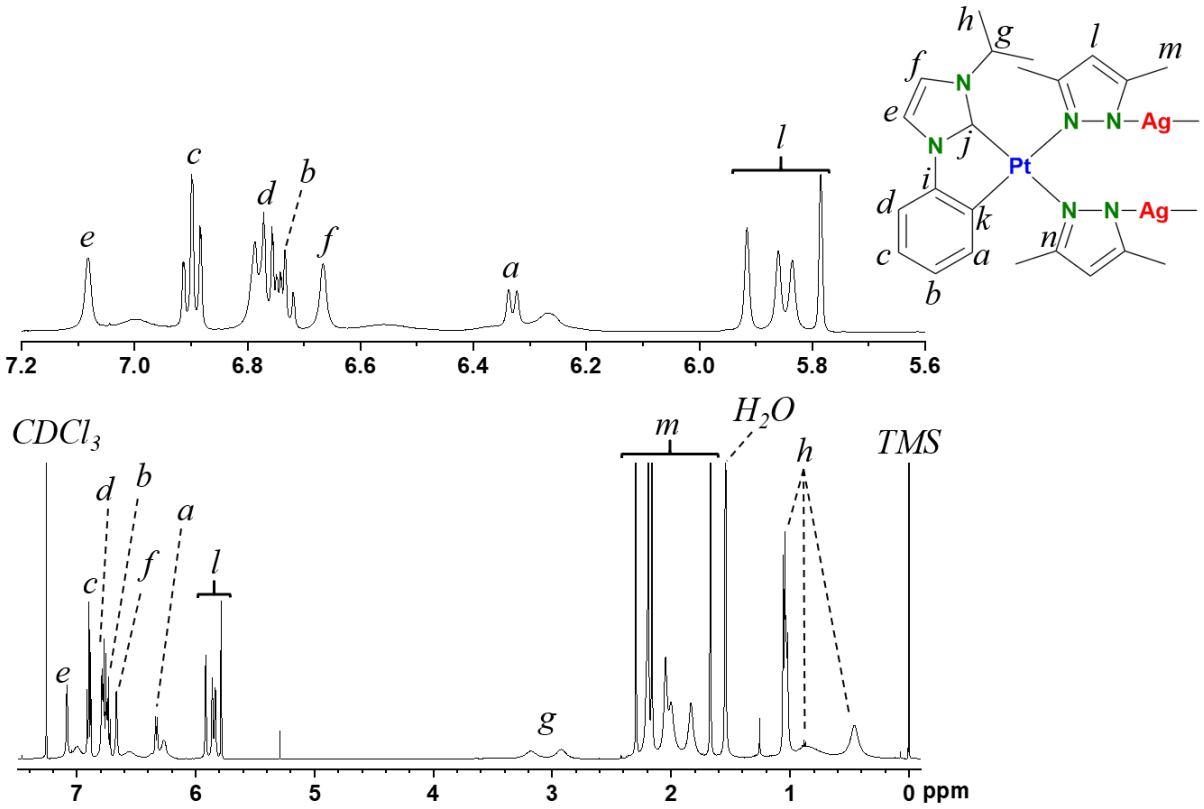

Figure 4-23. ^{1}H NMR spectrum (500 MHz, $CDCl_3$, 25 °C, TMS) of [(Ph-NHC)$_2$Pt$_2$Ag$_2$(Me$_2$pz)$_4$] (**8**) containing of two stereoisomers.

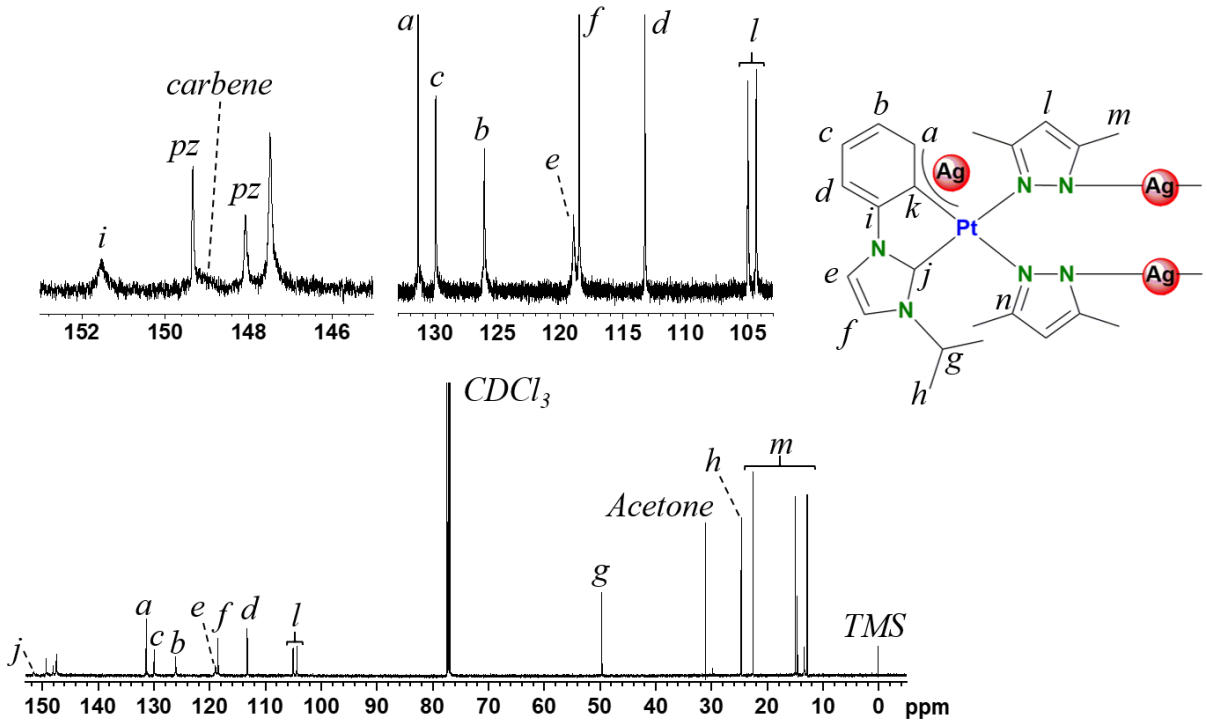

Figure 4-24. $^{13}C\{^{1}H\}$ NMR spectrum (500 MHz, $CDCl_3$, 25 °C, TMS) of $[(Ph\text{-}NHC)_2Pt_2Ag_2(Me_2pz)_4]$ (**8**) containing of two stereoisomers.

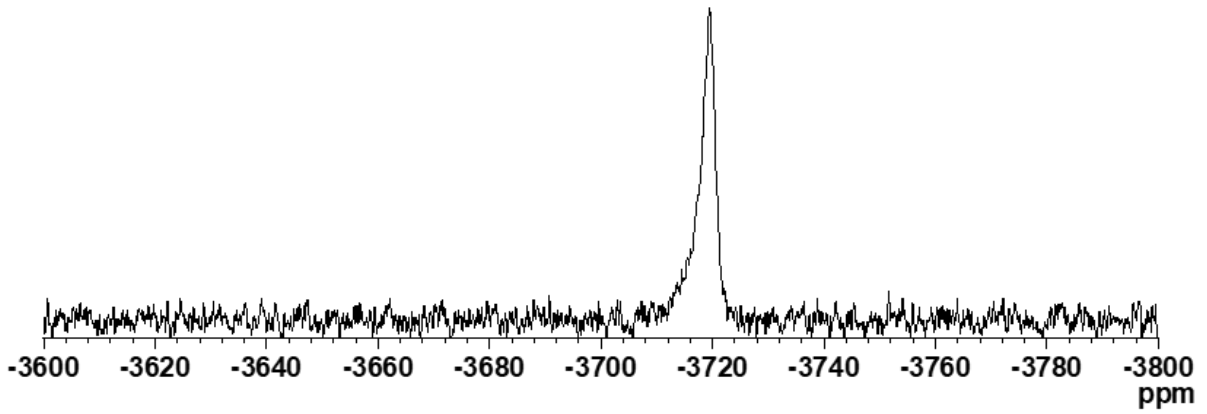

Figure 4-25. ^{195}Pt NMR spectrum (86 MHz, $CDCl_3$, 25 °C, H_2PtCl_6 in D_2O) of $[(Ph\text{-}NHC)_2Pt_2Ag_2(Me_2pz)_4]$ (**8**) containing of two stereoisomers.

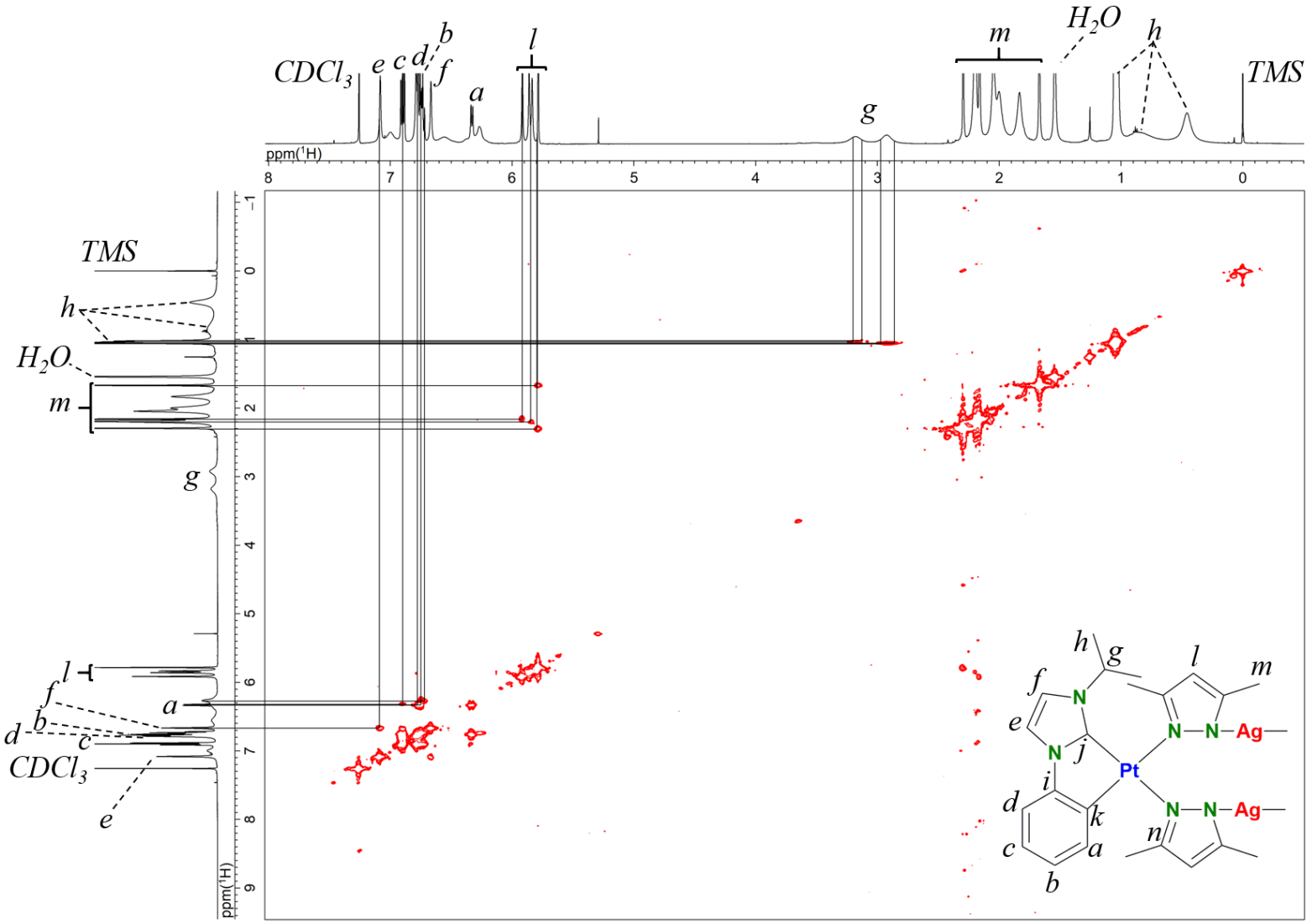

Figure 4-26. ^{1}H-^{1}H COSY spectrum (500 MHz, $CDCl_3$, 25 °C, TMS) of $[(Ph\text{-}NHC)_2Pt_2Ag_2(Me_2pz)_4]$ (**8**).

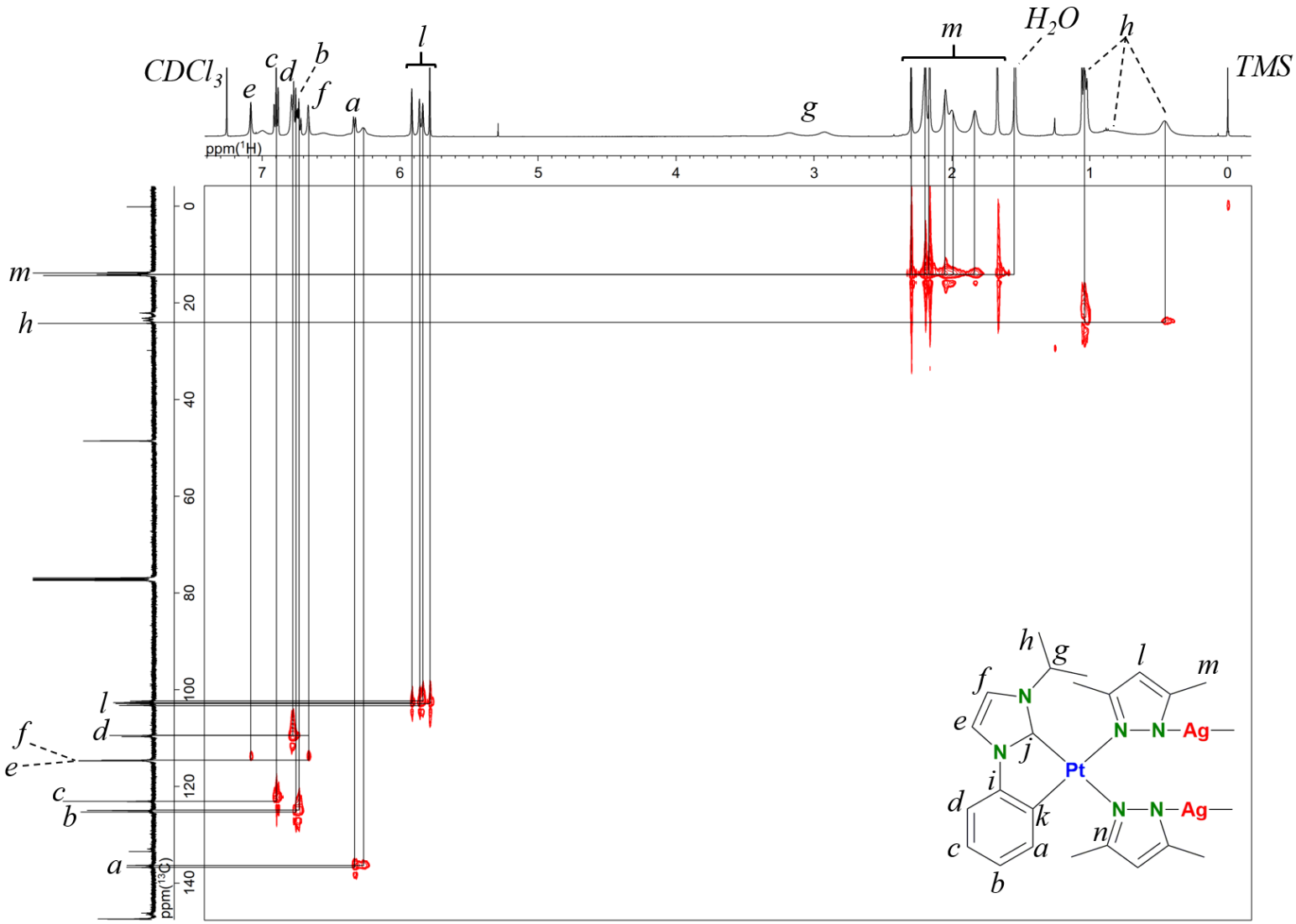

Figure 4-27. ^{1}H-^{13}C HSQC spectrum (500 MHz, $CDCl_3$, 25 °C, TMS) of $[(Ph\text{-}NHC)_2Pt_2Ag_2(Me_2pz)_4]$ (**8**).

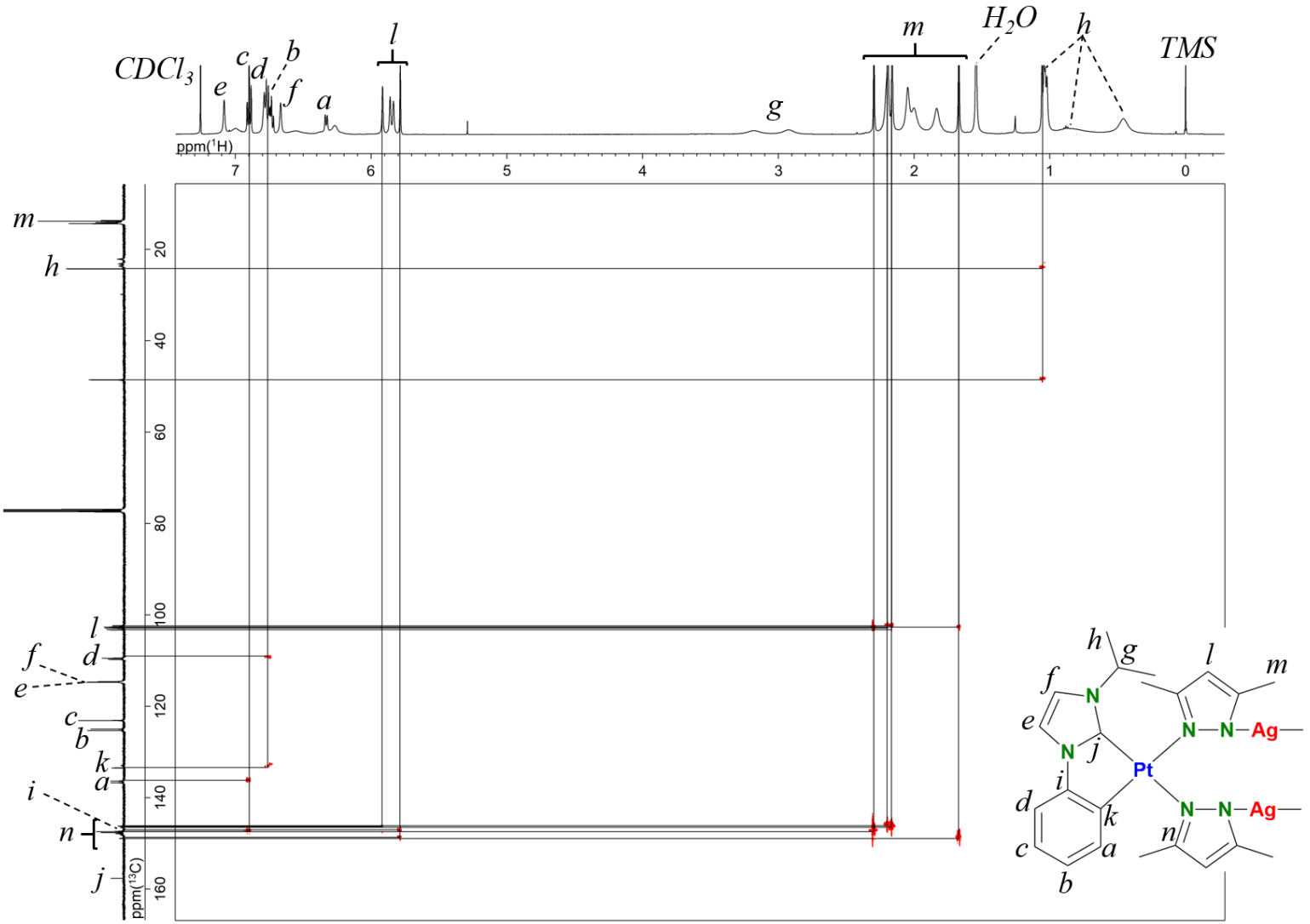

Figure 4-28. ^{1}H-^{13}C HMBC spectrum (500 MHz, $CDCl_3$, 25 °C, TMS) of $[(Ph\text{-}NHC)_2Pt_2Ag_2(Me_2pz)_4]$ (**8**).

4-2-5. Synthesis of [(Ph-NHC)$_2$Pt$_2$Ag$_3$(Ph$_2$pz)$_4$]BF$_4$ (9)

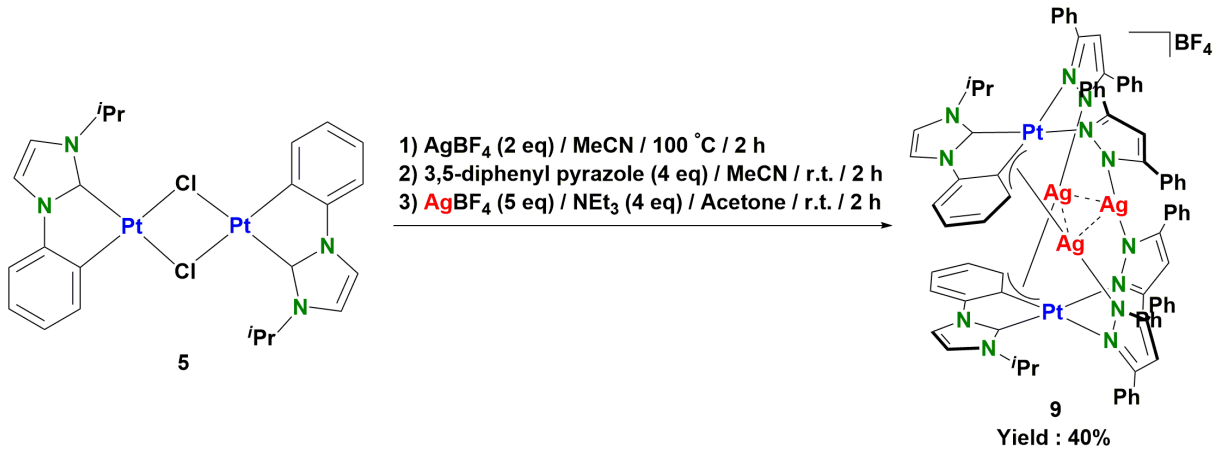

Scheme 4-5. Synthesis of [(Ph-NHC)$_2$Pt$_2$Ag$_3$(Ph$_2$pz)$_4$]BF$_4$ (**9**).

A mixture of dinuclear Pt complex **5** (43 mg, 52 μmol) and AgBF$_4$ (26 mg, 134 μmol) in acetonitrile (5 mL) was refluxed for 2 h in the dark. After the reaction mixture was filtered to remove white precipitate (AgCl), 3,5-diphenyl pyrazole (Ph$_2$pzH, 46 mg, 209 μmol) was added to the filtrate. The solution was stirred at room temperature for 2 h, filtered and dried in vacuo. The residue was mixed with AgBF$_4$ (49 mg, 250 μmol) and triethylamine (28 μL, 200 μmol) in acetone (10 mL) and the mixture was stirred at room temperature for 2 h. After the reaction mixture was filtered and dried, the residue was dissolved into dichloromethane (DCM). The solution was washed with water and dried over MgSO$_4$. After the organic phase was concentrated under reduced pressure, *n*-hexane was added to the solution to afford **9** as a yellow powder. The yellow precipitate was collected and dried in vacuo. Yield: 77 mg (40%). Anal. Calcd for C$_{84}$H$_{70}$Ag$_3$N$_{12}$Pt$_2$·0.25(CHCl$_3$): C, 48.70; H, 3.41; N, 8.09. Found: C, 48.74; H, 3.36; N, 7.88. A single crystal of **9** was obtained from chloroform/*n*-pentane. ^{1}H NMR (500 MHz, CDCl$_3$, 25 ℃, TMS): δ = 8.24 (d, *J* = 2.0 Hz,, 2H, *H$_e$*), 7.59 (dd, *J* = 8.0, 1.0 Hz, 4H, *Ph*$_2$pz), 7.29 (d, *J* = 8.0 Hz, 2H, *H$_d$*), 7.27–7.25 (m, *Ph*$_2$pz), 7.23–7.16 (m, *Ph*$_2$pz), 7.15 (d, *J* = 8.0 Hz, 2H, *H$_a$*), 7.15–7.00 (m, *Ph*$_2$pz), 6.99 (t, *J* = 8.0 Hz, 2H, *H$_c$*), 6.98–6.95 (m, *Ph*$_2$pz), 6.94 (d, *J* = 2.0 Hz,, 2H, *H$_f$*), 6.86 (s, 2H; Ph$_2$*pz*), 6.85–6.81 (m, *Ph*$_2$pz), 6.67 (s, 2H, Ph$_2$*pz*), 6.31 (t, *J*

= 8.0 Hz, 2H, H_b), 2.92 (sept, J = 6.5 Hz, 2H, H_g), 1.08 (d, J = 6.5 Hz, 6H, H_h), 0.50 (d, J = 6.5 Hz, 6H, H_h) ppm. ^{13}C NMR (125 MHz, $CDCl_3$, 25 °C, TMS): δ = 154.7 (C_j), 154.5 (Ph_2pz), 153.4 (Ph_2pz), 152.9 (Ph_2pz), 150.8 (C_a), 145.1 (Ph_2pz), 133.3 (Ph_2pz), 133.0 (Ph_2pz), 132.8 (Ph_2pz), 132.7 (Ph_2pz), 132.5 (C_k), 129.9 (Ph_2pz), 128.5 (Ph_2pz), 128.4 (Ph_2pz), 128.3 (Ph_2pz), 128.1 (Ph_2pz), 128.0 (Ph_2pz), 127.8 (Ph_2pz), 127.6 (Ph_2pz), 126.5 (Ph_2pz), 126.2 (C_b), 125.6 (Ph_2pz), 119.8 (C_e), 119.5 (C_c), 113.5 (C_d), 105.1 (Ph_2pz), 104.6 (C_f), 49.7 (C_g), 24.8 (C_h), 23.6 (C_h) ppm. ^{195}Pt NMR (86 MHz, $CDCl_3$, 30 °C, H_2PtCl_6 in D_2O): δ = –3145 ppm (d, $J(^{195}Pt\text{-}^{109/107}Ag)$ = 456 Hz); ESI-MS for $[(Ph\text{-}NHC)_2Pt_2Ag_3(Ph_2pz)_4]BF_4$: *m/z* 1961.4 $[M\text{-}BF_4]^+$.

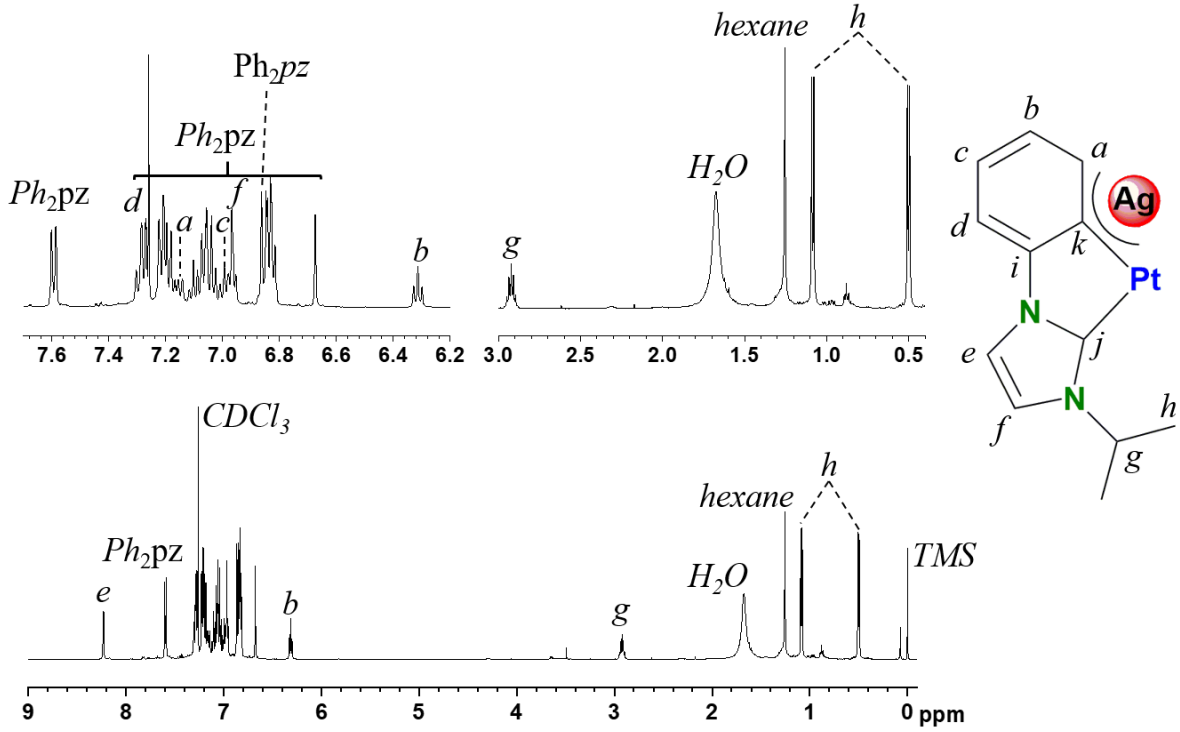

Figure 4-29. ^{1}H NMR spectrum (500 MHz, $CDCl_3$, 25 °C, TMS) of $[(Ph\text{-}NHC)_2Pt_2Ag_3(Ph_2pz)_4]BF_4$ (**9**).

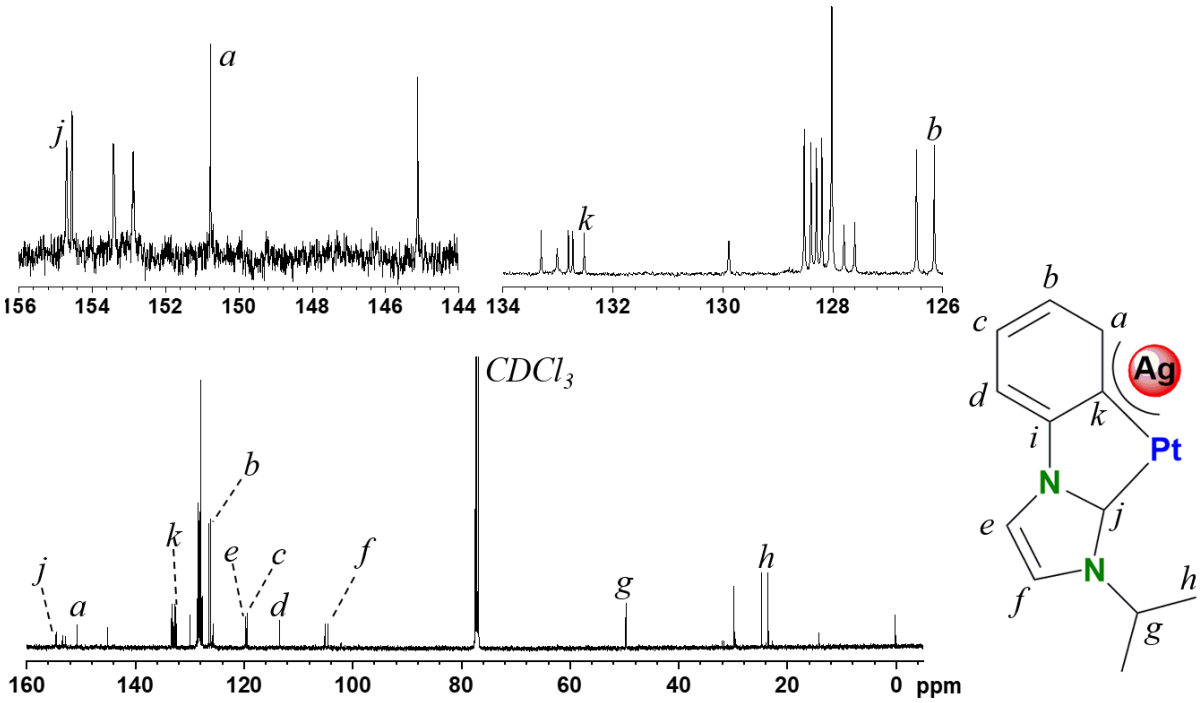

Figure 4-30. $^{13}C\{^{1}H\}$ NMR spectrum (125 MHz, $CDCl_3$, 25 ℃, TMS) of $[(Ph\text{-}NHC)_2Pt_2Ag_3(Ph_2pz)_4]BF_4$ (**9**).

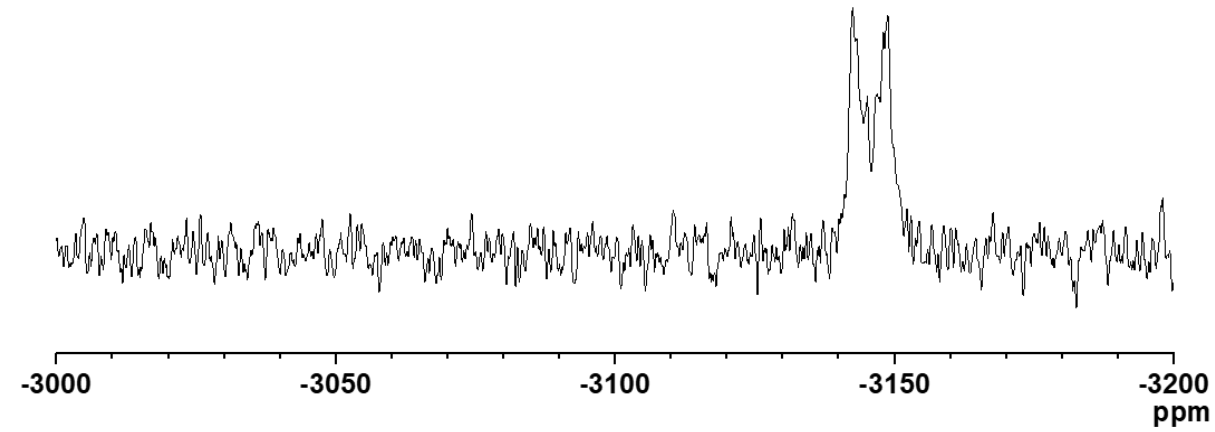

Figure 4-31. ^{195}Pt NMR spectrum (86 MHz, $CDCl_3$, 30 ℃, H_2PtCl_6 in D_2O) of $[(Ph\text{-}NHC)_2Pt_2Ag_3(Ph_2pz)_4]BF_4$ (**9**).

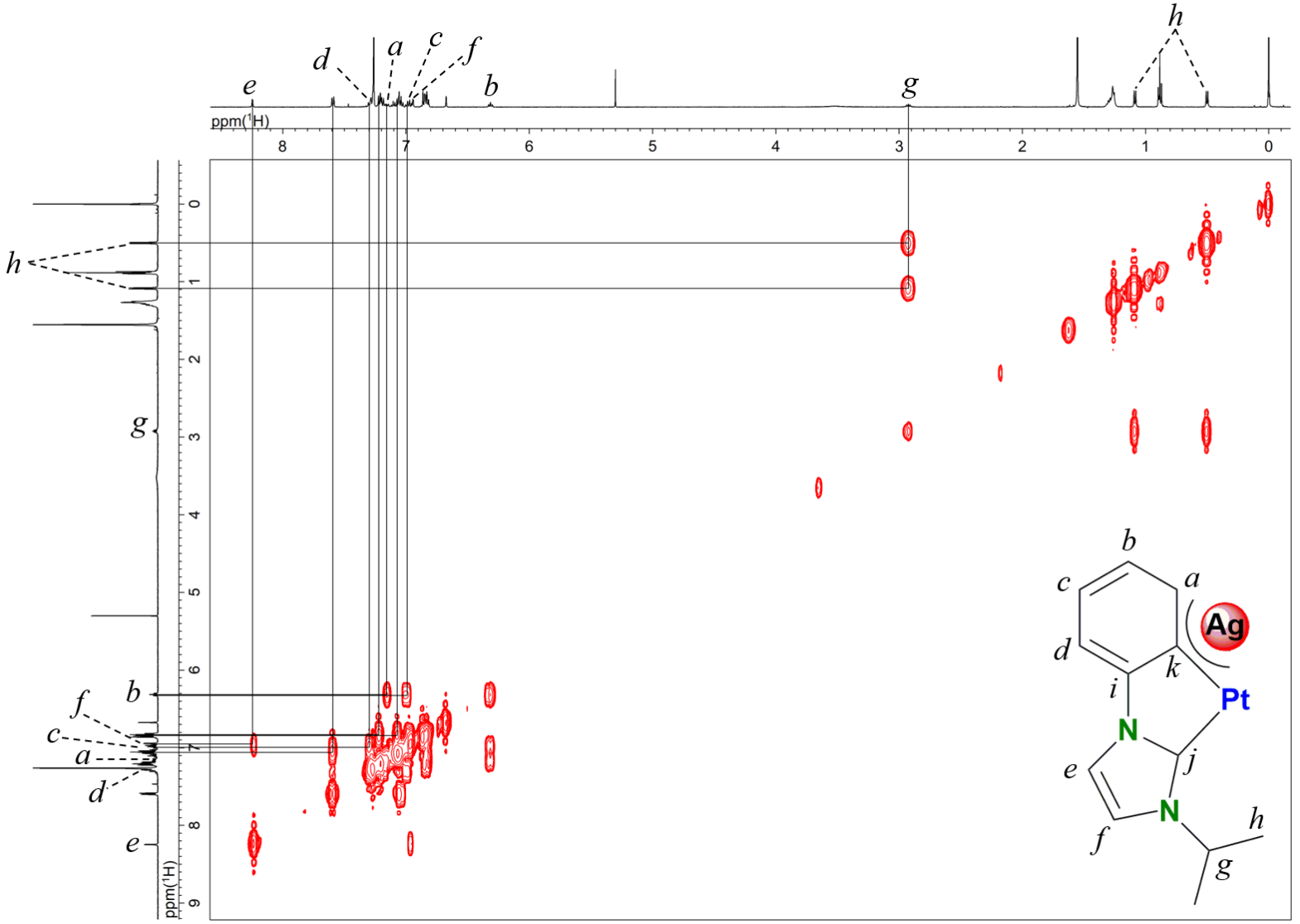

Figure 4-32. ^{1}H-^{1}H COSY spectrum (500 MHz, $CDCl_3$, 25 ℃, TMS) of $[(Ph\text{-}NHC)_2Pt_2Ag_3(Ph_2pz)_4]BF_4$ (**9**).

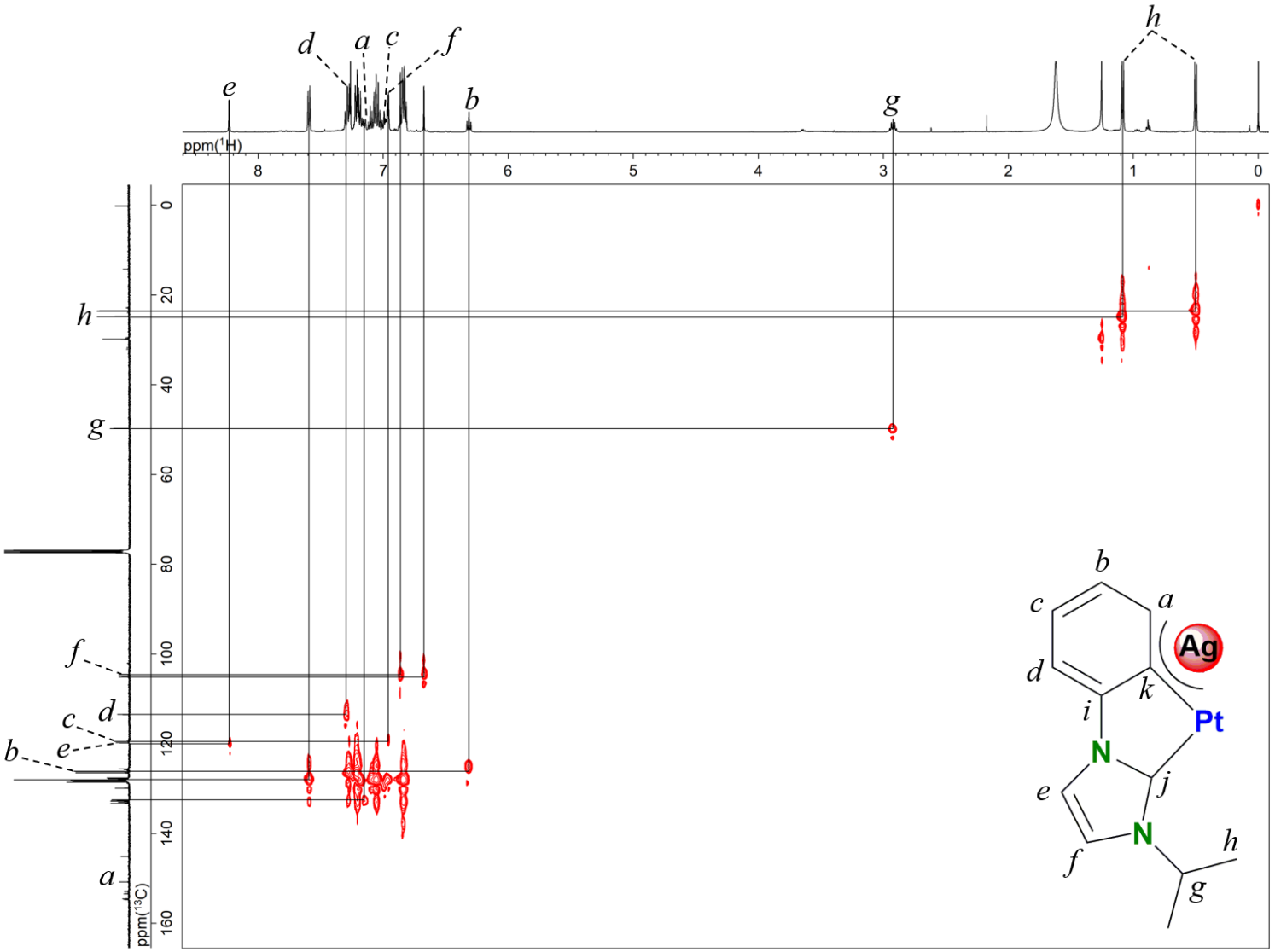

Figure 4-33. ^{1}H-^{13}C HSQC spectrum (500 MHz, $CDCl_3$, 25 °C, TMS) of $[(Ph\text{-}NHC)_2Pt_2Ag_3(Ph_2pz)_4]BF_4$ (**9**).

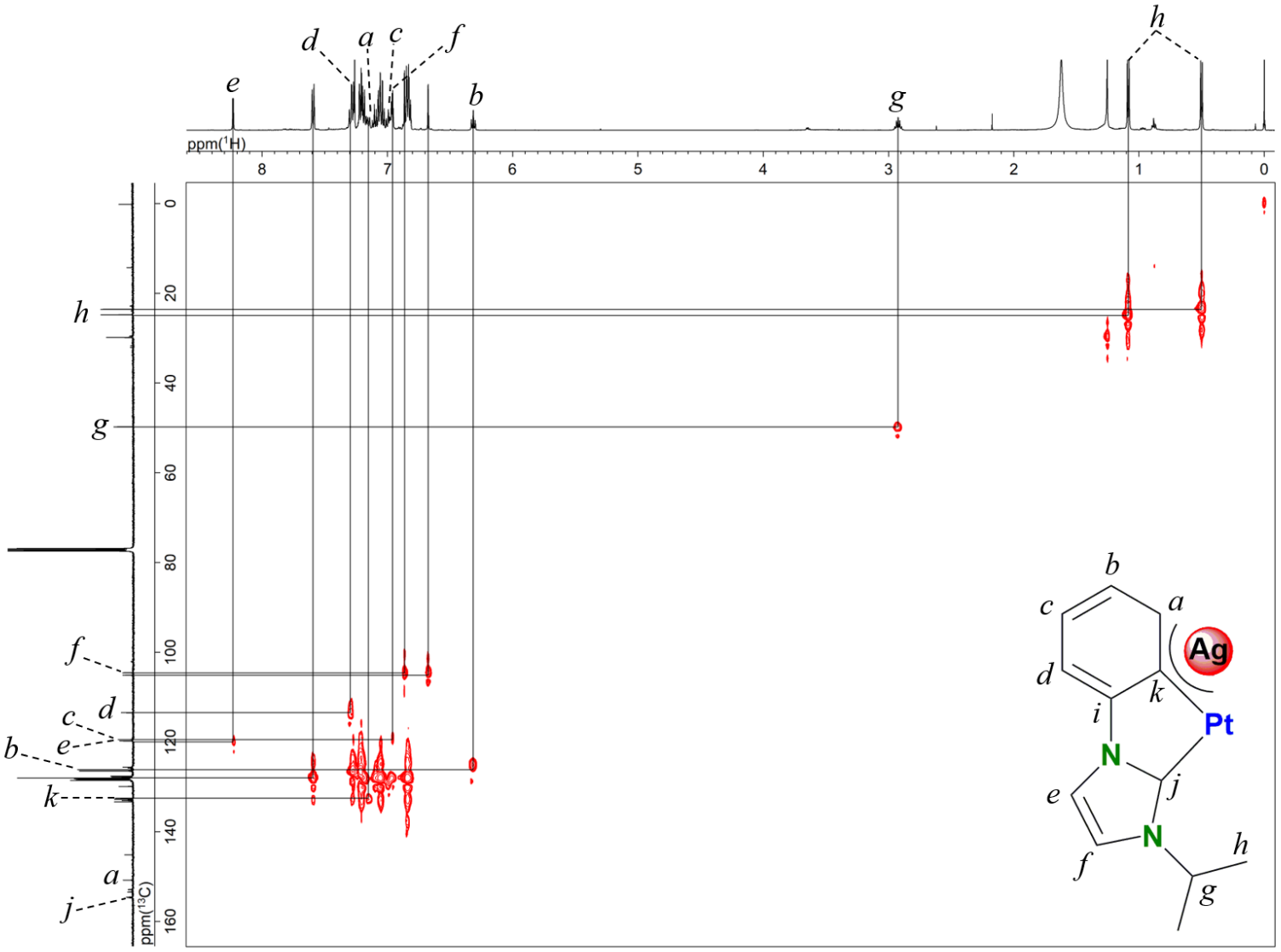

Figure 4-34. ^{1}H-^{13}C HMBC spectrum (500 MHz, $CDCl_3$, 25 ℃, TMS) of $[(Ph\text{-}NHC)_2Pt_2Ag_3(Ph_2pz)_4]BF_4$ (**9**).

4-3. Structural properties of heteropolynuclear complexes

4-3-1. Structural properties of [(Ph-NHC)Pt(Me$_2$pzH)$_2$]Cl (6)

The single crystal of mononuclear complex [(Ph-NHC)Pt(Me$_2$pzH)$_2$]Cl (**6**) was obtained from DCM/*n*-hexane solution. Single crystal X-ray structural analysis revealed that the complex cation consists of monoanionic C^C chelate ligand (Ph-NHC) and two molecules of 3,5-dimethyl pyrazole. The chloride ion is stabilized by two Cl···H–N$_{pz}$ hydrogen bonding

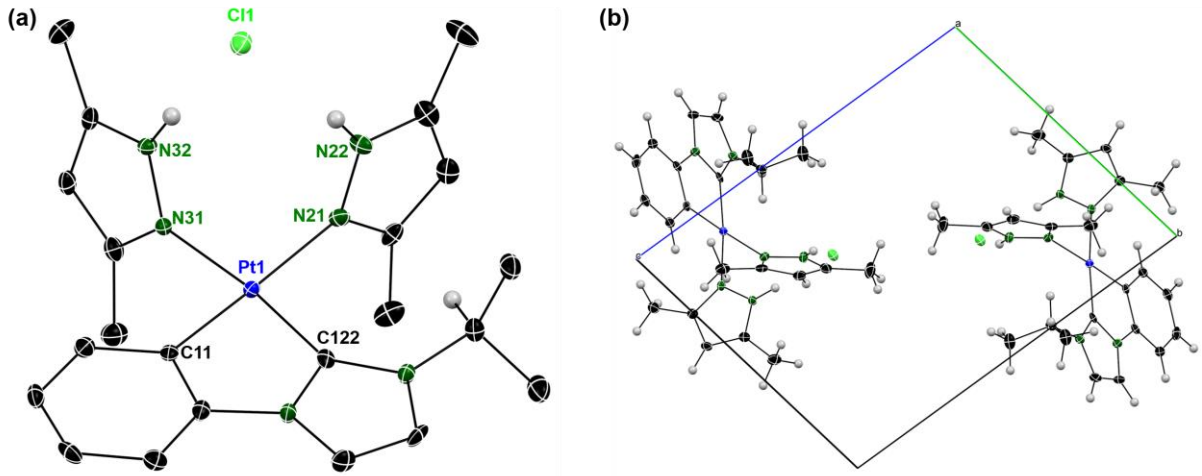

Figure 4-35. (a) Molecular structure and (b) packing structure view along a-axis of [(Ph-NHC)Pt(Me$_2$pzH)$_2$]Cl (**6**). Hydrogen atoms were omitted for clarity. Selected bond length (Å): Pt1–C122 1.982(3), Pt1–C11 2.001(3), Pt1–N21 2.118(3), Pt1–N31 2.064(3).

(Cl1···N22 3.167(3) Å, Cl1···N32 3.123(3) Å) (**Figure 4-35**, **Table 4-1**). The complex has two different types of carbon atoms (carbene carbon and phenyl carbon). The Pt-C$_{NHC}$ distance (1.982(1) Å) is shorter than the Pt-C$_{phenyl}$ distances (2.001(3) Å).[23,24] Significantly different Pt–N distances (Pt–N21, 2.118(3) Å; Pt1–N31, 2.064 (3) Å) suggest that pyrazole ligand which is trans to carbene carbon is influenced by stronger trans-effect than phenyl carbon, similarly to the case of mononuclear Pt(II) complex having Py-NHC chelate ligand. The ^{1}H NMR spectrum for **6** showed single sets of signals of syn-configuration at pyrazole moieties. Thus, the mononuclear complex **6** takes the same structure in the solid state and in solution. The upfield

shifts ($\Delta\delta$ = –2 to –3 ppm) of the tertiary proton at the ^{i}Pr group and the ortho-proton on phenyl group owing to the shielding effect from Me_2pzH moieties indicate that these protons are perpendicularly oriented to the center of each pyrazole ring, respectively, in solution (**Figure 4-35**).

4-3-2. Structural properties of [(Ph-NHC)$_2$Pt$_2$Ag$_3$(Me$_2$pz)$_4$]BF$_4$ (7)

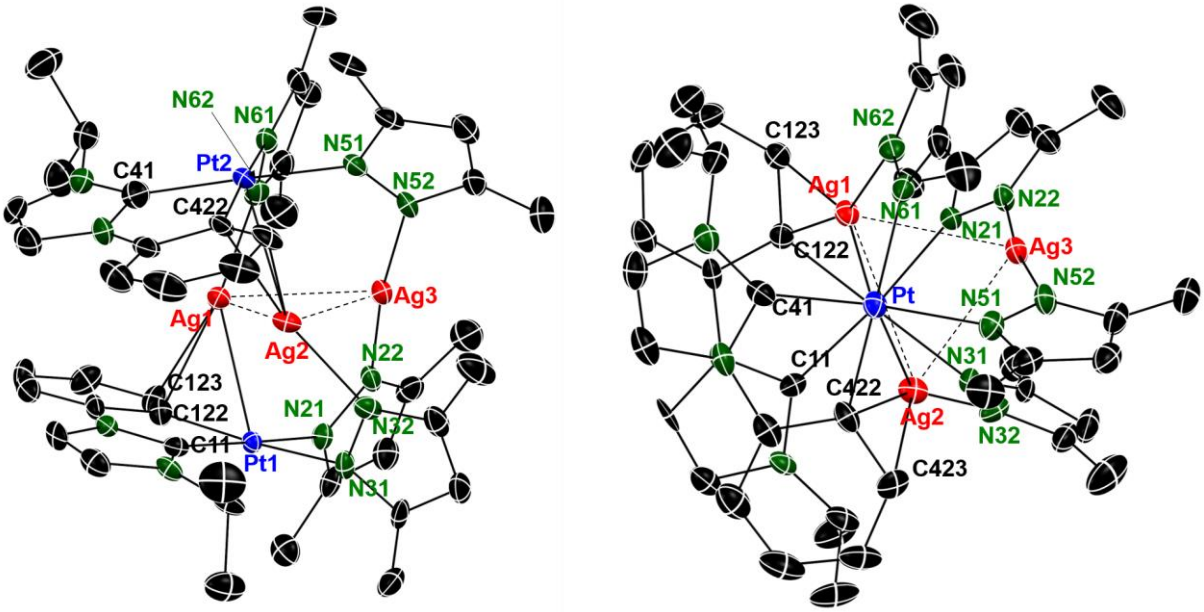

Figure 4-36. ORTEP drawing (50% probability ellipsoids) of [(Ph-NHC)$_2$Pt$_2$Ag$_3$(Me$_2$pz)$_4$]BF$_4$ (**7**): (left) side view, (right) viewed along the Pt···Pt axis. Hydrogen atoms, BF$_4$ and solvent molecules are omitted for clarity. Selected bond length (Å): Pt1–Ag1 2.8397(8), Ag1–C122 2.327(8), Ag1–C123 2.636(8), Pt2–Ag2 2.8192(8), Ag2–C422 2.329(8), Ag2–C423 2.630(8). Selected metal···metal distance (Å): Ag1···Ag2 3.2904(10), Ag1···Ag3 3.0100(10), Ag2···Ag3 3.0143(10).

The molecular structure of **7** was revealed by single crystal X-ray analysis. A colorless crystal of **7** was obtained from CH_2Cl_2/*n*-pentane solution. Crystal structure of **7** clearly showed that the Ag_3 unit was trapped between two Pt complex unit, [(Ph-NHC)Pt(Me$_2$pz)$_2$]$^{-}$, in

which all Ag ions take linear coordination geometry (**Figure 4-36**). The intramolecular Ag···Ag distances in $[\mathbf{7}]^+$ (Ag1···Ag3: 3.0100(10), Ag2···Ag3: 3.0142(10) and Ag1···Ag2: 3.2903(9) Å) are considerably shorter than those of trinuclear Ag(I) pyrazolato complexes (3.296–3.702 Å),[9,10] suggesting that the Ag ions in **7** strongly interacted with each other via argentophilic interaction.[8] One Ag ion (Ag3) was coordinated by only two pyrazolato ligands, whereas the other two Ag ions (Ag1 and Ag2) were supported by concerted coordination from two Pt complex units, that is, pyrazolato ligands, dative bonds from Pt ions (Pt1···Ag1: 2.8397(8), Pt1···Ag2: 3.0773(8), Pt2···Ag1: 3.1372(8), and Pt2···Ag2: 2.8192(8) Å) and π-coordination from phenyl moiety (Ag–π interaction) concertedly worked to stabilize the multinuclear sandwich framework. These multiple coordination modes of Ag1 and Ag2 probably contributed to the shrinking Ag_3 structure sandwiched by two Pt complex units. It is

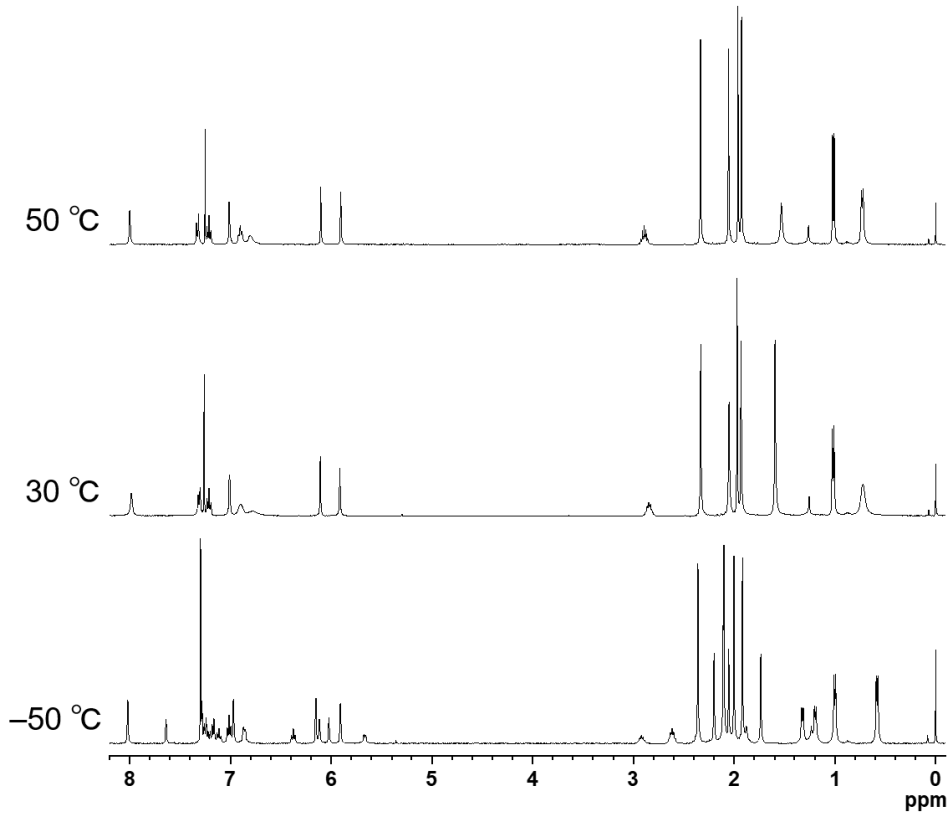

Figure 4-37. ^{1}H NMR spectra of **7** in $CDCl_3$ (400 MHz, TMS). The signals assigned to $[\mathbf{7}]^+$ showed single set of signals at 50 ℃ (top). At –50 ℃, the signals clearly split into two sets of signals (bottom).

noted that the Pt_2Ag_3 framework in $[\mathbf{7}]^+$ was considerably different from the similar Pt_2Ag_3 system containing ppy chelating ligands reported in our previous paper, whose structure contained one Ag ion trapped by two dative bond from Pt metal centers.[21]

Interestingly, the Ag_3 sandwich complex showed remarkable fluxional behavior in solution,

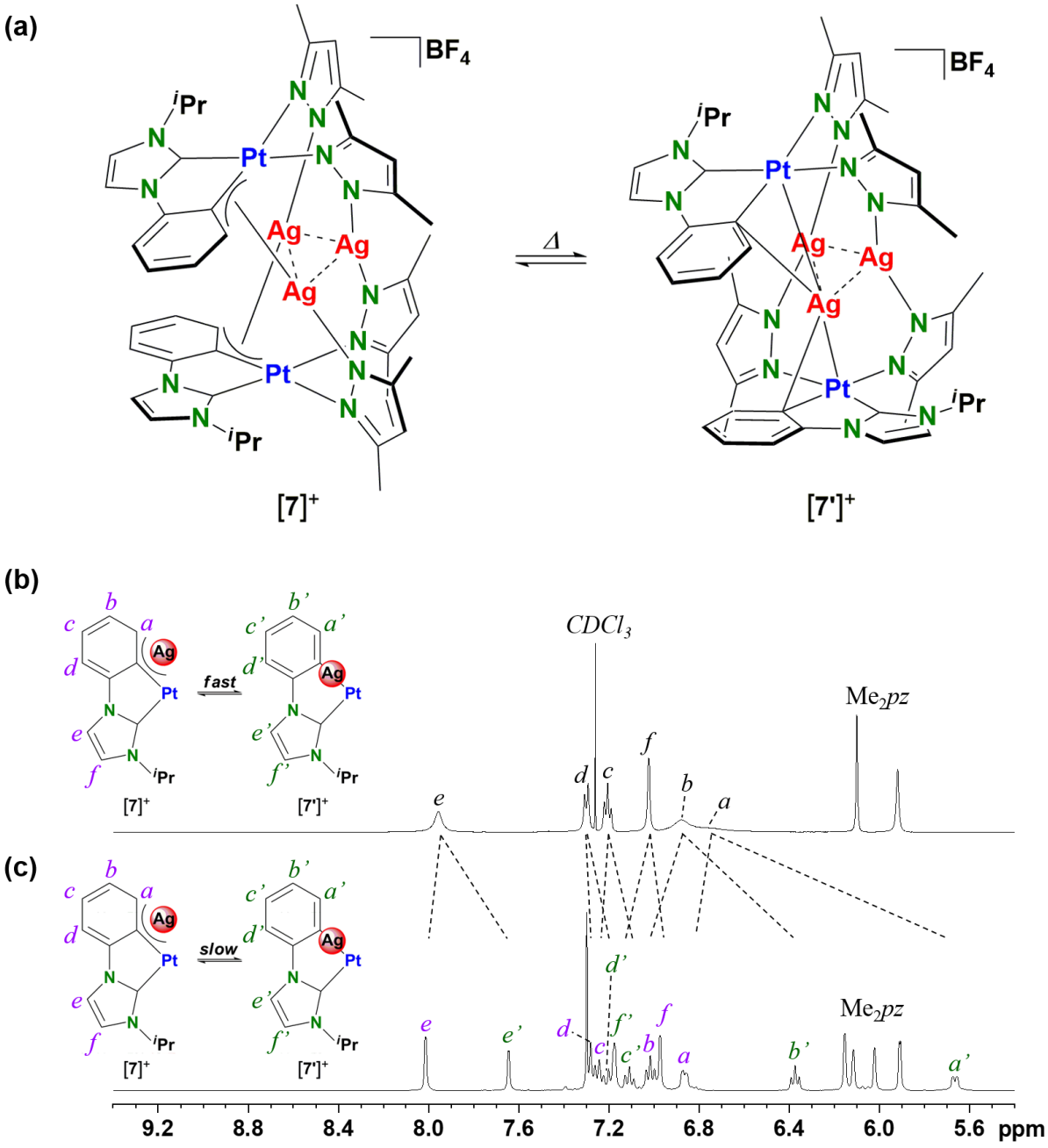

Figure 4-38. (a) Schematic representation of the isomerization between $[\mathbf{7}]^+$ and $[\mathbf{7'}]^+$. (b,c) ^{1}H NMR spectra (400 MHz, $CDCl_3$) of the Ag_3 sandwich complex recorded at (b) 25 °C and (c) –50 °C.

although multiple coordination from two Pt complex units toward the Ag_3 core were observed in the crystalline state. In the ^{1}H NMR spectrum of **7** recorded in $CDCl_3$, the signals assigned to [**7**]$^+$ showed single set of signals (coalescence) at 50 ºC, meanwhile clearly split into two sets of signals at –50 ºC (**Figure 4-37**). Variable temperature (VT) ^{195}Pt NMR also showed one doublet signal at –3247 ppm ($^1J(^{195}Pt–^{107,109}Ag)$ = 480 Hz) at 30 ºC and two doublet signals at –3275 ppm ($^1J(^{195}Pt–^{107,109}Ag)$ = 528 Hz) and –3279 ppm ($^1J(^{195}Pt–^{107,109}Ag)$ = 682 Hz) at –50 ºC, respectively (**Figure 4-18**). These results indicate that intramolecular isomerization of [**7**]$^+$ takes place reversibly in solution, which is also supported by the 2D ^{1}H–^{1}H EXchange SpectroscopY (EXSY) experiments recorded at –50 ºC (**Figure 4-22**).

The structure of Pt_2Ag_3 isomer [**7'**]$^+$ was assumed by the analysis of low temperature NMR spectroscopy (**Figure 4-15**) and the results of X-ray structural analysis (**Figure 4-36**). In comparison with the signal at 6.23 ppm assigned to the ortho-protons marked with "*a"* at phenyl moieties of the Ph-NHC ligand in [**6**]$^+$ (**Figure 4-8**), the corresponding signal of [**7**]$^+$ measured at –50 ºC splitted largely into two signals (5.67 ($\Delta\sigma$ = –0.6 ppm) and 6.87 ppm ($\Delta\sigma$ = +0.6 ppm)). According to our previous studies concerning the formation of Pt_2Ag_3 complexes having ppy (2-phenylpyridinate) as a chelate ligand, the signal of the ortho-proton was up-field shifted after formation of Pt_2Ag_3 framework whose Ag ion was trapped by two Pt → Ag dative bonds.[21] It suggests that the signal observed at 5.67 ppm can be assigned to the isomer [**7'**]$^+$ whose structure is similar to ppy analogue. Thus, the down-field shifted signal at 6.87 ppm can be assigned to [**7**]$^+$, characterized by X-ray crystallographic analysis in this study (**Figure 4-36**). Indeed, this type of down-field shift is typically observed in the π-coordination of carbon-carbon double bond to acidic Ag ion.[25–29] Thus the crystal structure and the observations of VT and solid state NMR spectroscopy can be reasonably explained if we assume a rapid rotation on the Ag_3 core to afford the stereoisomer [**7'**]$^+$ in solution.

The isomerization between $[\mathbf{7}]^+$ and $[\mathbf{7'}]^+$ was not observed in the crystalline state, as confirmed by ^{13}C cross-polarization/magic angle spinning (CP/MAS) NMR measurements (**Figure 4-17**). The ^{13}C NMR spectrum of single crystals of **7** showed two sets of signals corresponding to the different environment of Pt complexes units in contrast to the solution spectrum (**Figure 4-16**). This observation was good agreement with the X-ray structure of $[\mathbf{7}]^+$ with C_1 symmetry. Thus, the close packing of the complex salt in the solid state effectively spoiled the fluxional nature of $[\mathbf{7}]^+$.

4-3-3. Structural properties of $[(Ph\text{-}NHC)_2Pt_2Ag_2(Me_2pz)_4]$ (8)

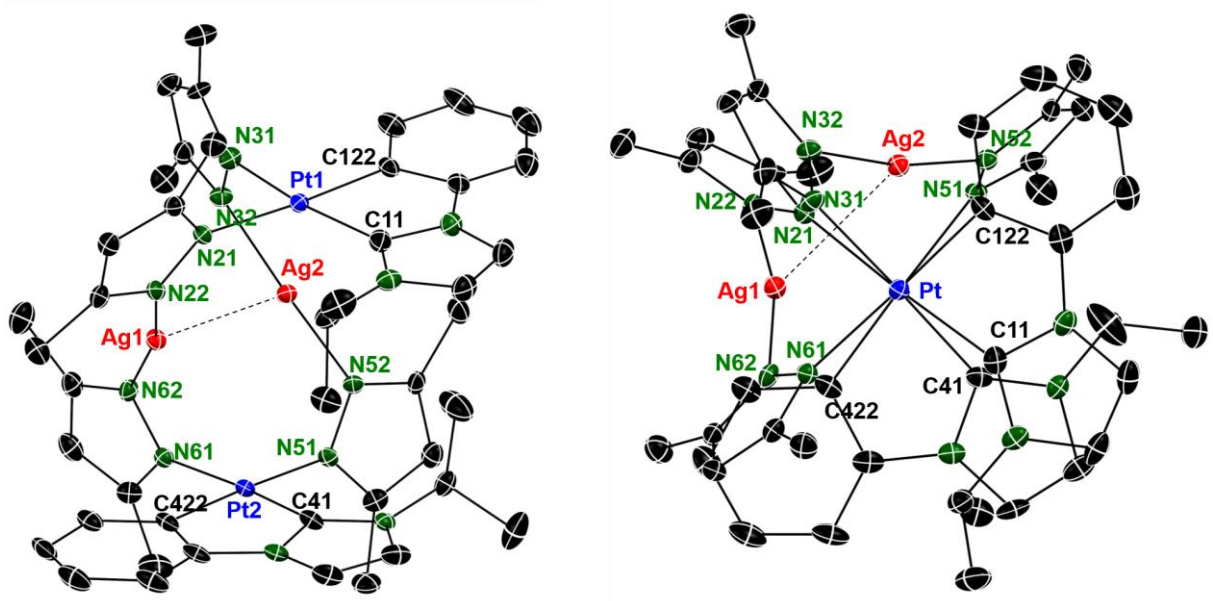

Figure 4-39. ORTEP drawing (50% probability ellipsoids) of $[(Ph\text{-}NHC)_2Pt_2Ag_2(Me_2pz)_4]$ (**8**): (left) side view, (right) viewed along the Pt···Pt axis. Hydrogen atoms are omitted for clarity. Selected metal···metal distance (Å): Ag1···Ag2 2.9384(6), Pt1···Ag1 3.7452(7), Pt1···Ag2 3.2793(5), Pt2···Ag1 3.1793(4), Pt2···Ag2 3.6430(7).

The Ag_3 core showed demetalation–metalation sequence. Multinuclear Ag_3 sandwich complex **7** reacted with Cl anion to afford a corresponding Ag_2 sandwich complex **8** in 52%

yield, whose structure was clearly revealed by X-ray crystallographic analysis (**Figure 4-39**). The Pt_2Ag_2 complex was supported only by pyrazolato ligands and argentophilic interaction between the Ag ions (Ag1···Ag2: 2.9384(7) Å), forming U-shaped Pt_2Ag_2 structure $\mathbf{8_U}$.[30] This Pt_2Ag_2 framework can incorporate additional Ag ion within the U-shaped cavity to regenerate $[\mathbf{7}]^+$ quantitatively (**Figure 4-40**).

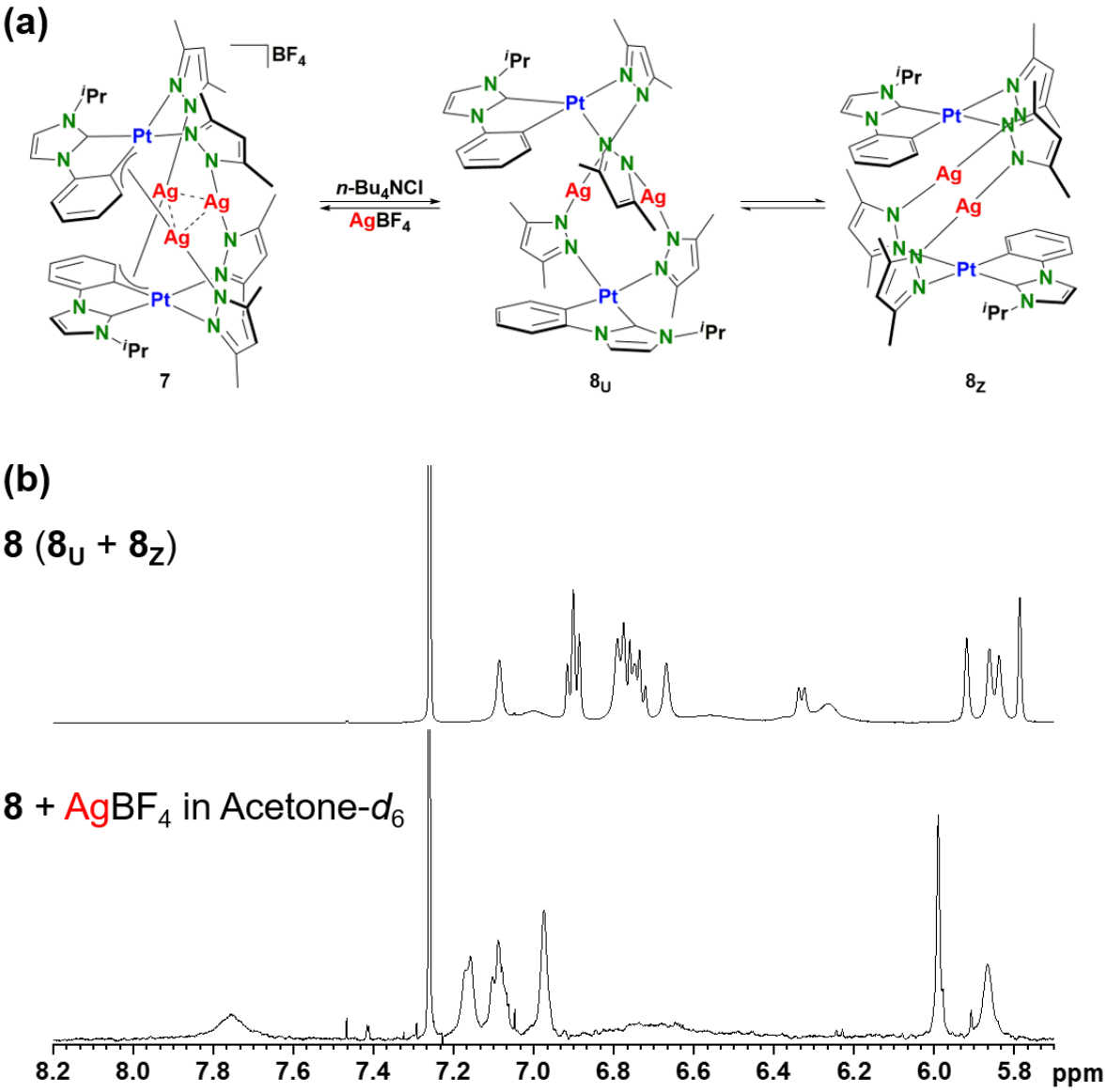

Figure 4-40. (a) Schematic representation of the demetalation-metalation process of Pt_2Ag_3 complex **7** and Pt_2Ag_2 complex **8**. (b) ^{1}H NMR spectra (500 MHz, 25 °C, TMS) of **8** ($CDCl_3$) and mixture of **8** and $AgBF_4$ (acetone-d_6/$CDCl_3$).

The sandwich Ag_2 complex **8**$_U$ also showed a fluxional behavior which is different from that of [**7**]$^+$ in solution. When single crystal of U-shaped Pt_2Ag_2 complex **8**$_U$ was dissolved into $CDCl_3$, new sets of signals appeared in the ^1H NMR spectrum and their intensities increased with time, suggesting the occurrence of U- to Z- isomerization of the Pt_2Ag_2 complex. The reaction rate depended on the concentration of the complex, indicating that the isomerization reaction proceeded through an intermolecular process, as reported in our previous paper.[19] The isomerization reached to U : Z = 1:1 ratio in a thermodynamic equilibrium state within 30 min, suggesting that the U- to Z- isomerization rate of Pt_2Ag_2 complex **8**$_U$ is faster than that of Pt_2Ag_2 complex cation having pyridyl-NHC chelating ligands (**Figure 4-41**). Although the reaction mechanism of the isomerization was still unclear, this rate acceleration might originate from the charge of the complexes. Thus, the neutral Pt_2Ag_2 complexes can easily access to both structures to show a rapid intermolecular bond recombination. On the other hand, dicationic Pt_2Ag_2 complex might be more difficult to access to the other structure owing to electrostatic repulsion between two Pt_2Ag_2 complex cations.

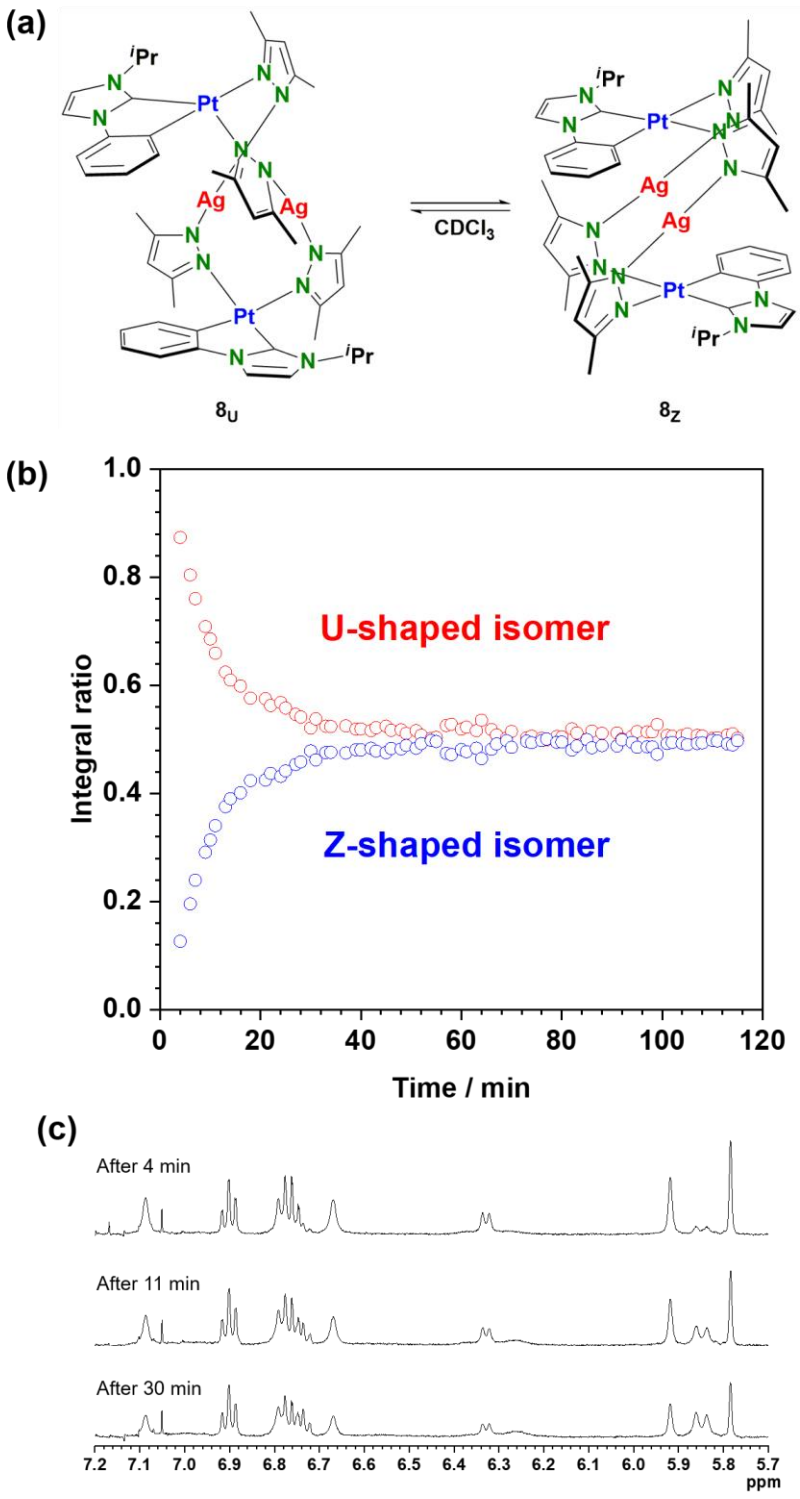

Figure 4-41. (a) Schematic representation of the isomerization from the U-shaped isomer **8**U to the Z-shaped isomer **8**Z. (b) The variation with the time of the relative value of the integrated intensities H4 on the pyrazolato of **8**U (δ = 5.92, 5.79 Hz) and **8**Z (5.86, 5.84 Hz), which are proportional to the concentration of **8**U and **8**Z, respectively, after single crystal of **8**U were dissolved in $CDCl_3$ in the dark at 25 °C. (c) ^1H NMR spectra (500 MHz, $CDCl_3$, 25 °C, TMS) of **8**U and isomer mixture of **8**.

4-3-4. Structural properties of [(Ph-NHC)$_2$Pt$_2$Ag$_3$(Ph$_2$pz)$_4$]BF$_4$ (9)

The fluxionality of the Pt_2Ag_3 complex strongly depended on the steric bulkiness of the bridging pyrazolato ligands and electronic nature of the chelating ligand on the Pt metal centers in solution. When sterically demanded diphenylprazolato (Ph_2pz) ligands were introduced to the sandwiched Pt_2Ag_3 complex instead of dimethylprazolato (Me_2pz) ligands, corresponding Pt_2Ag_3

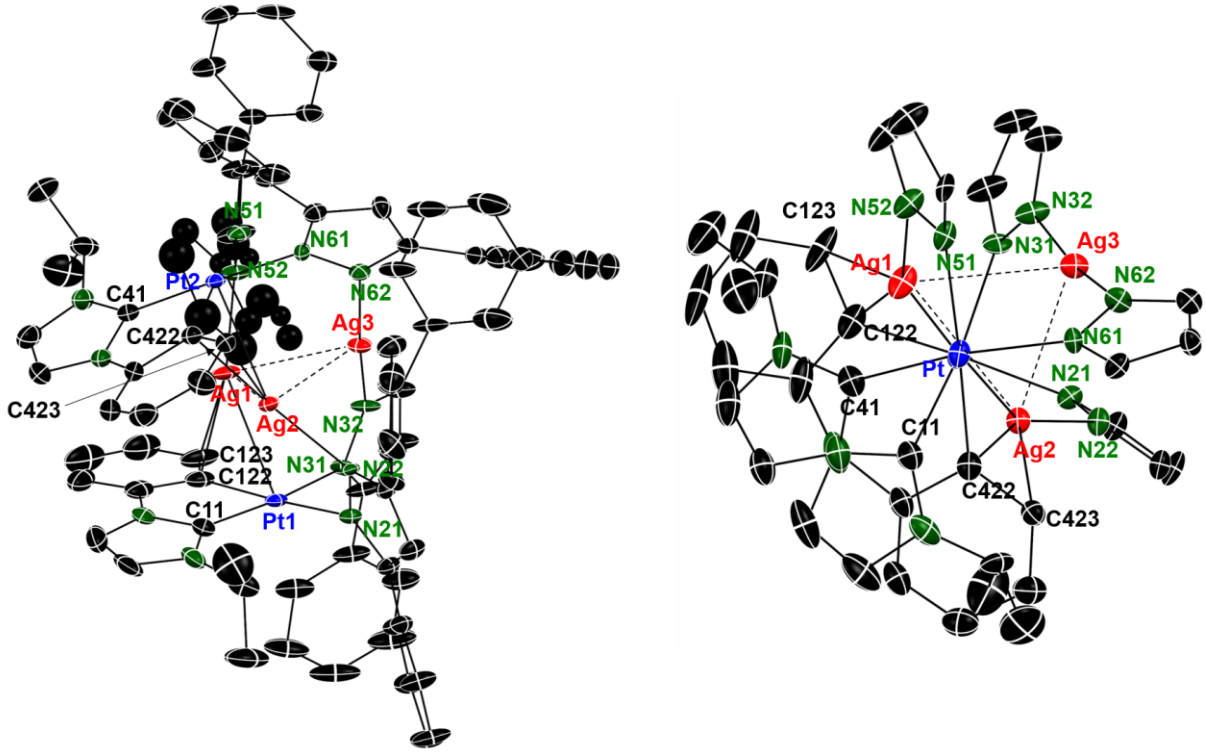

Figure 4-42. ORTEP drawing (50% probability ellipsoids) of [(Ph-NHC)$_2$Pt$_2$Ag$_3$(Me$_2$pz)$_4$]BF$_4$ (**7**): (left) side view, (right) viewed along the Pt···Pt axis. Hydrogen atoms, BF_4 and solvent molecules are omitted for clarity. Selected bond length (Å): Pt1-Ag1 2.9253(7), Ag1-C122 2.319(7), Ag1-C123 2.585(8), Pt2-Ag2 2.8506(7), Ag2-C422 2.336(7), Ag2-C423 2.674(7). Selected metal···metal distance (Å): Ag1···Ag2 3.1995(9), Ag1···Ag3 3.0579(10), Ag2···Ag3 2.9116(9).

complex **9** was formed in a similar synthetic manner, whose structure was mostly identical to **9**, as confirmed by X-ray crystallographic analysis (**Figure 4-42**). The ^{1}H NMR spectrum of [**9**]$^+$ did not change significantly at elevated temperature, indicating that the Pt_2Ag_3 having Ph_2pz

bridging ligands did not show isomerization (**Figure 4-43**). The bulky phenyl groups on pyrazolato ligands may sterically control the rigidity of the Pt_2Ag_3 framework and prevent multiple bond recombination between the Ag_3 core and the Pt complex unit, resulted in the effective inhibition of the thermal slippage of Pt complex unit on the Ag_3 core. In addition, the Pt_2Ag_3 complex having ppy chelating ligands and Ph_2pz bridging ligands, which was reported in our previous paper,[21] also did not show isomerization like [**7**]$^+$, determined by VT NMR measurements. This result suggests that weak π-acidic nature of the NHC ligand in [**7**]$^+$ effectively weakens the Pt → Ag dative bond, endowing the flexibility in the Ag_3 core.[31–33]

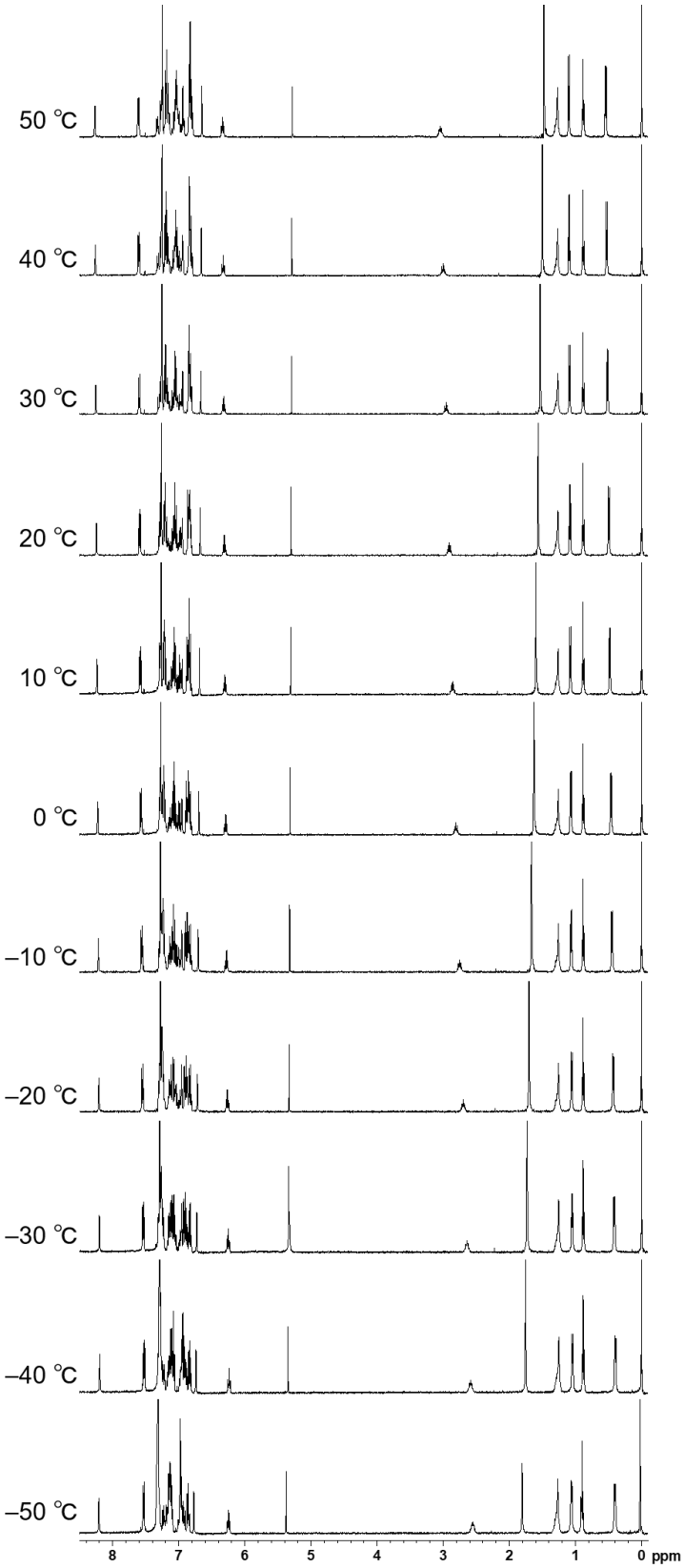

Figure 4-43. VT ^{1}H NMR spectra of **9** in $CDCl_3$. The single sets of signals of **9** do not split at any temperature, indicating that the Pt_2Ag_3 complex having Ph_2pz ligands **9** do not isomerize in solution.

Table 4-1. Crystallographic data for [(Py-NHC)Pt(Me_2pzH)$_2$]Cl·(**6**), [(Ph-NHC)$_2$Pt$_2$Ag$_3$(Me_2pz)$_4$]BF_4·$CHCl_3$·(C_5H_{12})$_{0.5}$ (**7**·$CHCl_3$·0.5C_5H_{12}), [(Ph-NHC)$_2$Pt$_2$Ag$_2$(Me_2pz)$_4$] (**8**$_U$), [(Ph-NHC)$_2$Pt$_2$Ag$_3$(Ph_2pz)$_4$]BF_4·($CHCl_3$)$_{3.5}$ (**9**·3.5$CHCl_3$)

	6	**7**·$CHCl_3$·0.5C_5H_{12}	**8**$_U$	**9**·3.5$CHCl_3$
Empirical formula	$C_{22}H_{29}ClN_6Pt$	$C_{47.5}H_{61}Ag_3BCl_3F_4N_{12}Pt_2$	$C_{44}H_{54}Ag_2N_{12}Pt_2$	$C_{84}H_{70}Ag_3BF_4N_{12}Pt_2$
Formula weight	608.05	1707.03	1356.91	2465.97
Temperature (K)	93(3)	93(3)	93(3)	93(3)
Wavelength (Å)	0.71075	0.71075	0.71075	0.71075
Crystal system	triclinic	triclinic	monoclinic	triclinic
Space group	*P*-1 (#2)	*P*-1 (#2)	$P2_1/n$ (#14)	*P*-1 (#2)
Unit cell dimensions				
a (Å)	8.6817(14)	12.845(3)	13.2708(16)	13.310(2)
b (Å)	10.4750(18)	13.262(3)	22.131(3)	13.993(3)
c (Å)	13.283(2)	16.821(3)	15.5897(18)	24.165(4)
α (deg)	100.065(3)	88.816(7)	90.0000	100.635(3)
β (deg)	91.495(3)	87.817(7)	92.7894(16)	90.315(3)
γ (deg)	101.561(3)	82.528(5)	90.0000	96.471(3)
V (Å^3)	1162.9(4)	2838.8(11)	4573.2(10)	4393.6(15)
Z	2	2	4	2
ρ_{calcd} (g/cm^3)	1.736	1.997	1.971	1.864
μ(Mo Kα) (mm^{-1})	6.144	6.103	6.961	4.1955
F(000)	596	1638	2608	2398
Index ranges	-10<=h<=10	-16<=h<=16	-17<=h<=17	-17<=h<=17
	-12<=k<=11	-17<=k<=12	-24<=k<=28	-18<=k<=18
	-15<=l<=15	-22<=l<=21	-20<=l<=14	-31<=l<=28
Reflections collected	8139	23695	37669	36992
Independent reflections	4043 [R_{int} = 0.0186]	12539 [R_{int} = 0.0411]	10470 [R_{int} = 0.0372]	19461 [R_{int} = 0.0375]
Data / restraints / parameters	4043 / 0 / 271	12539 / 7 / 649	10470 / 0 / 535	19461 / 81 / 1065
Goodness-of-fit on F^2	1.034	1.095	1.075	1.072
Final *R* index [$I>2\sigma(I)$][a]	R_1 = 0.0218	R_1 = 0.0670	R_1 = 0.0392	R_1 = 0.0721
R indices (all data)[a,b]	R_1 = 0.0187	R_1 = 0.0509	R_1 = 0.0330	R_1 = 0.0581
	wR_2 = 0.0451	wR_2 = 0.1235	wR_2 = 0.0596	wR_2 = 0.1556
Largest diff. peak and hole (eÅ^{-3})	0.69 and -0.69	3.38 and -2.05	1.44 and -1.04	3.77 and -2.62
CCDC number	1001723	1001724	1001727	1001725

[a] $R_1 = \sum||F_o| - |F_c||/\sum|F_o|$. [b] $wR_2 = [\sum w(F_o^2 - F_c^2)^2]/\sum[w(F_o^2)^2]]^{1/2}$.

4-4. Photophysical properties of complexes

4-4-1. UV/Vis absorption spectra and TD-DFT calculations

All of photophysical data of complexes **6**–**9** were summarized in **Table 4-2** (in DCM) and **4-3** (in the solid state). **Figure 4-44** shows UV/Vis absorption spectra of complexes **6**–**9**. The Pt_2Ag_3 complex **7** and Pt_2Ag_2 complex **8** having Me_2pz ligands isomerized in solution. The isomerization is faster than that of pyridyl-NHC analogue and starts just after dissolution. Thus, the UV/Vis absorption spectra of **7** and **8** exhibit superposition of the spectra of two isomers, respectively. These UV/Vis absorption spectra show higher-energy absorption bands at λ_{abs} < 270 nm, which may be assigned to singlet π-π^* transition. Mononuclear Pt(II) complex **6**

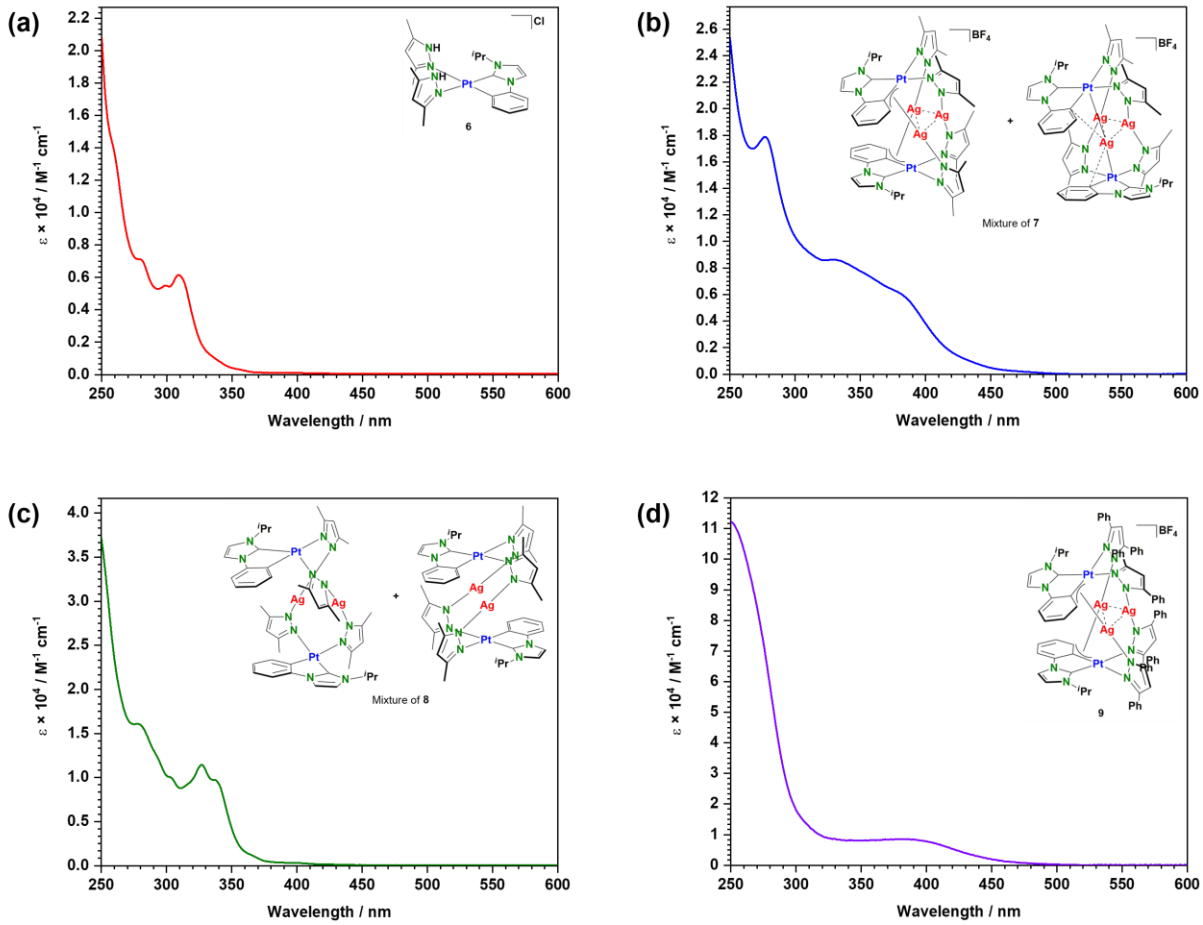

Figure 4-44. UV/Vis absorption spectra of (a) [(Ph-NHC)Pt($Me_2pzH)_2$]Cl (**6**), (b) [(Ph-NHC)$_2Pt_2Ag_3(Me_2pz)_4$]BF_4 (**7**), (c) [(Ph-NHC)$_2Pt_2Ag_2(Me_2pz)_4$] (**8**) and (d) [(Ph-NHC)$_2Pt_2Ag_3(Ph_2pz)_4$]BF_4 (**9**) in DCM at room temperature.

shows similar absorption spectrum with that of Pt(II) analogue having pyridyl-NHC chelate ligand in solution at room temperature (**Figure 4-44**a).[34] Thus the absorption bands at 300-350 nm are assigned to the singlet MLCT (Metal-to-Ligand Charge transfer) transition.

The Pt_2Ag_3 complexes **7** and **9** show several absorption bands between 270 nm and 480 nm, which are similar to the ppy analogue (**Figure 4-44**b,d).[21] The lowest-energy absorption bands of ppy analogue were assigned to the charge transfer transition from the pyrazolato ligand to the $Pt_2Ag_3(ppy)_2$ moiety, LMM'L'CT [pz → Pt/Ag/π^*(ppy)] transition. Thus, the lowest-energy absorption bands of Pt_2Ag_3 complex having Ph-NHC chelate ligand **7** and **9** may be assigned to LMM'L'CT [pz → Pt/Ag/π^*(Ph-NHC)] transition.

The UV/Vis absorption spectrum of the Pt_2Ag_2 complex **8** is shown in **Figure 4-44**c. The lowest-energy absorption bands in Pt_2Ag_2 analogues having bpy,[20] ppy,[21] and pyridyl-NHC chelate ligand (Chapter 3, complex **4**)[22] were assigned to the combination of LLCT and MLCT transitions. Thus, the lowest-energy absorption bands of the Pt_2Ag_2 complex **8** may also be assigned to the combination of LLCT [pz → π^*(Ph-NHC)] and MLCT [Pt → π^*(Ph-NHC)] transitions.

To shed light on the absorption spectra of complexes **6**–**8**, the absorption bands were theoretically investigated with the time-dependent density functional theory (TD-DFT) method (**Figure 4-45** to **47**, **Table 4-4** to **9**). The DFT calculation clearly visualized the highest-occupied molecular orbitals (HOMOs) and the lowest-unoccupied molecular orbitals (LUMOs) in the complexes. The LUMOs of the mononuclear Pt(II) complex **6** and the Pt_2Ag_2 complex **8** consist of the π^* orbital of the phenyl-NHC chelate ligand. Additionally, the LUMOs of **8** consist of the 4d orbital of Ag atoms. In constrast, the HOMOs of **6** and **8** consist of the π orbital of pyrazolato moieties and the 5d orbital of Pt atoms. These calculations suggest that the lowest-energy absorption bands of mononuclear Pt(II) complex **6** can be

assigned mainly to the combination of LLCT [pz → π^*(Ph-NHC)] and MLCT [Pt → π^*(Ph-NHC)] transitions. In addition M'LCT [Ag → π^*(Ph-NHC)] transitions further contribute to the lowest-energy absorption band in **8** due to the formation of heteropolynuclear Pt_2Ag_2 complex.

Table 4-2. Photophysical data for complexes **6**–**9** under air at room temperature in DCM. Complexes **7** and **8** immediately isomerized in solution after dissolution.

complex	λ_{abs} / nm ($\varepsilon \times 10^4$ M^{-1} cm^{-1})	λ_{em} / nm[a]	τ_1 (A_1) / μs	τ_2 (A_2) / μs
6	279 (0.71), 298 (0.55), 310 sh (0.61), 337 sh (0.1)	-	-	-
7	277 (1.80), 331 (0.91), 379 sh (0.62)	531	0.79	-
8	278 (1.60), 303 (1.00), 327 (1.15), 337 (0.97), 362 sh (0.14)	414, 436	1.40×10^{-3}	-
9	378 (0.85)	529	0.49	-

complex	τ_3 (A_3) / μs	τ_{ave} / μs	k_r / $\times 10^5$ s^{-1}	k_{nr} / $\times 10^5$ s^{-1}	Φ_{em} / %[a]
6	-	-	-	-	-
7	-	-	0.4	12.3	3
8	-	-	3.7×10^2	6.93×10^3	5
9	-	-	2.4	18.0	12

[a] λ_{ex} = 355 nm

Table 4-3. Photophysical data for complexes **6**–**9** under air at room temperature in the solid state

complex	λ_{abs} / nm ($\varepsilon \times 10^4$ M^{-1} cm^{-1})	λ_{em} / nm[a]	τ_1 (A_1) / μs	τ_2 (A_2) / μs
6	-	424, 450, 479	10.0 (0.87)	15.7 (0.13)
7	-	516	0.62 (0.60)	1.68 (0.40)
8	-	431, 457, 484	0.86 (0.69)	2.24 (0.31)
9	-	527	0.76 (0.66)	1.67 (0.34)

complex	τ_3 (A_3) / μs	τ_{ave} / μs	k_r / $\times 10^5$ s^{-1}	k_{nr} / $\times 10^5$ s^{-1}	Φ_{em} / %[a]
6	-	11.1	0.7	0.3	72
7	-	1.3	3.5	4.1	46
8	-	1.6	1.4	4.9	22
9	-	1.1	4.4	4.4	50

[a] λ_{ex} = 355 nm

On the other hand, the HOMOs of Pt_2Ag_3 complex **7** consist of the π orbital of the pyrazolato moieties and 5d orbital of Pt atom. Interestingly, the LUMOs consist of in-phase combination of 6p of two Pt atoms and 5p of two Ag atoms, which is also seen in $[Pt_2Ag_4(Me_2pz)_8]$ and $[Pt_2Au_2M_2(Me_2pz)_8]$ (M = Ag, Cu).[35,36] Thus, the lowest-energy absorption band of **7** may be assigned to LMM'L'CT [pz → Pt/Ag/π^*(Ph-NHC)] transition. The Pt_2Ag_3 complex **9** shows similar structure and arrangement of metal atoms to Pt_2Ag_3 complex **7** in the single crystal. Therefore, the Pt_2Ag_3 complex **9** seems to show similar composition of HOMO and LUMO.

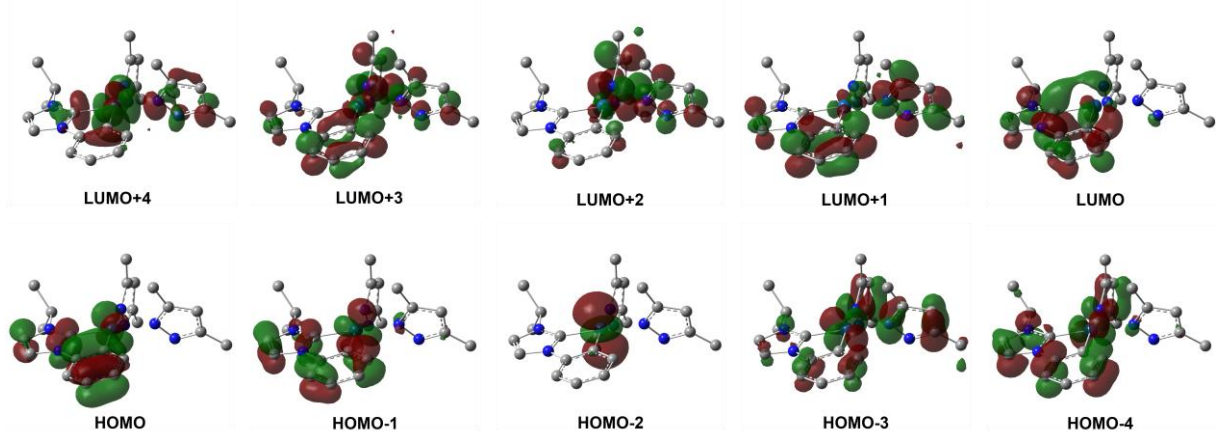

Figure 4-45. Molecular orbitals of the singlet state for $[\mathbf{6}]^{+}$.

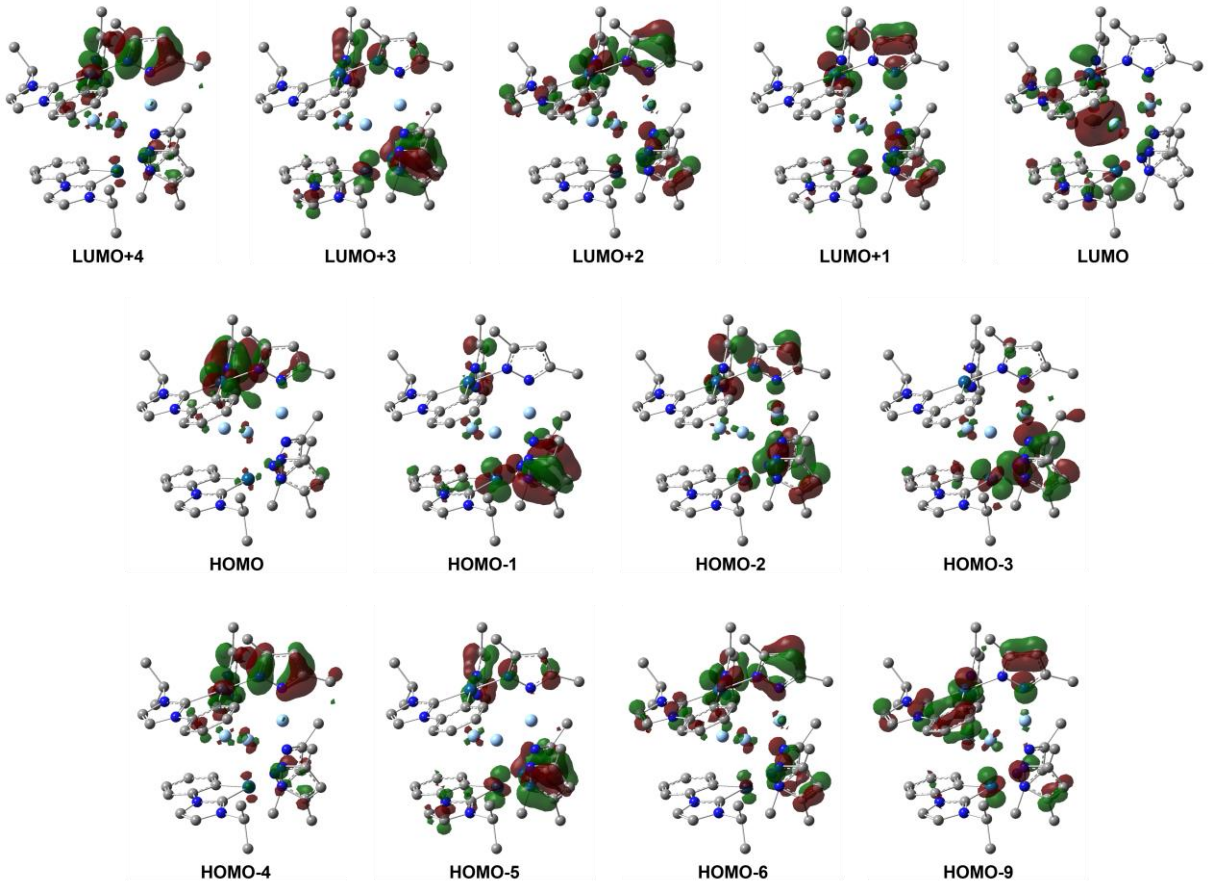

Figure 4-46. Molecular orbitals of the singlet state for $[\mathbf{7}]^{+}$.

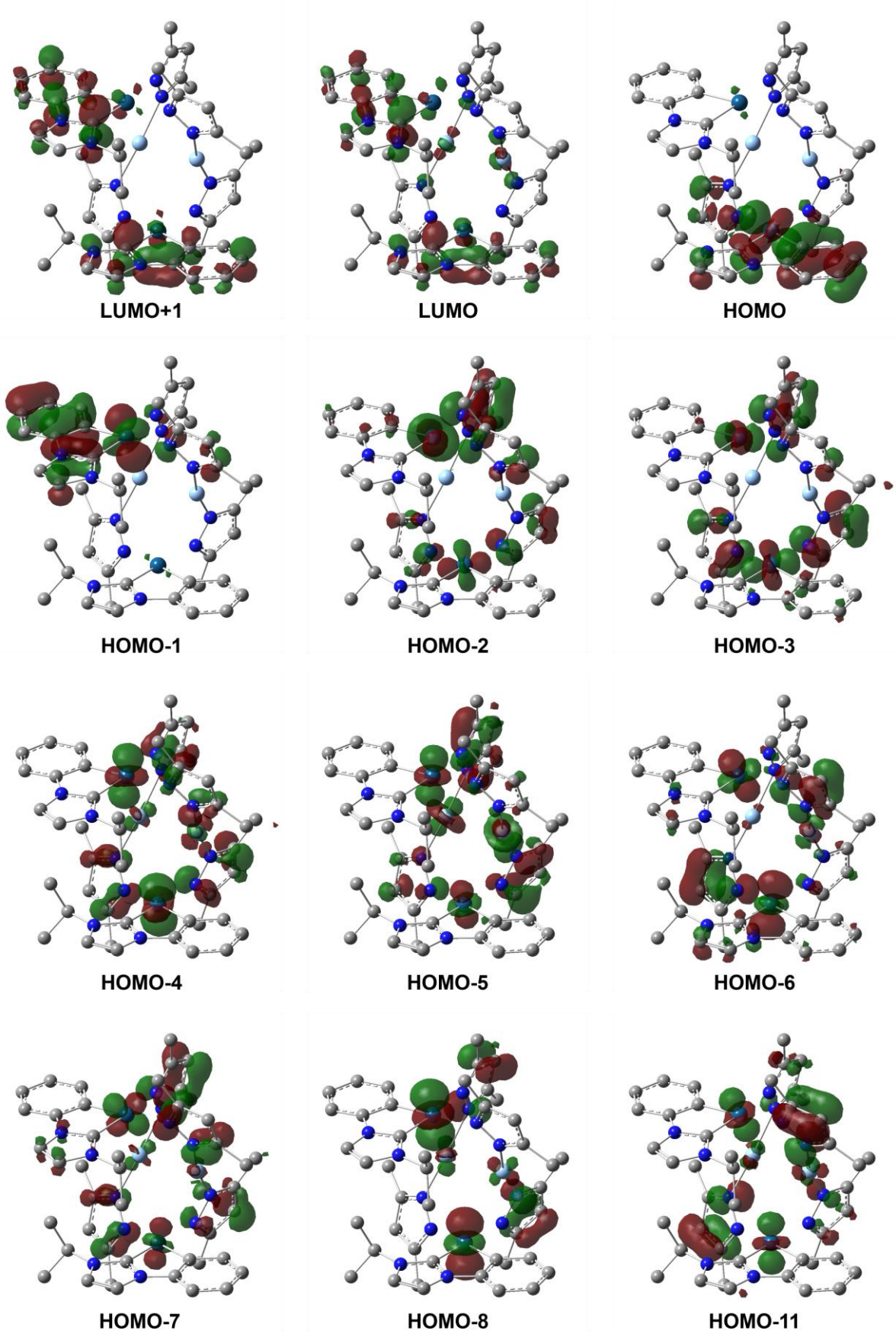

Figure 4-47. Molecular orbitals of the singlet state for **8**.

Table 4-4. Calculated Singlet Excited States (S_1–S_{25}) of $[\mathbf{6}]^{+}$.[a]

Excited State	Transition	Energy (Wavelength)	Oscillator Strength
S1	HOMO → LUMO	3.8040 eV (325.93 nm)	0.0038
S2	HOMO-2 → LUMO (73%) HOMO-1 → LUMO (27%)	4.4097 eV (281.16 nm)	0.0411
S3	HOMO-1 → LUMO	4.4460 eV (278.87 nm)	0.1331
S4	HOMO-4 → LUMO (19%) HOMO-3 → LUMO (52%) HOMO-2 → LUMO (10%) HOMO → LUMO+4 (19%)	4.5983 eV (269.63 nm)	0.0132
S5	HOMO → LUMO+1 (50%) HOMO → LUMO+4 (50%)	4.6768 eV (265.10 nm)	0.0182
S6		4.7535 eV (260.83 nm)	0.0728
S7		4.9243 eV (251.78 nm)	0.0064
S8		5.0365 eV (246.17 nm)	0.0006
S9		5.0711 eV (244.49 nm)	0.1246
S10		5.1455 eV (240.96 nm)	0.1583
S11		5.1888 eV (238.94 nm)	0.0741
S12		5.2275 eV (237.18 nm)	0.0024
S13		5.2790 eV (234.86 nm)	0.1977
S14		5.4343 eV (228.15 nm)	0.0034
S15		5.4542 eV (227.32 nm)	0.0045
S16		5.4659 eV (226.83 nm)	0.0007
S17		5.4678 eV (226.75 nm)	0.0067
S18		5.5135 eV (224.87 nm)	0.0084
S19		5.5417 eV (223.73 nm)	0.0197
S20		5.5769 eV (222.32 nm)	0.003
S21		5.6193 eV (220.64 nm)	0.0045
S22		5.6450 eV (219.64 nm)	0.0213
S23		5.7104 eV (217.12 nm)	0.0616
S24		5.7340 eV (216.23 nm)	0.0277
S25		5.7663 eV (215.01 nm)	0.0278

[a] Transition details for S6-S25 are omitted.

Table 4-5. Calculated Singlet Excited States (S_1–S_{25}) of [**7**]$^+$.[a]

Excited State	Transition	Energy (Wavelength)	Oscillator Strength
S1	HOMO-6 → LUMO (10%) HOMO-1 → LUMO (40%) HOMO → LUMO (50%)	2.9136 eV (425.53 nm)	0.0086
S2	HOMO-1 → LUMO	2.9302 eV (423.12 nm)	0.0175
S3	HOMO-9 → LUMO (16%) HOMO-6 → LUMO (19%) HOMO-4 → LUMO (65%)	3.0641 eV (404.63 nm)	0.0105
S4	HOMO-6 → LUMO (17%) HOMO-5 → LUMO (13%) HOMO-4 → LUMO (14%) HOMO-3 → LUMO (22%) HOMO-2 → LUMO (34%)	3.0700 eV (403.85 nm)	0.0048
S5	HOMO-2 → LUMO	3.1250 eV (396.75 nm)	0.0001
S6		3.1405 eV (394.79 nm)	0.0191
S7		3.1562 eV (392.83 nm)	0.0065
S8		3.2707 eV (379.07 nm)	0.0153
S9		3.2999 eV (375.72 nm)	0.0072
S10		3.3276 eV (372.60 nm)	0.076
S11		3.4326 eV (361.20 nm)	0.0759
S12		3.5527 eV (348.98 nm)	0.0001
S13		3.6161 eV (342.87 nm)	0.0531
S14		3.7913 eV (327.02 nm)	0.0241
S15		3.8634 eV (320.92 nm)	0.0408
S16		3.9113 eV (316.99 nm)	0.0048
S17		3.9168 eV (316.55 nm)	0.002
S18		4.0210 eV (308.34 nm)	0.0005
S19		4.0340 eV (307.35 nm)	0.0081
S20		4.0816 eV (303.77 nm)	0.0195
S21		4.1073 eV (301.86 nm)	0.0188
S22		4.1248 eV (300.59 nm)	0.0059
S23		4.1349 eV (299.85 nm)	0.012
S24		4.1654 eV (297.65 nm)	0.0146
S25		4.2194 eV (293.84 nm)	0.0078

[a] Transition details for S6-S25 are omitted.

Table 4-6. Calculated Singlet Excited States (S_1–S_{25}) of **8**.[a]

Excited State	Transition	Energy (Wavelength)	Oscillator Strength
S1	HOMO → LUMO (64%) HOMO → LUMO+1 (36%)	3.7184 eV (333.43 nm)	0.0080
S2	HOMO-1 → LUMO	3.7220 eV (333.11 nm)	0.0090
S3	HOMO-2 → LUMO	3.8983 eV (318.04 nm)	0.0120
S4	HOMO-8 → LUMO (16%) HOMO-3 → LUMO (84%)	3.9253 eV (315.86 nm)	0.0080
S5	HOMO-11 → LUMO (13%) HOMO-5 → LUMO (15%) HOMO-4 → LUMO (58%) HOMO-3 → LUMO+1 (14%)	4.0085 eV (309.30 nm)	0.0065
S6		4.0202 eV (308.40 nm)	0.1039
S7		4.1406 eV (299.44 nm)	0.0671
S8		4.1527 eV (298.56 nm)	0.0740
S9		4.2164 eV (294.05 nm)	0.0028
S10		4.2252 eV (293.44 nm)	0.0053
S11		4.2317 eV (292.99 nm)	0.0012
S12		4.3194 eV (287.04 nm)	0.0058
S13		4.3367 eV (285.89 nm)	0.0049
S14		4.3448 eV (285.36 nm)	0.0030
S15		4.3555 eV (284.66 nm)	0.0031
S16		4.3729 eV (283.53 nm)	0.0001
S17		4.4357 eV (279.51 nm)	0.0022
S18		4.4552 eV (278.29 nm)	0.0297
S19		4.5055 eV (275.19 nm)	0.0159
S20		4.5343 eV (273.44 nm)	0.0183
S21		4.5401 eV (273.08 nm)	0.0044
S22		4.5493 eV (272.54 nm)	0.0031
S23		4.5944 eV (269.86 nm)	0.0014
S24		4.6013 eV (269.46 nm)	0.0219
S25		4.6713 eV (265.42 nm)	0.0099

[a] Transition details for S6-S25 are omitted.

Table 4-7. Molecular-Orbital populations of [**6**]$^+$.

Molecular Orbital	MO population / %			
	Pt	Ph-NHC		Me_2pz
		Ph	NHC	
LUMO+3	6.42	24.16	8.60	60.82
LUMO+2	4.28	8.82	4.45	82.45
LUMO+1	5.92	31.52	12.21	50.35
LUMO	21.75	26.27	38.06	13.92
HOMO	30.91	44.16	23.34	1.59
HOMO-1	41.26	29.59	22.06	7.09
HOMO-2	92.15	3.32	1.89	2.64
HOMO-3	34.47	14.05	7.07	44.41

Table 4-8. Molecular-Orbital population of [**7**]$^+$

Molecular Orbital	MO population %						
	Pt	Ag (A)	Ag (B)	Ph-NHC		Me_2pz	
				Ph	NHC	(A)	(B)
LUMO+3	8.96	11.14	2.33	59.05	12.50	2.69	3.33
LUMO+2	3.29	8.56	1.83	61.28	22.25	0.95	1.84
LUMO+1	13.98	12.23	0.39	37.97	30.17	2.28	2.98
LUMO	21.39	26.09	3.35	19.12	14.77	9.88	5.40
HOMO	21.98	4.01	1.43	6.19	3.16	47.55	15.68
HOMO-1	22.32	4.82	1.14	8.49	4.66	45.78	12.79
HOMO-2	10.07	5.24	4.72	2.49	0.83	40.67	35.98
HOMO-3	15.50	3.84	3.32	7.88	1.89	19.74	47.83

* Me_2pz(A) and Me_2pz(B) are Me_2pz at trans-positions to phenyl and NHC moieties, respectively. Ag(A) and Ag(B) are the Ag atoms coordinated by Me_2pz(A) and that between two Me_2pz(B) moieties, respectively

Table 4-9. Molecular-Orbital populations of **8**.

Molecular Orbital	MO population / %					
	Pt	Ag	Ph-NHC		Me_2pz	
			Ph	NHC	(A)	(B)
LUMO+3	8.54	8.56	60.05	18.81	2.94	1.10
LUMO+2	4.96	8.14	56.59	25.14	2.39	2.78
LUMO+1	16.11	1.99	33.39	41.22	2.76	4.53
LUMO	17.76	8.94	23.88	33.58	7.92	7.92
HOMO	39.08	0.84	31.41	12.98	11.64	4.05
HOMO-1	38.81	0.80	32.75	13.84	10.43	3.37
HOMO-2	30.33	2.70	9.27	3.78	21.93	31.99
HOMO-3	28.28	0.81	9.88	4.65	23.31	33.07

* Me_2pz(A) and Me_2pz(B) are Me_2pz at trans-positions to phenyl and NHC moieties respectively.

4-4-2. Emission spectra of complexes

Although the mononuclear Pt(II) complex **6** did not display phosphorescence in solution at room temperature, it showed blue phosphorescence (λ_{max} = 450 nm) in the solid state (**Figure 4-48**a, **Table 4-3**). The Pt_2Ag_3 complex **7** which formed by the reaction of **6** with silver ions showed green emission color both in the solid state (solid line, λ_{max} = 516 nm) and in DCM (broken line, λ_{max} = 531 nm) (**Figure 4-48**b), though the emission band shifted ($\Delta\lambda_{max}$ = +66 nm) due to the formation Pt → Ag dative bond. The red-shift of emission band was also observed for the heteropolynuclear Pt_2Ag_3 complex having ppy chelate ligand and Pt → Ag dative bond.[21,37–39] The formation of Pt → Ag dative bond influenced on the excited state, and

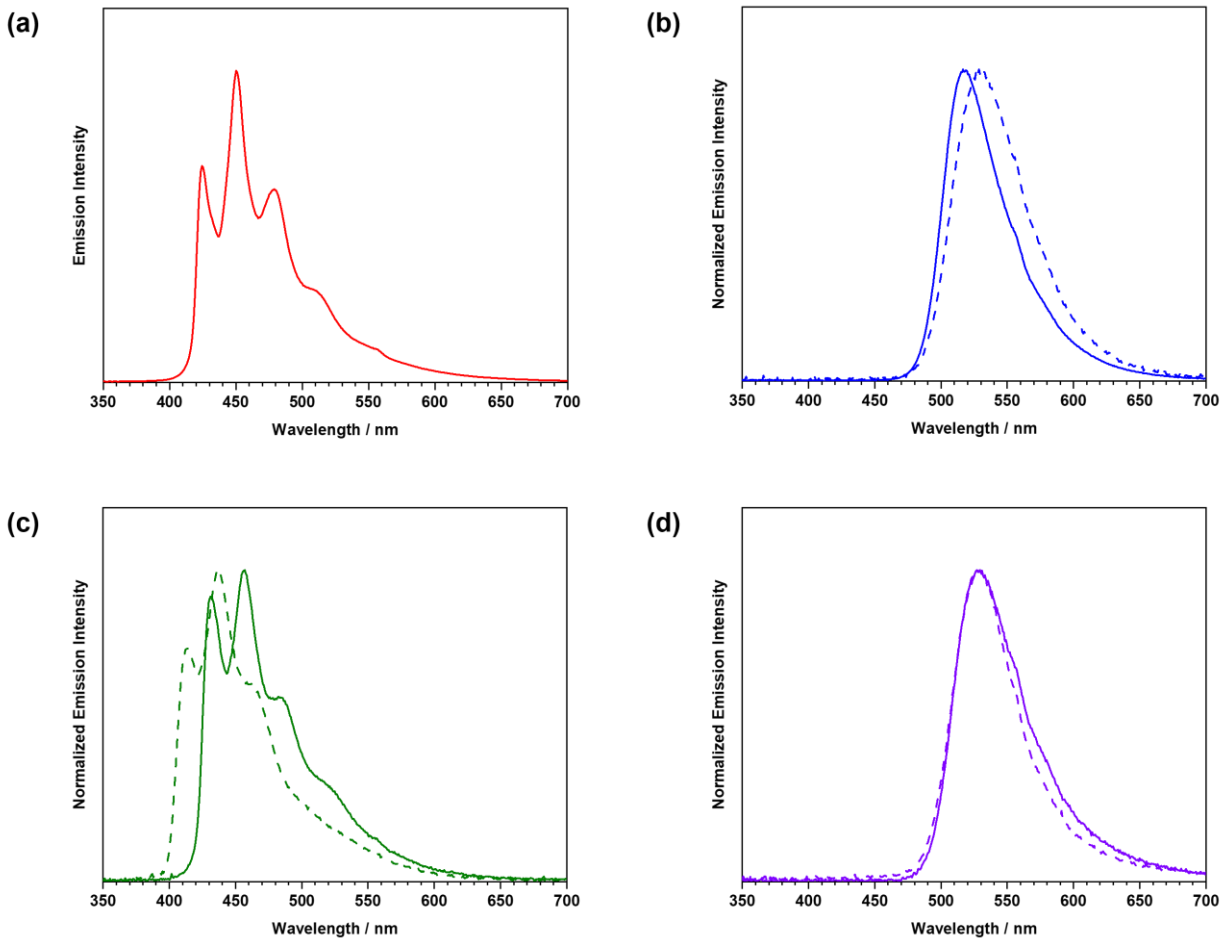

Figure 4-48. Emission spectra of (a) $[(Ph\text{-}NHC)Pt(Me_2pzH)_2]Cl$ (**6**), (b) $[(Ph\text{-}NHC)_2Pt_2Ag_3(Me_2pz)_4]BF_4$ (**7**), (c) $[(Ph\text{-}NHC)_2Pt_2Ag_2(Me_2pz)_4]$ (**8**) and (d) $[(Ph\text{-}NHC)_2Pt_2Ag_3(Ph_2pz)_4]BF_4$ (**9**) in the solid state (solid line) and DCM (broken line).

changed emission process. In other words, the mononuclear Pt(II) complex **6** showed phosphorescence that derived from ^{3}MLCT and ^{3}LLCT excited state. However, the Pt_2Ag_3 complex **7** showed phosphorescence that derived from ^{3}LMM'L'CT excited state due to the formation of Pt → Ag dative bond. The Pt_2Ag_3 complex having Ph_2pz ligand, **9**, have similar structure to **7**. Therefore, **9** showed similar photophysical properties (such as emission lifetime and emission spectrum) to **7** in the solid state. The Pt_2Ag_2 complex **8** that obtained by demetalation reaction of **7** with Cl^- showed blue phosphorescence in the solid state. It was elucidated that the formation of the Pt → Ag dative bond affect to phosphorescence properties. In DCM, the Pt_2Ag_3 complexes **7** and **9** showed different emission quantum yield (**Table 4-2**). Since, Me_2pz bridged Pt_2Ag_3 complex **7** showed fluxional behavior in solution, phosphorescence of **7** is quenched. On the other hand, since **9** has bulky substituent on the pyrazolato bridge and does not show fluxional behavior, **9** has higher emission quantum yield in DCM.

4-5. Conclusion

In summary, I synthesized a heteropolynuclear sandwich complexes having phenyl-NHC chelate ligand and Pt → Ag dative bond. The Pt_2Ag_3 complex having Me_2pz bridge showed fluxional behavior in solution and fluxional behavior was confirmed by 2D ^{1}H-^{1}H EXchange SpectroscopY (EXSY) at –50 ℃. The Pt_2Ag_2 complex was obtained by demetalation reaction of Pt_2Ag_3 complex having Me_2pz bridge with Cl^-. Although the as-prepared Pt_2Ag_2 complex exists as a mixture of two isomers, it selectively crystallized to afford only a U-shaped isomer in the solid state, allowing us to elucidate the thermodynamically favored isomer as well as the U to Z structural isomerization in solution. Since Pt_2Ag_3 complex having Ph_2pz bridge has bulky substituent on the pyrazolate, Pt_2Ag_3 complex did not show fluxional behavior in solution. The mononuclear Pt(II) complex and Pt_2Ag_2 complex showed high energy emission color in the solid

state. Although two Pt_2Ag_3 complexes showed similar emission spectra in solution and in the solid state, two Pt_2Ag_3 complexes showed different emission quantum yield. Since Pt_2Ag_3 complex having Ph_2pz bridge dose not show fluxional behavior, it has higher emission quantum yield. This study gives an insight into the relationship between fluxional behavior and photophysical properties, leading to a construction of new types of functional molecules incorporating both dynamic molecular systems and light-emitting properties.

4-6. Experimental section

4-6-1. Physical measurement

The 1D (^{1}H, ^{13}C) and 2D (^{1}H–^{1}H COSY, ^{1}H–^{13}C HSQC, ^{1}H–^{13}C HMBC) NMR spectra were obtained at 500 MHz Varian NMR system 500PS spectrometer. ^{1}H–^{1}H EXSY (Exchange spectroscopy), Variable temperature ^{1}H and ^{195}Pt NMR (H_2PtCl_6 in D_2O was used as an external standard: δ = 0 ppm) measurements were performed at 400 MHz with JEOL JNM-AL400, and δ value of ^{195}Pt NMR spectrum was obtained by eq. 2.1.

$$\nu\,(\mathrm{Hz}) = \mathrm{OBFRQ} + \mathrm{OBSET} + \mathrm{OBFIN} + \text{frequency of sample}$$

$$\delta\,(\mathrm{ppm}) = \frac{\nu_S - \nu_R}{\nu_R} \cdot 10^3 \qquad (2.1)$$

Electrospray ionization mass spectroscopy were recorded by Waters ACQUITY SQD MS system. Fast atom bombardment mass spectroscopy were obtained from JEOL JMS-700N. UV/Vis absorption spectra were recorded on a Jasco V-560 spectrophotometer at 298 K. Diffuse reflectance spectra were conducted by a Jasco V-670DS spectrophotometer at 293 K. The corrected emission spectra were obtained by using a Hamamatsu PMA-12 multichannel photodetector (λ_{ex} = 355 nm) at 293 K. Emission quantum yields were determined by using a Hamamatsu Photonic Absolute PL Quantum Yield Measurement System C9920-02 with an integrating sphere and a PMA-12 multichannel photodetector at 293 K. The emission lifetime measurements were conducted by using a Hamamatsu C11200 streak camera as a photodetector by exciting at 355 nm using a nanosecond Q-switched Nd:YAG laser (Continum® Minilite™, fwhm ≈ 10–12 ns, repetition rate = 10 Hz).

An average emission lifetime (τ_{ave}) was obtained by eq. 2.2. Also, radiative rate (k_r) and non-radiative rate (k_{nr}) of complexes were calculated by eq. 2.3 and 2.4.

$$\tau_{ave} = \frac{\tau_1 \cdot A_1^2 + \tau_2 \cdot A_2^2 + \tau_3 \cdot A_3^2}{\tau_1 \cdot A_1 + \tau_2 \cdot A_2 + \tau_3 \cdot A_3} \quad (2.2)$$

$$k_r = \frac{1}{\tau_{em}} - k_{nr} = \frac{\Phi_{em}}{\tau_{em}} \quad (2.3)$$

$$k_{nr} = k_r \left(\frac{1}{\Phi_{em}} - 1 \right) = \frac{1}{\tau_{em}} - k_r \quad (2.4)$$

4-6-2. Single crystal X-ray analysis

Diffraction data were collected at –180 ºC under a stream of cold N_2 gas on a Rigaku RA-Micro7 HFM instrument equipped with a Rigaku Saturn724+ CCD detector by using graphite-monochromated Mo-Kα radiation. The frame data were integrated using a Rigaku CrystalClear program package, and the data sets were corrected for absorption using a REQAB program. The calculations were performed with a CrystalStructure software package.[40] The initial structure was solved by Patterson methods (DIRDIF99-PATTY).[41] The structures were solved by direct methods (SHELXS-97),[42] and refined on F^2 by the full-matrix least squares methods. Anisotropic refinement was applied to all non-hydrogen atoms with the exception of the crystal solvents (SHELXL-2014/7).[43] All hydrogen atoms were put at calculated positions.

4-6-3. Computational method

Ground-state geometries of the complexes were optimized by using the B3LYP density functional theory (DFT). X-ray structures were used as initial geometries without any geometrical constraints. The LandL2DZ and 6-31G(d,p) basis sets were used to treat the platinum/silver and all other atoms, respectively. Time-dependent (TD)-DFT calculations were

then performed to estimate the energies and oscillator strengths *f* of the lowest energy singlet and triplet absorption transitions. All of the calculation was carried out as in DCM by using Polarizable Continuum Model (PCM). All calculations were carried out using the Gaussian 16W package.[44] Molecular orbitals with the isovalue of 0.04 were drawn by the Gauss View 5.[45]

4-7. Reference

(1) Kealy, T. J.; Pauson, P. L. *Nature* **1951**, *168* (42), 1039–1040.

(2) Murahashi, T.; Fujimoto, M.; Oka, M.; Hashimoto, Y.; Uemura, T.; Tatsumi, Y.; Nakao, Y.; Ikeda, A.; Sakaki, S.; Kurosawa, H. *Science* **2006**, *313* (5790), 1104–1107.

(3) Pan, F. X.; Li, L. J.; Wang, Y. J.; Guo, J. C.; Zhai, H. J.; Xu, L.; Sun, Z. M. *J. Am. Chem. Soc.* **2015**, *137* (34), 10954–10957.

(4) Horiuchi, S.; Tachibana, Y.; Yamashita, M.; Yamamoto, K.; Masai, K.; Takase, K.; Matsutani, T.; Kawamata, S.; Kurashige, Y.; Yanai, T.; Murahashi, T. *Nat. Commun.* **2015**, *6*, 1–8.

(5) Murahashi, T.; Shirato, K.; Fukushima, A.; Takase, K.; Suenobu, T.; Fukuzumi, S.; Ogoshi, S.; Kurosawa, H. *Nat. Chem.* **2011**, *4* (1), 52–58.

(6) Masai, K.; Shirato, K.; Yamamoto, K.; Kurashige, Y.; Murahashi, T. *Chem. Commun.* **2016**, *52* (38), 6427–6430.

(7) Schmidbaur, H.; Schier, A. *Chem. Soc. Rev.* **2012**, *41* (1), 370–412.

(8) Schmidbaur, H.; Schier, A. *Angew. Chem. Int. Ed.* **2015**, *54* (3), 746–784.

(9) Fujisawa, K.; Ishikawa, Y.; Miyashita, Y.; Okamoto, K. I. *Inorg. Chim. Acta* **2010**, *363* (12), 2977–2989.

(10) Morishima, Y.; Young, D. J.; Fujisawa, K. *Dalton Trans.* **2014**, *43* (42), 15915–15928.

(11) Rawashdeh-Omary, M. A.; Rashdan, M. D.; Dharanipathi, S.; Elbjeirami, O.; Ramesh, P.; Dias, H. V. R. *Chem. Commun.* **2011**, *47* (4), 1160–1162.

(12) Jayaratna, N. B.; Olmstead, M. M.; Kharisov, B. I.; Dias, H. V. R. *Inorg. Chem.* **2016**, *55* (17), 8277–8280.

(13) Rasika Dias, H. V.; Palehepitiya Gamage, C. S. *Angew. Chem. Int. Ed.* **2007**, *46* (13), 2192–2194.

(14) Omary, M. A.; Mohamed, A. A.; Rawashdeh-Omary, M. A.; Fackler, J. P. *Coord. Chem. Rev.* **2005**, *249* (13–14), 1372–1381.

(15) Jayaratna, N. B.; Hettiarachchi, C. V.; Yousufuddin, M.; Rasika Dias, H. V. *New J. Chem.* **2015**, *39* (7), 5092–5095.

(16) Omary, M. A.; Rawashdeh-Omary, M. A.; Gonser, M. W. A.; Elbjeirami, O.; Grimes, T.; Cundari, T. R.; Diyabalanage, H. V. K.; Palehepitiya Gamage, C. S.; Dias, H. V. R. *Inorg. Chem.* **2005**, *44* (23), 8200–8210.

(17) Hahn, R.; Bohle, F.; Fang, W.; Walther, A.; Grimme, S.; Esser, B. *J. Am. Chem. Soc.* **2018**, *140* (51), 17932–17944.

(18) Hahn, R.; Bohle, F.; Kotte, S.; Keller, T. J.; Jester, S. S.; Hansen, A.; Grimme, S.; Esser, B. *Chem. Sci.* **2018**, *9* (14), 3477–3483.

(19) Tekarli, S. M.; Cundari, T. R.; Omary, M. A. *J. Am. Chem. Soc.* **2008**, *130* (5), 1669–1675.

(20) Nishihara, K.; Ueda, M.; Higashitani, A.; Nakao, Y.; Arikawa, Y.; Horiuchi, S.; Sakuda, E.; Umakoshi, K. *Dalton Trans.* **2016**, *45* (12), 4978–4982.

(21) Ueda, M.; Horiuchi, S.; Sakuda, E.; Nakao, Y.; Arikawa, Y.; Umakoshi, K. *Chem. Commun.* **2017**, *53* (48), 6405–6408.

(22) Horiuchi, S.; Moon, S.; Sakuda, E.; Ito, A.; Arikawa, Y.; Umakoshi, K. *Dalton Trans.* **2018**, *47* (21), 7113–7117.

(23) Tenne, M.; Metz, S.; Wagenblast, G.; Münster, I.; Strassner, T. *Dalton Trans.* **2015**, *44* (18), 8444–8455.

(24) Tenne, M.; Metz, S.; Wagenblast, G.; Münster, I.; Strassner, T. *Organometallics* **2015**, *34* (18), 4433–4440.

(25) Munakata, M.; Wu, L. P.; Ning, G. L. *Coord. Chem. Rev.* **2000**, *198* (1), 171–203.

(26) Dias, H. V. R.; Fianchini, M.; Cundari, T. R.; Campana, C. F. *Angew. Chem. Int. Ed.* **2008**, *47* (3), 556–559.

(27) Fianchini, M.; Dai, H.; Dias, H. V. R. *Chem. Commun.* **2009**, 6373–6375.

(28) Baudron, S. A. *Coord. Chem. Rev.* **2019**, *380*, 318–329.

(29) Ibad, M. F.; Schulz, A.; Villinger, A. *Organometallics* **2019**, *38* (7), 1445–1458.

(30) Arnal, L.; Fuertes, S.; Martín, A.; Sicilia, V. *Chem. Eur. J.* **2018**, *24* (37), 9377–9384.

(31) Back, O.; Henry-Ellinger, M.; Martin, C. D.; Martin, D.; Bertrand, G. *Angew. Chem. Int. Ed.* **2013**, *52* (10), 2939–2943.

(32) Huynh, H. V. *Chem. Rev.* **2018**, *118* (19), 9457–9492.

(33) Nelson, D. J.; Nolan, S. P. *Chem. Soc. Rev.* **2013**, *42* (16), 6723–6753.

(34) Ogawa, T.; Sameera, W. M. C.; Saito, D.; Yoshida, M.; Kobayashi, A.; Kato, M. *Inorg. Chem.* **2018**, *57* (22), 14086–14096.

(35) Umakoshi, K.; Kojima, T.; Saito, K.; Akatsu, S.; Onishi, M.; Ishizaka, S.; Kitamura, N.; Nakao, Y.; Sakaki, S.; Ozawa, Y. *Inorg. Chem.* **2008**, *47* (12), 5033–5035.

(36) Akatsu, S.; Kanematsu, Y.; Kurihara, T. A.; Sueyoshi, S.; Arikawa, Y.; Onishi, M.; Ishizaka, S.; Kitamura, N.; Nakao, Y.; Sakaki, S.; Umakoshi, K. *Inorg. Chem.* **2012**, *51* (15), 7977–7992.

(37) Forniés, J.; Sicilia, V.; Casas, J. M.; Martín, A.; López, J. A.; Larraz, C.; Borja, P.; Ovejero, C. *Dalton Trans.* **2011**, *40* (12), 2898–2912.

(38) Baya, M.; Belío, Ú.; Forniés, J.; Martín, A.; Perálvarez, M.; Sicilia, V. *Inorg. Chim. Acta* **2014**, *424*, 136–149.

(39) Forniés, J.; Ibáñez, S.; Lalinde, E.; Martín, A.; Moreno, M. T.; Tsipis, A. C. *Dalton Trans.* **2012**, *41* (12), 3439–3451.

(40) CrystalStructure 4.2: Crystal Structure Analysis Package, Rigaku Corporation, Tokyo, Japan, 2000-2017.

(41) Beurskens, P. T.; Beurskens, G.; Gelder, R. de; Gracia-Granda, S.; Israel, R.; Gould, R. O.; Smits, J. M. M. *The DIRDIF99 Program System*, **1999**, Technical Report of the Crystallography Laboratory, University of Nijimegen, The Netherlands.

(42) Sheldrick, G. M. *Acta Cryst.* **2008**, *A64*, 112-122.

(43) Sheldrick, G. M. *Acta Cryst.* **2015**, *C71*, 3-8.

(44) Gaussian 16, Revision A.03, Frisch, M. J.; Trucks, G. W.; Schlegel, H. B.; Scuseria, G. E.; Robb, M. A.; Cheeseman, J. R.; Scalmani, G.; Barone, V.; Petersson, G. A.; Nakatsuji, H.; Li, X.; Caricato, M.; Marenich, A. V.; Bloino, J.; Janesko, B. G.; Gomperts, R.; Mennucci, B.; Hratchian, H. P.; Ortiz, J. V.; Izmaylov, A. F.; Sonnenberg, J. L.; Williams-Young, D.; Ding, F.; Lipparini, F.; Egidi, F.; Goings, J.; Peng, B.; Petrone, A.; Henderson, T.; Ranasinghe, D.; Zakrzewski, V. G.; Gao, J.; Rega, N.; Zheng, G.; Liang, W.; Hada, M.; Ehara, M.; Toyota, K.; Fukuda, R.; Hasegawa, J.; Ishida, M.; Nakajima, T.; Honda, Y.; Kitao, O.; Nakai, H.; Vreven, T.; Throssell, K.; Montgomery, J. A., Jr.; Peralta, J. E.; Ogliaro, F.; Bearpark, M. J.; Heyd, J. J.; Brothers, E. N.; Kudin, K. N.; Staroverov, V. N.; Keith, T. A.; Kobayashi, R.; Normand, J.; Raghavachari, K.; Rendell, A. P.; Burant, J. C.; Iyengar, S. S.; Tomasi, J.; Cossi, M.; Millam, J. M.; Klene, M.; Adamo, C.; Cammi,

R.; Ochterski, J. W.; Martin, R. L.; Morokuma, K.; Farkas, O.; Foresman, J. B.; Fox, D. J. Gaussian, Inc., Wallingford CT, 2016.

(45) GaussView, Version 5, Dennington, Roy; Keith, Todd A.; Millam, John M. Semichem Inc., Shawnee Mission, KS, 2009.

Chapter 5

General conclusions

5-1. General conclusion

The metal···metal interaction is a very large research area that has been studying for more than half a century. When intra- and intermolecular metal···metal distance is shorter than the sum of van der waals radius of each metal atoms, metal atoms show intra- and/or intermolecular metal···metal interactions. Strength of the metal···metal interactions in the ground state can be estimated by the intra- and intermolecular metal···metal distances. Additionally, the metal···metal interaction in the excited state is recognized by the change of emission energy. The metal complex consisting of multiple metal atoms is called polynuclear metal complex. For the synthesis of polynuclear metal complex consisting of heterometal atoms, a careful molecular design and development of reasonable synthetic method are required to control geometrical structure and introduce heterometal atoms at the desired position in the complex. Fine turning of emission energy can be achieved by introducing different heterometal atoms.

In this thesis, a new system of heteropolynuclear platinum complexes having N-heterocyclic carbene chelate ligand have been constructed, and structural and photophysical properties of these heteropolynuclear complexes were elucidated.

First, the effect of Py-NHC chelate ligand on the structure and photophysical properties of the butterfly-shaped dinuclear Pt(II) complex having Me_2pz bridging ligands, $[(Py\text{-}NHC)_2Pt_2(\mu\text{-}Me_2pz)_2](BF_4)_2$ (**2**), was studied. The single crystal X-ray analysis revealed that butterfly-shaped dinuclear Pt(II) complex having pyridyl-NHC chelate ligands has infinite one dimensional pore in the crystal lattice. The intramolecular Pt···Pt distance in the Pt_2 complex **2** (3.129(9) Å) is shorter than those in analogous Pt_2 complexes having Me_2pz bridging ligands. Although complexes having pyridyl-NHC chelate ligand did not show emission in solution, it displayed phosphorescence in the solid state at room temperature. The Pt_2 complex showed bluish-green emission color. The lowest-energy absorption bands are mainly assigned

to the combination of MLCT and LLCT transitions. This study gives an insight into the tuning of emission energy of butterfly-shaped Pt_2 complexes having C^N chelate ligands.

I have also succeeded in the synthesis of heteropolynuclear platinum complex, $[(Py\text{-}NHC)_2Pt_2Ag_2(Me_2pz)_4](PF_6)_2$ (**4**), by the reaction of mononuclear Pt(II) complex having pyridyl-NHC chelate ligand and dimethyl pyrazole with Ag(I) ion. Although the as-prepared Pt_2Ag_2 complex exists as a mixture of two stereo isomers in solution, it selectively crystallized to afford only a U-shaped isomer in the solid state, allowing us to elucidate the thermodynamically favored isomer as well as the U to Z structural isomerization in solution.

The Pt_2Ag_2 complex having pyridyl-NHC chelate ligands, **4**, showed higher emission energy than the Pt_2Ag_2 analogues having other aromatic C^N chelate ligands like 2-phenylpyridine derivatives. This is probably due to the strong σ-donating ability of the carbene carbon atom on the Py-NHC ligand. These results give us new insight into the relationship between structural transformations and photophysical properties involving weak intramolecular metal-metal interactions, leading to a construction of new types of functional molecules incorporating both dynamic molecular systems and light-emitting properties.

When the phenyl-NHC ligand was employed as a chelate ligand, the Pt_2Ag_3 complex, $[(Ph\text{-}NHC)_2Pt_2Ag_3(Me_2pz)_4]BF_4$ (**7**), formed directly by the reaction of mononuclear Pt(II) complex with Ag(I) ions. The Pt_2Ag_3 complex having Me_2pz bridge exhibited fluxional behavior in solution, because of the existence of equilibrium between two stereoisomers. Although only one of the two stereoisomers has been structurally characterized, the structure of the rest of isomer was assumed by the comparison with Pt_2Ag_3 analogue having ppy chelate ligand. Additionally, when Ph_2pz was employed a bridging ligand, the fluxional behavior was not observed. The Pt_2Ag_2 complex having phenyl-NHC chelate ligand, $[(Ph\text{-}NHC)_2Pt_2Ag_2(Me_2pz)_4]$ (**8**), also showed U- to Z- isomerization in solution. This fluxional

behavior is similar to that of Pt_2Ag_2 complex having pyridyl-NHC chelate ligands, though the Pt_2Ag_2 complex having phenyl-NHC chelate ligands showed faster isomerization.

Although, mononuclear Pt(II) complexes having phenyl-NHC chelate ligand did not show phosphorescence in solution, it displayed strong emission in the solid state. The corresponding Pt_2Ag_2 and Pt_2Ag_3 complexes showed blue and green emission, respectively. Since the Pt_2Ag_3 complex having Ph_2pz bridge, $[(Ph\text{-}NHC)_2Pt_2Ag_3(Ph_2pz)_4]BF_4$ (**9**), did not show fluxional behavior in solution, it showed stronger phosphorescence than Pt_2Ag_3 complex **7** having Me_2pz bridge in solution.

5-2. Future perspective

In this thesis, I revealed the formation process of heteropolynuclear Pt-Ag complexes and their fluxional behavior in solution, which was followed by NMR spectroscopy. In addition, mononuclear Pt(II) complex having Ph-NHC chelate ligand showed strong blue emission in the solid state. Heteropolynuclear Pt-Ag complexes (Pt_2Ag_2 and Pt_2Ag_3) having Ph-NHC chelate ligand showed green emission both in the solid state and in solution. Furthermore, the inhibition of isomerization by introducing bulk substituent group in the bridging ligand led to stronger emission in solution. From these results, it is expected that this study can contribute to the design and development of new emitting materials which enable fine turning of emission energy.

Publication List

(1) "U- to Z-Shape Isomerization in a Pt_2Ag_2 Framework Containing Pyridyl-NHC Ligands"

Horiuchi, S.; **Moon, S.**; Sakuda, E.; Ito, A.; Arikawa, Y.; Umakoshi, K. *Dalton Trans.* **2018**, *47* (21), 7113–7117.

(2) "Synthesis and Photophysical Properties of Butterfly-Shaped Dinuclear Pt(II) Complex Having NHC-Based Chelate Ligands"

Moon, S.; Horiuchi, S.; Sakuda, E.; Ito, A.; Arikawa, Y.; Umakoshi, K. *Inorg. Chim. Acta* **2019**, *493*. 43–48

Thanks to

本研究を行うにあたり，終始暖かい激励とご指導，ご鞭撻をして頂いた長崎大学大学院工学研究科馬越　啓介教授，有川　康弘准教授，作田　絵里准教授，堀内　新之介助教，長岡　順子技術専門職員，鳥巣　恵美事務補佐員に心より感謝申し上げます。

理論計算をして頂いた高知工科大学の伊藤　亮孝講師，長崎大学研究開発推進機構の大浜　祐七郎さん，地福　寿史さん，津田　信明さん，岩田　光さんにお礼申し上げます。

留学を始め，研究室での生活，実験のテクニックや勉強をする際，熱く手伝ってくださった中村　卓生博士, 川手　崇裕先輩, 竹内　悠樹先輩, 西原　一樹先輩, 田口　響己先輩，同級生の上田　美沙，竹本　頌子，田中　寛隆，仁部　優也，東　剛史，丸田弘成，山口　佑にお礼申し上げます。

2020 年 1 月 31 日　MOON SANGJOON